UNIVERSITY OF SOUTHAMPTON

FACULTY OF ENGINEERING, SCIENCE AND MATHEMATICS

SCHOOL OF ENGINEERING SCIENCES

MATERIALS RESEARCH GROUP

MICROSTRUCTURAL MODELLING OF FATIGUE IN LAYERED BEARING ARCHITECTURES

BY

Muhammad Sarfraz Ali

Thesis for the degree of Doctor of Philosophy

June 2007

UNIVERSITY OF SOUTHAMPTON

ABSTRACT

FACULTY OF ENGINEERING, SCIENCE & MATHEMATICS

SCHOOL OF ENGINEERING SCIENCE

MATERIALS RESEARCH GROUP

Doctor of Philosophy

MICROSTRUCTURAL MODELLING OF FATIGUE IN LAYERED BEARING ARCHITECTURES

BY

Muhammad Sarfraz Ali

Small automotive plain engine bearings are used to provide the relative motion between the engine block and the crankshaft via the connecting rod. Under rapidly changing engine loads, these bearings may suffer fatigue damage during service. In modern multilayered bearing designs, fatigue resistance is a complex function of engine loading coupled with the layer architecture and a multiphase lining alloy. This research has mostly focussed upon micro-scale fatigue damage initiation on thin (0.2-0.3mm thickness) lining surface and its subsequent growth leading towards gross failure. The systems examined comprise *Al* alloys and sintered bronze as relatively soft and conformable lining layers. The weight percent composition of *Al* lining alloy was *Al-6.5Sn-2.5Si-1Cu-1Ni-0.25Mn* roll bonded to a stiffer and thicker backing steel layer (1.5-1.8mm thick) via an even thinner *Al* foil (0.04mm) as an interlayer. The other system comprised an *Al* lining (*Al-20Sn–1Cu*) alloy spray coated on to a medium carbon steel layer in the form of a flat bar. All these systems were compared with the previously investigated *Al* based designs with lining compositions: *Al-12Sn-4Si-1Cu* and *Al-20Sn-1Cu-0.25Mn* (manufactured by roll bonding processes). The performance evaluation was based upon the investigation of microstructural features involved in early fatigue initiation and their effect upon short crack growth on the surface. Subsurface crack growth through the layers has also been assessed and finally the observed fatigue life of various components linked to these behaviours. A 3-point bend test configuration was adopted for laboratory fatigue tests. Fatigue comparison was made on the basis of lining surface plastic strain amplitude vs. number of cycles to failure according to a uniform predefined criterion for all the systems. Maximum plastic strains developing at the lining surface were estimated using a combination of finite element analysis (FEA) and strain gauge measurements so that the fatigue life of all systems studied was presented as strain-life data. Specimens in the form of both finished bearings and flat bars were tested. Similar fatigue behaviour was observed for the two testing geometries, giving greater confidence in the fatigue evaluation process and allowing detailed observations of small crack initiation and growth processes in flat bars to be related to behaviour of the actual bearing geometry.

In the previous research, the coarser *Si* particles in the *Al-12Sn-4Si-1Cu* lining and *Sn* particles in the *Al-20Sn-1Cu-0.25Mn* alloys were identified as potential crack initiation sites, though the relationship between particle geometry and arrangement/clustering was found to be important. The newly developed *Al-6.5Sn-2.5Si-1Cu-1Ni-0.25Mn* lining alloy with finer and fewer *Sn* and *Si* particles showed a delayed initiation of short fatigue cracks compared to the previous systems. However, a large number of widely scattered intermetallics in the new linings were observed to fracture causing early fatigue initiation at the micro-scale level with some more complex processes of detaching *Sn* layers from harder intermetallics and *Si* particles. Using the mechanical property data for bulk lining and secondary phase particles obtained from tensile testing and instrumented hardness testing, stress fields were investigated within the hard particles (intermetallics), surrounding thin layers and the matrix on the basis of the analytical and numerical modelling. On the basis of these modelling results, optimum particle shapes were defined to minimize tensile stresses (within the particles) and hydrostatic stresses (at the particle matrix interfaces). The experimental growth data of a dominant crack when combined with a *Hobson* type growth model based upon measured particle distributions and experimental crack growth rates, helped in predicting fatigue life of a similar component at different stress levels. Surface crack driving force reduces considerably when subsurface crack deflection occurred within softer *Al* interlayer. Replacing this interlayer with a harder brazed sheet did not give any significant difference in the observed fatigue life. In the HVOF systems, crack initiation was observed to be from the weaker interface between a harder matrix and softer circular unmelts as well as from various scattered pores. The overall fatigue life of the HVOF systems was comparable to the previous roll bonded systems; however subsurface deflection of crack at the lining-backing interface resulted in the debonding of the lining and hence the observed lining fatigue resistance may not be a good indication of the overall performance in a bearing system.

At similar lining surface plastic strain levels, the bronze bearing with very thin *Sn* and *Ni* as overlay layers (~7 microns each) showed comparable fatigue resistance to the currently investigated RB *Al* based designs. However annealing this system resulted in the formation of hard Ni_3Sn intermetallics at the *Sn-Ni* interface, and the observed fatigue resistance of this system was higher than the RB systems. This has been linked to very fine scale local crack deflection in the overlay layers (although these have not been observed clearly).

All these layered bearing systems provide a complex fatigue problem. Factors which reduce initiation /early growth behaviour are likely to offer the best service performance enhancements in view of the relatively HCF nature expected in service.

DECLARATION OF AUTHORSHIP

I, Muhammad Sarfraz Ali, declare that the thesis entitled Microstructural modelling of fatigue in layered bearing architecture and the work presented in the thesis are both my own and have been generated by me as the result of my own original research. I confirm that:

- this work was done wholly or mainly while in candidature for a research degree at this University;
- where I have consulted the published work of others, this is always clearly attributed;
- where I have quoted from the work of others, the source is always given. With the exception of such quotations, this thesis is entirely my own work;
- I have acknowledged all main sources of help;
- where the thesis is based on work done by myself jointly with others, I have made clear exactly what was done by others and what I have contributed myself;
- parts of this work have been published as journal/conference proceedings:

  - M.C. Mwanza[1], M.S. Ali[1], S. Syngellakis[1], C. Perrin[2] and P.A.S. Reed[1], Fatigue evaluation of novel HVOF spray coated Al bearing alloys, Al alloy conference ICAA9, (2004), Australia.
  - M.S.Ali[1], P.A.S. Reed[1], S.Syngellakis[2], A comparison of fatigue performance of conventional roll bonded and HVOF spray coated Al bearing alloys, 9th international Fatigue Congress (2006), Atlanta, USA.
  - M.S. Ali[1, a], P.A.S. Reed[1, b], S. Syngellakis[2,c], Carl Perrin[3,d], Microstructural factors affecting fatigue initiation in various Al based bearing alloys, Mat. Sc. Forum, Vol 519-521 (2006), pp1071-1076

Signed: Muhammad Sarfraz Ali

Date: 13/06/07

Acknowledgement

The completion of this research was not possible without the support of a number of people from Materials Research Group; however, my supervisors Professor Philippa Reed and Dr. Stavrous Syngellakis made the most important contribution in this regard. I am extremely grateful for their dedicated supervision, constant encouragement and helpful discussions during the course of this work.

I would like to acknowledge the financial and materials support of Dana Glacier Vandervell Bearings, UK and School of Engineering Sciences, University of Southampton, UK. Dr. Carl Perrin (Director R & D DGV) deserves special gratitude for his participation in technical discussions and providing necessary data.

I am also grateful to Dr. Mathew Mwanza for his assistance during initial experimental work and providing me some of his experimental data.

I would like to acknowledge Dr Sunchai Wang and my colleague Andrew Moffat for their assistance in using some equipment.

I also acknowledge the support of technical and clerical staff; Dave Beckett, Eric Bonner, Bob Barnes and Gwyneth Skiller. Apart from that, I am also equally grateful to all other colleagues who provided me an amiable environment for the successful completion of this research.

At last but not least, I am grateful to my parents (Shamim Akhtar and M. Ali), siblings and my wife Dr. Saima for their constant support and encouragement.

LIST OF SYMBOLS

A	Area
A_f	Area fraction
a	Half the length of a crack (µm)
c	Subsurface length of crack (µm)
C	Paris constant
d_{CTOD}	Crack tip opening displacement
D	Deflected length
d_{mean}	Mean neighbour distance
E	Elastic modulus (MPa)
H_n	Nano-hardness number (GPa)
K	Stress intensity factor (MPa $(m)^{1/2}$)
K_{eff}	Effective stress intensity factor
N	Number of cycles
N_f	Number of cycles to failure
N_i	Crack initiation life
P	Load (in Kgs or Newtons)
r_a	Aspect ratio
UTS	Ultimate tensile strength (MPa)
V_f	Volume fraction
σ_e	Engineering stress (MPa)
σ_{true}	True stress (MPa)
σ_y	Yield stress (MPa)
$\sigma_{0.2}$	0.2% proof stress (MPa)
σ_{max}	Maximum tensile stress at the lining surface (MPa)
σ_{grad}	Stress gradient (MPa/mm)
σ_h	Hydrostatic pressure
σ_t	Tensile stress
ε_e	Engineering strain
ε_{true}	True strain
ε_t	Total strain at the lining surface
ε_p	Plastic strain at the lining surface

ε_s	Plastic shear strain intensity
$\Delta\varepsilon_p$	Plastic strain range
ΔK	Stress intensity factor
ν	Poisson's ratio

LIST OF ACRONYMS

BEI	Back scattered electron image
EBSD	Electron back scattered diffraction
EDX	Energy dispersive X-rays
FBT	Finite body tessellation
FEA	Finite element analysis
FEG SEM	Field emission gun SEM
HCF	High cycle fatigue
HVOF	High velocity oxy-fuel
LEFM	Linear elastic fracture mechanics
L.A.F	Local area fraction
LCF	Low cycle fatigue
MSC	Microstructurally short fatigue cracks
OM	Optical microscopy
PSB	Persistent slip bands
PSC	Physically short fatigue cracks
RB	Roll bonding
SEI	Secondary electron image
SEM	Scanning electron microscope/microscopy
TEM	Transmission electron microscope/ microscopy

TABLE OF CONTENTS

LIST OF TABLES

LIST OF FIGURES

1 INTRODUCTION

Plain automotive journal bearings form an important part of the internal combustion engine and may suffer a complex combination of various types of failures under normal engine operating conditions. The premature causes of failure are fatigue, sliding surface wear and erosion due to cavitation phenomena. 'Fatigue failure' of engine bearings is the subject of this research. This problem may hamper the life of the component and the continued functioning of the automotive engine. As engine designs are modified and more stringent performance targets are set for bearings, there is a growing potential for research in optimizing the fatigue resistance of such components.

1.1. Background

Competition between automobile manufacturers in achieving the best engine performance during the past few decades has resulted in sophisticated designs of automobile engines, which are lightweight, compact and have high output power. The high specific output power must be transferred from the piston-connecting rod assembly to the crankshaft via the plain bearings at the big end of the connecting rod. Location of bearings in a four-stroke car engine is shown in Figure 1.1. A simplified view of plain bearings present at the connecting rod big end and crankshaft periphery[1] is shown in Figure 1.2 (a). Innovations in the design of automobile engines push bearing manufacturers to search for new bearing materials that can withstand high output engine power and a more severe engine operating environment (such as high temperature and hydrodynamic pressures). The advent of new bearing materials, especially those used as linings has a great impact upon production techniques for bearings. The latest trend is to optimize the selection criteria of a manufacturing route based upon economic feasibility and the best possible use of the material's specific characteristics.

During engine operation, the bearing assembly is usually designed to operate with hydrodynamic lubrication i.e. the use of separating forces that are generated in a film of oil, which is dragged by a journal into a diminishing clearance space. These plain bearings consist of two half shells clamped together within a housing to support the journal. Since the function of the bearing is to transmit the engine load between the connecting rod and the crank pin while both have a relative movement with respect to each other, the former should therefore be able to withstand the high pressures developed there. These pressures are developed as a result of the

hydrodynamic action of the lubricating oil present in the form of a thin film between the surfaces of the plain bearing and the crank pin[2]. Figure 1.2 (b) shows the schematic of distribution of the hydrodynamic pressure along the lining surface of bearing.

The presence of a hydrodynamic oil layer with high pulsating load levels gives rise to complex fatigue failure mechanisms. The need for a bearing system that provides good sliding properties as well as mechanical strength has led to the use of multilayered bearing architectures. The layer architecture of bearing systems is equally important with regard to the loads encountered during functioning of the engine and the design integrity. Figure 1.3 shows the architecture of a modern bearing with different layers. The lining layer is typically a multiphase alloy in which hard and soft particles are combined to incorporate good tribological properties such as wear resistance, strength and low coefficient of friction together with good seizure resistance properties such as conformability. The stiffer and thicker steel backing layer provides the constraint to the bearing shell. The thin interlayer used in the *Al* based designs assures a strong bond between the lining and the backing layer as well as retarding any reaction of *A*l and *Fe* to form brittle intermetallic compounds in the steel[3]. The layer architecture of bronze bearings is more complex. A relatively harder lining layer (compared to the *Al* alloy lining) contributes to wear resistance and overall constraint, whereas a soft and thin *Sn* layer together with a harder *Ni* layer (underneath) used as an overlay provides the specific bearing lubrication characteristics. Since the main concern of this research is the fatigue performance evaluation of half shell plain bearings consisting of several layers of different types of materials, a strong micromechanistic understanding to fatigue failure will be developed on a metallurgical basis. A precise knowledge of specific microstructural characteristics of a material is essential to quantify the damage mechanisms under cyclic loading.

Gross fatigue failure of automobile engine bearings during service is far less likely than smaller scale fatigue damage that occurs at the lining surface giving rise to lining pitting or local lining decohesion.

1.2. Objectives

The fundamental objective of this research is to investigate fatigue behaviour of various multilayered bearing designs as a function of multiphase lining microstructures coupled with a layer architecture comprising materials of different mechanical properties. The total fatigue life of a bearing can be divided into two main phases i.e. (1) micro-scale fatigue damage

initiation and (2) growth of microstructurally short fatigue cracks. The focus of this work, building on previous research at Southampton, was to understand the micro-scale fatigue initiation phase and its subsequent growth through complex multilayered bearing designs and to define the optimum fatigue resistant microstructure and layer design. Specific aims of the current work could be described as follows:

- Understand the effects of modifications of the microstructure due to compositional or manufacturing alterations in the bearing-lining alloy.
- Identify the microstructure that is more resistant to fatigue initiation. Using analytical and numerical modelling, establish micromechanical approaches that may help in defining the optimum microstructures resistant to fatigue damage initiation.
- Establish approaches to predict the life of similar components at various stress levels.
- Assess the role of subsurface and overlay layers in providing resistance to crack growth and overall fatigue resistance.

In addition to the major objectives mentioned above, this research also aims to focus upon the contribution of the mesoscopic properties of different layers used in different subsystems to the overall fatigue response and hence performance of the system.

1.3. Thesis structure

After a brief introduction to the current research background and objectives, Chapter 2 comprises the literature review. Section 2.1 introduces bearing materials in general based on their historical evolution, characteristics required, most common *Al* and *Cu* based bearing alloys used as lining materials and various manufacturing routes. Section 2.2 briefly introduces fatigue and concepts including the behaviour of materials under cyclic loads, fatigue failure mechanisms and various appropriate modelling approaches. Section 2.3 describes the fatigue process in relation to engine bearings and hydrodynamic action occurring during engine operation.

Chapter 3 describes the materials assessed and the experimental methodology used to investigate various bearing systems based on their microstructural, mechanical and fatigue characteristics. Chapter 4 presents a detailed characterization of the various layers in each system based on their microstructure and local mechanical properties. Chapter 5 (Section 5.1) starts with a detailed analysis of the stresses and strains developed in the 3-point bend test (used for fatigue testing) in the layered systems. This analysis has been carried out based on numerical

modelling results validated through experimentally obtained strain gauge results. Section 5.2 describes the fatigue test results based on total life and short crack initiation and growth. Chapter 6 presents further analysis of the fatigue initiation process with a discussion of the micromechanical approaches adopted to explain fatigue initiation and growth together with further discussion on surface growth of short cracks and subsurface penetration. Chapter 7 summarizes the key results and conclusions as well as important areas of future research.

The references for each chapter are given at the end of the chapter followed by corresponding figures.

---

[1] Lorenz. Ratke, Bearing materials, Homepage research group polyphase solidification, 2(1999) (www.kp.dlr.de/Erstarrung/web_eng/lager_eng.html)

[2]Gyde, N. (1969). PhD. Thesis, Technical university of Denmark, Copenhagen.

[3] Braithwaite, E. R.(1967). Lubrications and Lubricants. European. Managegr of Chemical. Sales and Development. Elsevier. Pub. Co. London, 357

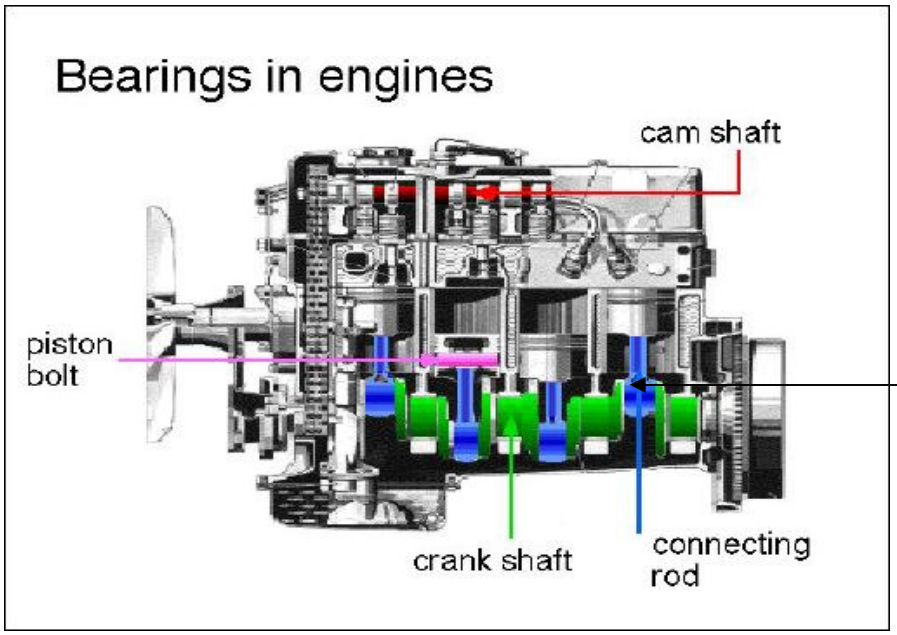

Figure 1.1: A view of 4 stroke car engine (After[1]) showing the location of plain bearings.

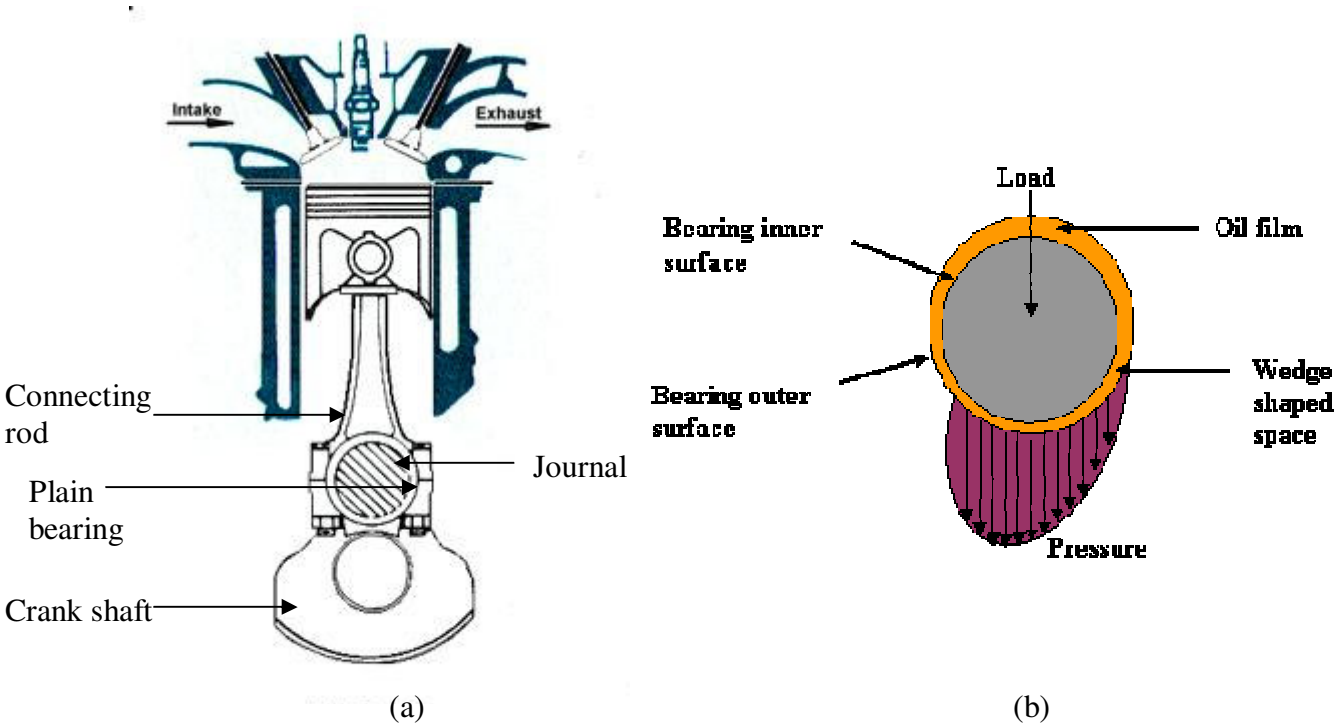

Figure 1.2: (a) Connecting rod-crank shaft assembly. (b) Hydrodynamic stress concentrations along the lining of bearing (courtesy DGV).

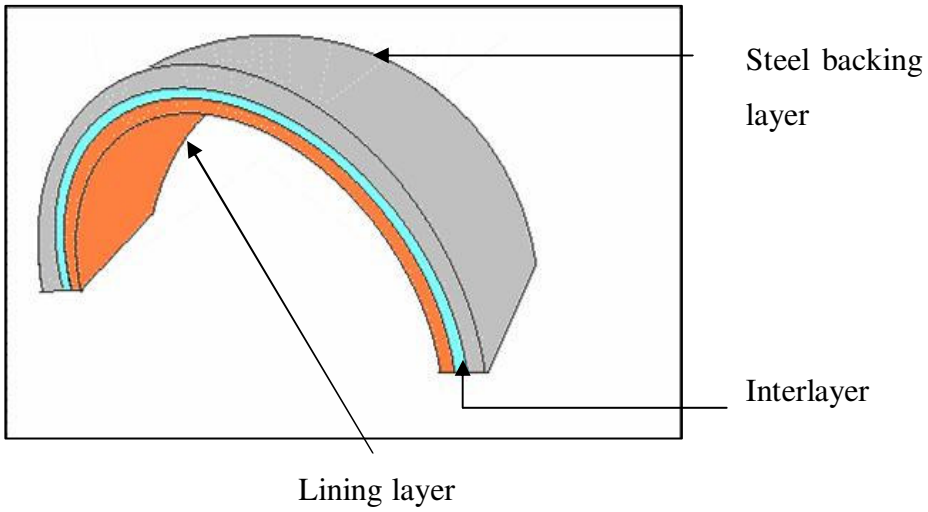

Figure 1.3: A multilayered bearing system showing various layers in an *Al* based bearing design.

2 LITERATURE REVIEW

The literature review related to this research encompasses three major topics (i) bearing materials (ii) fatigue failure and (iii) technical aspects of plain engine bearings. These are followed by various subheadings to explain the classical background and current relevent research.

2.1. Bearing materials

This section is concerned with historical evolution of bearing materials, characteristics required for bearing materials, phases present in different bearing alloys as well as effect of alloying elements on their mechanical properties and important manufacturing techniques. The main focus is *Al* lining alloys; however, a part of this literature is also dedicated to bronze lining materials.

2.1.1. Historical evolution of bearing materials

Bearings have been in use in the rotating parts of virtually all machines including automobile engines. The automobile industry is a major user of bearings and all moving parts in an engine must be supported by some kind of bearing. Since the purpose of the bearing is to transmit a load through two elements moving relative to each other, the friction characteristics of the bearing lining material are of immense importance. Development of bearing materials dates back to the emergence of tribology as a field of research as surface friction and wear together with conformability were the key aspects fundamental to the selection criterion of bearings[1].

Sn and *Pb* being soft and easily castable first attracted the attention of bearing manufacturers in the 19th century. However, their low strength and inability to carry appreciable loads pushed the manufacturers to search for means of improving their strength while maintaining their conformable characteristics. This led to the addition of alloying elements such as *Sb* and *Cu* to *Sn* (*Cu* and *Sb* improve strength and corrosion resistance respectively), which resulted in *Babbit metal*, the historical bearing alloy[2]. Since the invention of *Babbit metal* (*Sn-11Sb-6Cu*) by *Isaac Babbit* in 1839, further improvements in bearing alloys have taken place due to the emerging and changing demands of the automobile engines. *Babbit*

metal has now been replaced by *Cu-Pb* and *Al* based systems. *Cu-Pb* alloys were introduced in 1920 and consisted of a two-phase system and had much higher strength than any of the *Sn* or *Pb* based alloys. Recent developments in automobile engines to increase the engine power and to reduce the fuel consumption, size and weight of engines have added to the total stress to be carried by the bearings at crankshaft and connecting rods. The *Cu-Pb* bearing systems therefore experience wear, corrosion and seizure problems when subjected to these higher stresses, via the lubricating oil film and high temperature environments (*Mihara*)[3]. Hydrodynamic loading action will be discussed further in Section 2.3. Moreover, *Pb* being chemically hazardous to human life, was also considered a risk to the environment.

The requirement to achieve the best bearing properties along with strength, wear and corrosion resistance resulted in the large scale use of *Al-Sn* alloys in 1950. The *Al* alloy lining is suitable for corrosion resistance, but the cyclic loads that arise during the operation of the engine may result in early fatigue failure. Modifications in *Al* alloy compositions have been made in order to improve their fatigue resistance at higher temperatures[4]. The addition of elements such as hard *Si* and soft *Sn* improves the antiscoring and antifrictional properties of *Al* whilst addition of small amounts of *Cu, Ni* and *Mn* improves the strength and hardness of the bearings.

2.1.2. Bearing materials properties

The efficient and sustained functioning of bearings during the operation of an engine is sensitive to the design as well as the structural and mechanical characteristics of all the materials of the bearing system in general and the lining material in particular. The combination of multilayered bearing systems with the multiphase lining that may come in contact with the shaft or journal in the presence of hydrodynamic pressures gives rise to conflicting demands upon the materials properties.

The most important materials properties required by finished bearings are briefly summarized under the following subheadings[2,5]:

2.1.2.1.Load carrying properties

The bearing materials must possess enough strength and stiffness to withstand the load being transmitted between the journal and the housing. The level of strength required depends upon the amount of load being transmitted so that the bearing material can resist any

damage due to stresses which arise during operation of the automobile engine. In addition to these, local load concentrations may arise due to shaft misalignment or vibrations.

2.1.2.1.1 Fatigue resistance: Plain bearings are located at the connecting rod-crank shaft assembly where they experience cyclic engine-piston loads. Thus bearing lining is subjected to cyclic loads (acting through hydrodynamic oil layer) which give rise to cyclic stresses varying in intensity along the lining periphery as well through various layers of a multilayered bearing. The bearing lining material should be able to withstand these cyclic stresses and resist the initiation and growth of fatigue cracks that ultimately lead to catastrophic failure.

2.1.2.1.2 Toughness: Toughness of the bulk bearing is an important mechanical property that resists the accumulation of micro-cracks because the latter may result in catastrophic damage under cyclic loading. The toughness level in a finished component depends upon the post fabrication heat treatments.

2.1.2.1.3 Cavitation erosion resistance: Localized reduction in the oil pressure may cause the formation of bubbles. These bubbles upon further implosion may result in concentrated impact loading at the bearing surface. The bearing material must have sufficient resistance to bear such impact loads.

2.1.2.1.4 Shock Resistance: The bearing surface may also come across shock loads while in operation and must be capable of absorbing them in order to minimize damage to the lining.

2.1.2.2.Wear resistance

Where a strict control of the bearing clearance is required, the dimensional stability of the system is one of the key issues. During operation of the bearing, the thin oil film may lose its continuity and direct contact between the mating surfaces may result in severe wear of the bearing functional surface. While choosing the lining materials for the bearing, the wear resistance of the material is always one of the most important factors to be considered. Wear of the bearing lining may result from dirt particles in the lubricant or excessive wear debris. The ideal bearing lining must have the ability to absorb these contaminants.

2.1.2.2.1 Embeddability: The clearance between the bearing surface and the surface of shaft or journal may encounter contaminations such as local or foreign particles that may circulate with the lubricant. These particles must be absorbed by the bearing surface in order to reduce the potential damage by wear and seizure which could be caused by these particles.

2.1.2.3.Miscellaneous properties

2.1.2.3.1 Compatibility: The bearing material must have resistance to welding or joining to its mating surface under conditions of rubbing and friction.

2.1.2.3.2 Conformability: The bearing is usually in contact with the shaft and its housing. Therefore minor irregularities or misalignments may cause load concentrations or localized overloading and inadequate oil films that may cause wear. The bearing surface should be conformable to accommodate this.

2.1.2.3.3 High thermal conductivity: High thermal conductivity of the bearing could facilitate the dissipation of frictional heat if produced during operation.

2.1.2.3.4 Corrosion resistance: The lubricant between the bearing surface and the journal may be decomposed or degraded. Such degraded lubricant could result in chemical attack on the bearing lining if the latter does not have sufficient resistance to chemical attack. The lining material of the bearing surface must therefore possess the ability to withstand such occasional chemical attacks.

The aforementioned properties have been explained explicitly as independent of each other. However, to optimize all of them in one system is a challenging matter. For example the load carrying capacity could be enhanced but at the cost of a high rate of wear of the shaft or journal. Similarly low strength and hardness encourage deep embedding and so reduce wear but also encourage the release of entrapped particles. The bearing manufacturers therefore try to achieve the best compromise between the properties required taking into account the maximum load to which the bearing is to be subjected during operation.

2.1.3. Al bearing alloys

Al alloys are now being used extensively as bearing lining and interlayer materials (as mentioned earlier). The most commonly used alloys are *Al-Sn, Al-Si, Al-Sn-Si* with or without small additions of *Cu, Ni* and *Mn*. Manufacturers of bearing materials use various combinations of different alloying elements in order to achieve desired properties and for complete understanding of each alloy, full multi component phase diagrams of these complex alloys are required. However, a general view of the effect of different alloying elements based upon simpler already established phase diagrams is quite helpful to understand the nature of secondary phases present in these newly developed bearing materials.

Al-Si systems show some solubility of *Si* in *Al* that forms α phase. The *Al-Si* binary phase diagram for slowly cooled alloys is shown in Figure 2.1 (a). It is evident from the diagram that *Si* also exists as a distinct phase in the alloy.

The high castability and low expansion coefficient of this alloy is useful in many applications such as casting of complex shaped engine pistons using gravity casting techniques. In bearing linings, the *Si* content is usually less than 5 %, under such conditions, the primary α is present in large proportions. A fine and uniform grain size is often required in many *Al-Si* alloys to have good mechanical properties such as tensile strength, ductility and fatigue resistance. *Sr* in amounts 0.03-0.05 % is used as a modifier for *Si* refinement. Other elements such as *Zr, Ti* and *V* seem to be effective in α grain refinement. *Edward et al*[6] carried out a detailed study on the effects of small additions of *V, Ti*, and *Zr* to quantify the grain refinement based upon a grain refinement parameter.

The effects of small additions of *Cu* (0.5-1.5%) and *Ni* (0.1-1%) along with *Sr* (as grain refiner) in a hypoeutectic *Al-7Si* alloy have been reported by *Garcia*[7]. The purpose of *Cu* is to improve mechanical properties such as strength (but at the cost of ductility). An *Al-Cu* phase diagram is shown separately in Figure 2.1 (b). *Cu* forms the compound $CuAl_2$ (θ phase) [8] which is fully incoherent with the matrix and appears as fine eutectic colonies if *Sr* (0.02-0.03) is added (Figure 2.2 and Figure 2.3). *Ni* usually forms intermetallics such as *AlNi* and $AlNi_3$, the exact formation of which is still not understood[9]. The addition of *Sr* as modifier seemed to be more effective in refining *Si* and $CuAl_2$ eutectic. The mechanical properties such as yield strength and UTS (by *Cu* addition compared to *Ni*) were improved to a greater extent because the grain refiner *Sr* had little effect on $AlNi_3$ morphologies (that actually remain coarse).

2.1.3.1.Aluminium-Tin System

Sn containing aluminium systems are replacing conventional copper-based bearing alloys and a variety of such alloys are being developed by bearing materials manufacturers. The *Sn* content in these systems varies from 5 to 20%, but improvements in the microstructures and hence the mechanical properties are usually carried out by adding some other elements. An *Al-Sn* phase diagram[2] is shown in Figure 2.4. *Al* and *Sn* show no solubility in each other and remain as distinct phases in all proportions depending upon the rate of cooling. Alloys containing more than 10% *Sn* have a structure in which primary *Al* grains are surrounded by envelopes of *Sn*. The hardness and stiffness of such alloys is equivalent to white metal (a term usually used for

both *Sn* and *Pb* base alloys) at room temperatures but remarkably improved at higher temperatures. *Sn* is also corrosion resistant and *Al-Sn* alloys are therefore superior in corrosion resistance to other bearing materials such as *Al-Pb* alloys. The strength of *Al-Sn* alloys can be greatly improved by the addition of up to 1% *Cu* that brings about solid solution hardening of the *Al* phase. The roll bonding process typically used for the manufacture of bearings is accompanied by cold working and annealing during which the *Al* grains recrystallize and *Sn* being molten at the annealing temperature redistributes it in such a manner that it no longer isolates the *Al* grains from each other. This gives rise to the reticular structure of the *Sn* phase.

2.1.3.2. Aluminium-Tin-Silicon Systems

Both *Al-Si* and *Al-Sn* alloys have excellent tribological and mechanical properties and find extensive use in many engineering applications the most important of which is the plain bearings, internal combustion engine pistons and cylinder liners[10]. *Al-Sn* alloys have good resistance to seizure but poor resistance to fatigue under high engine loads. *Al-Si* alloys on the other hand are excellent against wear but are less resistant to seizure under poor lubricating conditions[11]. A combination of both of these alloy systems provides the best combination of properties required for bearing materials. A detailed study of crystallization behaviour and microstructure of *Al-Sn-Si* systems has been carried out by *Yuan et al*[12] using X-Ray diffraction as well as optical and scanning electron microscope. An unfolded *Al-Sn-Si* ternary phase diagram is shown in Figure 2.5. Alloys varying in *Sn* content from 10-20% and *Si* content from 0-8% were cast and assessed with the aforementioned analytical techniques. The solidified structure consisted of *Al*, *Si* and *Sn* in which the *Sn* phase is present as a network and attached mostly to eutectic *Si*. Homogenization brings about the spheroidization of *Sn* and *Si* particles (Figure 2.6) where the *Sn* phases gather around the *Si* phase. The presence of *Mn*, *Ni* and *Cu* produces complex intermetallics (as mentioned for *Al-Si* systems) which add to the strength and hardness of the component. These intermetallic compounds form a class of materials, which has properties lying between metals and ceramics, and their bond is a mixture of metallic and covalent. The intermetallics such as *NiAl*, $NiAl_3$ and $CuAl_2$ expected to be present in various bearing materials have *Young's* moduli in the range of 200-400 GPa but very low ductility[13]. However, it is hard to predict the exact mechanical properties of the complex mixtures of intermetallics present in *Al* bearing alloys. Intermetallics being brittle in nature appear to initiate

fatigue cracks in some alloys. Figure 2.7 shows for example the cracking of Al_7Cu_2Fe intermetallic in a 7010 alloy.

2.1.4. Bronze bearings

The term 'bronze' is used for a wide variety of *Cu-Sn* systems (sometimes with small amounts of *Zn*). The content of *Sn* may vary from 5-40%. Some other terms relevant to bronze are *phosphor bronzes*[14] (phosphorous content not less than 0.05%) and *leaded bronze* (lead over 0.5% and *Sn* less than 10%). *Leaded bronzes* are used for special bearing applications. Another term is *nickel bronze*, in which *Sn* is less than 10% and *Ni* over 10%.

The bronze bearings investigated in the current work are a modified form of *bronzes* in which *Ni* was up to 1 %. In order to understand the presence of various phases in these alloys[14], a phase diagram of *Cu-Sn* system is given in Figure 2.8 (a). The type and nature of various phases present at various percentages of *Sn* shows a series of complex intermetallic compounds of *Cu* with *Sn*. However, considering only the lower portion of the diagram (room temperature), the phases expected to be present were α (solid solution) and ε (intermetallic compound: Cu_3Sn). The alloy studied in this work is a low *Sn* bronze and hence expected to be principally a *Cu-Sn* solid solution. The amount of *Ni* in this alloy was only 1%. It is evident from the ternary diagram of the *Cu-Sn-Ni* systems that most of the added *Ni* forms a solid solution with *Cu.*

2.1.5. Manufacturing processes

2.1.5.1.Roll bonding techniques

The roll bonding technique is popular in the manufacture of bi- and tri-metal strips. In the manufacture of bearings, the lining layer is cladded to the backing steel layer by the application of pressure through the rolls.

A typical lay out of the roll bonding process has been given in the "Glacier Vandervell Engine Bearings Materials and Design" brochure. In this particular example, starting from a continuous casting plant, the *Al* alloy lining layer after passing through the billet reduction, welding and heat treatment units is cladded to an *Al* foil (used as an interlayer between steel backing and the lining layer). This bimetal strip is further bonded to a steel layer through different steps of rolling and heat treatment and the multilayered strip is subsequently reduced to the desired thickness and then converted to plain bearings by mechanically bending

over a rotating wheel. Finally, the bearing lining surface is broached to give a desired finish. This set up is shown in Figure 2.9(a) . Both cold and hot rolling processes are in use for the manufacture of multilayered bearings. The production of bimetal strips using cold rolling processes poses problems to good bonding and induces high work hardening[15]. It has been reported[16] that the hot rolling process provides a better solution if carried out in a protective environment. The application of a hot rolling technique to clad *Al-Pb* bearing alloy to the steel backing layer through an aluminized interlayer has shown that the latter could achieve the best bond between the lining and the steel layer.

2.1.5.2.Thermal spray coating techniques

Thermal spray coating techniques are gaining much popularity due to their ability to produce coatings of numerous materials on different substrates. Thermal spray coatings exhibit excellent tribological properties in corrosive, erosive and sliding wear. Among a large number of spray coating techniques, high velocity oxygen fuel spray coating (commonly abbreviated as HVOF) finds widespread applications in the aerospace, automotive, biomedical and marine industry.

In the HVOF process, a metal/alloy in powder form is injected into a chamber where the high thermal energy produced by fuel gases melts and propels it on to the surface to be coated. HVOF processes are developed to produce metal, carbide and other speciality coatings. There are two modifications of the process depending upon the type of the fuel used. If gaseous fuel such as hydrogen or propylene is employed, the process is known as high velocity oxy gas fuel (HVOGF) whereas with liquid fuel such as kerosene oil, the process is termed high velocity oxy liquid fuel (HVOLF). Figure 2.9(b) shows a typical HVOF nozzle developed in a spray coating modelling process[17]. Both oxygen and fuel mix in the combustion chamber and produce a flame of very high temperature (3300^{o}C) that helps in depositing the powder upon the substrate. The key parameters that control the quality of the deposit are the ratio of fuel gas/liquid to oxygen as well as velocity of the fuel/oxygen and powder injection.

The use of this technique for coating *Al* alloy lining on flat steel bars has been reported[18]. Spray coating of *Al-20Sn-1Cu* with and without additions of small quantities of *Mn* and *Ni* were carried out using HVOF techniques. It was observed that this technique with subsequent heat treatment produced microstructures with much finer grain size and fine *Sn* particles (~25nm) if compared with those obtained by roll bonded materials. Comparison of the

spraying performance of both HVOGF and HVOLF has been carried out[19] by applying these techniques on *Al-20Sn-3Si* powder coatings. It has been concluded that the liquid fuel resulted in higher energy density, high kinetic energy and less heat transfer and therefore produced incomplete melting of solid particles of the powder as well as imposition of plastic deformation on solid particles. Therefore, the microstructure of the solidified material revealed only partial *Sn* dispersion. In the case of HVOGF, the solid particles are fully melted and upon solidification they resulted in a more homogeneous fine dispersion of *Sn* particles, however problems were encountered in keeping the nozzle clear during repeated spraying.

2.1.5.3.Powder metallurgy methods

Powder metallurgy techniques are also employed for the manufacture of bearings in which the lining material in the form of fine particles is sintered on to the surface of the backing layer. Recently, hot extrusion techniques have been used for the manufacture of *Al-Pb* bimetal bearing. It has been reported[20] that the hot extrusion method makes it possible to produce the optimum lead grain distribution and strong adhesion between powder particles. The new manufacturing method produces an *Al-Pb* bearing material which shows 30% or more increase in fatigue strength over the conventional sintered *Al-Pb* bearing material. The increase in the fatigue strength was due to the textures and refined structure in which *Pb* particles were elongated in the direction perpendicular to the fatigue crack growth. This process has been further elaborated[21] where powder metallurgy techniques were incorporated to produce *Al*, *Pb, Sn Cr* powders by atomization. Cold isostatic pressing and hot extrusion of the powder were used to consolidate the mass in to a compact form. The extruded sheets were further subjected to rolling to convert them into bearings. It was concluded that the mechanical properties and tribological characteristics of the new *Al-Pb P/M* (powder metallurgy) alloy were superior to those of conventional *Al-Sn* I/M (ingot metallurgy) alloy. The new alloy is designed as an advanced material for application to automotive engine bearings.

2.1.6. Summary of materials

Bearing lining materials demand a conflicting combination of properties which can only be fulfilled by complex multiphase alloys. A range of alloy systems can thus be employed as lining layer in various multilayered bearing architectures. Various manufacturing and processing routes adopted for the manufacture of these systems may affect the microstructure

and mechanical properties and hence the fatigue resistance. Fatigue performance of these systems needs to be evaluated in a systematic way.

2.2. Fatigue of materials

A comprehensive analysis of fatigue failure of a component is based upon external conditions such as load amplitudes and environments and also the micromechanics (affected by the microstructure) of the fatigue damage phenomenon. Starting from fundamental definitions of fatigue, the following sections therefore illustrate current understanding of the fatigue damage processes.

2.2.1. Basic definitions

The term "fatigue" applies to those changes in a material that lead to cracking or failure under repeated stresses or strains. If the failure is merely due to fluctuations in applied stresses or strains, the term "mechanical fatigue" is more appropriate. On the other hand, if external conditions such as temperature, fluctuations in temperature, presence of aggressive chemicals or sliding surfaces are considered, the appropriate terms used are creep-fatigue, thermomechanical fatigue, corrosion fatigue or fretting fatigue respectively. It is useful to review some fundamental terms related to the quantification of the cyclic loading that causes fatigue failure. These expressions are briefly described below.

Mean stress or set point—is defined as mean value of the maximum and minimum stresses during a complete cycle:

$$\sigma_m = \frac{\sigma_{max} + \sigma_{min}}{2} \qquad 2\text{-}1$$

Stress range—is defined as the difference between maximum and minimum stress during a stress cycle:

$$\Delta\sigma = \sigma_{max} - \sigma_{min} \qquad 2\text{-}2$$

Stress amplitude—is defined as the maximum value of the stress on either side of the set point:

$$\sigma_a = \frac{\Delta\sigma}{2} = \frac{\sigma_{max} - \sigma_{min}}{2} \qquad 2\text{-}3$$

Load ratio—is defined as the ratio of minimum to maximum load:

$$R = \frac{\sigma_{min}}{\sigma_{max}} \qquad 2\text{-}4$$

2.2.2. Nucleation and growth of fatigue cracks in ductile materials

Cyclic plastic deformation is the decisive factor in the progress of cumulative damage taking place during cyclic loading. Cyclic deformation throughout the volume of the loaded metal may also cause changes in the mechanical response i.e. hardening/softening. After a number of cycles, the intensity of variation in the hardening and softening decreases and a saturation stage is reached when a hardening or softening process stabilizes as represented by hysterises loops in Figure 2.10 (a and b). For example[22], when polycrystalline copper was cycled at different total strain amplitudes, the stress amplitude increased quickly and then reached a more or less constant saturated value in a fraction of the total number of cycles to failure. The fatigue hardening and softening of materials stems from the movement, generation and interaction of structural defects such as dislocations. During the initial rapid hardening stage, a large number of dislocations is produced, the pile up of which hinders the slip process[23]. With continued cycling, the dislocation density increases and the spacing among the bundles of dislocations and the dislocation free area decreases. At high strain amplitudes, a three dimensional dislocation cell structure is produced. During the saturation stage, slip bands of inhomogeneous plastic deformation are produced provided the cyclic strain amplitude was sufficient[24]. These slip bands have a different dislocation structure from the matrix and are softer[25] than the matrix. This phenomenon gives rise to the creation of persistent slip bands. The term persistent slip bands (PSBs) arose from the fact that these slip bands were reformed in the same locations even after electropolishing the fatigued specimen[26]. Figure 2.11 shows a micrograph of polycrystalline *Cu* showing these PSBs. For homogeneous microstructures with a smooth polished surface (i.e. in the absence of local stress concentration features) the nucleation of a crack starts along the PSBs.

The process of nucleation of a crack under cyclic load is not simple to understand as it commences within the atomic structure of the crystal from the first few cycles of stress and will continue growing over thousands or millions of subsequent cycles until the eventual failure.

It was postulated by *Gough*[27] that fatigue crack initiation is a consequence of exceeding the limit of local strain hardening. Further to that, *Orowan*[28] concluded that the local exhaustion of ductility leads to the localized increase of stress and ultimately to cracking.

Fundamental knowledge of crack initiation was refined during the 1950s when dislocation theory was further developed. *Stroh*[29] postulated that piling up of dislocations around microstructural obstacles increases the local stress field, which then becomes sufficiently high to cause local cleavage. Various researchers carried out further investigations[30] . For example, dislocation models were proposed by *Cottrell* and *Hull*[31], which were based upon the intersecting slip systems generating a microcrack. Further models proposed by *Mott*[32] were based upon generation of vacancies.

In the case of homogeneous materials, the microcracks usually originate at the free surface. This is also true for those non-homogeneous materials in which maximum stress (i.e. bending and torsion loading conditions) occurs at the surface. This is because, at the free surface, the restraint on cyclic slip is lower than inside the material. In addition, microcracks start more easily at slip bands with slip displacements normal to the material surface[33].

The idealized behaviour of slip systems during cyclic deformation has been depicted[34] in Figure 2.12. This figure shows the creation of extrusions and intrusions during cyclic slip, with extrusions and intrusions along slip bands. These extrusions and intrusions for polycrystalline *Cu* fatigued at -183^{o}C are shown in Figure 2.13. According to *Wood*[35] , repeated cyclic straining of the material leads to different amounts of net slip on different glide planes. The shear displacements produced are irreversible. The reason for this irreversibility is the cyclic strain hardening that stops all the dislocations from coming back to their original positions[36]. Another important reason may be environmental factors, during slip when a fresh surface is exposed to the non-inert environment; it is covered with a very thin oxide layer or some chemo-absorption of foreign atoms. These phenomena may be effective together or alone depending upon the inherent characteristics of the material such as resistance to oxidation and mechanisms of slip i.e. planar or wavy.

In the early work by *Forsyth*[30] and *Plumbridge*[37]on the fatigue initiation of soft and hard metals, it was found that the crack usually initiated at slip bands and that the number of cycles required to produce a detectable crack was a small proportion of the total life. Early work reported by *Tryon et al*[38] showed that in a continuous material, microcracks have been

observed to initiate from slip bands formed in the early stage of damage accumulation and stretch across one grain

The initial crack developed along the slip plane (stage I) eventually propagates across other grains along appropriately oriented slip planes. The crack may only grow in stage I in a polycrystalline metal for a few grain diameters before it changes its direction to be perpendicular to the direction of the maximum applied tensile stress. During this stage (II), a well-defined crack propagates at a relatively rapid rate. Fatigue striations may be created as the crack advances across the cross section of the specimen. In stage III, the local crack tip stress states are reaching static failure levels while the remaining uncracked material is insufficient to support the applied load giving rise to rapidly increasing crack growth rates until final rupture.

2.2.3. Total fatigue life approaches

Fatigue damage in engineering components is often characterized by the nucleation of defects in initially undamaged sections and then their stable propagation until catastrophic fracture occurs. The conditions for the nucleation of microdefects and the rate of advance of dominant fatigue cracks are strongly influenced by a wide range of mechanical, microstructural and environmental factors. Fatigue behaviour of components is usually evaluated on the basis of a total life approach and/or a damage tolerant approach. For a design engineer, fatigue life is often the key issue which gives the total number of stress or strain cycles at a certain load level the component can withstand up to a set criterion of failure. The total fatigue life is usually characterized as a function of applied stress range, strain range, mean stress and environment.

2.2.3.1.Stress life approach

The stress life approach involves the characterization of the total fatigue life in terms of the *S-N* curve. Sample life times are related to the maximum applied stress. In the *S-N* curve the stress amplitude *S* is plotted against the number of cycles to failure *N*. *Wöhler*[39] carried out a series of experiments in the 19th century to obtain *S-N* curves. In the 20th century, many rotating beam fatigue tests have been carried out upon both notched and un-notched specimens to get a large number of *S-N* curves for the statistical analysis of the fatigue behaviour of many industrial components. Under constant load amplitude conditions, many materials exhibited a plateau in the *S-N* curve beyond 10^7 cycles. At the stress level below this point, the material may be cycled indefinitely without fatigue failure. This critical stress amplitude is known as the

fatigue limit. For some non-ferrous metals and alloys such as *Al* alloys, the fatigue limit is not well defined. For such materials the fatigue tests are generally stopped after long testing times e.g. 10^7 cycles and the term endurance limit is used for the associated stress amplitude[40].

When the *S-N* curve for steel (with load ratio of -1) was redrawn on a log-log scale[41] with true stress amplitude as a function of number of cycles or load reversals to failure, a linear relationship was observed. Incorporating the relation for stress amplitude as given in Equation 2.3 in a fully reversed constant amplitude fatigue test to the number of load reversals to failure i.e. $2N_f$, the resulting expression is given as

$$\sigma_a = \sigma_f (2N_f)^b \qquad 2\text{-}5$$

where σ_f is the fatigue strength coefficient (which is equal to the true fracture strength corrected for necking) and *b* is the *Basquin* exponent. In many loading situations fully reversed stress cycle conditions (zero mean stress) may not exist rather, the mean stress (Equation 2.1) may have a certain value or set point. The fatigue life has a strong dependence on the mean stress value as shown in Figure 2.14 (a). This figure shows that the fatigue life decreases with increasing mean stress. Mean stress effects have been reproduced in terms of constant life diagrams where different combinations of mean stress and stress amplitude have been plotted against the number of load reversals to failure. The most popular among them are those of *Gerber*[42], *Goodman*[43] and *Soderberg*[44]). The relevant curves are given in Figure 2.14 (b).Goodman based his curve upon the variation of limiting range of stress $\sigma_{max} - \sigma_{min}$ with the mean stress 'σ_m'. As the mean stress becomes more tensile, the allowable range of stress is reduced until it becomes zero at UTS. A conservative view of *Goodman's* approach could be presented in the form of a straight line drawn from the fatigue limit to the tensile strength (for completely reversed stress). An alternative way of presenting mean stress data is given by *Haig-Soderberg*[40] i.e. as a plot of the mean stress versus the alternating stress. A parabolic curve was suggested by *Gerber*. The relevant expressions are given in the following equations.

$$\sigma_a = \sigma_a\Big|_{\sigma_m=0}\left\{1-\frac{\sigma_m}{\sigma_y}\right\} \quad \text{Gerber} \qquad 2\text{-}6$$

$$\sigma_a = \sigma_a\Big|_{\sigma_m=0}\left\{1-\frac{\sigma_m}{\sigma_{TS}}\right\} \quad \text{Goodman} \qquad 2\text{-}7$$

$$\sigma_a = \sigma_a\Big|_{\sigma_m=0}\left\{1-\left(\frac{\sigma_m}{\sigma_{TS}}\right)^2\right\} \text{ Soderberg} \qquad 2\text{-}8$$

where

$\sigma_a\Big|_{\sigma_m=0}$ = Stress amplitude for fully reversed loading (R=-1)

σ_{TS} = Tensile strength of the specimen

σ_y = Yield strength of the specimen

The *Goodman*'s model is based on the assumption that the effect of mean stress is linear between σ_m =0 and σ_{UTS} whereas the *Gerber* approach presents it as a parabolic line. Test data for ductile metals generally falls closer to the parabolic curve, but due to large scatter in the data (and due to the fact that tests on notched specimens fall closer to the Goodman line), the linear relationship is usually preferred in engineering design[60].

The stress life approach basically pertains to elastic and unconstrained deformation and is therefore mostly applicable to elastic situations i.e. where $\sigma_{max} < \sigma_y$

2.2.3.2.Strain life approach

Many engineering components undergo a certain degree of localised plastic flow particularly at locations of stress concentrations where the local stress exceeds the elastic limit. Under such circumstances, an approach based upon strain life is more useful. *Coffin*[45] and *Manson*[46] characterised the fatigue life based upon plastic strain amplitude the expression of which is given below:

$$\frac{\Delta\varepsilon_p}{2} = \varepsilon'_f (2N_f)^c \qquad 2\text{-}9$$

Where ε'_f the fatigue ductility coefficient and *c* is the fatigue ductility exponent.

In a constant strain amplitude test, the total strain may be written as the sum of elastic and plastic strains:

$$\frac{\Delta\varepsilon}{2} = \frac{\Delta\varepsilon_e}{2} + \frac{\Delta\varepsilon_p}{2} \qquad 2\text{-}10$$

Modifying equation 2.11 by using the *Basquin* relation (2.6), the resultant relation is given as

$$\frac{\Delta\varepsilon}{2} = \frac{\sigma'_f}{E}(2N_f)^b + \varepsilon'_f (2N_f)^c \qquad 2\text{-}11$$

The first and second terms indicate the elastic and plastic components of the total strain amplitude. Equation 2.11 is the basis for the strain life approach.

2.2.3.3.Application of stress or strain life approach

The choice of a particular life approach is dependent upon the stress levels encountered and the occurrence of plastic deformation in a component. Under high cycle low stress fatigue situations, the material deforms primarily elastically and the fatigue life is assessed in the form of a curve between applied stress levels and the number of cycles to failure. The stresses associated with low cycle fatigue are generally high enough to cause appreciable plastic deformation before actual failure occurs. Under these conditions, the fatigue life is presented as number of cycles to failure at different strain ranges.

2.2.4. Damage tolerant approach to fatigue

The key factors that a design engineer must consider for an engineering component are the strain rate, fluctuating stress, stress concentrations, metallurgical flaws, high and low temperature and corrosion effects (that may also create flaws). The designer needs to be aware that these variables can cause an engineering component to fail by propagation of an existing sharp defect that may lead to a catastrophic disaster far earlier than predicted by a simple *S-N* approach. Thus a damage tolerant lifing approach is required that can characterise the growth of an existing defect to final failure. Fracture mechanics parameters can be applied to such a situation. Before discussing the applicability of fracture mechanics theory to fatigue failure, some fundamental concepts and mathematical expressions along with basic terminology regarding fracture are outlined here briefly.

2.2.4.1.Griffith theory

Linear elastic fracture mechanics (LEFM)) dates back to the earlier works of *Griffith*[47] who focused upon the cause of the discrepancy between the observed and the theoretical strength of a material. *Griffith* developed a concept to explain how a stable crack could exist in a material. He formulated criteria for unstable extension of a crack in a brittle solid in terms of the balance between changes in the stored strain energy and surface energies of new crack surfaces. In more precise terms, for the unit extension of a crack under the influence of the applied stress, the decrease in the potential energy of the system by virtue of the displacement of the outer boundaries and the change in the stored elastic energy must equal the

increase in the surface energy due to crack extension. *Griffith*'s model was originally applied to an elliptical crack in a semi-infinite slab as shown in Figure 2.15. The mathematical formulation is given as

$$W = -\frac{\pi a^2 \sigma B}{E'} + 4aB\gamma_s \qquad 2\text{-}12$$

where

W_P = potential energy and stored energy loss

B=width of the slab

a = crack length

σ = applied stress

E' = modulus of elasticity

E'=E/1-v^2 (plane strain) {v=Poisson's ratio}

E'=E (Plane stress)

γ = surface energy per unit area

The surface energy is thus increasing linearly with the crack length whereas the energy released by the formation of the crack increases with the square of the crack length.

According to Griffith, the threshold between the stable and unstable crack occurs when an increment of crack growth causes more energy to be released than can be absorbed in the material. Thus the critical condition for crack to grow is $dW/dA = 0$ where $A=2aB$ is the crack area. The following relation gives the critical stress for fracture initiation

$$\sigma_f = \sqrt{\frac{2E'\gamma_S}{\pi a}} \qquad 2\text{-}13$$

where σ_f is the critical stress for the fracture initiation and γ_S is the representative critical value of γ.

The energy dissipative processes at the crack tip will absorb however a much larger amount of energy due to plastic deformation. In engineering materials such as steel, the plastic deformation at the crack tip may absorb at least a thousand times the surface energy requirement[48].

Orowan[49] modified *Griffith's* model in 1952 by including the nonlinear deformation near the crack tip (due to stress concentration) and put in an extra term for plastic strain energy.

$$\sigma_f = \sqrt{\frac{2E'(\gamma_S + \gamma_p)}{\pi a}} \quad \text{OR} \quad \sigma_f \sqrt{\pi a} = \sqrt{2E'(\gamma_S + \gamma_P)} \qquad 2\text{-}14$$

where γ_p is the plastic work done per unit area of surface created and is much larger than γ_S.

Irwin[50] presented a mathematical relationship for energy release rate *G* in an elastic cracked body as given below

$$G = \frac{-dW_P}{dA} \quad \rightarrow \quad G_c = 2\gamma_S \qquad 2\text{-}15$$

2.2.4.2.Linear elastic fracture mechanics

Apart from *Griffith*'s energy concepts, linear elastic fracture mechanics theory (LEFM) characterizes the growth of flaws by considering the local stress and strain fields ahead of the crack that provide the crack driving force. Before considering this theory various modes of failure are mentioned below.

2.2.4.2.1 Loading modes: There are three distinct loading modes for a crack as shown in Figure 2.16. In mode I loading, the crack surfaces are displaced in a direction normal to the plane of the crack and the displacements of the crack wall are symmetric with respect to the x-z and x-y planes. This is also called the tensile opening mode. In mode II in-plane shear or sliding takes place and the crack faces are mutually sheared in a direction normal to the crack front. Here the displacements of the crack walls are symmetric with respect to the x-y plane and anti symmetric with respect to the x-z plane. Mode III is characterized by anti-plane strain with all deformation occurring in the direction normal to the plane and the displacements of the crack walls in this case are anti-symmetric with respect to both the x-y and x-z planes.

Irwin[51] used the analytical methods of *Westergaard*[52] to quantify the near tip fields in the vicinity of a sharp crack in a large plate as shown in Figure 2.17. The local elastic stress distributions at co-ordinates (r, θ) close to the crack tip are given by:

$$\sigma_x = \frac{K}{\sqrt{2\pi r}} \cos\left(\frac{\theta}{2}\right)\left[1 - \sin\left(\frac{\theta}{2}\right)\sin\left(\frac{3\theta}{2}\right)\right] \qquad 2\text{-}16$$

$$\sigma_y = \frac{K}{\sqrt{2\pi r}}\cos(\frac{\theta}{2})\left[1+\sin(\frac{\theta}{2})\sin(\frac{3\theta}{2})\right] \quad 2\text{-}17$$

$$\tau_{xy} = \frac{K}{\sqrt{2\pi r}}\sin(\frac{\theta}{2})\cos(\frac{\theta}{2})\sin(\frac{3\theta}{2}) \quad 2\text{-}18$$

$$\sigma_z = \frac{2\nu K}{\sqrt{2\pi r}}\cos(\frac{\theta}{2}) \quad \text{(Plane strain)}, \quad \sigma_z = 0 \text{ (plane stress)} \quad 2\text{-}19$$

Here K is the mode I stress intensity factor, which incorporates the boundary conditions of cracked body and is a function of loading, crack length and geometry.

2.2.4.2.2 Stress intensity at Cracks: *Irwin* observed that stresses are proportional to $\sqrt{\pi a}$ for a sharp crack in an infinitely wide plate, where a is the half length of the crack. On this basis the stress intensity factor K is defined as

$$K = \sigma\sqrt{\pi a} \quad 2\text{-}20$$

The stress intensity factor is utilized in characterizing elastic stress distribution near the crack tip. Its unit is MPa √m.

2.2.4.2.3 Fracture toughness: The value that K must exceed for catastrophic fracture to occur is known as the critical stress intensity factor K_c or *fracture toughness* of the material. In order to extend the applicability of LEFM beyond the case of a central crack in an infinite plate, K is usually expressed in more general form as given below:

$$K = Y\sigma\sqrt{\pi a} \quad 2\text{-}21$$

where Y is the geometric factor and a is the half length of a central crack or full length of an edge crack. Combining equations 2.14 and 2.15.

$$K_c = \sqrt{2E'\gamma_s} = \sqrt{E'G_c} \quad 2\text{-}22$$

K_c is a function of mode of loading, the chemical environment, the material microstructure, the test temperature, the strain rate and the state of stress. Test specimens used for the determination of fracture toughness must conform to the conditions described in fracture test standards E-399 developed by ASTM (1974).

2.2.4.2.4 Stress intensity factor and strain energy release rate: The strain energy release rate for a crack growing under tension in an infinite plate has therefore a direct equivalence to the

stress intensity factor. For the general three dimensional case involving the plane strain and anti plane strain loadings

$$G = \frac{(1-v^2)}{E}(K_I{}^2 + K_{II}{}^2) + (\frac{1+v)}{E}K_{III}{}^2 \qquad 2\text{-}23$$

and for plane stress

$$G = \frac{1}{E}(K_I{}^2 + K_{II}{}^2) \qquad 2\text{-}24$$

Where ν is the Poisson's ratio of the material.

2.2.4.3.Elasto-plastic fracture mechanics

The concept of elasto-plastic fracture mechanics (EPFM) is used where considerable plastic deformation occurs. The stress intensity factor *K* provides a unique characterization of crack tip stress fields under small scale yielding. If there is appreciable plastic deformation or the stresses cause the elasto-plastic straining of the whole cross-section, the corresponding parameter that characterizes the crack tip stress fields is the *J* integral as proposed by *Rice*[53] . It is based upon the finding that for a two dimensional crack situation, the sum of the strain energy density and the work terms along a path completely enclosing the crack tip are independent of the path taken. It is also assumed that the crack faces are traction free and the tractions surrounding the crack tip are independent of crack size. Under small scale yielding conditions in plane strain, *J* is related to *K* by the following equation:

$$J = \left(\frac{1-v^2}{E}\right)K^2 \qquad 2\text{-}25$$

where '*v*' is the Poisson's ratio. From a more physical view point *J* may be interpreted as the potential energy difference between two identically loaded bodies having crack sizes *a* and *a*+*da*.

$$J = -\frac{1}{B}\frac{\partial U}{\partial a} \qquad 2\text{-}26$$

where *B* is specimen width and *U* is the strain energy and work done which is actually the area under the load displacement curve. The *J* integral is based upon non-linear

elastic assumptions; it is therefore unable to accommodate irreversible plastic deformation that is accompanied by unloading.

2.2.4.3.1 Plastic Zones ahead of a crack tip: According to the stress field equations given earlier (2.16-2.19), the predicted elastic stresses would become very large in the vicinity of the crack tip where $r<a$. In a ductile material this region becomes plastically deformed and hence these stresses do not occur practically. Stress redistribution at the crack tip due to local yielding is shown diagrammatically in Figure 2.18. LEFM techniques could still be applied if an equivalent crack length is used which means that the total crack length is equal to the physical crack length plus the allowance for the extent of the plastic zone. This zone is generally represented by a circular boundary of radius $r_{p.}$

Irwin[54] presented an estimation of the boundary of plastic zone ahead of a crack in a ductile solid by considering the crack tip zone within which the Von Mises equivalent stresses exceeds the tensile flow stress. The extent of this zone ($\theta=0$) is found to be proportional to the square of the stress intensity factor. The plastic zone sizes ahead of the crack under monotonic mode I loading under plane stress conditions are given as

$$r_p = \frac{1}{3\pi}\left(\frac{K_I}{\sigma_y}\right)^2$$

$$r_p = \frac{1}{\pi}\left(\frac{K_I}{\sigma_y}\right)^2 \qquad 2\text{-}27$$

These are for plane strain and plane stress conditions respectively. It is obvious that the extent of the plastic zone is less for plane strain cases.

According to *Dugdale*[55], the plastic region can be depicted as a narrow strip of near zero height which extends a distance r_p ahead of the crack tip which is loaded by the traction $\sigma_{yy=}\ \sigma_y$ over the length r_p. For $\sigma_{yy} = 0$ over the whole length a far field tensile stress σ^∞ would produce a positive stress intensity factor given as

$$K_I = \sigma^\infty \sqrt{\pi(a + r_p)} \qquad 2\text{-}28$$

using the traction $\sigma_{yy=}\ \sigma_y$ simultaneously along the length of the strip and superposition results, the relation for r_p is given as

$$\frac{r_p}{a} = \sec\left(\frac{\pi\sigma^\infty}{2\sigma_y}\right) - 1 \qquad 2\text{-}29$$

For $\sigma^{\infty} << \sigma_y$ and hence for $r_p <<$a this equation asymptotically leads to a plastic zone size

$$r_p = \frac{\pi}{8}\left(\frac{K_I}{\sigma_y}\right)^2 \qquad 2\text{-}30$$

2.2.4.3.2 Plastic zone size in cyclic loading: Fracture mechanics can only be applied to fatigue after a crack initiation phase to enable crack growth to be characterized. *Paris*[56] and *Rice*[57] recognised and analysed the stresses within the reverse yield zone at the fatigue crack tip. For a crack which is partially unloaded from a far field tensile load, there exists a region (within the monotonic plastic zone) of reversed flow known as cyclic plastic zone of size r_c in which residual compressive stresses are induced. r_c is given by

$$\mathrm{r_c} = \frac{1}{\pi}\left(\frac{\Delta K_I}{2\sigma_y}\right)^2 \qquad 2\text{-}31$$

where ΔK_I is the amplitude of stress intensity factor defined as

$$\Delta K_I = K_{\max} - K_{\min} \qquad 2\text{-}32$$

where K_{max} and K_{min} are extreme values of stress intensity factor within the stress cycle

2.2.4.3.3 Fatigue and damage tolerant approach

In the damage tolerant approach, the useful life of a component is that period (in terms of number of cycles) during which an existing flaw of initial size (a_o) grows to a critical size. This growth rate is expressed as crack length increment per cycle (*da/dN*). Stress intensity factor is used to characterize the fatigue growth rates provided that small scale yielding conditions are not violated. *Paris*[58] reported that the following law governs the growth of a crack under cyclic loading:

$$\frac{da}{dN} = C\Delta K^m \qquad 2\text{-}33$$

where *da/dN* is the change in the length of the fatigue crack per load cycle. *N* is the number of fatigue cycles. The terms *C* and *m* are empirical constants which are functions of the materials properties and microstructure, fatigue frequency, mean stress or load ratio, loading mode, environment, stress state and test temperature. The value of *m* is typically between 2 and 4 for ductile metallic materials. Equation 2.33 is the empirical crack growth law which is most

widely used in characterizing fatigue crack growth rates for a vast spectrum of materials and test conditions. It is worth mentioning that stable fatigue crack growth occurs at stress intensity factor levels, $K_{max} = \Delta K/(1-R)$, which are well below quasi static fracture toughness. A two parameter characterization for fatigue crack growth as demonstrated by *Schmidt and Paris*[59] is sometimes used as given below

$$\frac{da}{dN} = f(\Delta K, R) = g(\Delta K, K_{\max}) \qquad 2\text{-}34$$

Here f and g are functions, which determine the numerical values of c and m in equation 2.38.

2.2.4.3.4 Various regimes of crack growth: Based upon the power law (Equation 2.33), a plot of $log\ (da/dN)$ vs $log(\Delta K)$ can be used to explicitly define three distinct regimes of crack growth. For stage I, cracks can not grow appreciably below a certain stress intensity factor range i.e. a threshold stress intensity factor ΔK_{th} Regime II exhibits a linear variation of log (da/dN) with $log(\Delta K)$ corresponding to Equation 2.33. Regime III corresponds to high ΔK values where rapid increase in crack growth rate leads to catastrophic damage. All these regimes[60] are shown in Figure 2.19.

2.2.4.4.Fatigue crack closure

The build up of residual plasticity behind a crack tip can affect the crack growth rate and is a strong function of the loading history. This was first proposed by *Elber*[61]. As shown in Figure 2.20, the reduction in crack opening displacement causes a contact between faces of the crack. *Elber* argued that a crack can propagate only during that fraction of fatigue loading cycle in which crack faces are separated. During one cycle of crack growth, residual strains are left in the material behind the advancing crack front as only elastic recovery occurs after the creation of the fracture surface. The plastic wake produced thus severely retards the growth of the fatigue crack by causing their flanks to come into contact prematurely. The effective stress range and the stress intensity factor are given by

$$\begin{aligned} \Delta\sigma_{eff} &= \sigma_{\max} - \sigma_{op} = U\Delta\sigma \\ \Delta K_{eff} &= K_{\max} - K_{op} = U\Delta K \end{aligned} \qquad 2\text{-}35$$

where $\Delta\sigma$ and ΔK are the applied stress range and the stress intensity factors respectively. The fatigue crack growth based on LEFM is given by the following expression

$$\frac{da}{dN} = C(U\Delta K)^m \qquad 2\text{-}36$$

In addition to the residual plastic strains, additional mechanisms for fatigue crack closure also have been recognized[62]. These mechanisms include corrosion layers formed within a crack, microscopic crack closure, viscous fluids penetrated inside the crack, stress or strain induced phase transformations at the crack tip and closure due to surface roughness. All these mechanisms have been discussed in Section 2.2.8 with reference to various environmental factors affecting fatigue crack growth. Several other mechanisms such as crack deflection, crack trapping and crack shielding due to microcracking also impede the growth of cracks.

2.2.5. Short fatigue cracks

Durability analysis of engineering components is concerned with the regime of initiation and growth of short fatigue cracks during early life[63] (cracks <1mm in length). The term short or small fatigue crack has a number of definitions depending upon whether it is being described physically, microscopically, mechanically or chemically. *Miller et al*[64] have subdivided short fatigue cracks into microstructurally (MSC) and physically short cracks. A fatigue crack is said to be physically small if it is less than a millimetre or two but larger than the microstructural scale. If it is comparable to microstructural features such as grain size or distance between two particles in a particulate composite, it is known as microstructurally short. *Miller*[65] has further described the overall fatigue behaviour of metals by three distinct regimes, i.e. microstructurally short crack, physically short crack (PSC) and long cracks. Small fatigue cracks in smooth specimens for which near tip plasticity is comparable to the crack size are also known as mechanically short fatigue cracks.

Some factors considered responsible for the difference in small and long crack behaviour are diminishing of near tip shielding for small cracks, impedance of crack growth by local grain boundaries, influence of non-uniform growth and higher plastic strains at their tips[66].

2.2.5.1.Initiation of microstructurally short fatigue cracks

The demarcation between fatigue initiation and growth life depends upon the size of the microscopically detectable crack. For microstructurally short fatigue cracks, this could be considered equivalent to the grain size for a single-phase material, size of secondary phase particles in a multiphase alloy or size of microstructurally visible defects such as pores and inclusions.

In a continuous material, the actual initiation process of a crack is linked with slip mechanisms in crystal planes during initial load cycles (detail given in Section 2.2.2), however commercial alloys used to manufacture various engineering components usually have heterogeneous microstructures showing grain boundaries, secondary phase particles, shrinkage defects, pores and inclusions. Hence, fatigue behaviour of such alloys is perhaps better explained, based on the role of one or more of these microstructural inhomogeneites.

.

2.2.5.1.2 Crack initiation from grain boundaries

In ductile solids, grain boundary fatigue initiation is quite uncommon in the absence of any environmental effects (grain boundaries are potential sites for environmental attack) or elevated temperature (where grain boundary sliding is more prone). During cyclic loading, the cracking of a grain boundary may be due to the impingement of PSBs (Section 2.2.2) at a grain boundary at low to intermediate plastic strain amplitude[67]. At higher plastic strain amplitudes, grain boundary cracking was observed to be the result of surface steps formed at the grain boundary[68]. Many researchers[69,70] have addressed the effect of grain boundary orientation on the fatigue crack initiation and introduced the concept of 'grain boundary design and control' to improve the performance of materials. The effect of grain boundary orientation on fatigue cracking was further studies by *Zhang* and *Wang*[71] using *Cu* bi-crystals with embedded grains. It was concluded that large angle grain boundaries often become an obstacle to slip deformation and stimulates the slip of secondary slip systems resulting in severe plastic strain incompatibility near the large angle grain boundary. The low angle grain boundaries on the other hand showed good plastic strain compatibility as they transferred both PSBs as well dislocations. This gives rise to fatigue cracking along large angle grain boundaries as they obstruct PSBs and dislocations that result in local stress concentrations.

2.2.5.1.3 Crack initiation from secondary phase particles

In many commercial alloys, additionally added elements form secondary phase particles, which are microstructurally distinguishable from the continuous matrix. The mechanical properties of these particles such as yield strength and stiffness may be different from the rest of the matrix. Apart from the secondary phase particles, many commercially produced alloys may have other inclusions of various types and sizes. Under applied fatigue loads, the local stress levels within the particle may be different from the surrounding matrix because of a mismatch between their mechanical behaviour. Under these circumstances cracks may initiate from such

locations where the secondary phase particles are present (either by debonding or by fracturing of a brittle particle). For example, in *Al-Si* casting alloy (A356) previous studies[72,73] have shown that debonding or fracturing of *Si* particles was responsible for early micro-scale fatigue initiation. Depending on the external loading conditions, microstructural studies of initiation carried out by *Marrow et al*[74] has showed that secondary phase particles such as nodules in ductile iron were observed to be potential crack initiation sites. Similarly decohesion of secondary phase particles[125] such as *Sn* and *Si* has been reported during previous research on *Al* bearing alloys. Fatigue initiation from secondary phase particles has also been considered an important mechanism causing the failure of metal matrix composites[75].

A number of researchers have investigated the cause of fatigue initiation from secondary phase particles in various alloys. *Nutt* and *Needleman*[76] hypothesized that crack initiation as a result of interfacial decohesion occurs when the normal stress (hydrostatic stress assumed in latter work) at the particle-matrix interface reaches a critical value. Further work by *Clyn*[77] experimentally proved this hypothesises when he observed void nucleation along particle-matrix interface. *Dighe and Gokhae*[78] considered that particle size was important with regards to the initiation. Their work showed that coarser *Si* particles in *Al-Si-Mg* alloys showed an enhanced propensity for crack initiation. This was linked to the greater probability of a larger particle containing an interfacial flaw and promoting decohesion.

Apart from particle size their shape and orientation was considered to be important. Particles with sharp corners may give rise to stress concentrations and depending upon their mechanical properties, such stress raisers may result in the fracturing of the particle. The orientation effect of the particle was investigated in detail by *Gal et al*[79] who showed that the magnitude of the matrix hydrostatic stress was inversely proportional to the radius of curvature presented to the tensile axis of the embedded *Si* particle. When the particle major axis is aligned with the tensile axis, a small radius of curvature is presented to the tensile axis, giving rise to the maximum evolved hydrostatic stress.

2.2.5.1.4 Crack initiation from defects

Material defects such as pores exists in many commercial alloys. These pores may act as stress raisers under the applied load and hence they may be considered as fatigue crack precursors. Numerous studies have shown that fatigue life in the cast *Al-Si* alloys is controlled by the presence of large scale casting porosity[80]. The possibility of a high pore density population is increased in the alloys manufactured by spray casting or sintering processes due to

incomplete diffusion bonding between constituent particles. In such systems, the overall fatigue life is largely controlled by the amount and size of pores present. It was observed[81] that a reduction in microporosity in *Al-Si-Mg* alloys resulted in the increased fatigue initiation life. *Holmes* and *Queeney*[82]proposed that relatively high stress concentrations at pores particularly those near the surface are responsible for localized slip, which lead to crack initiation. *Lindstedt et al*[83]reported that angular pores create higher stress concentrations and stress intensity factor than the round pore. However; *Christian* and *German*[84] have showed that the fatigue behaviour of the powder-metallurgy materials is dependent upon various features of the pore population such as pore size, pore shape and pore separation.

2.2.5.2. Growth of short cracks under fatigue

Short cracks once initiated from the most favourable microstructural entities such as favourably oriented grains, secondary phase particles or various other defects tend to grow under the applied cyclic load. It was pointed out by *Pearson*[85] that the growth behaviour of short fatigue cracks is significantly different from long fatigue cracks. He pointed out that short cracks in precipitation hardened aluminium alloy grew 100 times faster than long cracks at the same level of ΔK. Similarly, other researchers such as *Dowling*[86] have observed that in the microstructurally short crack stage, the scatter in growth rates for short cracks was higher than long cracks. *Morris*[87] pointed out that periods of growth rate retardation occurred when the crack tip approached a grain boundary which hinders the advancing plastic zone ahead of crack tip (dislocations movement on slip planes is restricted due to irregular structure of grain boundaries). Typical short crack growth behaviour is shown in Figure 2.21. This scatter increased with fatigue cycling until growth rate reached a maximum value at the transition point into physically short crack growth behaviour. It then decreased and tended to a saturation level. At this stage, the crack tip starts sampling the bulk material in a more uniform way and its growth exhibits the behaviour of a long crack.

Crack closure effects (Section 2.2.4.4) are far less pronounced for microstructurally and physically short fatigue cracks compared to long cracks as the latter has a greater length in the material along which closure may occur. The growth behaviour of microstructurally short fatigue cracks is more complicated compared to physically and mechanically short fatigue cracks as the former interact largely with multiple microstructural inhomogeneities such as grain boundaries, secondary phase particle and materials defects.

2.2.5.2.1 Characterizing growth of short fatigue cracks

Due to the small size of the crack compared to its plastic zone size, LEFM cannot strictly be applied to truly characterise the growth rate of short fatigue cracks as it may result in large errors in the growth behaviour. *Dowling*[88] suggested that a cyclic *J* integral 'J_C' could be used to characterize the driving force for elasto-plastic short flaws (half penny shaped flaws)

$$J_C = 3.2(\Delta w_e)a + 5(\Delta w_p)a = \frac{1.6(\Delta\sigma)^2 a}{E} + \frac{5(\Delta\sigma\Delta\varepsilon_P a)}{\frac{n+1}{n}} \qquad 2\text{-}37$$

where ΔW_e and ΔW_p are elastic and plastic components of nominal strain energy density range, a is the depth of the surface flaw and n is the strain hardening exponent. $\Delta\sigma$ and $\Delta\varepsilon_p$ are the applied stress and plastic strain ranges. This method appears quite useful compared to other characterisation methods but J_C may not be so practicable as fatigue processes involve irreversible (plastic) deformation that appears to violate the fundamental basis of the *J* integral.

Various methods for calculating ΔK levels for short fatigue cracks have been suggested by *Newmann and Raju*[89] and *Scott and Thorpe*[90]. The *Scott* and *Thorpe* method has been used in this work to calculate ΔK levels assuming semi-elliptical shapes of cracks. The detail of this method is given in Chapter 5.

2.2.6. Short crack growth modelling

Short crack growth modelling needs a careful consideration of a variety of factors related to the microstructure of a material. Experimentally obtained short crack data for most of the commercial alloys shows large scatter as a result of the interaction of crack tip with microstructural anomalies (Section 2.2.5.2). Various semi-empirical and microstructural crack growth models exists which are based upon physical, empirical or semi-empirical approaches. One example of empirical model is the *Hobson*[91] model in which it was assumed that crack growth is proportional to the distance between crack tip and the grain boundary (on the basis of previous experimental). This model is described by the following equation.

$$\frac{da}{dN} = C_1\left(\frac{n}{2}D - a\right)^{1-\alpha} a^{\alpha} \qquad 2\text{-}38$$

Where D is the grain size, n the number of grain spacing along the crack and C_1 and α are constants. *Hobson* fitted the above equation with some experimental data to obtain the values of constants. In this model, it was assumed that the crack retardation occurs at grain

boundaries. This method was implemented by various other researchers such as *Grabowski*[92] and *Bomas et al*[93]. These researchers defined the boundary conditions of the model (maximum and minimum growth rates) based upon their experimental data on *Ni*-based super alloys and carbon steel respectively. Once the boundary conditions of crack growth were defined they assumed a linear growth of crack between grain boundaries (α=0 in Equation 2-38).

Zhang and *Edwards*[94] (characterizing crack growth for 7000 series *Al* alloys) found that the plastic zone size ahead of a crack tip is an important parameter in characterizing the growth behaviour of small fatigue cracks. They noted that relatively large plastic deformation zone associated with the short crack could be used to explain their fast growth rates compared to the long cracks. They modelled growth behaviour of short fatigue cracks based on their accelerations and decelerations in terms of the interaction of their plastic zones with the grain boundaries. The cracks were assumed to be retarded (supported by experimental observations) at the grain boundary. Their further growth starts only when enough plastic deformation (or plastic zone size) develops in the next grain.

The observed higher growth rate of small fatigue cracks compared to the long fatigue cracks at comparable ΔK levels was attributed to fatigue crack closure mechanism by *Elber*[95]*et aI.* Normally, that portion of the load cycle is used to compute the effective ΔK values for which cracks are fully open (LEFM). A small crack initiating from an inclusion or void is too small to have any prior plastic history that may cause closure (plasticity-induced closure). Hence, a small crack may not be closed for much of the loading cycle and the stress intensity range remain fully effective resulting in higher growth rates of short fatigue cracks. Using the concepts of crack closure effects, *Newman and Raju*[96]developed more accurate short crack growth models in which they used finite element analysis to investigate plasticity induced closure effects as the small crack grows. *Newman*'s model provides numerical justification of the transient retardation behaviour in the growth of small crack as the crack length increase (when plasticity induced closure becomes effective). The plasticity induced closure model was further used by *Newman et al*[97] to compare the estimated short crack growth results with the available experimental crack growth data for *Al* alloy (7075T6) specimens. A good agreement was found that helped in predicting the fatigue life of the tested specimens.

2.2.7. Fatigue crack deflection

Fatigue cracks can deviate from normal mode I growth due to a number of factors such as

- Deflection at grain boundaries.
- Deflection at particle-interface (i.e. interface of a secondary phase particle in a multiphase alloy or a particulate composite)
- Deflection at the reinforcement in a fibre or lamellar composites (i.e. depending upon the mechanical properties of the reinforcement and the matrix).
- Deflection at the interface between two layers or within a layer depending upon the difference between their mechanical properties. (i.e. in multilayered systems such as some composites with thin interlayer[98] and automobile engine bearings with a number of layers of different materials).

A particular interest in crack deflection mechanisms arise from the fact that it results in the retardation of crack growth and may lead to improved fatigue resistance[60] in some engineering materials. *Suresh*[60] has shown that even small deflections in the path of fatigue crack (compared to the length of crack) can lead to a reduction in the crack growth rates by several orders of magnitudes. A branched or deflected crack with periodic deflections in its path is depicted in Figure 2.22. Here 'θ' is the kink angle, D is the distance over which the tilted crack advances along the kink and S is the distance over which the plane of growing crack is normal to the far field tensile axis. The elastic solution for local mode I and mode II stress intensity factors are given

$$k_1 = \cos^3\left(\frac{\theta}{2}\right) K_I \qquad 2\text{-}39$$

$$k_2 = \sin\left(\frac{\theta}{2}\right)\cos^2\left(\frac{\theta}{2}\right) K_I \qquad 2\text{-}40$$

Where K_I is the instantaneous value of the mode I stress intensity factor. The average local stress intensity factor for periodically deflected crack is given as

$$\overline{\Delta k} = \left\{\frac{D\cos^2\left(\frac{\theta}{2}\right) + S}{D+S}\right\}\Delta K_I = \left\{D' \cos^2\left(\frac{\theta}{2}\right) + \left(1 - D'\right)\right\}\Delta K_I \qquad 2\text{-}41$$

Where $D' = \frac{D}{D+S}$

Equation 2-41 describes the modification in the stress intensity factor (driving force of crack growth) only due to a deflection in the crack path without considering the closure effects.

In multilayered components having layers of varying strength and stiffness, crack deflection effects on the growth rate are more than those in a multiphase alloy. *Erdogan et al*[99] derived stress fields near the crack tip approaching perpendicularly to an interface between two dissimilar elastic materials. Based on calculated energy release rate (for the crack impinging and the crack deflected), they concluded that the interface toughness range could be determined relative to the bulk material toughness that will ensure the crack deflection. Behaviour of fatigue cracks approaching an interface was experimentally investigated by *Suresh et al*[100,101] in which they considered ferrite-austenite bi-material couple with similar elastic properties but different strain hardening and yield strength. They reported that a fatigue crack approaching normally from the interface from the harder side would remain undeflected whilst a crack approaching from the softer side showed a reduced crack growth rate, crack defection and finally arrest. *Sugimura et al*[102]further extended *Suresh*'s work by using a *J* integral to characterize the driving force for crack growth and its variation for a propagating crack under quasi-static conditions. It was concluded that the crack approaching the interface from the softer side towards the harder side experiences a drop in the crack driving force as it neared the interface. Hence, this shielding effect was considered to be the cause of the experimentally observed reduction in the crack growth rate.

Using *J* integral as a characterizing parameter for crack driving force, *Joyce*[103] investigated the effect on crack deflection as it approached from a harder lining layer (~0.3mm) to a thinner and softer interlayer (~0.05mm) which was backed by a stiffer and thicker steel layer (~1.5mm). An enhanced crack tip driving force was found as the crack reaches the softer interlayer from the relatively harder lining and penetrates the interlayer without deflection until the crack tip is in the soft interlayer and the shielding effect and propensity for deflection due to the far harder, stiffer steel backing becomes apparent. This phenomenon was supported by the experimentally observed crack deflection within a thin and soft *Al* interlayer when crack approached from *Al-Sn-Si-Cu* type lining to the interlayer backed by a thicker and much harder steel layer.

2.2.8. Effect of external environment on crack growth behaviour

The initiation of fatigue under cyclic loading may take place under all types of environments; however, the length of initiation and growth periods could be affected in different environments. Various researchers such as *Gough* and *Sopwith*[104] have studied the effect of environment upon initiation and growth of fatigue cracks. They have shown that external environment significantly controls the extent of slip irreversibility. Their research showed that fatigue life was remarkably improved in a dry and oxygen free media as opposed to moist air. In vacuum or inert environment, when a ductile material is subjected to cyclic loading, slip steps are produced which could be offset during unloading or reverse loading. However in the presence of oxygen, moist air or hydrogen, the freshly formed free surface of the slip steps is attacked by these chemical species that result in the formation of an oxide layer. Hence, the reverse slip becomes difficult and the surface becomes rough. In addition to that, these embrittling species are transported to the bulk material along PSBs and results in fatigue initiation. Figure 2.23 shows the schematic of this process.

The effect of oil environment upon fatigue behaviour is not as simple as various other factors are equally important to be considered. *Endo et al*[105] studying the crack growth rate in white metal (used as lining in bi-metal bearings with steel as backing) showed that the growth rate was lower in an oil environment. He hypothesized that oil penetration has reduced the growth rate because of a closure mechanism (Section 2.2.4.4). They assumed that oil completely penetrated into the crack irrespective of the crack size and loading conditions.

Tzou et al[106] considered capillary flow using paraffin and silicone oil environments. In their experimental work, they tested 2.25%*Cr*-1%*Mo* steel samples in these oil environments. Silicone oil viscosity used was 5, 1000, 15000 and 60000 mm^2/s, while the paraffin oil viscosity was 25 and 75 mm^2/s. They found that crack growth rate in oil was generally slower than air. However, they observed that at near threshold conditions (~10^{-6}mm/cycle) a slightly higher growth rate was evident in the oil environment. The found that at low load ratios (growth rate above 10^{-6}mm/cycle), growth in high viscosity oil was faster than in the low viscosity oil. *Tzouet et al* proposed that crack growth rate in oil is dependent upon two factors (i) corrosion fatigue mechanisms such as hydrogen embrittlement and active path corrosion which increase crack growth rate (ii) closure mechanisms which slow down fatigue crack growth. At higher load ratios and higher growth rates (*Tzou et al*) the corrosion mechanisms appeared to dominate while at near threshold conditions, the effect of closure mechanisms becomes important.

2.2.8.1. Effect of Hydrogen embrittlement

Hydrogen embrittlement is a mechanism by which various metals become brittle and crack following exposure to hydrogen. The overall process consists of two phases[107] (i) a series of transport steps to cause atomic hydrogen (as a result of dissociation of water vapours) to be absorbed into metal surrounding the crack tip and (ii) absorbed hydrogen act to embrittle the metal. This embrittlement mechanism is highly dependent upon alloy composition and generally consists of hydrogen diffusing along and causing the segregation on grain boundaries and thus promoting intergranular fracture[108].

2.2.8.2.Oxide induced crack closure

In the *Al* alloys the reduced crack growth rate in an inert environment is linked to the reduction in the striation formation. *Pelloux*[109] hypothesized that the slip process by which these striations form may be reversible in an inert environment due to the absence of an oxide layer. Studying the effect of oil environment, *Vasudevan*[110] reported that corrosion debris were 20-40 times thicker in fatigue cracks grown in moist air than those grown in oil environments. Hence, closure via an oxide induced mechanism is expected to be reduced in oil environment. *Suresh et al*[111] studied the effect of different environments on oxide induced closure. They found that oxide induced closure is more pronounced in moist air at near threshold conditions. At various load ratios (0.1 and 0.75) they showed that in an inert oil environment the fatigue crack driving force appeared to be far less restricted by oxide induced closure mechanisms(than it was in an air environment) at low load ratios. Fatigue tests carried out at low load ratio (0.75) showed negligible difference between air and oil environments. Hence, whilst an oil environment reduces oxide formation and thus reduces oxide induced closure mechanism, it was shown that an increase in crack growth rate compared to ambient conditions would only be seen at low load ratios. Hence, the formation of an oxide layer may cause enhanced crack growth rates by promoting irreversible slip at the crack tip. In the case when an oxide layer becomes thicker (at low load ratios), an oxide induced closure mechanism may become active causing reduced crack growth rates.

2.2.8.3.Viscous induced crack closure

In an oil environment, oil may penetrate into the fatigue crack and build a pressure during unloading process. *Tzou et al*[106] showed that this pressure will act as a closure

mechanism and its magnitude depends upon oil viscosity. They calculated the maximum stress intensity factor K^*_{max} caused by the oil pressure. The effective stress intensity range ΔK is given as

$$\Delta K_{eff} = K_{\max} - \left(K_{\min} + K^*_{\max}\right) \qquad 2\text{-}42$$

Tzou showed that closure by this mechanism would increase with viscosity until at very high viscosity, K^*_{max} will be limited by the oil's inability to penetrate into the crack. Oils with viscosity lower than 12500 mm^2/s were able to penetrate fatigue cracks. As these mechanisms merely depend upon oil viscosity rather than materials chemistry, therefore these should be considered equally important for *Al* bearing alloys operating in oil environments.

2.2.9. Summary of fatigue literature

The total fatigue life of engineering components is expressed on the basis of applied stress or strain amplitudes, the choice of either depends upon the deformation behaviour of the material in question. Past research on fracture mechanics has introduced various parameters to characterize the growth behaviour of fatigue cracks depending upon the domination of purely elastic or elasto-plastic conditions in the vicinity of crack tip. Various researchers have introduced fatigue as a local failure mechanism dependent upon the local microstructure. The total fatigue life is therefore considered as a sum of short crack initiation and growth periods. The initiation and early growth of microstructurally short fatigue cracks depends upon a number of materials and geometrical parameters related to microstructural heterogeneities. In addition, the external environment affects the growth behaviour of fatigue cracks significantly in some materials. In multilayered systems, the deflection of cracks during their propagation along various interfaces also plays a key role in affecting the total life of the component. The fatigue behaviour of multilayered plain engine bearings, the subject of this research, is therefore considered as a complex function of applied loads, materials microstructure, mechanical properties, layer architecture and external environment.

2.3. Technical aspects of engine bearings

Prior to understanding the fatigue failure mechanisms in the actual plain bearing designs, the nature of the loads encountered by them in service under hydrodynamic conditions must be considered.

2.3.1. Load Cycles in plain bearings

Plain engine bearings are subjected to cyclic loads during the operation of the automobile engine. In order to minimize the power dissipation due to friction between the journal and the bearing surface, a thin layer of oil is maintained between the two surfaces. This is achieved either by external oil pressurization or by using appropriate geometries of the bearing and journal to keep a high oil pressure that separates the two surfaces and carries a part of the load. The latter method applies to plain bearings in internal combustion engines and is known as *hydrodynamic action*. In hydrodynamic action, the load tending to bring the surface of bearing and journal together is supported entirely by fluid pressure generated by relative motion of the surfaces (as journal rotation). Typical film thicknesses at the thinnest point are 0.008-0.02 mm. A schematic view of such a bearing is shown in Figure 2.24. In a hydrodynamic system, the diameter of the connecting rod big end is kept slightly larger than the crankpin that gives rise to eccentricity between the centres of the crankpin and the connecting rod big end. The wedge shape thus formed is shown in Figure 2.24. The oil is squeezed into this wedge shape and creates high pressure that together with the high speed keeps the two surfaces apart during the operation of the engine. The bearings in both petrol and diesel engines are thus subjected to complex and substantial dynamic loads that vary in magnitude and direction.

2.3.1.1.Hydrodynamic theory

Hydrodynamic theory is based upon certain assumptions. The first assumption is that the oil should have a laminar flow (must comply with *Newton's* definition of viscosity)*. Inertial forces resulting from the acceleration of liquid are small as compared to the viscous shear forces. The third assumption is that the liquid is incompressible. Various attempts have been made to estimate the magnitude and location of the peak pressure in an oil film on the bearing surface. *MacKee*[112] was the first who suggested that the peak pressure in eccentric loading moves away from the axial centre of the bearing involving misalignment torque.

A simplified relation for the pressure at any point on the film is given below after a number of mathematical modifications to the original *Reynolds equation*[113]

$$p = \frac{3U\eta c\varepsilon \sin\theta}{Rc^3(1+\varepsilon\cos\theta)^3}\left(\frac{L^2}{4} - y^2\right) \qquad 2\text{-}43$$

*The force that is necessary to maintain a velocity difference between two parallel planes of a liquid is proportional to the difference of speed through the liquid. This assumption led to a relation for velocity given as

Viscosity = shear stress/shear rate

where p = pressure

U = surface speed of shaft

η = viscosity

L = axial bearing length

R= bearing radius

y=coordinate axis along vertical direction

c=nominal radial clearance

ε=eccentricity of the journal and bearing axis.

In addition to the geometric eccentricity of the journal and bearings as well as the events of elastic deflections and thermal distortions in the shaft, misalignments can occur during the operation of the engine under dynamic loading conditions. A detailed study on dynamic performance characteristics of two misaligned crankshafts belonging to 4 stroke petrol engines has been carried out by *Lahmar et al* [114].They concluded that the presence of even a small skew of the journal axis during the operating cycle can cause a metal to metal contact that may lead to surface lining failure. Figure 2.25 shows the variation of rotational speed versus friction along with different operating regimes for a journal bearing with fluid film lubrication.

The presence of high oil pressure at the central region of the bearing gives rise to circumferential surface stresses in the lining material[115]. These stresses which are cyclic in nature during the operation of an engine lead to the initiation of surface and subsurface cracks on the lining material. The small cracks characterize a predominant mode of bearing fatigue. *Glyde*[77] observed that fatigue failure mostly occurs in the central part of the lining surface leaving the edge areas intact as they did not contain an oil film. The central portion of the lining is hence supposed to support the load as a result of which many discontinuities occur at small regions giving rise to tangential tensile stresses.

2.3.2. Fatigue behaviour of engine bearings

Research on the fatigue behaviour of engine bearings has been growing for the past few decades. Fatigue behaviour is not only dependent upon specific material characteristics, as described in Section 2.1, but also on the design aspects and the external environment.

2.3.2.1.Design aspects

The geometric attributes that affect fatigue performance are the lining and backing layer thickness, oil film thickness, bearing and journal shape and housing compliance. The materials parameters include strength, hardness and the microstructural features that affect the fatigue crack growth mechanisms. The most significant geometrical parameters are lining and steel layer thicknesses. It was suggested by *Love et al*[116]that a thinner lining should improve the fatigue resistance as it transfers more load to the backing steel layer which is stronger than the lining. They postulated that if both the lining and backing layer thicknesses are in proportion to their elastic moduli, the fatigue life would be increased. Further work by *Duckworth* and *Walter*[117] proved that reduction in lining thickness caused an increase in the fatigue resistance of the bearing.

Blount and *Glyde*[118] observed the effects of bearing clearance on fatigue strength. They concluded that increasing the clearance between journal and bearings results in lower fatigue resistance. Increasing the clearance actually increases the journal orbit eccentricity that results in high distribution of peak pressure (the pressure increases along the periphery of the bearing). *Glyde*[119] has observed that in well aligned plain bearings, fatigue failure occurred predominantly at the central portion. This research when linked with the work at the Glacier Metal Company has concluded that the oil film is not present at the edges and hence only the central portion carries the load due to the presence of the oil film there[5].

2.3.2.2.Effect of lining microstructure

Extensive research has been carried out on the effect of microstructural features of the lining material on the fatigue resistance of plain bearings. Early work on the fatigue resistance of white-metal by *Blount*[120] showed that a coarse, statically cast microstructure results in a shorter fatigue life compared to a finer strip cast microstructure.

Effect of *Sn* particle size on the fatigue resistance of *Al-20Sn-1Cu* (AS15) bearing alloys was studied by *Romer*[121]. It was argued that the fatigue behaviour was unaffected by any change in the size of *Sn* particles in the range 1.6-8.4 μm^2 in the as received bearings; however the results for the tests conducted on the heat treated specimens showed a decrease in the fatigue life with an increase in the *Sn* particle size. The reduction in fatigue strength was associated with a destruction of the bond layer occurring at the *Sn* boundary, during the heat treatment process.

A detailed study of fatigue crack propagation in *Al-Sn* alloys has been carried out by *Bushby*[122]. He conducted a series of fatigue tests at constant *R* on alloys varying from 0 to 18% *Sn*. The alloys were machined into compact tension specimens with the aim of studying how the microstructure of bearing alloys affects the fatigue crack propagation rates. He observed that increasing the *Sn* content increased the fatigue crack growth rates. It was also shown that at low *R* ratios, the crack closure effects are more prevalent and hence the fatigue crack propagation rates and thresholds are more dependent upon morphologies of the *Sn* phase than its volume fraction. He also concluded that the decohesion at the *Al-Sn* interface is due to hydrogen embrittlement (due to interaction with moisture in the laboratory air). Multiple crack initiation and growth in multiphase alloys has been reported by *Shenton et al*[123] Further research[124] on the study of microstructural influences on fatigue crack initiation and growth for *Al-12Sn-4Si-1Cu* alloys has shown that the fatigue cracks initiate preferentially at the *Al-Si* interface. Finite element modelling at the microstructural level has shown that stress concentrations exist at these sites[127].

A more detailed investigation has been carried out by *Mwanza*[125] to determine the influence of *Sn* and *Si* phases on fatigue crack initiation and growth in two alloys designated as AS16(*Al-20Sn-1Cu-0.25Mn*) and AS1241(*Al-12Sn-4Si-1Cu*). The analysis was based upon finite body tessellation, adaptive numerical modelling and mechanistic approaches to explain fatigue initiation sites. It was shown that, in AS1241, *Si* particles were more likely to cause initiation of cracks if their long axis were aligned parallel to the tensile axis. For AS16, initiation seemed to be more favourable when the long axis of the *Sn* particle (larger than average) were aligned perpendicular to tensile axis. Due to respective differences in compliance between the second phase particles relative to the *Al* matrix, these two different preferential orientations maximized the hydrostatic stress around the particle which was believed to promote a decohesion effect that caused the observed crack initiation experimentally.

2.3.2.3.Effect of external environment

In order to study the effect of environment on the fatigue life of *Al-12Sn-4Si-1Cu* (AS1241) system life time curves have been evaluated on the basis of three point bend test configuration[126] conducted in ambient , vacuum and oil environment. It was concluded that the oil environment increased the lifetime; however with similar crack growth mechanisms as observed in the ambient environment. An even more increased lifetime of the bearing specimen

was observed when the test was conducted in vacuum (in addition, crack growth rates in oil were significantly lower than in air for the AS1241). Effect of oil environment on the fatigue performance of AS16 (*Al-20Sn-1Cu*-0.25 *Mn*) was also studied by *Mwanza*[127] and little effect on crack growth rate or lifetime was observed for the AS16 system oil environments (cf. air). This was attributed to the presence of a fully and partially inert environment in vacuum and oil at the crack tip respectively (vacuum showed a more profound effect in reducing the crack growth than oil) that might have reduced the rate of combined oxide formation and hydrogen embrittlement mechanism occurring in AS1241. However, for the AS16 the presence of oil environment did not show any effect on the growth of short fatigue cracks compared to their behaviour in air. It was thought that AS16 alloy was perhaps chemically more sensitive to the environment than AS1241 and the oil environment which was not completely inert could not suppress the environmentally assisted fatigue damage processes.

2.3.2.4. Layer architecture

Various bearing designs considered during current and previous research comprised a complex combination of layers of various materials and different thicknesses. The mechanisms of subsurface crack deflection in general discussed in Section 2.2.7 are particularly important for these bearing systems. In the previous reseach[127,103] on tri-layer systems, subsurface crack deflection was experimentally observed to be within the thin and soft *Al* interlayer layer sandwiched between a harder lining layer and a hardest and thickest backing steel layer. However, the role of interlayer to shield the subsurface crack growth is one of the important issues to be investigated during this research.

2.3.3. Summary of bearings fatigue literature

It can be seen that in-service fatigue failure of engine bearings is a complex phenomenon and service hydrodynamic loading conditions cannot be replicated easily during laboratory fatigue tests. However, micromechanical based studies of fatigue initiation and subsequent growth have been carried out to understand the fundamental initiating fatigue mechanisms in different *Al* based systems, manufactured via various processes. In previous work, combined experimental and finite element analysis has elucidated the micromechanics of fatigue initiation allowing identification of improved microstructures whereby finer and fewer secondary phase particles are required. Subsequent surface and subsurface crack growth has

also been studied in layered systems. Laboratory based analysis has provided basic information on the intrinsic fatigue resistance of different alloys. Fatigue behaviour of new lining alloys produced by HVOF and RB processes with reduced *Si* and *Sn* content (albeit increased *Ni* and *Cu* content) needs to be evaluated in the context of this previous work. The aims of this thesis are then to compare the fatigue performance of these newly developed alloys with previously studied systems, and based on this understanding to identify the microstructures with optimised initiation and crack growth resistance, leading to development of an overall lifing approach suitable for these systems.

References:

[1] Dowson, D. (1998). History of Tribology, Second Edition, Professional Engineering Publishing Edition, 185.

[2] Braithwaite, E. R.**.** (1967). Lubrication and Lubricants, European Manager of Chemical Sales and Development, Elseveir. Pub. Co. London.

[3] Mihara, K.. Inada, Y. Mashiko, T. (1991). SAE Technical Paper, 910890, 2. (www.sae.org/technical/papers/910890)

[4] Desaki, T. Kamiya, S. (2000). JSAE. Review 21, 143.

[5] Dana Glacier Vandervell Bearing Company, UK. (Private Communication).2004.

[6] Edward, W.M. Thomson, R.C. and Barnes, S. J.(2002). Mater. Sc. Forum 396-402, 625.

[7] Garcia-Hinojosa, J.A. Gonzalez, C.R. Gonzalez, G.M. (2003). Mater. Proc. Tech 143-144, 306.

[8] Polmear, I.J**.** Light alloys—The Metallurgy of Light Metals, R.W.K Honeycomb and P.Hancock, Eds., Publ. Arnold, 338.

[9] Hogerls, J. Spaic, S. and Tensi, H. (1998).Aluminium 74 (Jahrgang 10), 780.

[10] Torbin, H. and Pathak, J.R. (1994). Tribo. Int 27, 171.

[11] Torabin, H. and Pathak, J.P. (1994). Wear 177, 47.

[12] Yuan, G.C. Li, Z.J. and Lou, Y.X**.** (2000). Mater. Sc. Eng A 280, 108.

[13] Smallman, R.E. and Bishop, R.J**.** (1995) Metals and Materials, Science, Processes, Applications, Butterworth-Heinmann. Ltd, 327.

[14] Butts, A. (1970). Copper, The Science and Technology of the Metal and its Alloys. Hafner Pubs. Comp. New York, 510

[15]Pan, D. Gao, K andYu, J. (1989).Mater. Sc. Techl 5, 934.

[16] Jian, A. Yongbing, L. You, L and Daren, S. (2001). Mater. Characterization 47, 3-4, 291.

[17] Mostaghimi, J**.** Chandra, S. Ghafouri-Azar, R. and Dolatabadi, A. (2003). Surface.Coat. Tech 163-164, 1.

[18] Harris, S.J. McCartney, D. G, and Horlock, A. J. (2000). Mater. Sc. Forum, 331-337, 519.

[19] Kong, C. J, Brown, P. D, Horlock, A.J and McCartney, D.G. (2005). Mater. Sc. Eng A 403, 205.

[20] Ogita, Yukio, Ido, Yasuo; Sakamoto, Masaaki. (1990) SAE. Transactions 9, 1.

[21]Shioda, M. Arita, M. Matsuyama, A. Ohkawa, K. Sakai, T. (1990) Advances in Powder Metallurgy 51-63.

[22] Bily, Matej.(1993). Mat. Sc. Monographs. Cyclic Deformation and Fatigue of Metals, Elsevier, London, 78.

[23] Grosskreutz, J.C**.** (1971). Phys. Stat. Sol., (b) 47, 11 Phys. Stat. sol., (b) 47, 359.

[24] Mughrabi, H. Ackermann, F. and Herz, K. (1969). (J. T. Fong, ed), STP 675, ASTM, Philadelphia.

[25] Helgeland, O. J. (1965). Inst. Metals 93, 570.

[26] Thomson, N. Wadsworth, N. J. and Louat, N. (1956). Philosophical Magzine 1, 113.

[27] Gough, H.J. (1933). Proc. ASTM 33, 3-114.

[28] Orowan, E**.** (1939). Proc. Roy. Soc A171, 79.

[29] Stroh, A.N. (1955). Proc. Roy. Soc. A223, 404.

[30] Forsyth, P.J.E. (1953). Nature 171, 172.

[31] Cottrell, A.H.and Hull, D. (1957). Proc. Roy. Soc. A242, 211.

[32] Mott, N.F. (1958). Acta. Metall 6, 195.

[33] Backofen, W. A. (1959). Proc. Int. Conf. Atomic. Mechanism. Fracture. Tech Press MIT, John Wiley and Sons 435.

[34] Benham,P. P. Crawford, R.J. and Armstrong, C.G**.** (1996). Mechanics of Engineering materials, Second Edition, Prentice Hall.

[35] Wood, W.A. (1958). Formation of fatigue cracks, Philosophical magazine 3, 692.

[36]Schijve, J. (2003). Int. J. Fat. 25, 679.

[37] Plumbridge, W.J. and Ryder, D.A. (1969). Metal. Mater. Review 136, 3, 321

[38] Tryon, R.G. and Cruse, T.A. (1998). Fat. Frac. Eng. Mater. Struc 21, 257

[39] Wöhler, A. (1860) Zeitschrift fur bauwesen 10, 178; English Summary.(1867). Eng 4, 160

[40] Stanzl-Tschegg, S. and Mayer, H**.** (2001) Proc. Int. Conf. Inst. Metereology and phy.

[41] Basquin, O. H**.** (1910). Proc. ASTM 10, 625.

[42] Gerber, H. (1874). Bestimmung der zulassigen spannungen in eisen-konstruction, Zeitschrift des bayerischen architeteckten und ingenieur-vereins 6, 101.

[43] Goodman, J. (1899). Mechanics Applied to Engineering. London: Longmans Green.

[44] Soderberg, C.R.(1939). Trans ASME 52, 13.

[45] Coffin, L. F**.** (1954). A .Trans. ASME 76, 15.

[46] Manson, S.S**.** (1954). National Advisory Commission on Aeronautics: Report 1170.

[47] Griffith, A.A .(1921). Phil. Trans. Roy. Soc A221, 163.

[48] Congleton, J. and Petch, N.J. (1966). Acta Metall 14, 1179.

[49] Orowan, E**.** (1952). Fat. Frac. Metals (ed W.M.Murray), 139.

[50] Irwin, G.R**.** (1956). Second Sagamore Conf II, 289. New York.

[51] Irwin, G.R. (1957). J. Applied Mechanics 24, 361.

[52] Westergaard, H.M**.** (1939). J. Applied. Mechanics 61, A49-53.

[53] Rice, J.R**.**(1968). A Trans ASME J. Applied mechanics 35, 379.

[54] Irwin, G.R**.** (1960). Proc7th Sagamore Ordnance Materials Conf. 4, 63.

[55] Dugdale, D.S**.** (1960). J. Mechanics. Phy. Solids 8, 100.

[56] Paris, P.C**.** (1960). PhD. Thesis Bethlehem: Lehigh Univ.

[57] Rice, J.R**.** (1967). In: Fatigue Crack Propagation, Special Technical Publication, ASTM, 415, 247.

[58] Paris, P.C**.** Gomez M.P. and Anderson, W.P. (1961). In: A Rational Analytic Theory of Fatigue, The Trend in Engineering 13, 9.

[59] Schmidt, R.A. and Paris, P.C. (1973). Special Technical Publication 536, 79. Philadephia. ASTM. materials.

[60] Suresh, S**.** (2003). Fatigue of Materials, Second Edition, Cambridge University Press.

[61] Elber, W**.** (1971). Special Technical Publication, ASTM 486, 230.

[62] Parks, S and Ritche, D.M**.** (1982). Fat Thresholds1, Warley: Engineering Materials Advisory services.

[63] Rudd, J.L. Yang, J.N. Manning, S.D. and Garver, W. R. (1982). Design of Fat and Frac. Resist. Struc. ASTM. STP.761. Philadelphia, 133.

[64] Miller, K.J. and Rios, E.R. (1986). EGF (ESIS) Publication No 1, MEP. Inst. Mech. Engrs. London, 560

[65] Miller, K.J. (1993). Mater. Sc. Tech 9, 453

[66] Ritchie, R.O. Lankford, J. (1986) Proc of second Eng. Foundation. Int. Conf. Santa Barbra, Califoria, 3.

[67] Figueroa, J. C and Laird, C. (1983). Mater Sc. Eng 60, 45.

[68] Kim, W.H. and Laird, C. (1978). Acta Metall 26, 789.

[69] Watanabe, T. (1988). Mater. Sc. Forum 11, 284.

[70] Lim, L.C. and Watanabe, T. (1990). Acta. Metall 38, 2507.

[71] Zhang, Z.F. and Wang, Z. G. (1999). Mater. Sc. Eng A284, 285.

[72] Couper, M.J. Neeson, A.E. and Griffiths, J. R. (1990). Fat. Frac. Eng. Mater. Struc 13, 213.

[73] Plumtree, A. and Schafer, S. (1986). Mechanical Behaviour of Short Fatigue Cracks. Suffolk, UK, 215.

[74] Marrow, T. J. Cetinal, H. Al-zalmah, M. Macdonald, S. Withers, P. J. and Walton, J. (2002). Fat. Frac. Eng. Mater. Struc 25, 635.

[75] Hasan, S. T. Beynon, J. H. and Faulkner, R. G. (2004). J. Mater. Proc. Tech 153, 758.

[76]Nutt, S.R. and Needleman, A. (1987). Script. Met 21, 705.

[77] Clyne, T. W. and Whitehouse, A. F. (1995). Acta. Metall 43, 2107.

[78] Dighe, M. D. and Gokhale, A. M. Script. Met 37, 1435.

[79] Gall, K. Yang, N. Horstemeyer, M. McDowell, D. and Fan, J. (1999). Met. Trans 30A, 3079.

[80] Couper, M. J. Neeson, A. E. and Griffiths, J. R. (1990). Fat. Frac. Eng. Mater. Struct 13, 213.

[81] Stanzl, S.E. Mayer, H. R. Beste, A. and Krol, S.(1995). Int. J. Fat 17, 149.

[82] Holmes, J. and Queeney, R. A. (1985). Powder. Metall 28, 231.

[83] Lindstedt, U. Karlsson, B. and Masini, R. (1997). Int. J. Powder. Metall 33, 49.

[84] Christian, K. D. and German, R. M. (1995). Int. J. Powder. Metall 31, 51.

[85] Pearson, S . (1975). Eng. Frac. Mechanics 7, 235.

[86] Dowling, N.E. (1977) Crack Growth During Low Cycle Fatigue of Smooth Axial Specimens. In: Cyclic Stress-Strain and Plastic Deformation Aspects of Fatigue Crack Growth, STP 637, ASTM, Philadelphia, 97.

[87] Morris, W.L. .(1979) .Met. Trans10A, 5.

[88] Dowling, N.E. (1977). Special Technical Publication, ASTM 637, 97.

[89] Newmann, J.C. and Raju, I.S**.** (1981). Eng. Fract. Mech 15, 185.

[90] Scott, P. M. Thorpe, T. W. (1981). Fat. Eng. Mater. Struct 4, 291.

[91] Hobson, P.D. (1982). Fat. Eng. Mater. Struc 5(4), 323.

[92] Grabowski, L. and Yates, J. R. (1992). Int. J. Fat 14 (4), 227.

[93] Bomas, H. Linkewitz, T. and Mayr, P. (1996). Fat. Fract. Eng. Mater. Struc 19 (2/3), 299.

[94] Zhang, Y. H. Edwards, L. (1992). Srcipt. Metall. Mater 26, 1901.

[95] Elber, W. (1971). ASTM. STP 486, 230.

[96] Newman, J. R. and Raju, I.S. (1983). ASTM. STP 791, 238.

[97] Newman, J. R. Phillips, E. P. and Swain, M. H. (1999). Int. J. Fat 21, 109.

[98] Jenny Winn, E. and Chen, I. (2000). J. Amer. Ceram. Soc 83, 3222.

[99] Erdogan, F. Biricikoglu, V. (1973). Int. J. Eng. Sc 11, 745.

[100] Suresh, S. Sugimura, Y. and Tschegg, E. K. (1992). Script. Metall 27, 1189.

[101] Suresh, S. Sugimura, Y. and Ogawa, T. (1993). Script. Metall 29, 237.

[102] Sugimura, Y. Lim, P. G, Shih, C. F. Suresh, S. (1995). Acta. Metall 43, 1157.

[103] Joyce, M.R. Syngellakis, S. and Reed, P.A.S, (2003). Mater. Sc. Eng A342, 11.

[104] Gough, H. J. and Sopwith, D. G. (1932). J. Inst. Metals 49, 93.

[105] Endo, k. Okada, T.and Hariya, T. (1972). Bulletn. JSME. 15 (82). 439.

[106] Tzou, J. L. Suresh, S. and Ritchie, R. O. (1983). Mech. Behav. Maters 4, 711.

[107] Henaff, G. Marchel, K. and Petit, J. (1995). Acta. Metal. 43, 2931.

[108] Song, R. G. Tseng, M. K. Zhang, B. J. Liu, J. Jin, Z. H. (1996). Acta. Mater 44, 3241.

[109] Pelloux, R. M. N. (1969). Trans. ASME. 62, 281.

[110] Vasudevan, A. K. Suresh, S. (1982). Met. Trans. 13A, 2271.

[111] Suresh, S. Parks, D. M. Ritchie, R. O. (1982). Int. Fat. Thresh 1, 391.

[112] MacKee, S.A. and MacKee, J.R. (1932) Trans. ASME 54, 149.

[113] Ocvirk, F.W. and Dubois, G.B. (1953) .National Advisory Committee for Aeronautics, Washington, Report, 1157.
(http://ntrs.nasa.gov/archive/nasa/casi.ntrs.nasa.gov/19930085158_1993085158.pdf)

[114] Lahmar, M. Hrouadi, F. Frihi, D. (2000). Proc. Inst. Mech. Engrs 14, 991.

[115] Kollaman, K. and Harbordt, J. (1977). HOPE International Symposium, JSME, Tokyo, 317.

[116] Love, P.P. Forrester, P.G. and Burke, A.E**.** Functions of materials in bearing operations.

[117]Duckworth, W. E and Walter, G.H**.** (1956). Int. Conf. Fat. Metals, 582.

[118] Blount, E.A. Glyde, N**.** (1961). Proc. Inst. Mech. Engrs 175, 513.

[119] Gyde, N**.** (1969). PhD Thesis, Technical university of Denmark, Germany.

[120] Blount, E.A. (1961). Proc. Inst. Mech. Engrs 175, 10.

[121] Romer, H.F**.** (1969). Report No 514, AE No 114/072/69,

[122] Bushby, A.K. and Martin, J.W**.** (1988). Mater. Sc. Tech 4, 518.

[123] Shenton, P. and Perrin,C**.** Private communication, Dana Glacier Vanervell (2004).

[124] Joyce, M.R. Syngellakis, S. and Reed, P.A.S**.** (2000). Mat Sc. Forum 331-337, 1445.

[125] Mwanza, M.C. Joyce, M.R. Lee, K.K. Reed, P.A.S**.** (2003). Int. J. Fat 25**,** 1135.

[126]Joyce, M.R. Syngellakis, S. and Reed, P.A.S, (2004). Mater.Sc. Tech 20, 47.

[127] Mwanza, M.C**.** (2004). PhD Thesis, University of Southampton, 122.

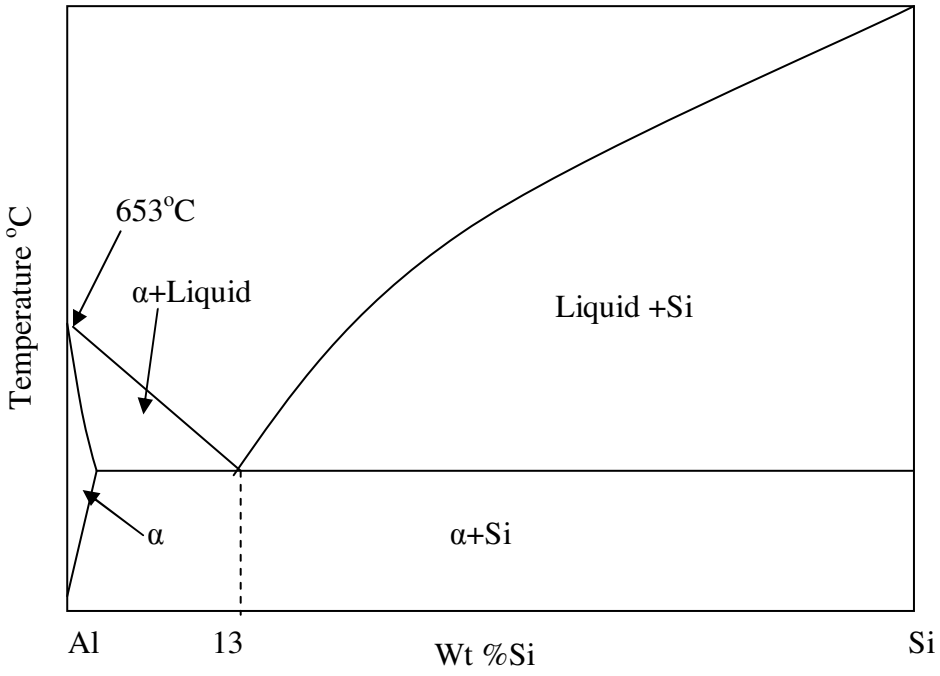

(a)

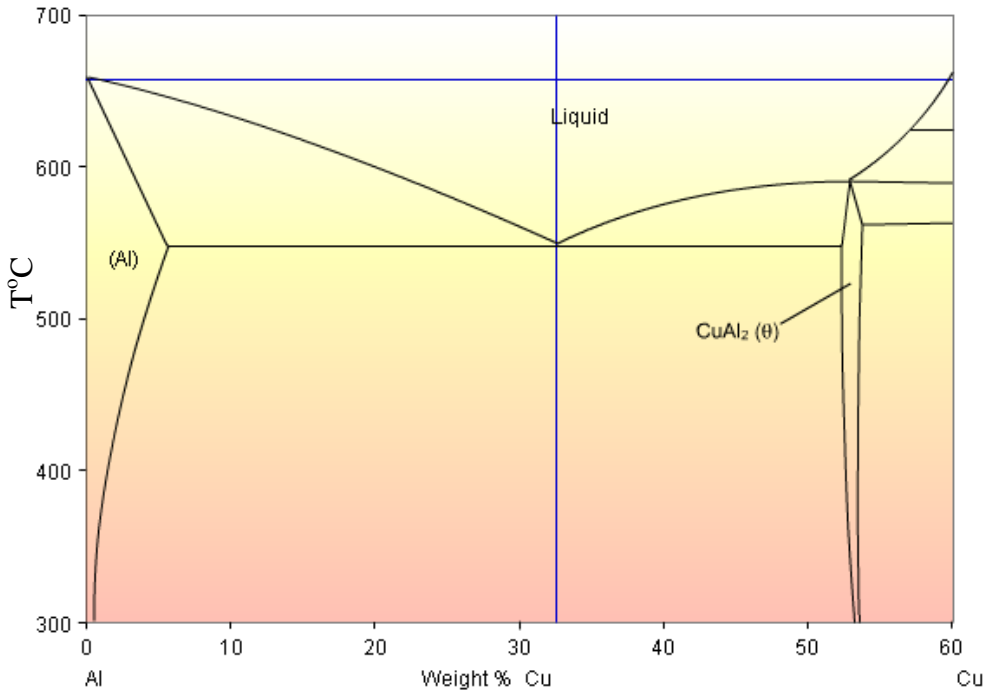

(b)

Figure 2.1. (a) *Al-Si* phase diagram (b) *Al-Cu* phase diagram (After[8]).

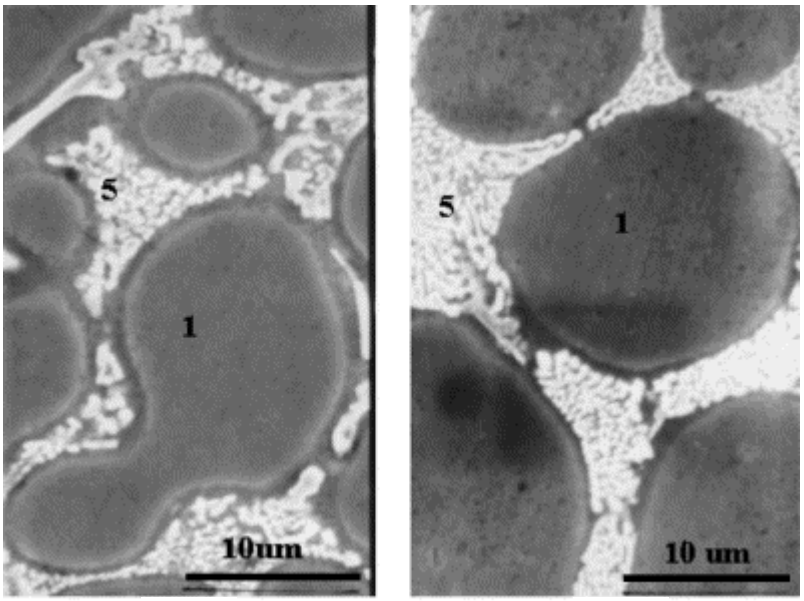

(a) (b)

Figure 2.2: Microstructure of (a) *Al-0.5Si-1Cu (*b) *Al-1.5Si-0.5Cu. Si* and globular $CuAl_2$ is denoted by 5 and *Al*(α) is denoted by 1. These are modified with 0.002%*Sr*. (After Garcia[7]).

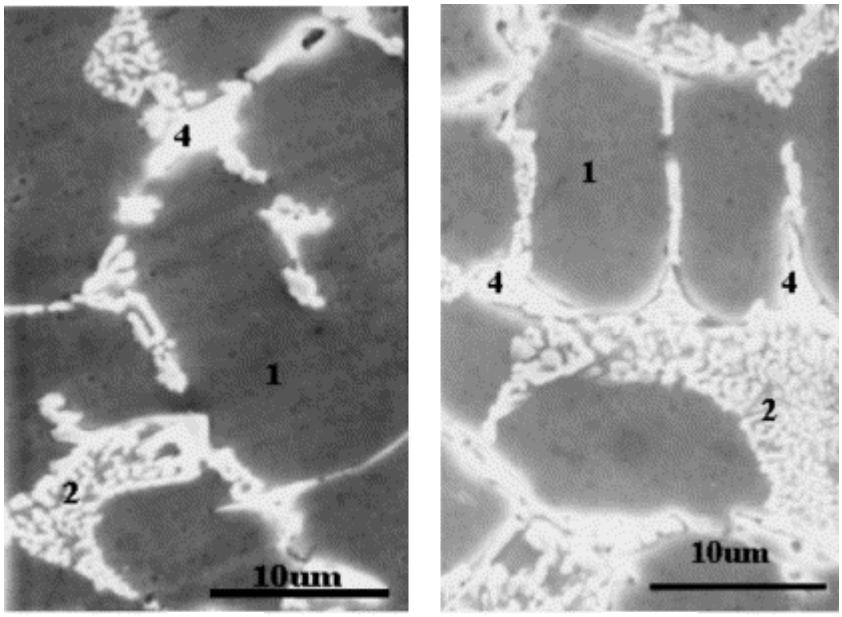

(a) (b)

Figure 2.3: (a) *Al–7Si–0.5Ni* and (b) *Al–7Si–1.0Ni* both of them modified. α (*Al*) solid solution is denoted by 1, globular-fibrous Si of the eutectic phase is marked with 2, and $NiAl_3$ block particles are denoted by 4 (After Garcia[7]).

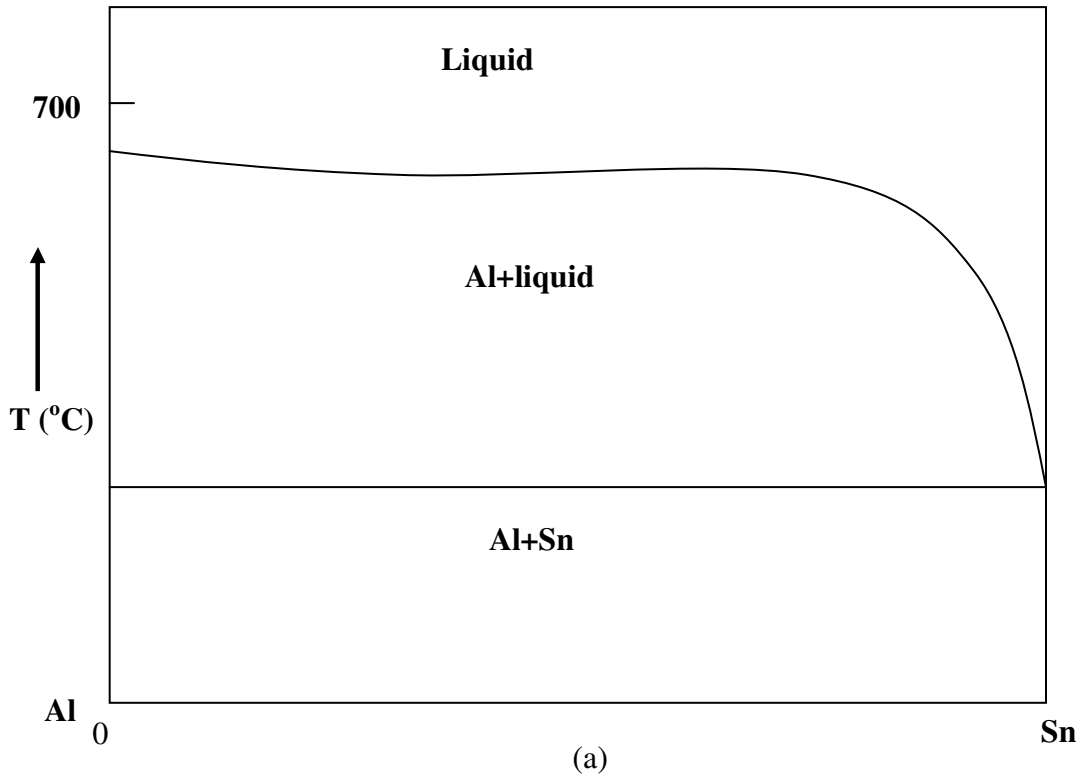

(a)

Figure 2.4: *Al-Sn* phase diagram (After Braithwaite[2]).

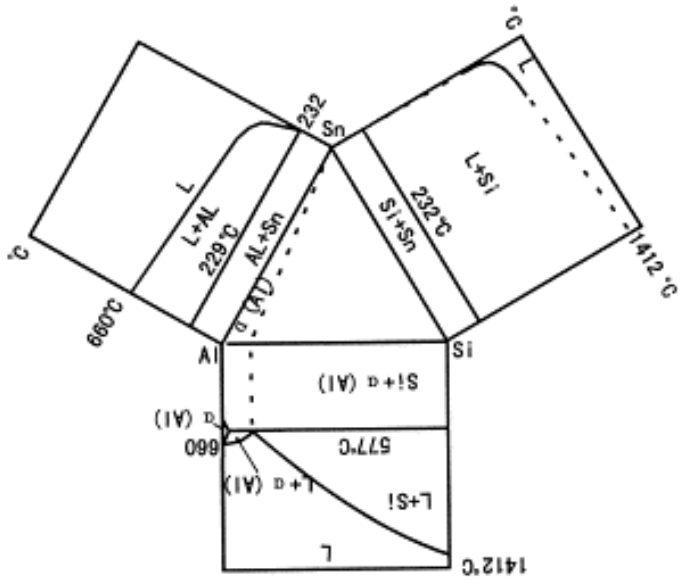

(b)

Figure 2.5: The unfolded ternary diagram and projection of liquid phases face for *Al–Sn–Si* system. (After Yuan[12]).

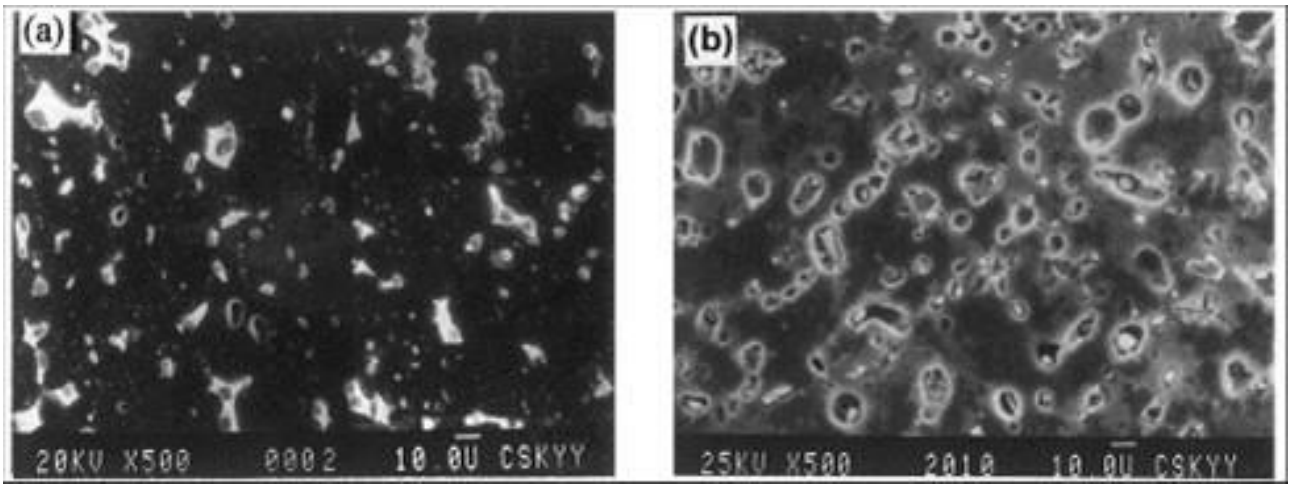

Figure 2.6: SEM morphology of *Al–10Sn–4Si-0.8Cu* alloy after homogenization (a) back-scattering electronic image (b) secondary electronic image (After Yuan[12]).

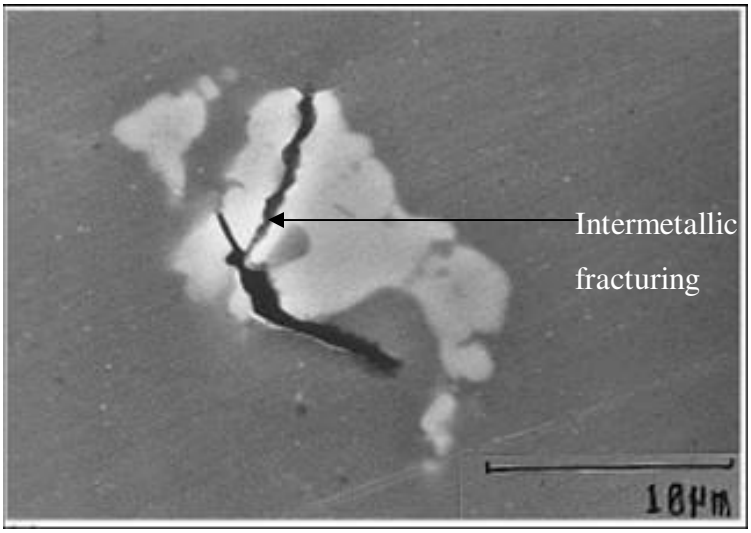

Figure 2.7: Fatigue crack initiation sites: fracture of brittle Al_7Cu_2Fe intermetallic (Optical micrograph) in 7010 alloy (After[9]).

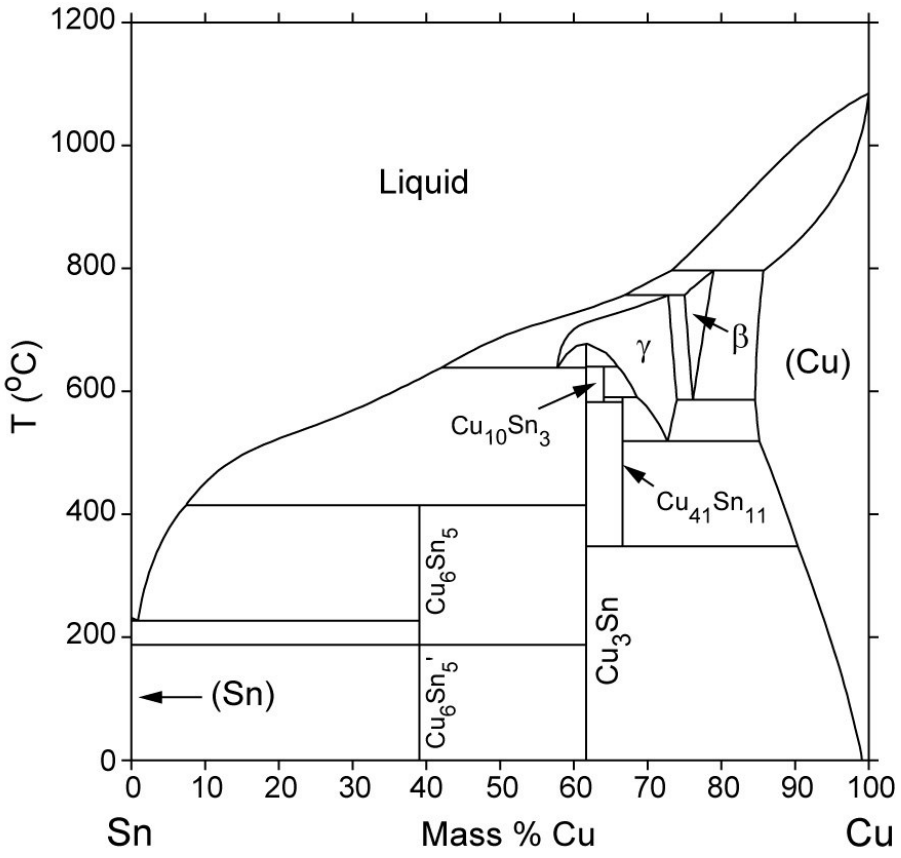

(a)

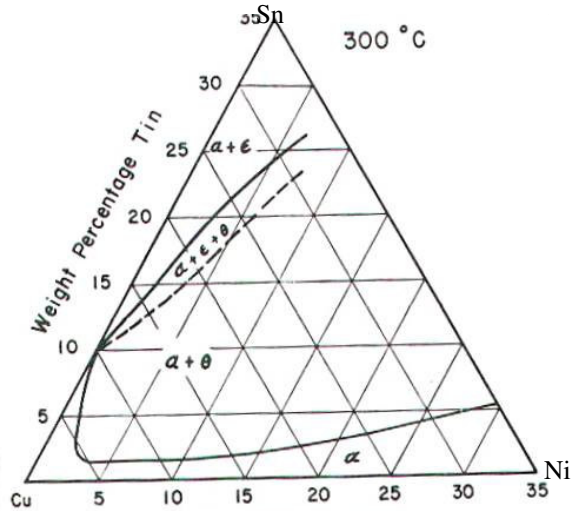

(b)

Figure 2.8:(a) Binary phase diagram of *Cu-Sn* systems (b) ternary diagram of *Cu-Sn-Ni* systems (After[14]).

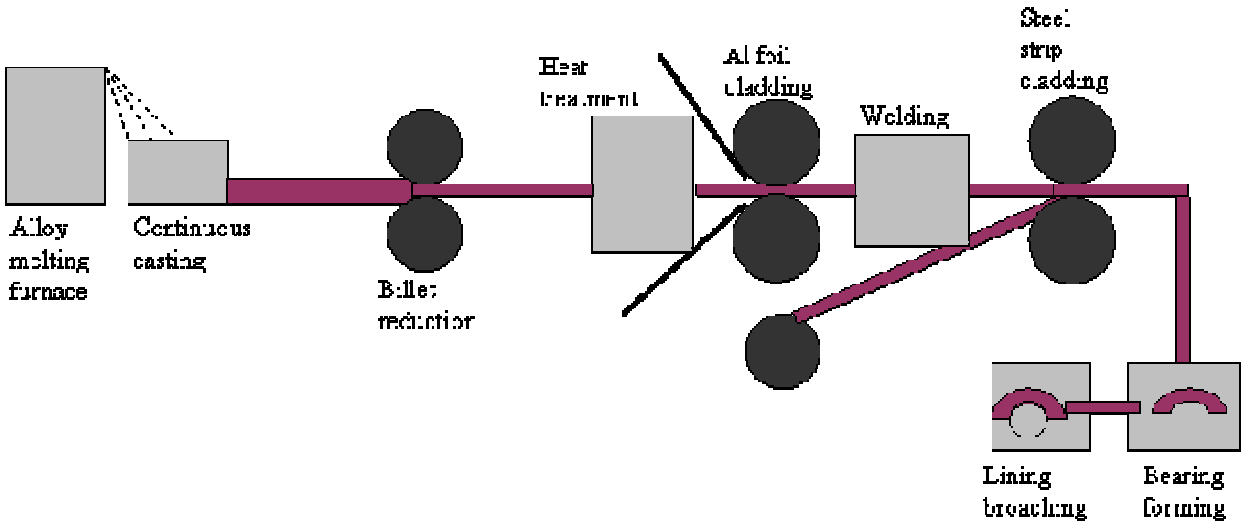

(a)

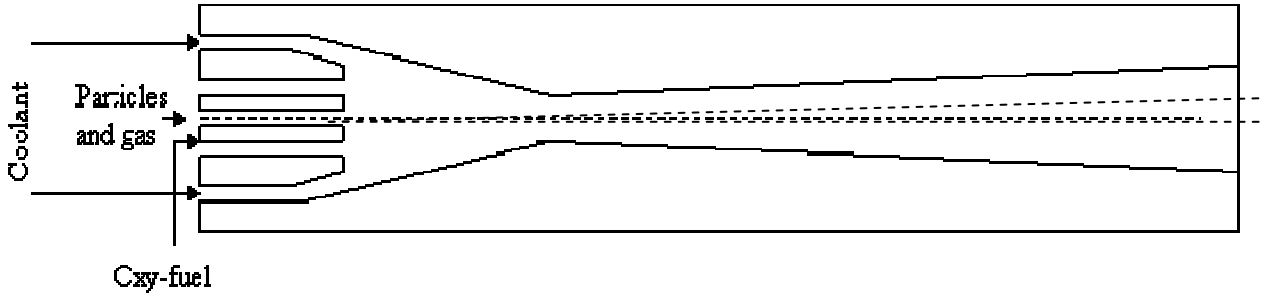

(b)

Figure 2.9: (a) A schematic of commercially adopted roll bonding processes for *Al* and *Cu* based bearings (b). A modelled spray coating gun used for HVOF process (After[18]).

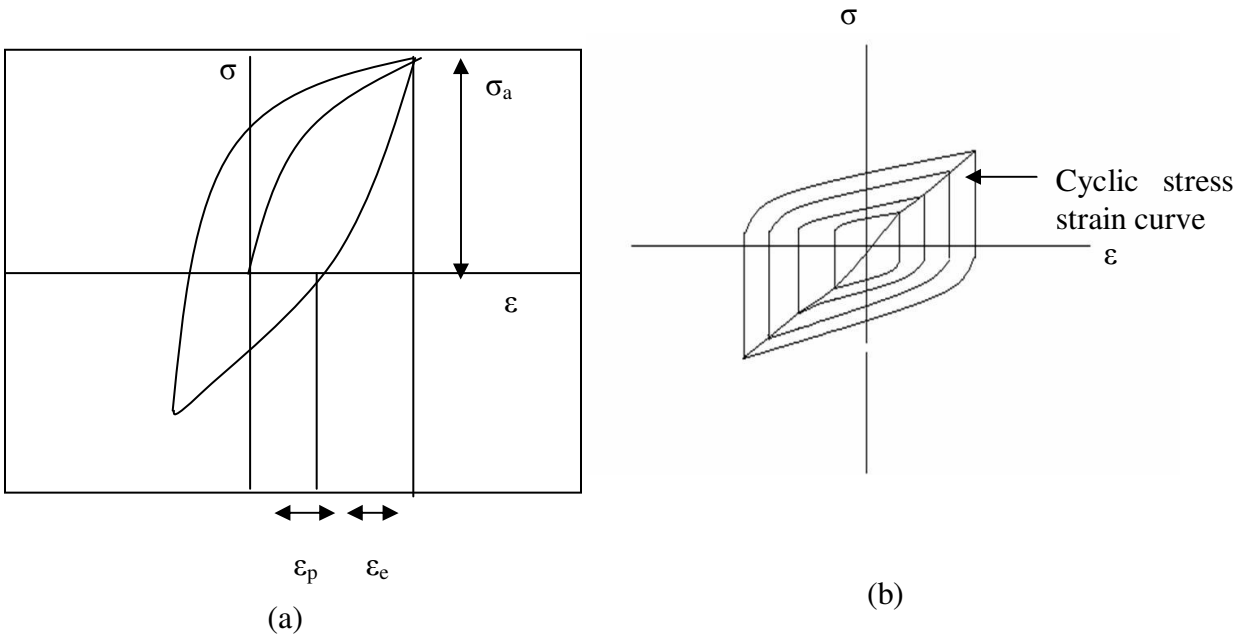

Figure 2.10: (a) Schematic of hysteresis loop developed during cyclic deformation. (b) Cyclic stress strain curve obtained from hysteresis loops (After[22]).

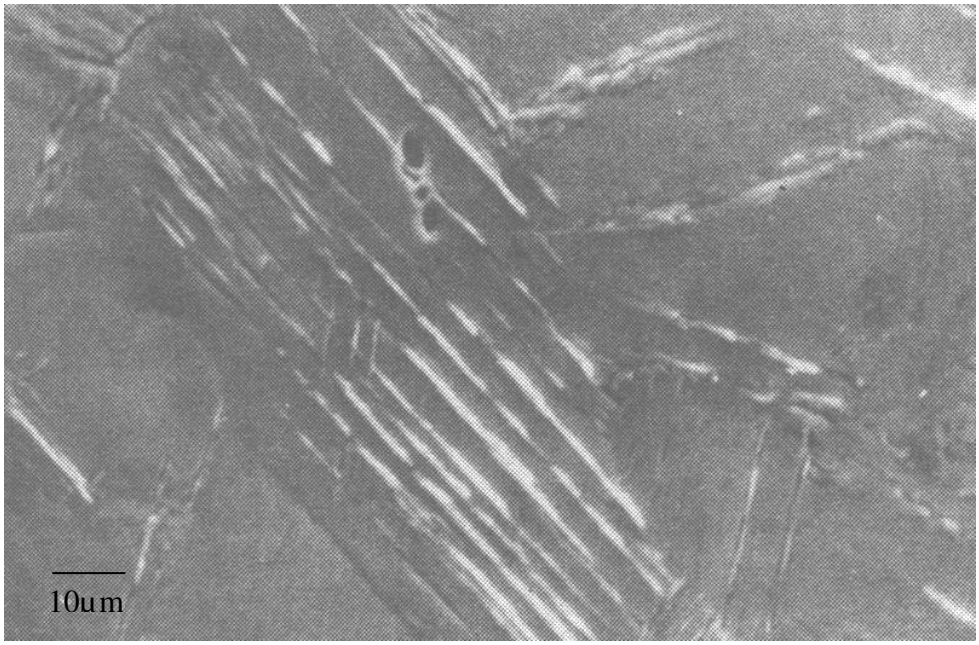

Figure 2.11: Persistent slip bands in cycled polycrystalline *Cu* (After[22]).

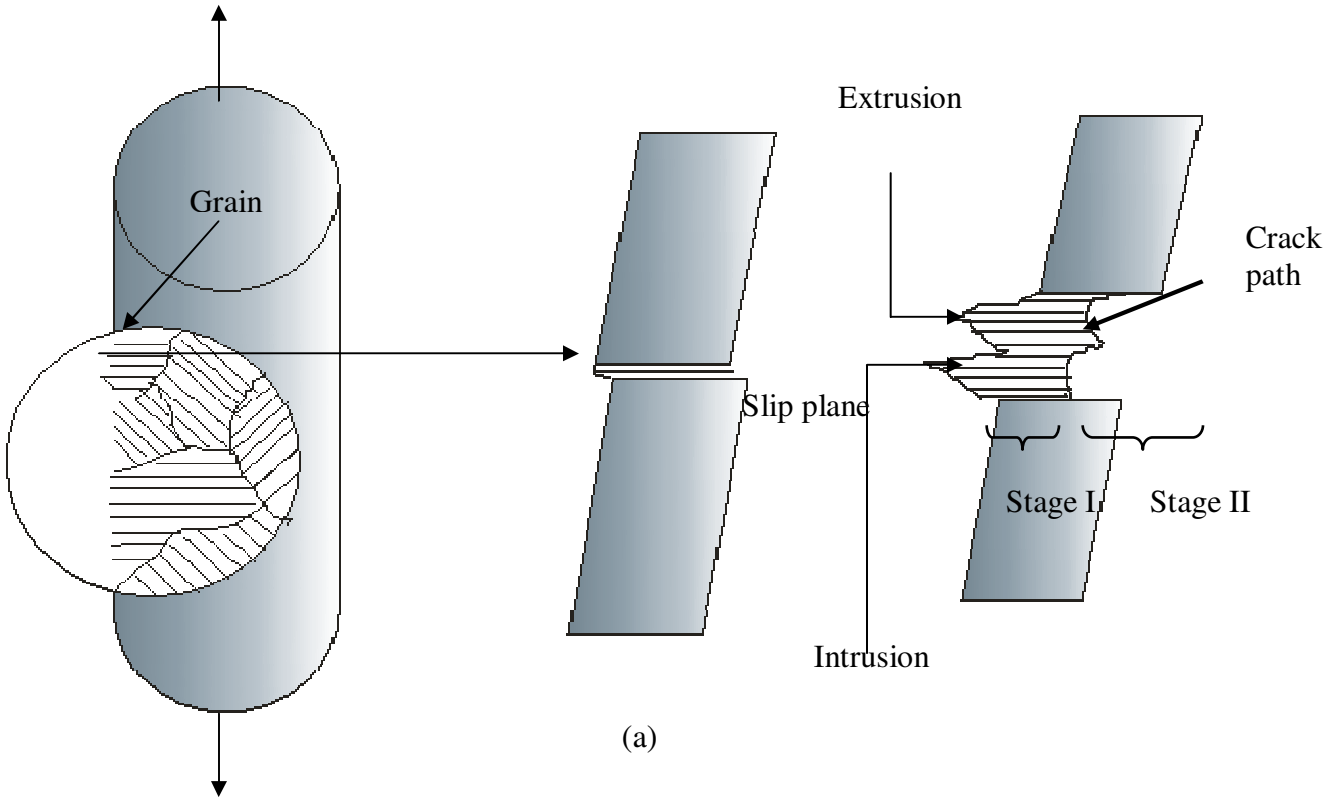

Figure 2.12:Development of a crack along slip planes (After Benham[34]).

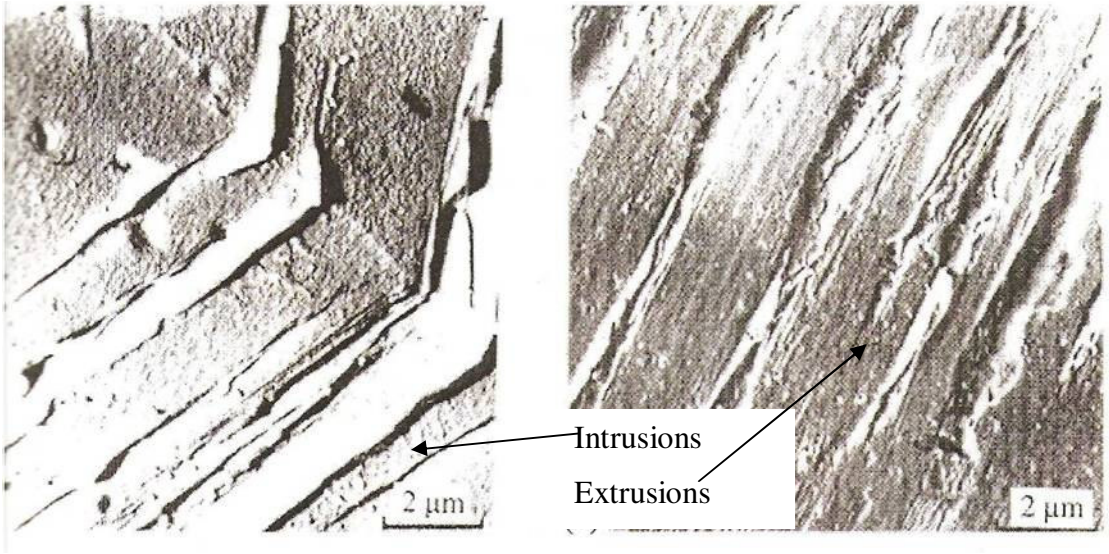

Figure 2.13: (a) Intrusions and (b) extrusions on *Cu* surface fatigued at -183°C (After[60]).

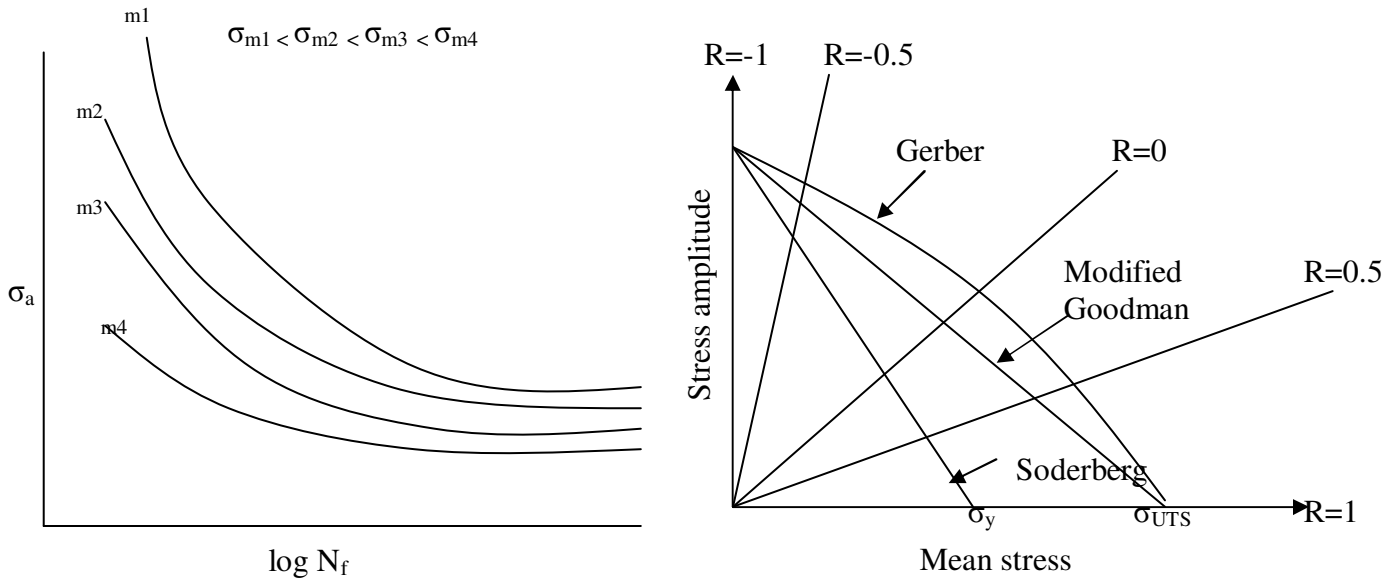

Figure 2.14: (a) Effect of mean stress on fatigue life. (b) Constant life curves for fatigue loading.

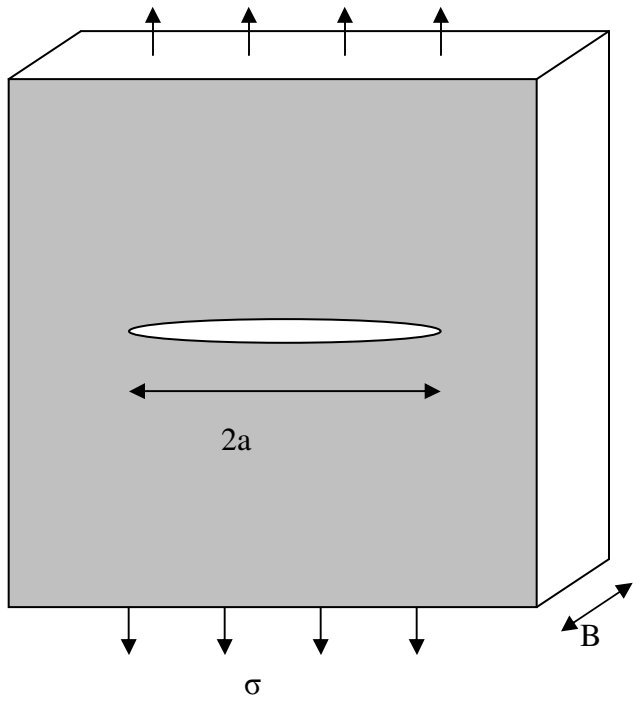

Figure 2.15: An elliptical crack in an infinite slab under far field applied stress (After Suresh[60]).

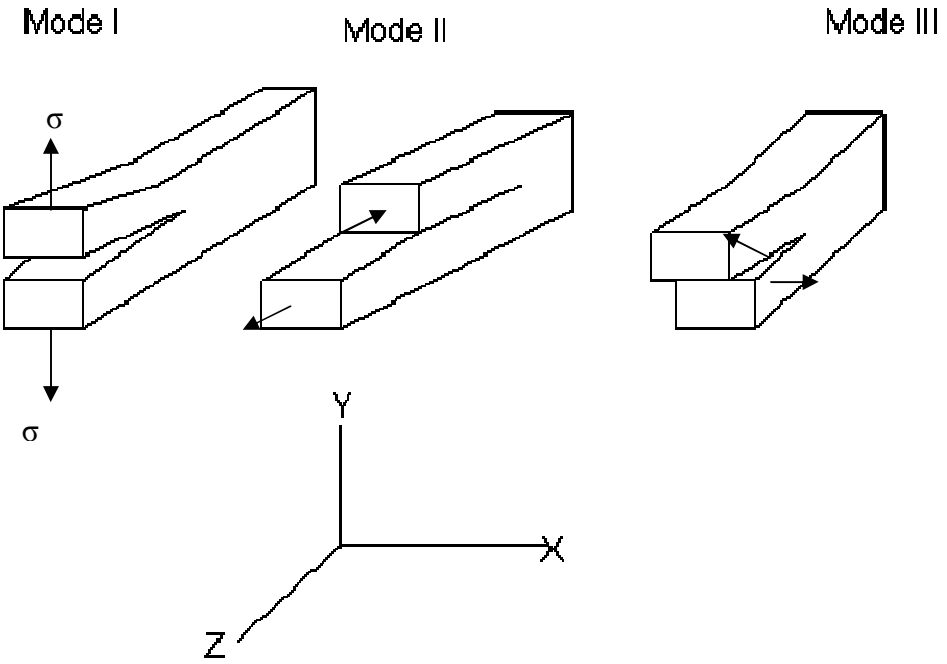

Figure 2.16: Crack opening modes (mode I-tensile opening, mode II, in-plane sliding, mode III anti-plane shear (After[60]).

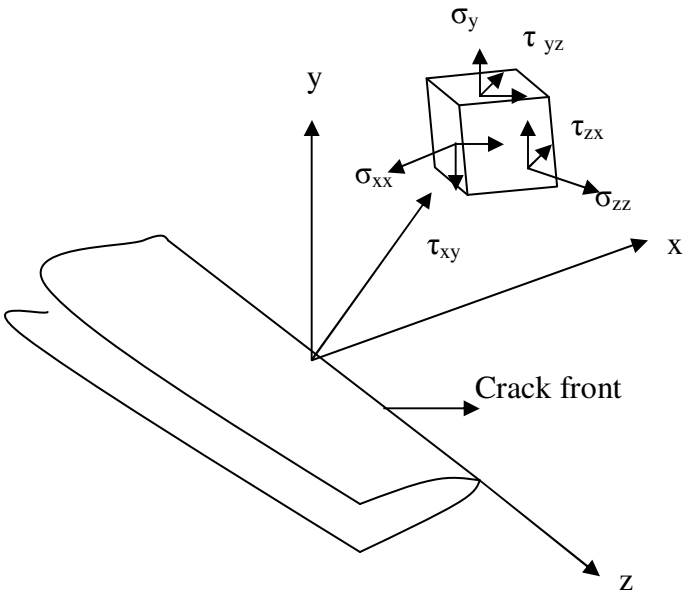

Figure 2.17: Components of stress in the crack tip stress field. (After Suresh[60]).

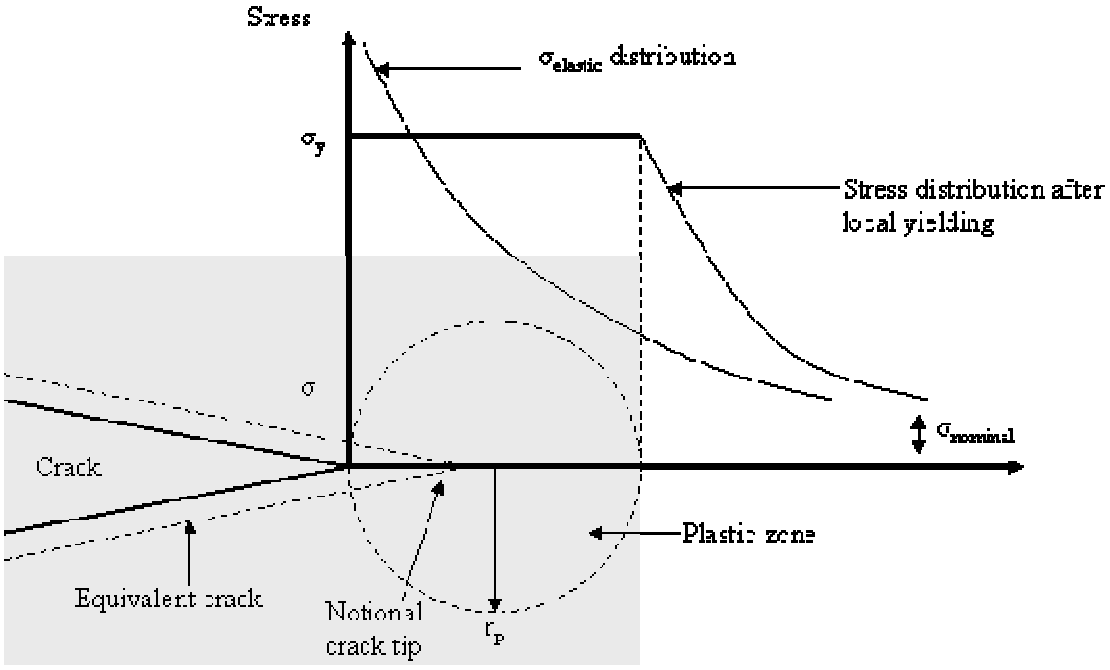

Figure 2.18: Stress distribution at a crack tip due to local yielding (After Benham[34]).

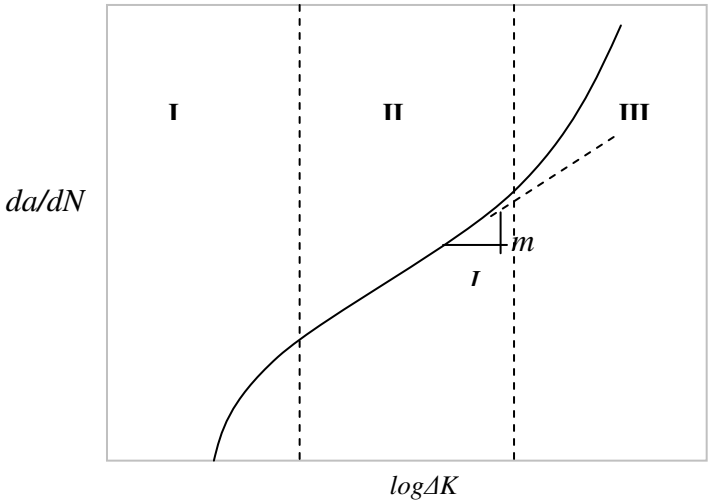

Figure 2.19: Different regimes of stable fatigue crack growth (After Suresh[60]).

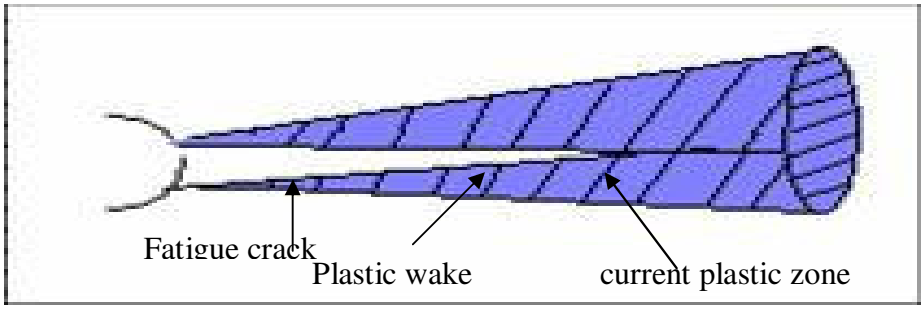

Figure 2.20: A schematic illustration of the plasticity induced crack closure.

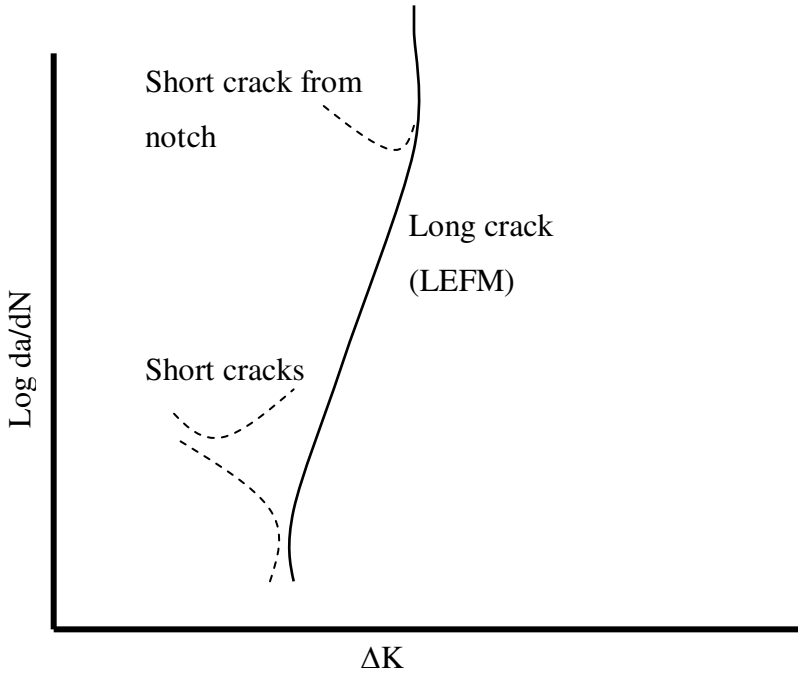

Figure 2.21: Difference between growth behaviour of short and long fatigue cracks (After[60]).

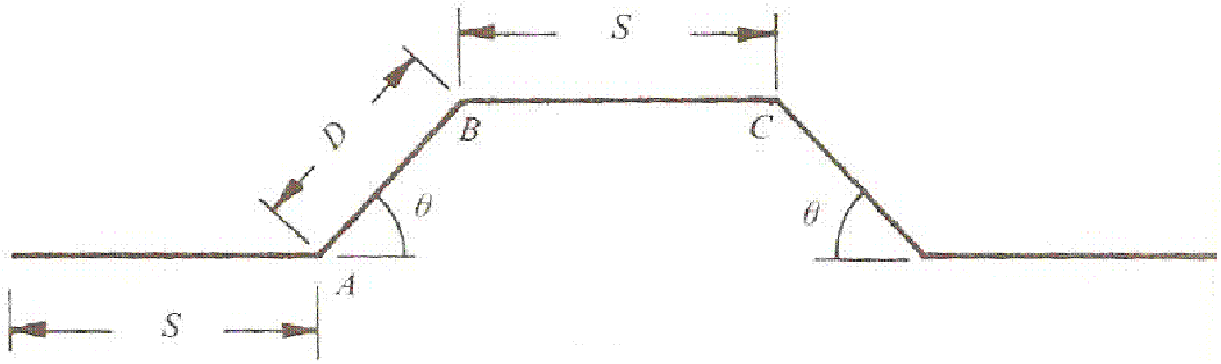

Figure 2.22: Mechanism of crack deflection (After Suresh[60]).

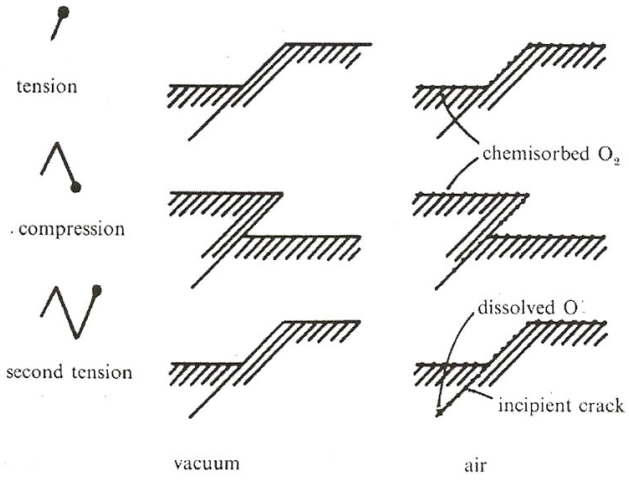

Figure 2.23: Schematic of fatigue crack initiation near a free surface by the synergistic effect of single slip and environmental effect[60].

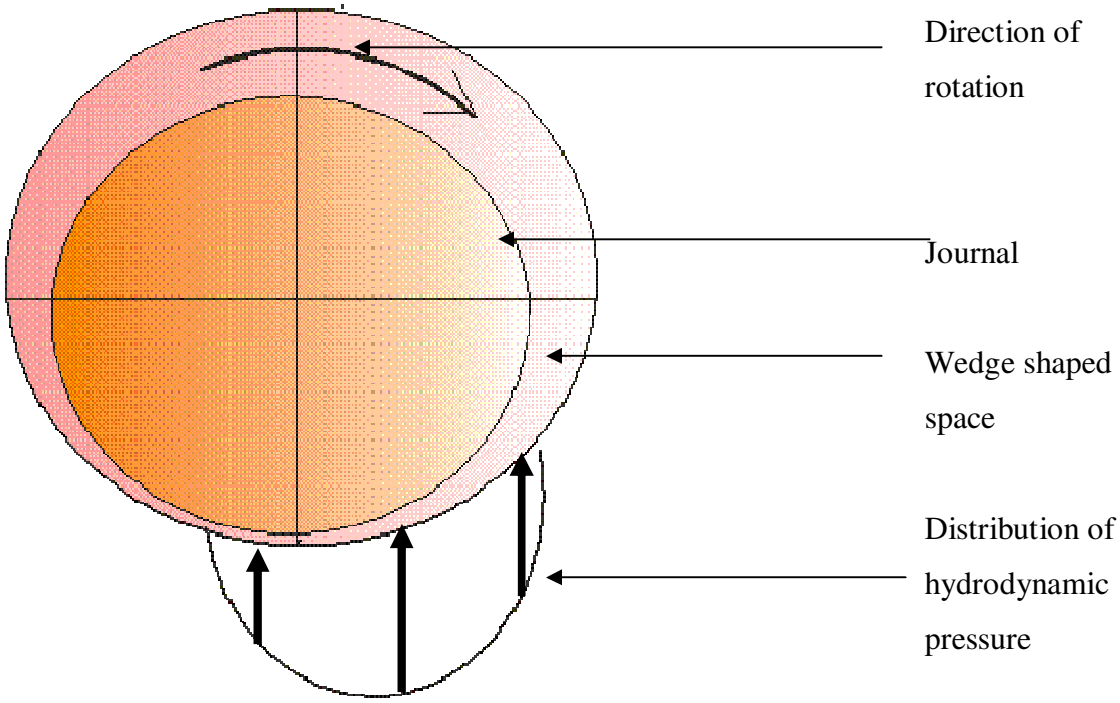

Figure 2.24: Development of pressures during hydrodynamic action

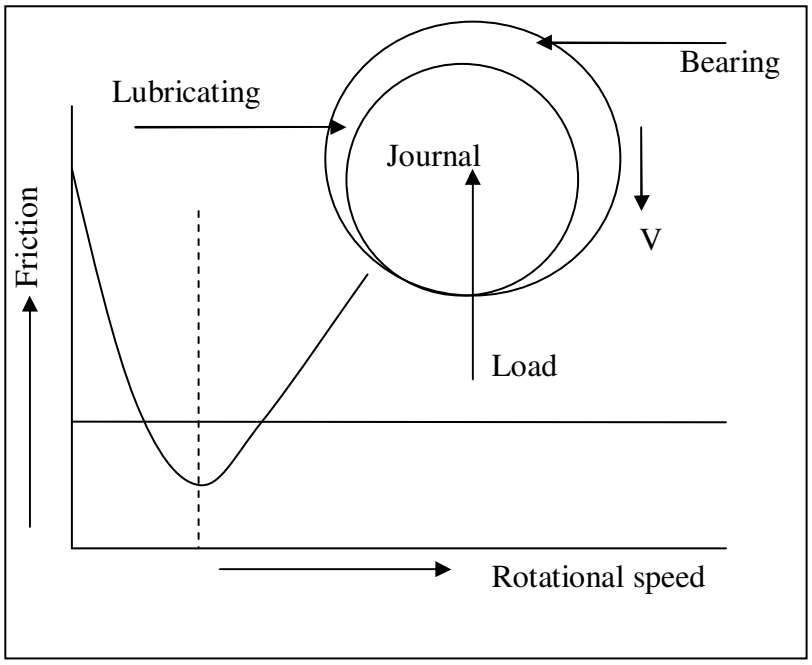

Figure 2.25: Schematic diagram showing different operating regimes for a journal bearing with fluid film lubrication ((After[9])

3 MATERIALS AND EXPERIMENTAL TECHNIQUES

The main experimental techniques used to investigate the microstructural, mechanical and fatigue characteristics of the available multilayered systems are presented in the following sections with a brief description of all types of materials and equipment used.

3.1. Materials

The multilayered bearing systems investigated during the current research were grouped into two types: (a) tri-layer systems with *Al* based lining alloys and (b) complex four - layer systems having *Cu* based lining alloys with *Ni* and *Sn* as overlays. The *Al* based systems were manufactured by roll bonding (RB) and high velocity oxyfuel (HVOF) spray coating processes. The RB *Al* based systems consisted of a thin layer (0.15-0.35mm) of *Al-Sn* alloy (with small additions of *Si, Cu, Ni* and *Mn*) roll bonded on a thicker and stiffer backing steel layer (1.80-1.85mm) via a very thin (0.04-0.05mm) *Al* interlayer. The HVOF system consisted of a thin coating (0.2—0.4mm) of *Al-Sn* alloy as a lining on the surface of a thicker (~1.9mm) annealed plain carbon steel layer.

The *Cu* based systems had a comparatively complex layer architecture in which a very thin (5-10μm) *Sn* layer was electroplated on top of a *Ni* layer which was itself electroplated on the surface of a *Ni*-bronze layer (0.3-0.4mm) roll bonded to a thicker (1.45-1.55mm) carbon steel layer. A view of the actual bearing is given in Figure 3.1(a) and the schematic of the layered architecture of both types of systems is shown in Figure 3.1(b), (c) and (d) respectively. All RB systems were manufactured commercially by the Dana Glacier Vandervell bearing company while the spray coated system was produced by the materials department of the University of Nottingham. All *Al* based RB bearing systems were available in the form of finished bearings and flat bar specimens whiles the HVOF systems was only available as flat bars. The *Cu* based systems was only available as finished bearings in both heat treated and non-heat treated conditions. Some *Cu* bearings without the overlay layers were also provided by DGV.

A brief summary of all current and previously investigated systems with their specific names, layer types, compositions and thicknesses is given in Table 3.1.

Table 3.1: Materials and geometrical thicknesses of various layers used in different multilayered systems investigated during current and previous research. The thickness values highlighted are those related to the flat bar specimens.

		Systems investigated during current research			
Layers		AS20S	AS20	RB168	HVOF
Overlay-layer	Thickness (mm)	N.A	N.A	0.005—0.008 0.005—0.008*	N.A
	Composition (Weight %)	N.A	N.A	Sn Ni*	N.A
Lining layer	Thickness (mm)	0.2—0.30 0.15—0.35	0.2—0.30 0.15—0.35	0.2—0.30 N.A	N.A 0.20—0.35
	Composition (Weight %)	Al-6-8Sn-2.5Si-1Cu-1Ni-0.25Mn-0.06V	Al-6-8Sn-2.5Si-1Cu-1Ni-0.25Mn-0.06V	Cu-8Sn-1Ni	Al-20Sn-1Cu
Interlayers	Thickness (mm)	0.04—0.05 0.04—0.05	0.04—0.05 0.04—0.05	N.A	N.A
	Composition (Weight %)	Al	Brazed sheet*	N.A	N.A
Backing layer	Thickness (mm)	1.8—1.85 1.8—1.82	1.8—1.85 1.8—1.82	1.5—1.55	1.82—1.9
	Composition (Weight %)	Medium Carbon steel	Medium Carbon steel	Carbon steel	Low Carbon steel (annealed)
		Systems investigated during previous research[1]			
		AS1241	AS16	HVOF	
Lining layer	Thickness (mm)	0.2—0.30 0.15—0.35	0.2—0.30 0.15—0.35	N.A 0.20—0.35	
	Composition (Weight %)	Al-12Sn-4Si-1Cu	Al-20Sn-1Cu-0.25Mn	Al-20Sn-1Cu	
Interlayer	Thickness (mm)	0.04—0.05 0.04—0.05	0.04—0.05 0.04—0.05	N.A	
	Composition (Weight %)	Al	Al	N.A	
Backing layer	Thickness (mm)	1.5—1.6 1.5—1.6	1.5—1.6 1.5—1.6	1.82—1.9	
	Composition (Weight %)	Medium Carbon steel	Medium Carbon steel	Low Carbon steel (annealed)	

*The brazed sheet is a combination of two thin sheets made of 3003 and 4343 alloys having compositions: *Al-1.2Mn-0.6Cu-0.7Fe* and *Al-6Si-0.8Fe-0.25Cu* respectively

The dimensions of all the specimens were obtained after surface preparation of bearings and flat bars prior to fatigue testing. In addition to the multilayered bearings and flat bar systems, DGV also provided sheets of rolled monolithic lining layers of the AS20S/AS20 systems (66 x 25 x 0.05cm) as well as *Al* and brazed sheets (used as the interlayer in AS20S and AS20 systems respectively) of size 110x25 x0.2cm. The brazed sheet used is formed by brazing a 4343 clad layer onto a 3003 core layer.

3.2. Manufacturing Processes

The manufacturing processes described in this section were used for various types of multilayered systems investigated during current and previous work at Southampton.

3.2.1. Roll bonding process

The RB process was adopted by DGV to manufacture all current and previous RB bearing systems. They are made through a propriety route; therefore, complete manufacturing details can not be made available. The schematic of the general RB process is shown in Figure 3.2. The aluminium alloy (to be used as the lining layer) is melted in a resistance heating furnace. The molten alloy is continuously cast to form billets. The cast billets are then passed through a billet reduction unit to reduce the thickness by cold rolling. This cold rolling process results in the break up of weak *Sn* films at the *Al* grain boundaries. After passing through welding and heat treatment units, the alloy strip is clad to an *Al* foil (used as an interlayer between the steel backing and the lining layer). Usually the *Al* foil is attached on both sides of the lining alloy strip. The purpose of the interlayer is to prevent the diffusion of *Sn* into the steel backing layer that may otherwise make the steel brittle. The bimetal strip is further reduced in thickness by passing it through a series of different rolling and heat treatment operations. The reduced bimetal strip is further bonded to a steel layer through rolling and finally undergoes an annealing process. The multilayered long flat bars are then blanked to the desired size and subjected to the bearing forming operation. The lining surface of the bearings is then broached to remove the outer *Al* layer and achieve the desired lining thickness.

3.2.2. Manufacture of Bronze bearing

Bronze bearings with *Sn* and *Ni* as overlay layers were manufactured by DGV via a series of different processes. As a first step, a bimetal steel-bronze strip is produced by a

sintering process[2] shown schematically in Figure 3.3. *Cu* alloy in molten form is passed through a nozzle to produce powder particles which are then laid on a steel strip. The steel strip covered with powder particles is then passed through various sintering and compaction processes. The bimetal strip is ready to be converted to bearing through bending after the second sintering step. The sintered bronze layer (after forming bearings) is then electroplated with *Ni* and then *Sn* in order to form thin overlay layers (5-10μm). The process therefore involves a number of parameters such as sintering temperature, time, compaction pressure, electroplating bath temperature and composition. The process is proprietary and hence these parameters are not specified further.

3.2.3. Spray coating process

A brief and general introduction of the HVOF spray coating process has been given in the literature review Section 2.1.5.2. This process[3] consists of far fewer steps than the conventional RB process. Two spray coating processes i.e. (1) High Velocity Oxy-Liquid Fuel (HVOLF) and (2) High Velocity Oxy-Gas Fuel (HVOGF) were used at Nottingham University to deposit *Al* lining alloys on to a steel substrate. The former used a liquid such as kerosene as fuel whereas the latter used a fuel gas such as polypropylene along with oxygen. The HVOLF process provides higher kinetic energy and lower thermal input to the injected power particles that results in coatings of lower hardness and capable of providing the conformability and embeddability required during service (as compared to the coatings produced by HVOGF) process) . The HVOGF processes gave sufficient heat transfer to cause complete melting of low melting point powder particles which resulted in blockage of the barrel section of the spray gun.

The specimens analysed in the current research were produced by the HVOLF process (termed simply HVOF in subsequent text) due to the better quality of the coatings. Fig 3.4 shows a schematic of the HVOF spray coating process used. A mixture of kerosene fuel and oxygen is fed to combustion chamber where they react as shown below

$$C_{12}H_{26} + 18\ 1/2O_2 \rightarrow 12CO_2 + 13H_2O + Heat$$

The combustion heat is absorbed by the gas atomized feedstock powder of *Al-20Sn-1Cu* alloy (22-106 μm particle size) that is injected radially into the combustion chamber. The resultant molten powder is passed through a converging-diverging nozzle and then sprayed on mild steel coupon substrates. The substrate surface to be coated was grit blasted (using Al_2O_3 particles) prior to the coating process in order to improve the adhesion of the coating layer.

These flat steel substrates were mounted on the circumference of a horizontal turntable rotating at a tangential velocity of 1 ms^{-1}. The HVOF spray gun was located at 356 mm above the substrate. During the operation the gun traverses with a to and fro motion along the steel strip at a speed of 5 ms^{-1}. The spray coating process has a faster cooling rate[4] (~$10^6 Ks^{-1}$) as compared to the roll bonding process (~$100 Ks^{-1}$) which results in the formation of splats with nano-scale *Sn* particles (fast cooling causes many more nucleation sites during solidification). The spray coated flat strips were then normalized in air at 300^oC for up to 5 hours.

3.2.4. Heat treatment of bronze bearing

One of the available non-heat treated RB168 bearing specimens was sectioned into a number of small specimens which were subsequently subjected to heat treatment investigations. The purpose of heat treatment was to study the effect of heating time and temperature on the size and morphology of interfacial phases formed between the top *Ni* and *Sn* layers. The sectioned specimens were subjected to annealing in a Carbolite furnace at 180, 190 and 200^oC (similar to the ageing temperatures used by DGV) for various time intervals from 6 to 72 hours. The heat treated specimens were then examined by metallographic techniques as detailed in Section 3.3.

3.3. Materials Characterization

Evaluation of the available bearing systems on the basis of fatigue performance is the principal aim of this research, but the microscopic, mesoscopic and macroscopic characteristics of the individual layers in each system are crucial for a more precise analysis of fatigue behaviour. Four systems AS20S, AS20, RB168 and HVOF (defined in Table 3.1) were therefore characterised on the basis of the microstructural and mechanical properties of all the layers.

3.3.1. Microstructural characterization

In order to observe the microstructural details of finished bearings and flat bars, specimens were sectioned in a direction parallel to the top lining surface plane (to polish the lining surface) as well as transverse to the short and long edges in order to polish transverse sections to study the layer architecture of these systems. The specimen sectioning methodology

is shown in Figure 3.5. These sectioned specimens were mounted in conductive bakelite held at 170^{o}C for 7 minutes in a hydraulic press (Struers) at a load of 3 KN.

3.3.1.1.Grinding and polishing

For the AS20S and AS20 systems, the conventional grinding and polishing route was adopted which had been developed for AS16 and AS1241 by previous researchers using water and water based lubricants. The presence of hard and soft phases in the lining material makes the choice of polishing route complex. The problem becomes even more severe when polishing cross sections that contain a hard steel backing layer and soft *Al* based lining and interlayer. There is no well defined standard polishing route that could cover all these conflicting issues and the techniques established so far are mostly based upon a trial and error method. The suggestions provided by Struers[5] metal guide have been used with some alterations in order to get the best possible surface finish for AS20S and AS20 systems. The early work on HVOF lining at Nottingham[6] showed that the spray coated lining is prone to corrosion attack in aqueous environments when the *Sn* particle size is very small (20-100nm). Therefore, for the HVOF spray coated lining, methanol and other non-water based lubricants were used as the former method resulted in the formation of a structure full of a large number of oxidized pores.

All these specimens were polished to 0.04μm using Buehler-Motopol 8 automatic polishing machine before subjecting them to microscopic study. Precise details of the grinding and polishing routes are given in Table 3.2

3.3.1.2.Microscopy

The specimens polished to 0.04 μm were subjected to microstructural study in order to reveal the size, shape and distribution of different phases present as well as the interfaces among the various layers. Optical microscopy (OM) of the polished specimens was carried out using an Olympus BH2-UMA at magnifications from ×50-×500. The images were obtained using a digital camera attached to the microscope with the help of XCAP imaging software.

More detailed microstructural analysis was carried out using a JEOL 6500F field emission gun scanning electron microscope (FEG SEM). The field emission gun produces brightness (intensity of the electron beam) 100 times greater then the conventional SEM gun with a spatial resolution approaching up to 1 nm. The other major advantage is the much improved performance at a low accelerating voltage[7].

Table 3.2 Grinding and polishing routes adopted for different systems.

Note: Highlighted values are those for the RB168 system when different from other RB systems

Stage	Surface	Roll bonded systems (AS20S/AS20)	HVOF Spray coated systems
Grinding	Cloth	SiC	SiC
	Grit size	600→1200→4000	600→1200→4000
	Speed (rpm)	250	100
	Force (N)	90	70-90
	Lubricant	Water	Methanol
	Time (minutes)	5-7 5—10	5-10
1st Polish	Cloth	DP –Mol	DP-Mol
	Abrasive	3µm Diamond paste	3µm Diamond paste
	Speed(rpm)	120 150—200	100
	Force (N)	70-90 90	70
	Lubricant	DP-Blue	DP-Yellow
	Time (minutes)	5-12 5—10	10
2nd Polish	Cloth	DP-Mol	DP-Mol
	Abrasive	1µm Diamond paste	1µm Diamond paste
	Speed (rpm)	120 150	60
	Force (N)	70-90 90	50-70
	Lubricant	DP-Red	DP-Yellow
	Time (minutes)	6 8	8
3rd Polish	Cloth	OP-Nap	OP-Nap
	Abrasive	0.04µm OP-S suspension	0.04µm OP-S suspension
	Speed (rpm)	100	60
	Force (N)	25	25
	Lubricant	Distilled water(Very little amount)	Distilled water(Very little amount)
	Time (minutes)	2	4

Both secondary and back scattered electron (abbreviated as SEI and BEI) images were obtained at an accelerating voltage of 15 kV in order to assess the shapes and compositions of different phases. Using energy dispersive X-ray (EDX) analysis, the composition of individual phases as well as the bulk lining material was determined. For more precise information on the bulk composition, this EDX technique was applied to a large number of randomly selected areas.

In order to reveal orientation information of the grain structure within the lining alloy, the SEM was also operated in electron backscattered diffraction mode (EBSD). For EBSD analysis the mechanically polished lining surfaces of the AS20S/AS20 specimens (0.04μm) were subjected to electropolishing in a solution composed of methanol and nitric acid (3:1) at 30 volts for 10 seconds while maintaining a temperature of -30^{o}C using liquid nitrogen. The EBSD measurements were done at an accelerating voltage of 20 kV and probe current setting of 17-18 using an automated system (channel 5 software from HKL, Denmark). The specimen was tilted at 70^{o} (standard for the SEM) with a working distance of 30mm. The step size defines the distance between consecutive EBSD measurements on the specimen surface; the choice of the step size depends upon the expected grain size. Since the lining material used for AS20S/AS20 systems is similar to the previous AS16 and AS1241 systems (manufactured through the same route and having somewhat similar composition and heat treatments), their expected grain sizes lie within the range of 5-15 μm. The step size chosen (based upon expected grain size) was therefore 2μm (significantly smaller than the expected grain size). The success rate of identification of the Kikuchi patterns (and hence the grain orientation) was 60-90% depending on the alloy composition being analyzed.

3.3.1.3.Finite body tessellation

Finite body tessellation (abbreviated as FBT) methods have been developed to characterize high volume fractions of secondary phase particles of varying size and shape in multiphase systems. This method consists of generating a network of cells surrounding the bodies of a particular phase such that the material within the cell is closest to that body than any other. The FBT approach was proposed by *Boselli et al*[8] although the basic idea stemmed from the Dirichlet Tessellation approach[9] in which particle centroids are used to form a network of polygon cells such that any point within the cell is closest to that cell centre (Figure 3.6 (a)). Thus the *Dirichle*t tessellation ignores the particle size and shape of the included particle that

may result in particle-cell overlap. Figure 3.6 (b) shows an FBT image in which the cell network surrounds the individual features completely. FBT is thus more sensitive to the local particle distribution characteristics and useful for microstructures in which there is a large variation in particle sizes and shapes.

The tessellated images are obtained by digital image analysis using a windows based package developed by *Boselli et al*[8]. Interfaces or edges of objects are defined by grey level differences and used to create cells enveloping the objects. These cells provide information regarding the spatial distribution of different particles based upon individual particle/cell and near neighbour measurements. According to *Boselli* such a tessellation analysis is a useful tool for quantifying the distinguishing features of the spatial distribution of different phase particles. In previous work by *Mwanza*[10] *et al*, the lining materials AS16 and AS1241 were subjected to FBT analysis. Although features in these microstructures were distinguishable in the optical images, the grey level differences were not by themselves sufficient to produce a binary image in the FBT software. Therefore, binary images were manually produced by tracing the boundaries of particles (i.e. *Sn, Si*, intermetallics as separate populations). These binary images were then used to produce featured images with a non feature background in the tessellation software. These binarized images were then converted to distance transformation[11] images which convert each particle in the binary into grey scale images by assigning a grey level distinguishable from the background. These distance transforms were subjected to a watershed[12] in order to form a network of cells. The optical micrograph of AS20S/AS20 lining surfaces showed even finer scale features that are not adequately distinguishable and a sparse distribution of second phase particles (Figure 3.6 c and d). Therefore producing binary images manually from optical micrographs was not appropriate and, secondary electron (SEI) images were used systematically for the FBT analysis. These images reveal surface features with a better colour contrast and resolution (actual images are discussed in Section 4.1). In order to cope with the sparse distribution of particles and to get statistically representative data, FBT was implemented on relatively large areas after obtaining 10 images (each of 0.045mm^2 area) from both AS20S and AS20 flat bar systems. The important parameters determined for each individual particle population are briefly defined[13] below with the help of Figure 3.7:

Object/Cell area: The area of the individual cell/object.

Object /Cell AR: The ratio of the maximum chord length of the object/cell to the perpendicular width is known as the aspect ratio or AR.

Object/Cell angle: This is the angle of the object/cell's longest chord with respect to the horizontal axis between 0 and 90 degrees).

L.A.F: This the local area fraction obtained by dividing the object area by the cell area, presented as a percentage.

Number of NNs: This is the abbreviation of number of near neighbours i.e. number of objects sharing a cell boundary with the object of interest.

NN Dist (d_{min}): This is the shortest interfacial distance with any of the nearest neighbours

Mean NN (d_{mean}) : This represents the average of the interfacial distances to all the near neighbours

NN Angle: This is the angle of the line joining the centroid of the object to the centroid of the nearest neighbour measured with respect to the horizontal.

The FBT software calculates all these features when the appropriate binary image and the exact magnification are provided.

3.3.2. Mechanical testing

Most of the data for the mechanical properties of the lining and backing layers for the AS16 and AS1241 systems have already been produced in previous work[1]. For the present systems ; that is HVOF spray coated flat strips, AS20S and AS20 (both bearings and flat strips), the mechanical property data was obtained from a combination of microhardness and nanohardness tests and tensile tests performed upon monolithic lining layers, interlayers and steel backing layers.

3.3.2.1.Micro-hardness testing

Vickers micro-hardness tests were conducted using a *Matsuzawa Microhardness Indenter*. The micro indents were made in order to examine the hardness profile across the thickness of the multilayered systems as well as the variations of the length of the indent diagonal with applied load to allow comparison of the apparent plastic flow behaviour of different layers. For the former case, indents were made at a constant load value of 50g across the thickness (at the cross section) while traversing the lining to the steel backing layer through the interface. All these indents were made equal at spacings and maintaining an angle of approximately 45^{o} between the

longitudinal dimension of the specimen and the row of equally spaced indents. The experimental methodology is shown in Figure 3.8 (a). For statistically more reliable results, at least 15 sets of these indents were made at equal distances along the length (considered as y axis) and the width (considered as x axis). The results were presented as microhardness numbers with observed scatter.

For the indentation size-load relations, indents were made at varying loads betwen 10 and 1000 grams along the longitudinal dimension of the specimen. 10 sets of observations were obtained for each load on the steel backing layer, interlayer and lining layers. Each load was applied for 15 seconds. The straight rows of the indents were situated at a distance of approximately 200μm from the lining surface (for lining) and the interface (for steel layer) respectively. This method is also illustrated in Figure 3.8 (b).

3.3.2.2.Nano-hardness test

The nano-indentation or instrumented indentation technique is used to assess the mechanical characteristics of a material at micro or nano scale level. This technique is suitable for measuring the mechanical properties of very thin coatings (~1μm). In the current work, the hardness of the lining and steel layers were successfully measured with a Vickers Microhardness Tester. However, there were problems in getting enough data particularly for the AS20 interlayer (as it is composed of 3003 and 4343 layer in which 4343 is only 10μm thick). These individual layers could not be tested with micro-indentation and hence a smaller indenter size was required. In addition, the lining microstructure contains second phase particles which may affect the initiation and growth of short fatigue cracks. Knowledge of the mechanical properties of these second phase particles could be helpful in understanding the short crack initiation behaviour. An attempt to identify the mechanical properties of these second phase particles via nanoindentation was another goal.

A schematic of the Nanohardness-Tester is shown in Figure 3.9 (a) which explains the working principle of the equipment. A calibrated diamond probe (Berkovich indenter) is used which is shown in Figure 3.9 (b). This indenter is pushed against the specimen surface via a load applied by means of a coil and magnet located at the top of the pendulum. The resultant displacement of the probe into the surface is monitored with a sensitive capacitive transducer and displayed in real time as a function of load. To produce accurate nanohardness and modulus results, all instrument calibrations are performed automatically. The load range of the system

was 5-250 mN. The maximum noise in measuring the depth of the indentor is approximately 3-4 nm and hence the minimum distance (depth) that could be measured with certainty is approximately 4-5 nm which is also termed the distance resolution. A cross-section of each RB bearing system and the HVOF flat bar system was polished using the specified polishing route (Table 3.2). The specimen was attached to the specimen stub of the Nanohardness Tester (Micromaterials) with the help of glue, the effects of which have been calibrated prior to the test. The coordinate movement of the specimen was programmed in a "bombing raid" through the Nanohardness Tester software in such a way that three rows of indents (each row having 20 indents) were obtained across the lining and interlayers with a spacing of 20 microns. The raw data is obtained in the form of load vs. displacement (depth of indentation) during one load cycle (loading and unloading). A schematic of the loading and unloading curve is shown in Figure 3.10. The nanohardness value expressed in GPa is given by the relation

$$H = \frac{P_{\max}}{A} \qquad 3\text{-}1$$

Where P_{max} is the applied load and A is the contact area[14]. The contact area is described as a function of h_c , the depth along which contact is made, that is

$$A = F(h_c) \qquad 3\text{-}2$$

The elastic modulus is related to the contact area as shown in the equation below:

$$S = \frac{2}{\sqrt{\pi}} E_{eff} \sqrt{A} \qquad 3\text{-}3$$

S is the gradient of the unloading curve at maximum load and E_{eff} is the effective elastic modulus defined by

$$\frac{1}{E_{eff}} = \frac{1-\nu^2}{E} + \frac{1-\nu_i^{\,2}}{E_i} \qquad 3\text{-}4$$

where E is the *Young*'s modulus and ν is the Poisons ratio (subscript i indicates the indenter)

3.3.2.3.Tensile test

Standard dog bone tensile test specimens were sectioned from the monolithic lining, interlayers (*Al* and brazed sheet) and steel layers for AS20S and AS20 systems. For the RB168 system, tensile specimens of monolithic bronze were provided by DGV. Since the original steel

backing layer was not provided, the lining and interlayers were ground away from samples extracted from the flat bars. The geometry of the tensile specimen is shown in Figure 3.11. A monolithic layer for the HVOF spray coated lining was not available; therefore the tensile test data obtained for AS1241[13] monolithic lining was used for this material as the latter was close in hardness number values to those obtained for the HVOF lining. The test was conducted according to *British Standards*[15] at room temperature using an Instron Electromechanical Tensile Testing Machine (series 5569) at a strain rate of 5 mm/minute. This machine is interfaced with a computer through Instron Bluehill software and gives readings in terms of load and extension. A pre-calibrated extensometer was also attached to the tensile specimen in order to confirm the accuracy of the readings obtained from the crosshead movement of the machine. Six specimens from each material were tested in order to get consistent averaged data with a measure of scatter.

3.3.3. Fatigue test

3.3.3.1.Accelerated rig test

Fatigue tests on plain engine bearings are carried out by DGV in-house using an artificial accelerated rig test set up shown in Figure 3.12. These rigs aim to test bearings under loading conditions similar to those expected within an engine. The rig used by DGV is known as a Sapphire rig in which the bearing specimen is mounted between a piston cone rod and an eccentric portion of the main shaft. The rotation of this shaft in its slave bearing causes the piston to reciprocate in its oil filled cylinder. The applied loading is controlled by a hydraulic control unit. The oil temperature is controlled to set a desired operating temperature (temperature used is usually 140^{o}C). At a nominal load the rig will run for 20 hours after which, if no failure had occurred, maximum pressure on the hydraulic ram is increased by 10% to increase the load which is run for a further 20 hrs. This procedure of incremental load increase is continued until a marked rise in coolant temperature occurs indicating bearing failure. Data for these commercial fatigue tests is presented in the form of number of cycles to failure vs. an average projected pressure on the bearing surface.

3.3.3.2.Fatigue life time test

For fatigue testing of the flat bars and finished bearings, a digitally controlled 50 kN Instron Servo Hydraulic fatigue testing machine (8502) was used. Fatigue tests were carried out on the basis of two different techniques i.e. uninterrupted and interrupted experiments.

The purpose of the uninterrupted tests was to evaluate the life times of AS20S, AS20 and RB168 bearings at different load levels in both air and oil environments. A three point bend test configuration was used as shown in Figure 3.13 (a and b)) for the bearings and flat bar specimens. The simulation of lining surface stress conditions of bearings in service is not a trivial task, as the loading on bearings varies in magnitude and direction under the combined action of transferred gas pressures from the piston and inertial and centrifugal forces of the reciprocating and rotating component of engine systems[16]. Therefore, instead of replicating real loading conditions in service (e.g. an engine test), tests were conducted under simple and well defined loading states. The purpose of these tests was to get a comparison of the fatigue resistance of newly developed systems with the previously developed systems tested using the same methodology developed during previous research work at Southampton. Maximum load levels between 1800 and 3000N were used at a frequency of 10 Hz and a load ratio of 0.1. For tests in oil environment, Shell Rotella Engine X 10W oil was used. This type of oil is used in low to medium output diesel engines. Failure was deemed to have occurred after the actuator of the machine had moved 0.3 mm beyond its initial maximum position at the start of the test. The use of this criterion was established in previous work at Southampton, the basis of which was the appearance of a visible lining surface damage (long surface cracks) without gross failure of the bearings occurring after 0.3mm deflection. The same failure criterion was used in this work in order to obtain a comparison with the fatigue performance of previously studies bearing systems. The number of cycles to failure were noted and presented in the form of $\Delta\varepsilon_p$-N curve i.e. maximum plastic strain range vs. the number of cycles to failure. The values of plastic strain ranges for specific loads were obtained from elasto-plastic finite element models (which are discussed in detail in Chapter 5) for the bearings. Each of the AS20S and AS20 bearings that failed at the higher load of 3000 and 2800 N (respectively) were sectioned to get samples from the cracked location. Samples were obtained parallel and perpendicular to the lining surface in order to analyze the crack routes along the lining and across the lining, interlayer and backing layers. These specimens were mounted in bakelite, ground and polished

using the same methodology as mentioned in Section 3.3.1.1 The polished specimens were then observed under the optical and scanning electron microscope for post fatigue failure analysis.

3.3.3.3.Fatigue test with surface replication

A series of interrupted fatigue tests were performed on AS20S, AS20 and HVOF spray coated flat bars using the three point bend testing geometry as shown in Figure 3.13. The purposes of these experiments were to analyse the small crack initiation and growth behaviour at specific load levels. Higher maximum load levels that gave a maximum top lining strain of ~0.006 and life time of ~100,000 -200,000 cycles were chosen in order to finish the test within a reasonable time interval.

The flat bars for all these systems were in the form of thin bend bars which were ground and polished to 0.04 μm finish before subjecting them to fatigue tests. A special jig was used to hold the specimen during grinding and polishing operations. The corners of these flat bars were bevelled off in order to facilitate polishing. The size of the AS20S/AS20 flat bar was 60x20mm and that of the HVOF flat bar was 52x28mm. The specimen was fixed in a three point bend configuration. Acetate strips of 20x40mm were used to replicate the surface after dipping them in acetone for about 15-20 seconds. These acetate strips became soft enough to be manually pressed against the polished surface of the flat bar in order to record the microstructural features of the lining including any cracks. Replicas were taken at '0' cycles before starting the machine. After the test had started (at 10Hz and load ratio of 0.1), the machine was stopped after every 1000 cycles to monitor the surface by taking the replicas. As soon as the cracks appeared on the replicas under the optical microscope, replication intervals were decreased to 500 cycles in order to check the increments in the crack growth. If the cracks did not show any measurable growth, the replication interval was increased up to 1000 and 5000 cycles. The process was continued until the failure of the specimen, the criterion for which was set at 0.5 mm displacement of the actuator beyond its initial maximum position i.e. a deflection of 0.5mm in the flat bars. This criterion was chosen because the simple geometry of the flat bar is more compliant than the bearing (for which the failure criterion was 0.3mm deflection). Observation of the top lining surface of failed bearings (0.3mm deflection) and flat bar (0.5mm deflection) showed equivalent fatigue damage (almost same number of dominant cracks were observed at the lining surface where maximum plastic strain developed).

The top lining surface of the failed specimen was observed under the optical microscope in order to analyze the cracked surface. The acetate replicas did not show clearly distinguishable second phase particles that initiated the short cracks. In order to observe the particles that initiated cracks, flat bars of AS20S/AS20 were tested at similar plastic strain levels to a certain number of cycles after which small initiating cracks became visible on surface replicas under optical microscope. The lining surface of these specimens was then observed under the SEM operated in the BEI mode in order to observe the cracks at early stages of growth. Images from about 10 such regions were obtained in order to count crack initiation events and then quantify them by subsequently subjecting these images (showing cracked micron sized features) to finite body tessellation analysis.

For crack growth analysis, the high strain region (loading line where maximum $\Delta\varepsilon_p$ develops) of all three failed flat bars were subjected to a thorough scan by observing the acetate replicas under the optical microscope. The main results from these observations were expressed in the form of number of cracks emerging from different locations at different number of cycles, the effects of local microstructure on crack initiation and growth, crack coalescence to form dominant cracks, crack shielding effects and growth rate of individual cracks. Similar observations were made for low $\Delta\varepsilon_p$ regions.

The failed specimen was then sectioned transverse to the lining surface in order to observe the effect of different layers on the crack propagation through the thickness of the specimen. Both optical microscopy and FEG SEM were again used to carry out this analysis.

3.3.4. Measurement of total strain at the lining surface

In order to estimate the maximum total strain developed at the lining surface during a three point bend fatigue test in a single load cycle, a strain gauge set up was used for both finished bearings and flat bars (Figure 3.14). In the 3-point bend test, the maximum stresses and strains develop under the line of application of load. In order to measure the strains over an area (which is as small as possible), three small strain gauges of type KFG-1-120-C1-23 (Kyowa) and length 1mm were used. A smaller strain gauge (1mm) assures more accuracy in measuring the maximum strain that develops over a small curved surface of the bearings under the 3-point bend loading condition.

3.3.4.1.Strain gauge calibration

One of the available strain gauges was attached to a standard dog bone tensile test specimen made of pure *A*l. A pre-calibrated extensometer was also attached in order to compare the readings from the strain gauge and the extensometer. The tensile test specimen was subjected to a normal tensile test using the Instron Electro- Mechanical testing machine.

3.3.4.2.Measurement of total strain

One specimen from each of AS16, AS1241, AS20S, AS20, RB168 (non-plated) and HVOF systems was chosen. Both bearing and flat bar specimens were chosen for these systems with the exception of HVOF (only available in the form of flat bars) and RB168 (available only as bearings). The lining surface of all finished bearings and polished flat bars was cleaned and degreased prior to the attachment of strain gauges according to standard procedures[17]. The position directly underneath the loading point where the maximum bending strain develops was marked by HB pencil and then cleaned by M-Prep Conditioner A (MM group). A drop of M200 bond with 200 Catalyst C (MM group) was applied to the bonding surface of the strain gauge (with filaments attached) which was then pressed to the desired location for 2 minutes. The filaments of the strain gauge were subsequently joined to external leads. Three such strain gauges each of gauge length 1mm were attached following the same procedure.

The specimen was fixed in the specimen holding jig of the Instron Servohydraulic fatigue testing machine. The external leads from each strain gauge were joined to Yokogawa Universal Strain Measuring instrument (type 3107) with measuring range 200 to 10,000 με and sensitivity of 5 με. Each of the strain gauge amplifiers was calibrated prior to the test using a standard gauge giving a full scale deflection of 200μ strains. The amplifier was adjusted to give a maximum strain of 10000 με based on FE predictions of maximum total strain developed at the top lining surface. The specimen was subjected to gradually increasing load steps of 100 N up to a maximum load of 3000 N for finished bearings and 1000 N for flat bar specimens. The strain reading was noted down from three strain gauge amplifiers with each load step while the corresponding position of the actuator was also recorded from the Instron machine. The same procedure was adopted for all current bearings and flat bar systems. Available samples of AS16 and AS1241 bearings and flat bars from previous research were also tested in this way.

References:

[1] Mwanza, M.C, (2004). PhD thesis, University of Southampton, UK.

[2] Dana Glacier Vandervell Bearings, UK. (private communication).2004.

[3] Harris, J. and McCartney, D.G. (1998). EPSRC Final Report GR/K60640.

[4] Harris, S.J. McCartney, D.G. Horlock, A.J. and Perrin, C. (2000). Mater. Sc. Forum 331-337, 519.

[5] Jerregaad, L.B. Geels, K. Ottesen, B. and Ruckert, M. (1992). Metalog Guide, Strureres Tech.

[6] Horlock, A.J. Dent, A.D. McCartney, D.G. and Harris, S.J. (1992). Proc. 15th International Thermal Spray Coating Conference. ASM International, 38.

[7] Goodhew, P.J. Humphreys, J. and B, Richard. (2001). Electron Microscopy and Analysis. Oxford, 141.

[8] Boselli, J. Pitcher, P.D. Gregson, P.J. and Sinclair, I. (1999). J. Microscopy 195, 104.

[9] Burger, G. Koken, E. Wilkinson, D.S. and Embury, J.D. (1988). Advances in Phase Transitions, 247-266.

[10] Mwanza, M.C. Joyce, M.R. Lee, K.K. Syngellakis, S. and Reed, P.A.S. (2003). Int. J. Fat 25, 1135.

[11] Borgefors, G. (1986). Computer Vision Graphics Image Process 34, 344.

[12] Vincent, L. and Soille, P. (1991). IEEE Trans. Pattern Analys. Machine. Int 3, 583.

[13] Joyce, M.R.(2000). PhD Thesis. University of Southampton, U.K.

[14] Oliver, W.C. (2004). J. Mater. Res 19, 4

[15] BSI EN (1990): Tensile Testing of Metallic Materials. Method of Test at Ambient Temperature, 10002-1

[16] Braithwaite, E. R. (1999). Lubrication and Lubricants. European Manager of Chemical Sales and Development. Elseveir. Pub. Co. London, 312.

[17] Strain Gauge Attachment Manual, Vishay Measurement Group UK (www.vishay.com).

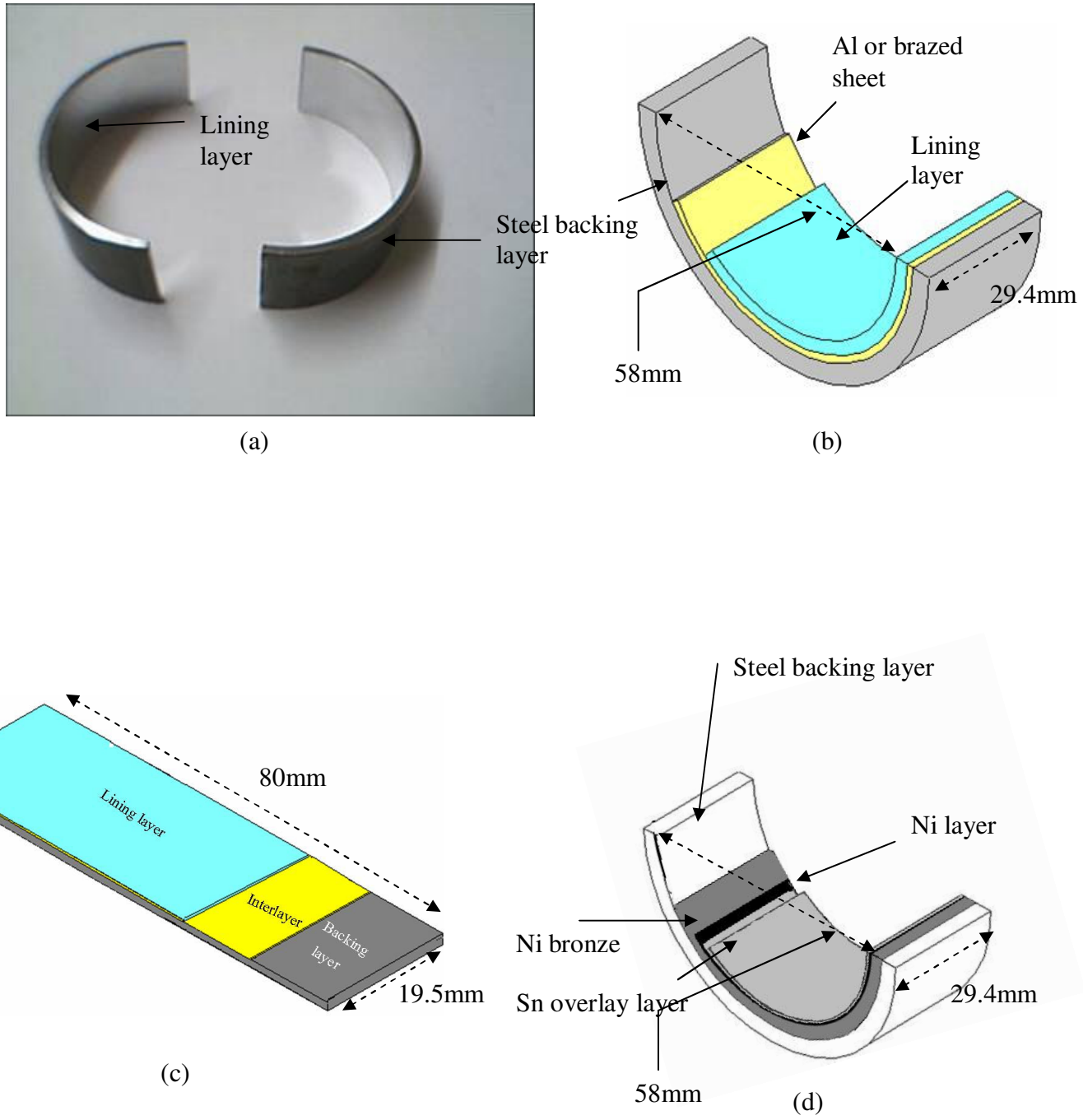

Figure 3.1: (a) A view of the actual finished bearings. (b) Schematic of half shell AS20S/AS20 bearing. (c) Flat bar specimen of AS20S/AS20 systems (d) RB168 bearing showing different layers.

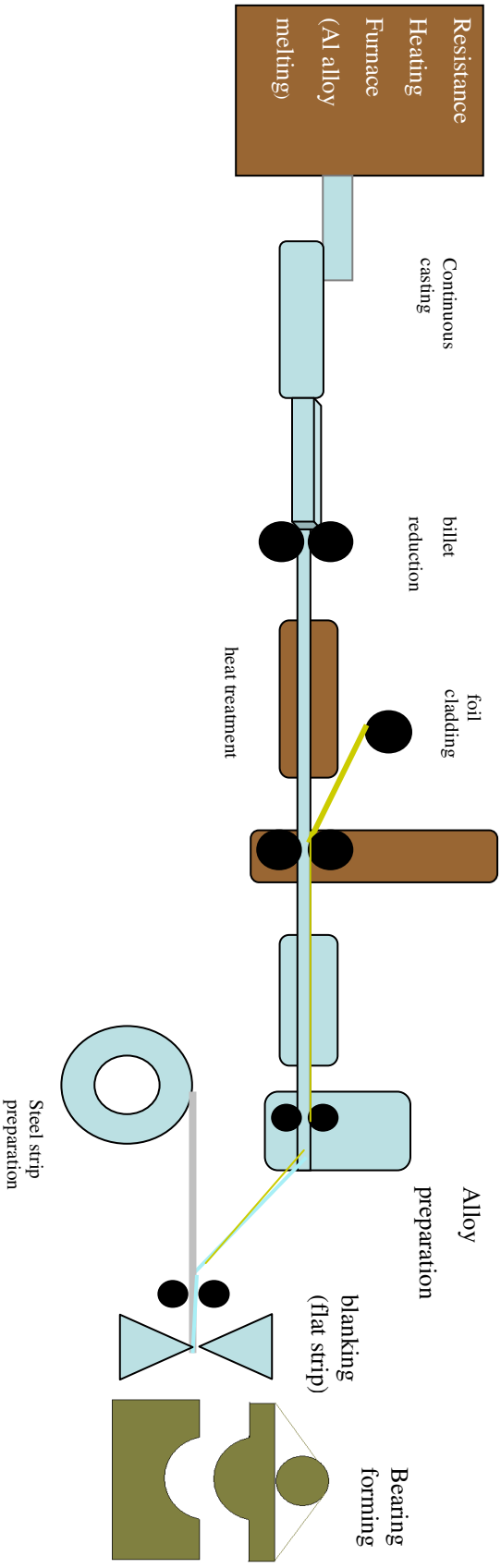

Figure 3.2:A schematic of the RB process for manufacture of *Al* alloy plain bearing half shells.

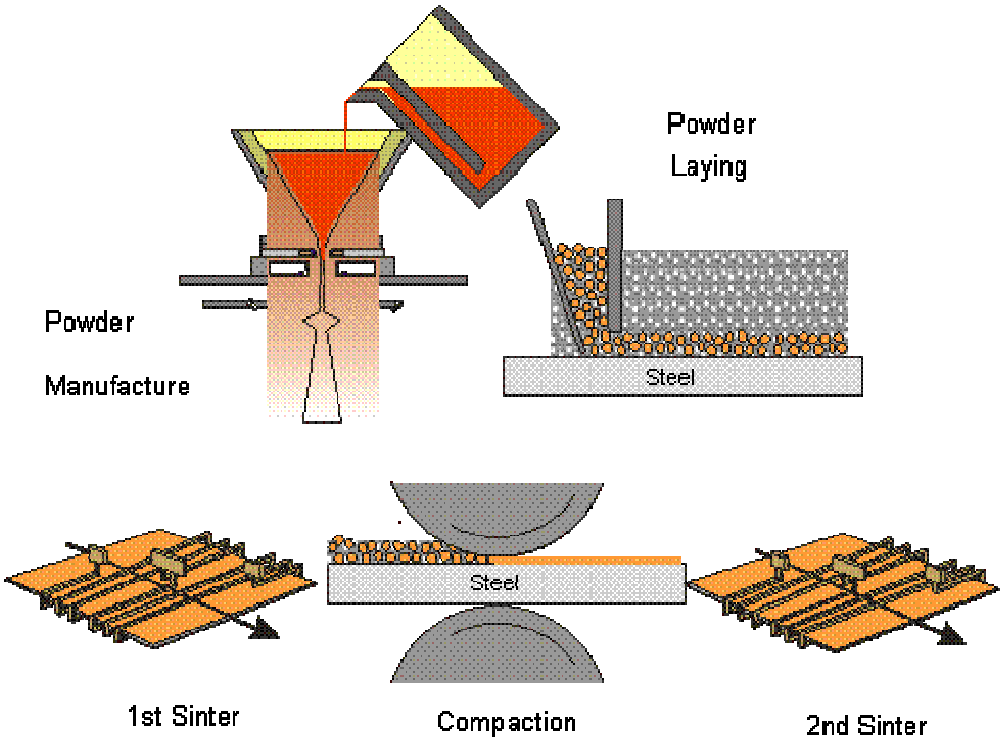

Figure 3.3: A schematic of manufacturing of bimetal strip used for the bronze bearing (courtesy DGV)

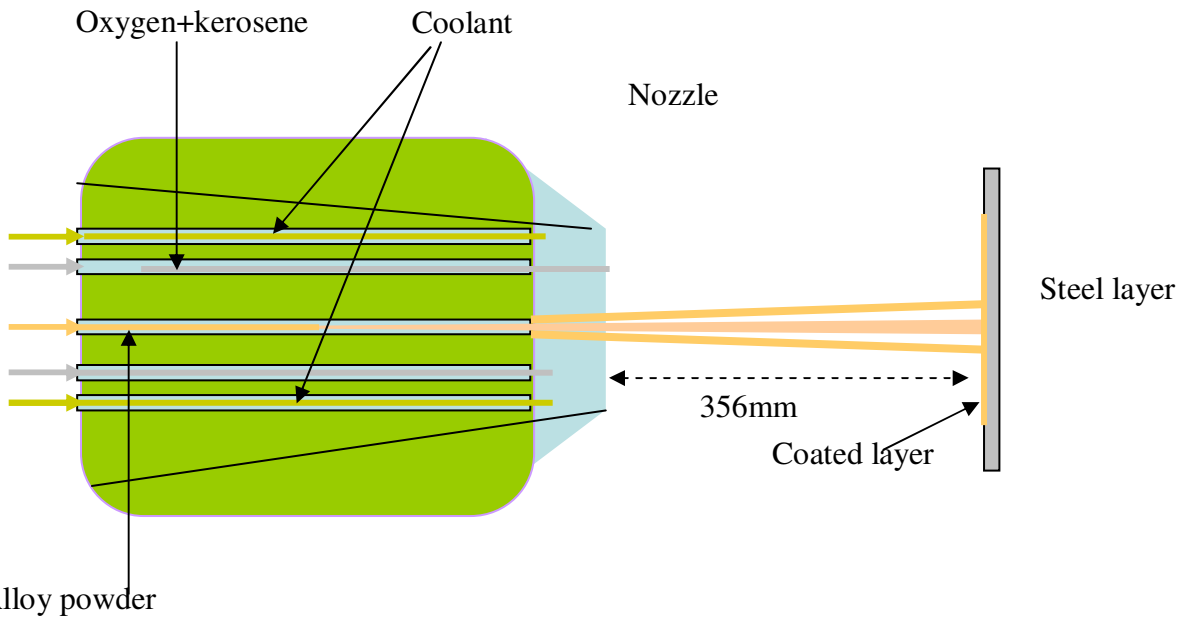

Figure 3.4:A schematic of the HVOF spray coating process used for coating *Al* alloy lining on flat steel strips (After[4]).

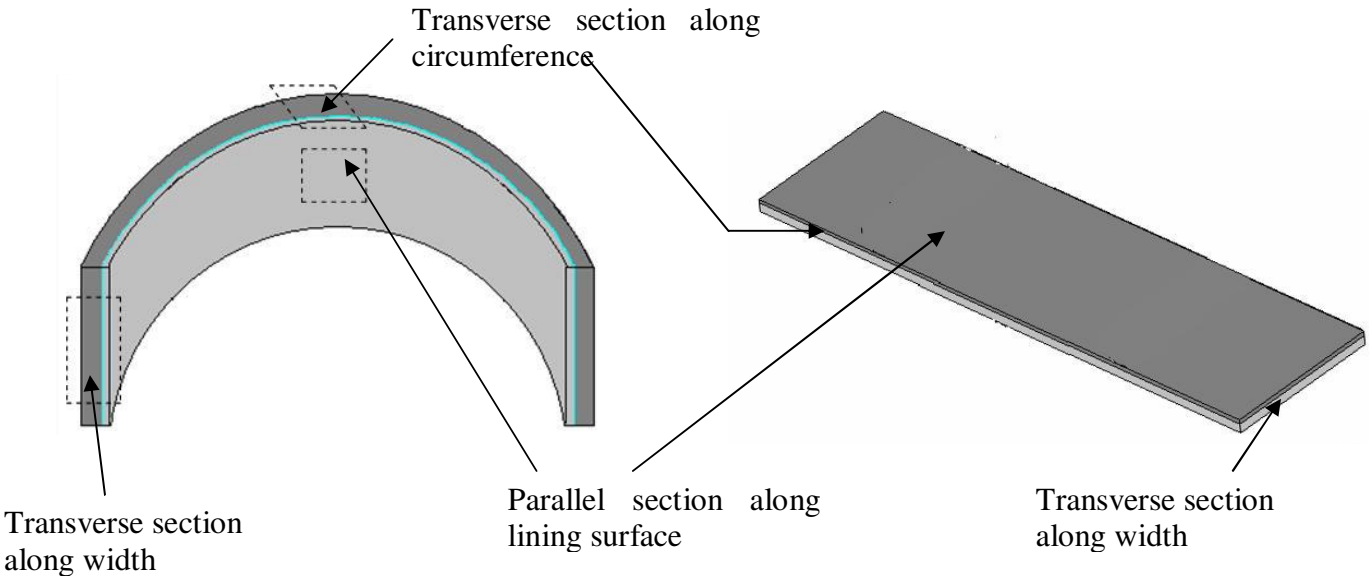

Figure 3.5: Specimen sectioning method for finished bearing and flat bar specimens to be used for metallography.

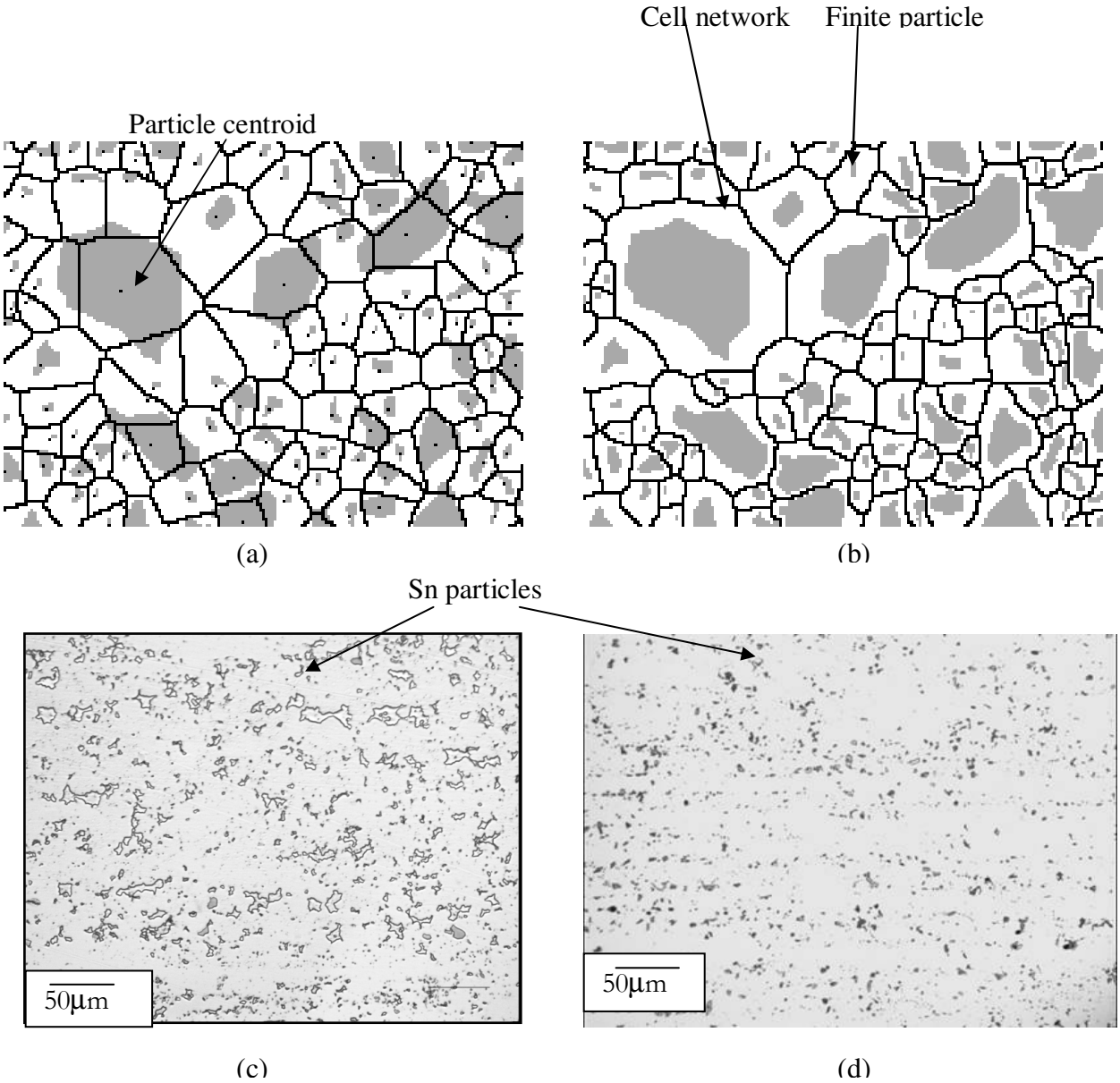

Figure 3.6: (a) A Dirichlet tessellated image. (b) An FBT image (c) Optical image of AS16 lining material (d) Optical image of AS20S lining material**.**

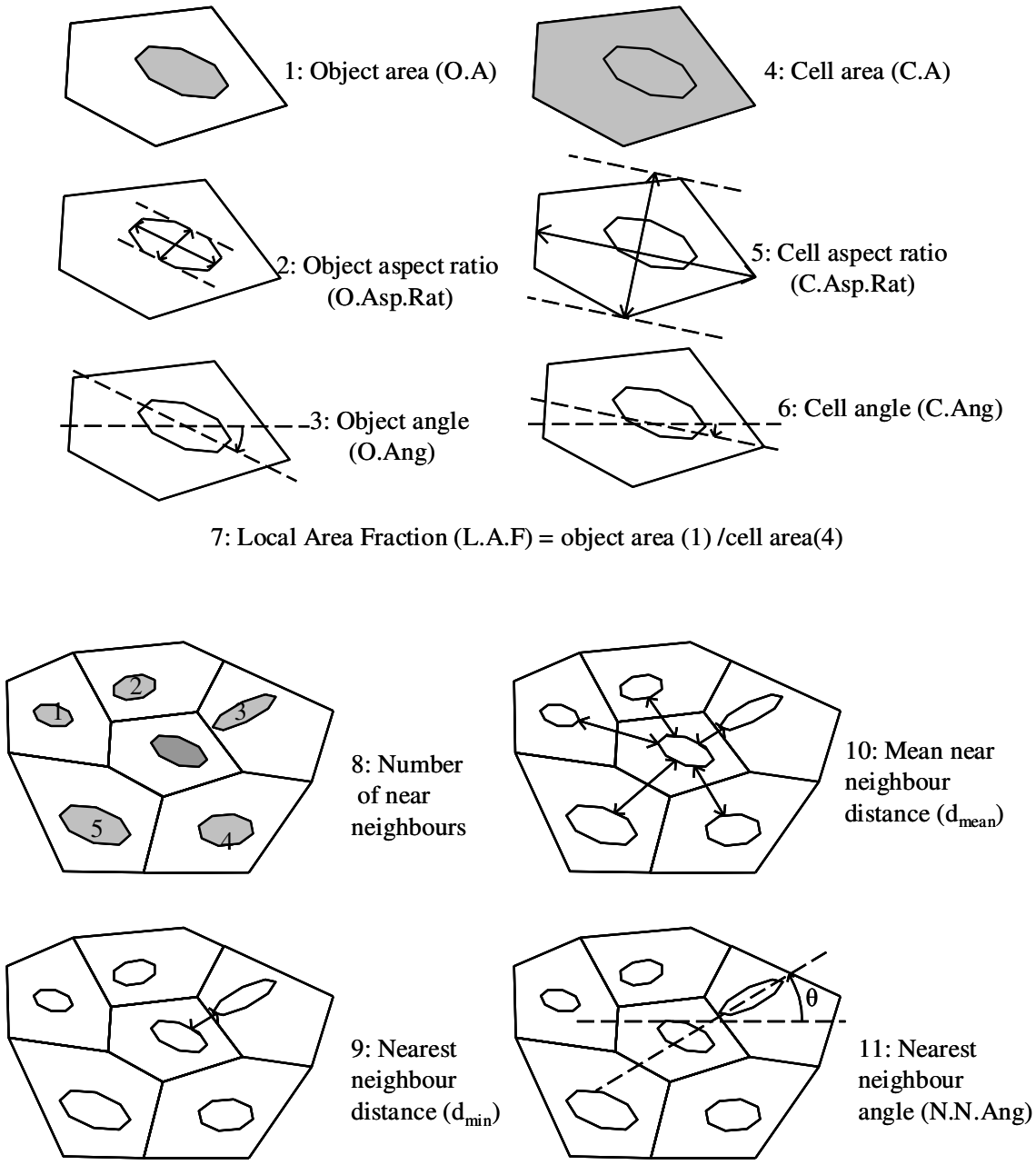

Figure 3.7:.Feature measurements obtained by FBT (After Joyce[13])

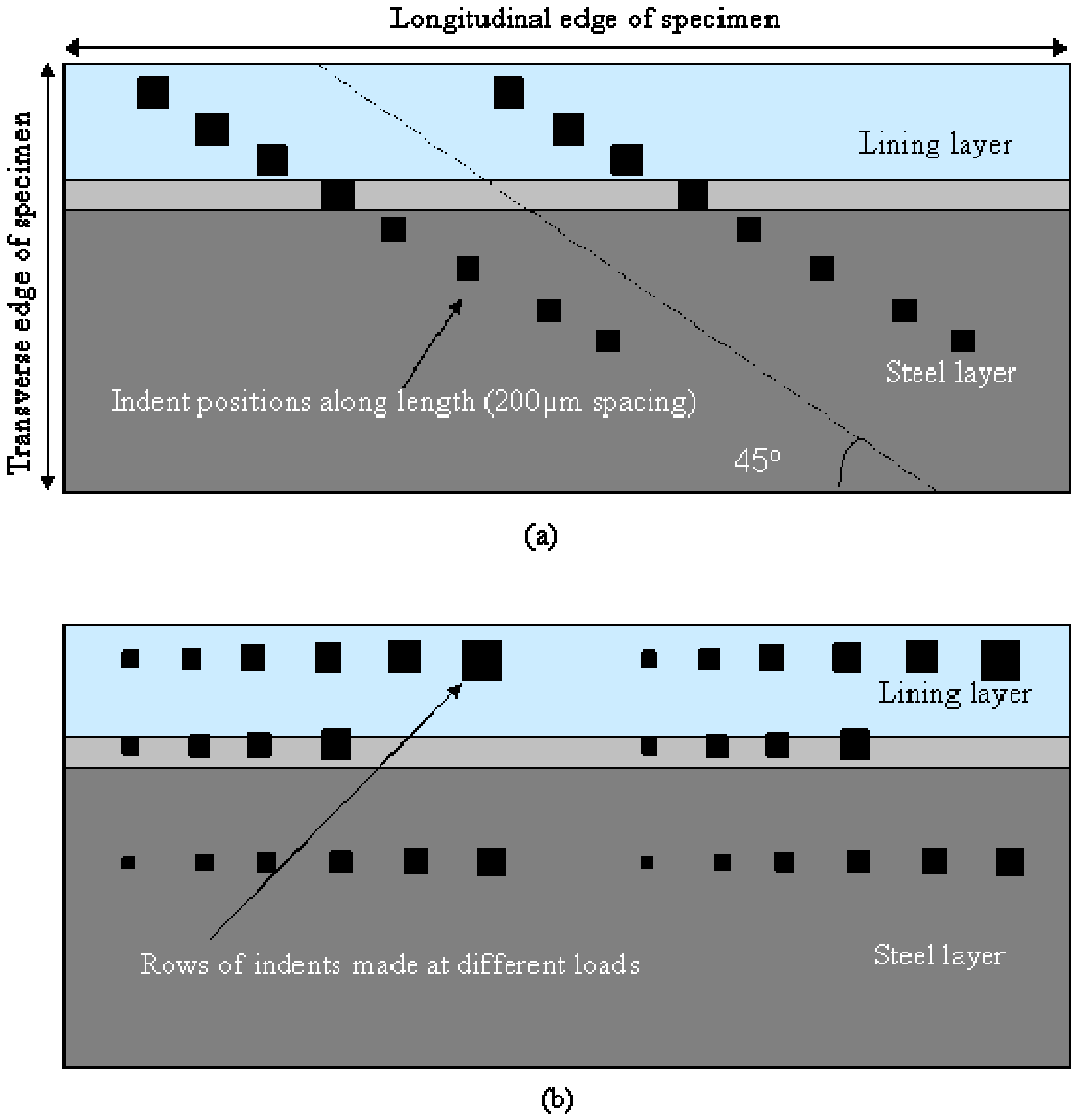

Figure 3.8: Methodology of microhardness indentation (a) Constant load micro-indentation. (b) Variable load micro-indentation within layers.

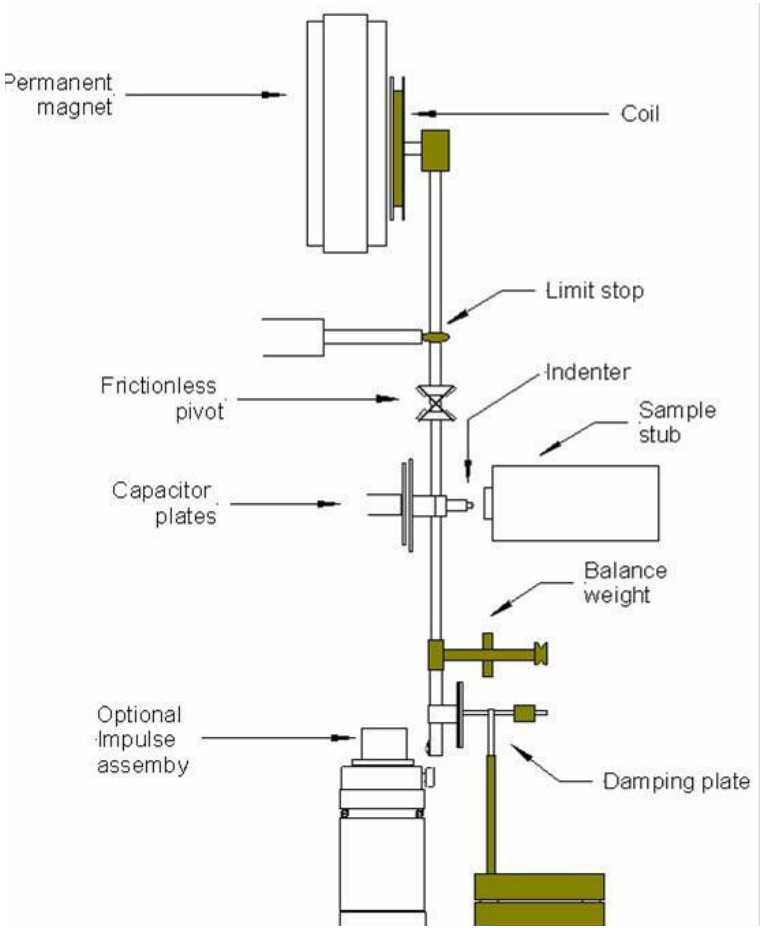

(a)

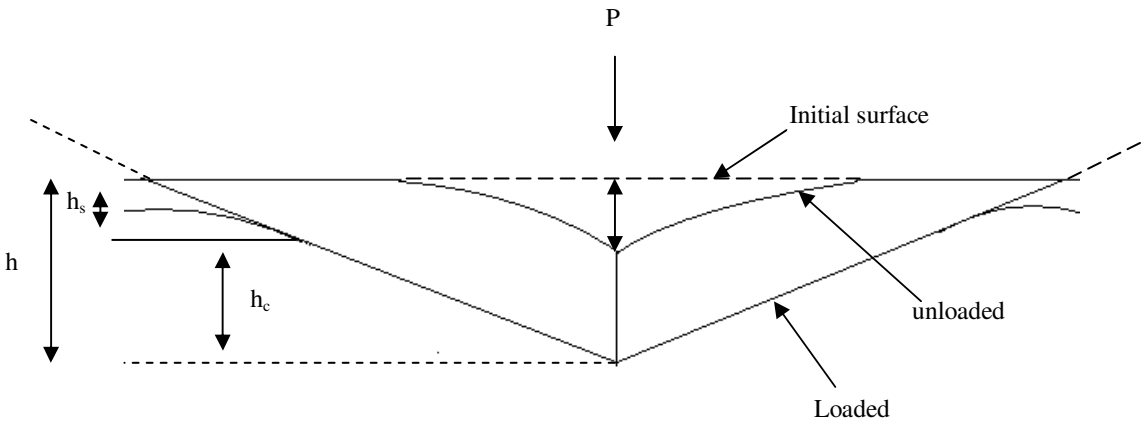

(b)

Figure 3.9: A schematic of (a) nanohardness-tester (After Micromaterials) (b) loading/unloading process of the indenter.

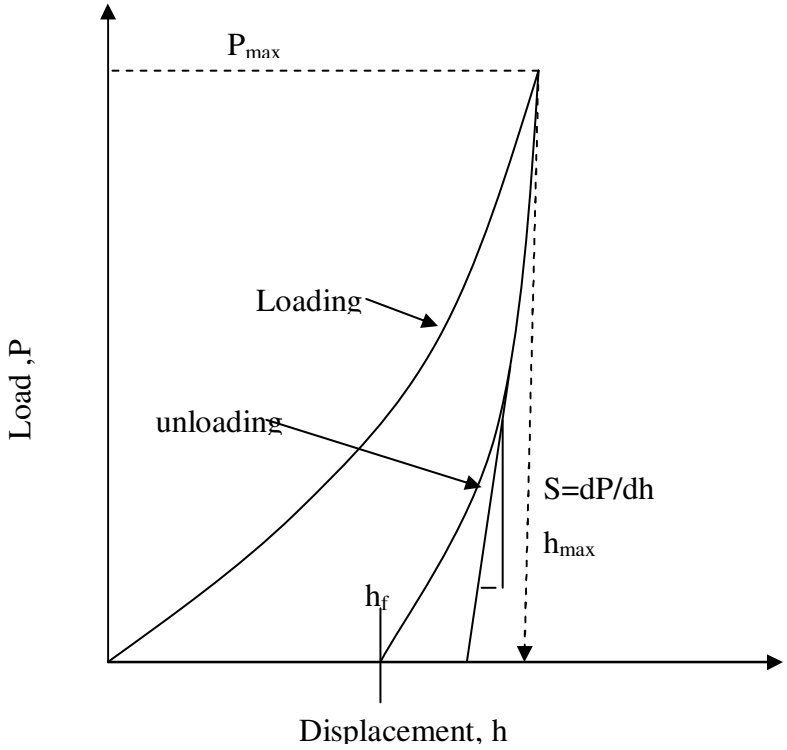

Figure 3.10: A schematic of the loading and unloading curve obtained from one load cycle during Nanoindentation.

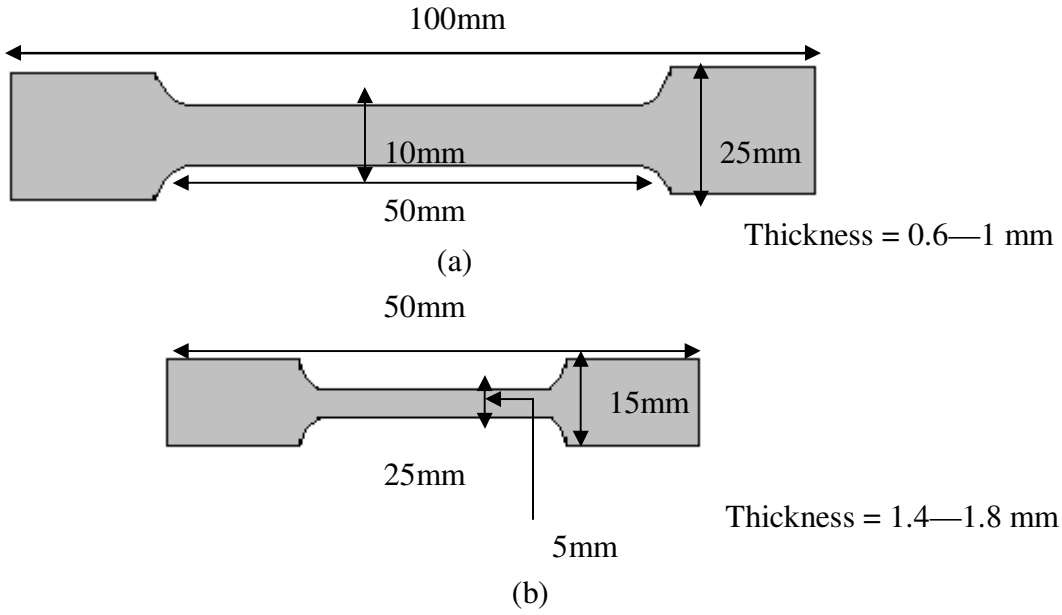

Figure 3.11: Tensile test specimen geometry (a) Monolithic lining and interlayers (b) Steel layer

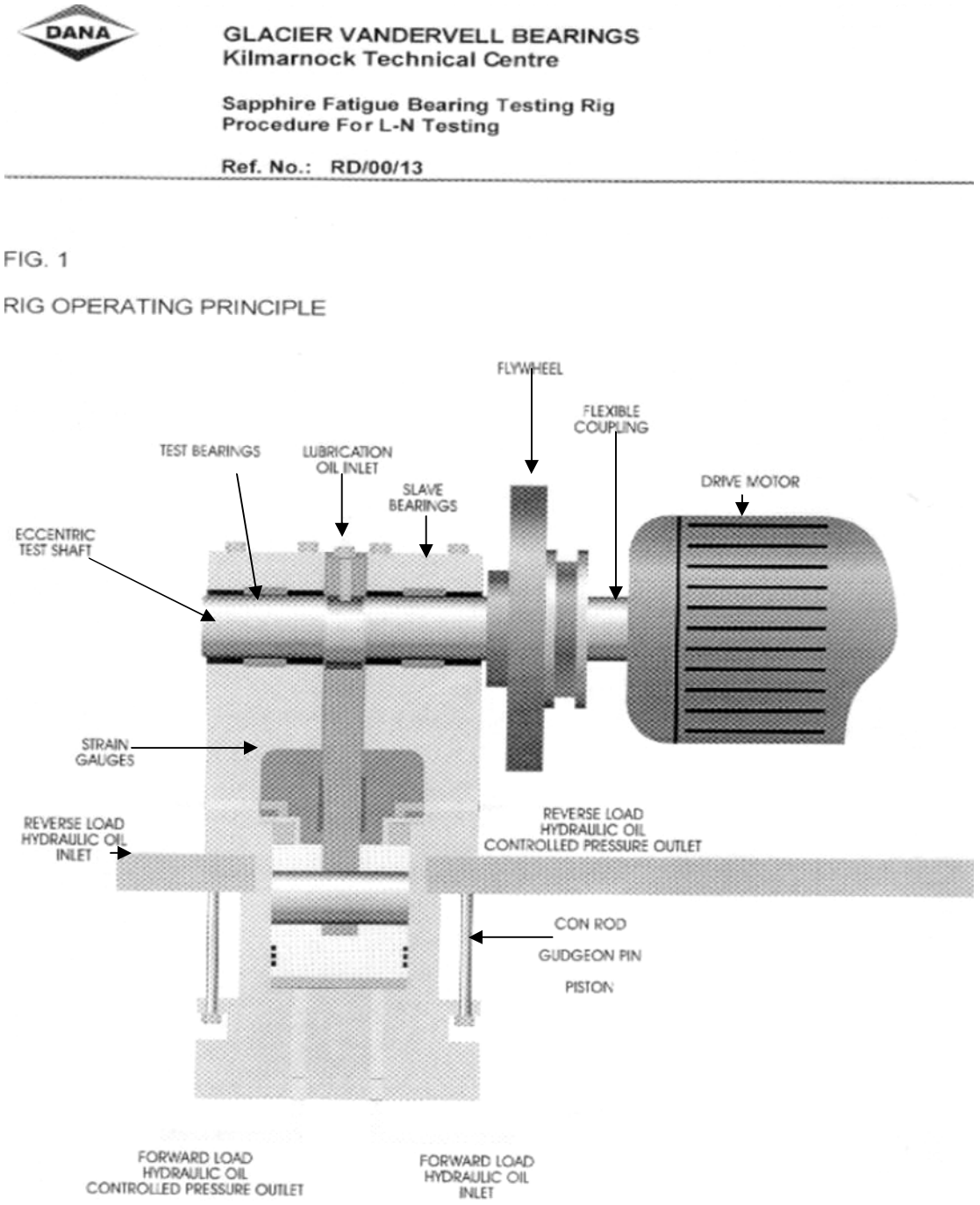

Figure 3.12: A schematic of accelerated rig test used for fatigue testing of bearings adopted by DGV (Courtesy DGV).

Load ratio =0.1

Frequency = 10Hz

Applied load = 1200-2600 N

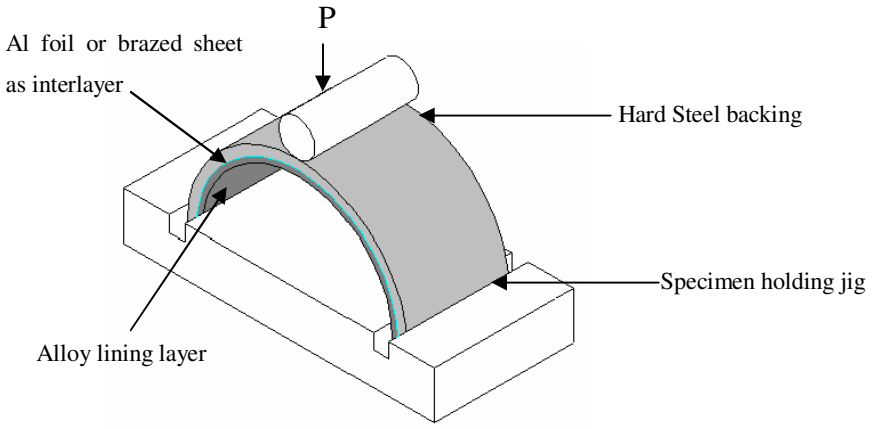

(a)

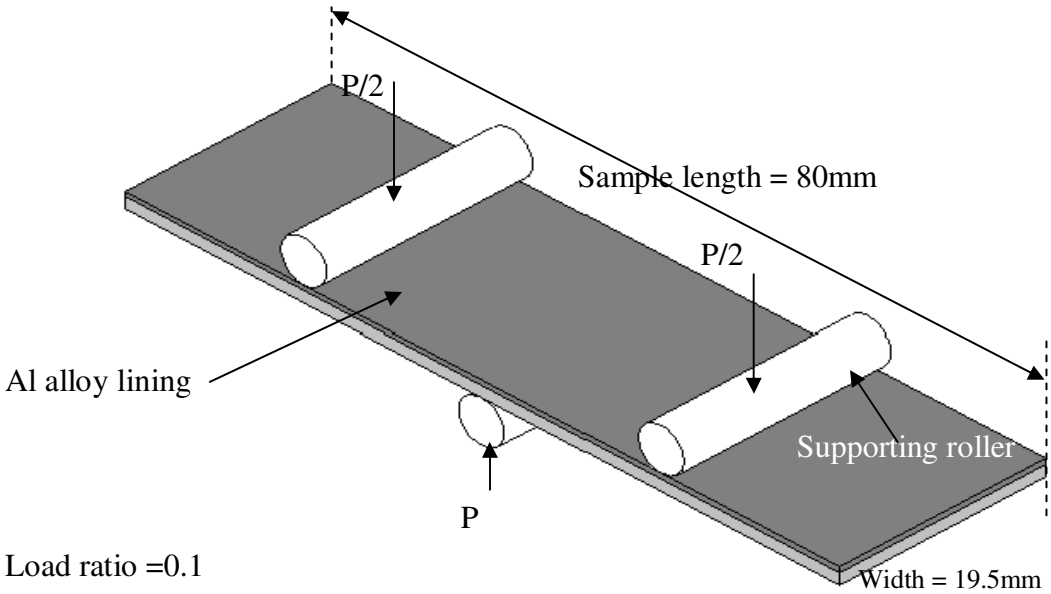

Load ratio =0.1

Frequency = 10Hz

Applied load = 500-1000N

(b)

Figure 3.13. Three point bend fatigue test configuration for (a) bearings and (b) flat bars.

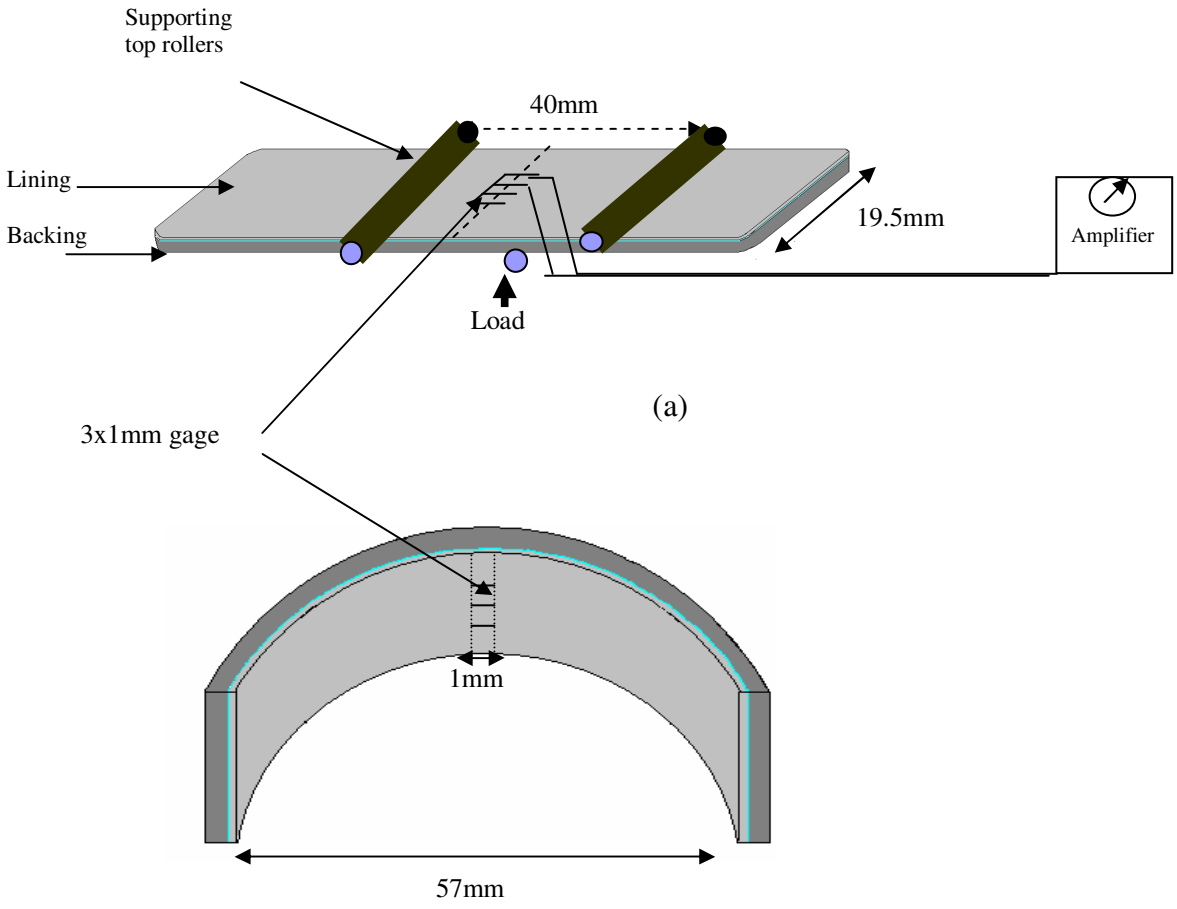

Figure 3.14:Strain gauge attachment to the top lining surface of (a) flat bars and (b) finished bearings

4 MATERIALS CHARACTERIZATION

Results obtained from various experimental techniques to characterize the different materials used in manufacturing the finished bearings have been presented and analyzed in the following subsections. This characterization comprises assessment of microstructural, compositional and meso-mechanical properties of the different materials making up the bearings.

4.1. Microstructural and compositional analysis

Microstructural analysis of the different systems was carried out on three surfaces, defined by three orthogonal lines *L*, *W* and *T* representing the length, width and thickness of the bearing and flat bar specimens respectively as shown in Figure 4.1. The *LW*, *LT* and *WT* planes represent the lining surface, transverse section along the edge and transverse section along the width respectively.

4.1.1. Microstructural view of the layered architecture of different systems

The systems considered were of two different types namely (i) *Al* based systems in which *Al* alloys (*Al-Sn-Si-Cu-Ni*) were used as a lining layer and (ii) *Cu* based systems in which *Cu* alloy (bronze with 1% *Ni*) was used as the lining layer. In order to reveal and characterize the layer construction of each system, 3-dimensional optical images of these systems were produced as shown in Figures 4.2-4.3.

Figure 4.2 shows 3-D optical images of all the *Al* based systems investigated. Figure 4.2 (a) and (b) show the optical micrographs of the roll bonded AS20S and AS20 bearing systems respectively. The lining layers (0.2-0.4mm thick after polishing) of both systems were the same[1] alloy and hence their microstructures are similar. The microstructural features in the lining surface are not easily distinguishable in these optical micrographs. *Sn* appears as a light outlined phase, presumably because of surface relief effects, with very few dark *Si* particles observed. Some light grey regions which were believed to be the intermetallics, appeared to be distributed in a scattered way throughout the microstructure and had a wide range of shapes whereas *Si* particles are more or less globular in shape. The overall distribution of secondary phases seem to be somewhat aligned in the rolling direction. The interlayer of the AS20S consisted of pure *Al* foil (0.04-05mm thick in the finished bearing) and appeared white in the optical microstructure. The interlayer of the AS20 system appeared to be

similar to that in the AS20S system in the optical micrograph; however, it was a rolled brazed sheet (a combination of 3003 and 4343 alloys), the individual layers of which were hard to distinguish under the optical microscope. However the individual layers were quite clear from the 3-D optical image of the originally provided monolithic brazed sheet shown in Fig 4.2 (c) as it was significantly thicker (~25 times) than the interlayer present in the finished bearing after considerable rolling. The top layer, which was the 4343 layer showed dark *Si* particles whereas the bottom 3003 layer, showed light grey intermetallic particles scattered throughout the microstructure.

A 3-D optical micrograph of the polished and unetched HVOF spray coated flat bar is shown in Figure 4.2 (d). The microstructure of the lining surface does not show clear distinguishable features, such as secondary phase particles, as seen in the RB system. Apart from some circular regions which could easily be distinguished from the rest of the matrix, a large number of tiny black marks were identified which indicate porosity. The circular features are believed to be the unmelts resulting from inefficient melting and high speed deposition of the original powder particles. The magnified optical image of an unmelt shown in Fig 4.2(d) indicates the presence of original dendrites of *Sn* particles. The interface of the HVOF systems appeared to be quite rough and irregular compared to that of the RB systems because of the grit blasting technique used prior to the deposition of the *Al* alloy powder.

Figure 4.3 shows the 3-D optical micrographs of the polished and unetched *Cu* based bearing systems in two different conditions namely (i) non-heat treated (abbreviated as RB168 NHT in all future references) and (ii) heat treated (abbreviated as RB168HT). The RB168 systems comprise a more complex combination of different layers compared to the *Al* based RB systems. The top layer of the NHT specimen is the *Sn* layer (bright layer in Figure 4.3 (a), 5-10µm thick) followed by a dark nickel layer (4-8µm thick). Both of these layers have been electroplated on to a thicker *Cu-Sn-Ni* layer (0.15-0.3mm thick lining layer) which was sintered to a still thicker (~1.5mm) carbon steel layer. As evident from Figure 4.3, these layers appeared as a homogenous material and did not show any distinguishable secondary phase features. Both *Sn* and *Ni* layers were relatively pure[1] and no secondary phase regions were expected. The heat treated (annealed at 190^{o}C for 6 hrs) specimen showed an additional interfacial layer between the *Ni* and *Sn* overlay layers (the dark wavy layer in the 3-D optical image shown in Figure 4.3 (b)). These layers are clearer in the optical image of the top layers obtained at higher magnification shown in Figure 4.3(c). In addition to that, the surface of the

heat treated specimen appears be covered by dark and bright regions which were thought to be due to the formation of an oxidized *Sn* layer (due to the elevated temperature in the presence of oxygen). The lining-backing interface of RB168 bearing systems (Figure 4.3 (a) and (b) shows some dark regions. These regions are may be due to an accumulated damage as a result of grinding and polishing the rough interface between sintered powder particles and the backing steel layer.

In the following sections, a more detailed microstructural analysis of all the layers of each system is presented.

4.1.2. Detailed microstructural and compositional analysis of *Al*-based systems

Microstructural analysis of each layer present in the *Al* based systems was carried out in the SEM in order to study different features in detail followed by a compositional analysis using EDX. Most of the microstructural analysis was focussed on the lining layer as it was important to the subsequent analysis of initiation and growth of microscale fatigue damage[4]; however subsurface layers and interfaces were also examined carefully.

4.1.2.1.AS20S/AS20

As various secondary phase particles in the microstructure of the AS20S/AS20 lining surface were not easily discernable under the optical microscope, subsequent analysis was carried out using SEM. A BEI image of the lining surface (LW plane) of the AS20S bearing is shown in Figure 4.4 (a) in which thin white *Sn* films are seen mostly encapsulating light grey intermetallics and dark grey *Si* particles and this is what makes the *Sn* distribution hard to distinguish in the optical microscope. An optical micrograph of the original cast lining material is shown in Figure 4.4(b), which reveals an equiaxed *Al* grain structure with *Sn*, and other secondary phase particles distributed along the grain boundaries. During the bearing manufacturing process (RB), the original *Sn* network is broken and redistributes itself around hard particles such as *Si* and intermetallics.

All observed phases in the BEI image were subjected to compositional analysis using the EDX analyzer attached to the FEG SEM. Table 4.1 gives the compositions obtained after the EDX analysis of the bulk material and individual phases present in the lining surface of the AS20S and AS20 bearings, respectively. The analysis was carried out on the basis of a full area map (to find out the overall composition) and sampling the individual phases (in order to determine the phase composition). Figure 4.4 (c) shows the location of various EDX spots

(red circles) selected on a BEI image of the AS20S lining in order to determine the composition of individual phases. A similar analysis was carried out for the AS20 lining. As the optical and BEI images of the AS20S/AS20 lining surface showed a sparse distribution of second phase particles, large areas (~2 mm^2) from the lining surface were subjected to the EDX analysis in order to get more consistent compositional data for the whole lining layer. To assess the composition of individual phase particles, a large number of similar phase particles were also subjected to EDX spots and the results were averaged out and are presented in Table 4.1. The white regions showed more than 90 % *Sn* whereas the composition of the grey phase indicated mostly the presence of *Cu* and *Ni* with some *Si*. Both *Cu* and *Ni* form intermetallics of the form $CuAl_2$ and *NiAl* or $NiAl_3$ (as discussed in the literature review Section 2.1.3). The nature of these intermetallics is complex and their exact composition could not be verified by the EDX analysis as the EDX sampling volumes may also include the *Al* matrix and other particles. The corresponding scatter in the results is also shown in Table 4.1. The composition of the lining alloy determined by this EDX analysis for both AS20S and AS20 systems falls within the range of the composition provided by DGV.

The only difference between the AS20S and AS20 systems is the interlayer which is a pure *Al* layer for the AS20S system and a brazed sheet (combination of 3003 core and 4343 clad alloy) for the AS20 system. However when the interlayer region (LT plane) was subjected to smart area mapping under the SEM (when operated in back scattered mode), some evidence of the presence of *Si* particles near the backing steel layer were found as shown in Figure 4.5 (a-c). However, the region adjacent to this and towards the lining layer showed *Mn* and *Ni* rich secondary phase regions. The boundary between the lining layer and 3003 layer of the brazed sheet was very unclear even at high magnifications. It was quite difficult to verify the composition of the AS20 interlayer as it is placed between the lining and backing layers and severely deformed due to rolling during the bearing manufacturing process. This made the compositional analysis of the individual layers (within the interlayer) a challenging process. For a more detailed study of the interlayer, an LT surface of the monolithic brazed sheet was observed in the SEM in order to examine the microstructural features more clearly. The BEI image of the original brazed sheet is shown in Figure 4.5 (d). The BEI image showed *Al* matrix in both layers with a large number of *Si* particles in the 4343 layer and complex white intermetallic particles in 3003 layer. However intermetallic particles are also clear in the 4343 layer as it contains *Fe* (0.06 wt %) and *Cu* (0.025 wt %). These intermetallics were observed to

be scattered throughout the microstructure of the brazed sheet. EDX analysis indicated these were complex *AlMnFe* compounds of varying ratios of these elements. The compositional results for the brazed sheet are shown in Table 4.2 for both 3003 and 4343 layers. 4343 is one of the 4000 series of *Al* alloys in which the major alloying element is *Si* (6%). 3003 is essentially an alloy of *Al* and *Mn* (1.2%*Mn*) with *Cu* and *Fe* up to 0.7% each.

The microstructure of the backing steel layer of the AS20S and AS20 bearing specimens is shown in Figure 4.6. White areas are ferrite grains elongated in the rolling direction whereas the darker areas are pearlite regions. These elongated grains are a result of plastic deformation under rolling operations carried out during the bearing manufacturing processes. The size and morphology of pearlite and ferrite grains in the steel layers of both systems is similar. The specifications of the steel used are given in Appendix A.

4.1.2.2.HVOF spray coated system

The BEI image of the lining surface (LW plane) of the HVOF spray coated system is shown in Figure 4.7(a) which clearly indicates the *Sn* phase (white areas), *Al* matrix (dark) and intermetallic particles (light grey areas). The BEI image hints at a very fine and scattered distribution of *Sn* but more clearly shows the larger smeared out white *Sn* regions between splats. There was some indication of a complex *Sn* distribution in the optical micrographs, although it is hard to resolve. Figure 4.7 (b) shows the TEM micrograph of the HVOF lining obtained from previous work[2] at Nottingham, which indicated that the expected distribution of *Sn* within the HVOF coating was very fine on the scale of nanometres. However, a heterogeneous distribution of *Sn* at the scale of splats/unmelts is likely to arise due to squeezing out of molten *Sn* between these features during the spray coating process (Figure 4.7a)

EDX analysis of the whole mapped area (with sampling volume of 720 μm^3) as well as of different individual phases in the HVOF lining was carried by targeting different regions shown as red spots in Fig Figure 4.7(a). The summary of the compositional results for the full area and individual phase compositions is given in Table 4.1. *Sn* rich areas appear white along with grey coloured patches that reflect areas where *Cu* was found in excess of *Sn* (more than 18%). The actual percentage weight composition of pure $CuAl_2$ is *Al-54Cu* which could not be verified by the EDX technique used as the sampling volume selected may also include the *Al* matrix which gave a higher percentage of *Al* than expected. The percentage composition obtained from the full area EDX analysis falls within the range of the expected composition.

Table 4.1: Composition of different materials measured via EDX analysis.

Material	Phase colour analyzed	Sampling volume (μm^3)	Wt% composition						
			Al	Sn	Si	Cu	Ni	Mn	V
AS20S lining	Full area	2×10^5	B	6.2±1.2	2.3±0.4	1.02±0.2	0.89±0.6	0.2±0.1	0.06±0.02
	Matrix	8	98.6±1.8	0.04±0.0	0.2±0.1	N.A	N.A	N.A	N.A
	White(Sn)	8	7.4±5.7	91±6	N.A	N.A	N.A	N.A	N.A
	Grey	8	76±1	N.A	0.86	18±3.2	14±4.5	N.A	N.A
	Dark grey	8	12.2	N.A	88±6	N.A	N.A	N.A	N.A
AS20 lining	Full area	800	B	6.6±1.76	1.8±0.9	1±0.2	0.91±0.12	0.2±0.1	0.08±0.04
	Matrix	10	98.6±2	N.A	1±0.2	N.A	N.A	N.A	N.A
	White(Sn)	25	7±4.4	87±4	N.A	N.A	N.A	N.A	N.A
	Grey	N.A	76±7	N.A	0.9	18±6.5	14±3	N.A	N.A
	Dark grey	N.A	12±12	N.A	89±6	N.A	N.A	N.A	N.A
HVOF lining	Full area	2×10^5	78±5	19.5±3	N.A	1.2±0.6	N.A	N.A	N.A
	Matrix	8	98±2	N.A	N.A	1.2±0.6	N.A	N.A	N.A
	White(Sn)	N.A	7±3	92±7	N.A	N.A	N.A	N.A	N.A
	Grey	N.A	76±6	N.A	N.A	18±3	N.A	N.A	N.A

Figure 4.8(a) shows the BEI image of the cross-section of the HVOF flat bar. The splats are quite clear from this cross-sectional image. There is no interlayer present and the interface is noticeably irregular. The rough interface is due to the shot blasting technique applied to the steel layer prior to the deposition of the *Al* alloy powder. The purpose of the shot blasting was to achieve a chemically and physically more active surface. The main objective of grit or shot blasting is to get a rough surface profile that promotes mechanical keying of the coating with the steel substrate. The exact nature of bonding between coating and the substrate is still a subject of investigation, but both mechanical interlocking and diffusion bonding are believed to occur[3].

Table 4.2: Compositional results of brazed sheet.

Layer Type	*EDX obtained composition (wt %)*				*Standard alloy composition (wt %)*			
	Cu	*Si*	*Mn*	*Fe*	*Cu*	*Si*	*Mn*	*Fe*
3003 (Balance Al)	0.8±0.02	NA	1.2±0.08	0.5±0.1	0.7	NA	1.2	0.7
4343 (Balance Al)	0.12±0.3	6.7±0.2	NA	0.6±.1	0.25	6	NA	0.8

Figure 4.8 (b) shows the micrograph of the etched HVOF backing steel layer (LW plane). The dark areas are pearlite (where the echant has attacked the Fe_3C/ferrite grain boundaries) whereas the light areas indicate the presence of pro-eutectoid ferrite. The microstructure of the spray coated flat bar steel layer shows comparatively homogeneous ferrite and pearlite grain structure as this steel was annealed at 300^{o}C after the manufacture of the flat bars and received little or no cold work during processing. The overall pearlite content in the HVOF steel layer appears to be less than the pearlite content in the AS20S and AS20 steels indicating lower carbon content.

4.1.2.3.Quantitative assessment of various features of the *Al* grain structures

The EBSD technique revealed grain size and grain orientation details of the *Al* matrix in the AS20S and AS20 bearing lining surface. The second phase particles embedded in the *Al* matrix such as *Sn*, *Si* and intermetallics could not be polished effectively during the electro-polishing process adopted and therefore were not picked out in the EBSD maps due to surface relief effects. Figure 4.9 shows the EBSD maps obtained for the AS20S and AS20 lining surface (LW plane) compared with similar EBSD maps obtained for the AS16 and AS1241 bearing lining[4]. Prior attempts by *Mwanza* to obtain EBSD results for a similar HVOF lining indicated that the grain size was far too fine (at 5-50nm as found during earlier work[2]) to achieve any resolution. Grain sizes of the AS20S and AS20 lining surface appear to lie between the grain sizes of AS1241 and AS16.

Histograms showing the grain size distribution of all these systems have been presented in Figure 4.10. Most of the grains of the AS20S and AS20 lining have grain sizes between 5 to 15µm, with the average grain size of approximately 9 µm, whereas in AS16 the grain size of most of the population is less then 10 µm. The grain size of the AS1241 lining appears to be mostly between 10 to 25µm with the average grain size equal to 11 µm. In the misorientation angle distribution histograms (Figure 4.11), the solid line shows the distribution for randomly orientated grains.

The random distribution curve has been derived from the well known *Mackenzie* plot[5] in which the peak frequency occurs at a misorientation angle of 45^{o}. For the AS20S/AS20 system, the misorientation angle distribution seems to be closer to the ideal random distribution whereas for the AS16 lining, the distribution of grain orientations deviates significantly from the random distribution curve and indicates a preferred alignment of the matrix grains. A brief summary of the EBSD results is shown in Table 4.3

Table 4.3: Average grain size and orientation results for *Al* obtained via EBSD

Lining type	Grain size (µm)	Grain misorientation angle (degrees)
AS20S	9±1.5	44.4±2.1
AS20	9.5±0.89	43.9±2.8
AS16	5±2.1	32.4±2.1
AS1241	11.5±3.4	42.4±2.1

4.1.2.4.Quantitative assessment of various features of secondary phase particles

Secondary phase particles such as *Sn*, *Si* and intermetallic compounds ($AlNi_3$) in the AS20S and circular unmelts in the HVOF lining were the most prominently distinguishable phases in the *Al* based systems. A quantitative assessment of various features of these particles measured by the FBT method (detailed in Section 3) is given here.

4.1.2.4.1 AS20S

Figure 4.12 shows the SEI images of the AS20S bearing lining surface along with the corresponding BEI image in which the most obvious secondary particles are *Sn* and intermetallics without frequent *Si* particles. It is evident from the images that intermetallics are distributed throughout the microstructure and *Sn* films mostly occur around these intermetallics. To obtain similar information on the distribution of these phases, SEI images were manually traced to produce binarized images of each particle population distribution separately. Binary tessellated images representing *Sn* and intermetallic particles obtained from the corresponding SEI image are shown in Figure 4.12(c) and (d), respectively, which demonstrates how the rest of the FBT analysis was carried out. These images show the network of cells defined by the relative particle positions. The main features obtained from this analysis are object area, object aspect ratio, object angle, cell area, cell aspect ratio, cell angle, number of near neighbours, mean near neighbour distance and local area fraction as shown in Figure 3.7 (Chapter 3). Measurements obtained for the edge cells were discarded as these were incompletely bounded. The summary of these results in the form of mean values, standard deviation and coefficient of variance COV is given in Table 4.4. The value of COV is obtained by dividing the standard deviation by the mean value. According to *Yang et al*[6], random homogeneous distributions are found to exhibit a COV (d_{mean}) equal to 0.36±0.02. Thus, the inhomogeneity level of any given distribution of second phase particles can be evaluated by matching the measured value with this value.

It is evident from the microscopic study of the AS20S lining surface (both optical and SEM) that all the second phase particles such as *Sn, Si* and intermetallics have a sparse distribution and wide particle size range. In order to get statistically representative data, an area of approximately 2 mm^2 was subjected to FBT analysis that calculated the aforementioned features for 500-1000 particles of each phase.

It is clear from Table 4.4 that the mean object area for both *Sn* and intermetallics are quite equivalent. The corresponding high values of standard deviation indicate a wide range

of particle size distribution for both *Sn* and intermetallics. Values of d_{mean} for *Sn* and intermetallics are 10.20 and 9.52 µm, however the $COV_{d(mean)}$ value for *Sn* is higher (0.50) than the $COV_{d(mean)}$ for intermetallics (0.44). Hence *Sn* particles show greater clustering than the intermetallics although both particle populations seem somewhat clustered. *Si* particles are widely spaced with d_{mean} equal to 44 µm and $COV_{d(mean)}$ equal to 0.37 which indicates a more random distribution of *Si* particles compared to both *Sn* and intermetallic particles.

All three types of particles show approximately the same number of nearest neighbours (NN). There is also a wide variation in the object angle of both *Sn* and intermetallics. The aspect ratio (r_a) for the various particles does not show any specific trend. Distributions of various measured features for the identified three secondary phase particles were analyzed. These results have been given in the form of histogram charts shown in Figure 4.13-4.17. Distribution of both object and cell area appear to be alike as shown in Figure 4.13 (a) and (b) respectively. No specific trend for any particle was observed for the r_a (Figure 4.14) and number of nearest neighbours. Both object and cell angles (Figure 4.15(a) and (b)) have wide range of distributions.

The FBT measured angle is defined by the maximum particle length axis relative to the normal to the rolling direction i.e. the closer the angle to 1.6 rad (90^o), the greater would be the alignment of the secondary phase particles to the rolling direction. From the results shown in Table 4.4, the intermetallics show slightly higher object angle (0.72 rad) than the rest of the particles. If the histogram showing the aspect ratio of the object angle is observed carefully, it indicated a wider distribution range of the aspect ratio of the intermetallic particles than that of *Sn* and *Si* particles.

One check of the FBT analysis is the comparison of the measured overall volume fraction with the estimation of the volume fraction of various constituent secondary phase particles. This assessment is based upon the area fraction calculated by obtaining the ratio of the total object area to the total cell area of each type of second phase particle acquired via FBT analysis. The actual composition determined by EDX analysis (also provided by the sponsors) was in terms of weight percentages and hence it was converted to volume percentages (using the relevant densities of each phase) in order to find the estimated volume fraction. The volume fraction evaluated in this way was compared with the FBT based area fraction in order to assess the validity of the FBT technique. The results obtained are shown in Table 4.5.

Table 4.4: Result of the FBT analysis of AS20S lining surface

Particle	**Measure**	**Object area (μm^2)**	**Object AR**	**Object angle (rad)**	**Mean NND(μm^2) (d_{mean})**	**L.A.F**
Sn (356 particles)	Mean	27.55	1.68	0.656	30.29	3.26
	St. Dev	±21.85	±0.41	±0.39	±15.32	±3.36
	COV	0.79	0.24	0.60	0.50	1
Si (98 particles)	Mean	14.71	1.29	0.64	43.88	0.93
	St. Dev	±14.21	±0.269	±0.547	±16.47	±0.97
	COV	0.96	0.208	0.8439	0.373	1.05
Intermetallics (501 particles)	Mean	26.05	1.51	0.72	28.88	3.46
	St. Dev	±16.64	±0.42	±0.38	±12.63	±3.29
	COV	0.64	0.28	0.53	0.44	0.95
	Measure	**Cell area (μm^2)**	**Cell AR**	**Cell angle (rad)**	**NND (μm^2) (d_{min})**	**No NN**
Sn	Mean	1407.33	1.61	0.843	10.20	5.53
	St. Dev	±1305.62	±0.54	±0.433	±9.96	±1.38
	COV	0.92	0.34	0.51	0.97	0.25
Si	Mean	2147.406	3.2	0.83	15.27	5.52
	St. Dev	±1618.662	±8.5	±0.499	±10.36	±1.41
	COV	0.75	2.6	0.59	0.67	0.25
Intermetallics	Mean	1156.542	1.628	0.855	9.52	5.55
	St. Dev	±865.20	±0.50	±0.45	±8.4	±1.25
	COV	0.75	0.30	0.53	0.88	0.22

According to the results shown in Table 4.5, the area fraction of *Sn* was found to be quite close to the volume fraction determined from the EDX analysis. The difference may be due to the clustering in *Sn* particles and closer agreement may be achieved if FBT is applied on even larger areas, but there still would be the probability of error in tracing the exact particle shape by drawing the binary image manually**.** No attempt was made to evaluate the FBT area

fraction of *Cu, Ni*, and other alloying elements as these mostly go to form intermetallics and could not be represented by simplistic volume estimation.

The measured volume fraction of *Si* was much less than the volume fraction calculated. The obvious reason is the rare occurrence of *Si* particles in the lining microstructure and hence very large areas need to be assessed in order to compare full information on the *Si* content. Also a portion of the *Si* content seems to be present in the intermetallics (EDX analysis) and hence all the *Si* present in the alloy may not appear as separate particles in the microstructure.

Table 4.5: Estimation of % age Volume fraction based upon FBT analysis

AS20S alloy	Al	Sn	Si	Intermetallics
%Weight	89	6.2	2.5	N.A
Density (g/cc)	2.69	7.29	2.33	N.A
Vol (W/ρ)	33.08	0.89	1.07	N.A
$\%Vol_{fraction}$	92.62	2.3	2.9	N.A
FBT% $Area_{fraction}$	N.A	1.6	1.3	2.2

4.1.2.4.2 HVOF lining

Both optical and SEM techniques revealed that the distribution of *Sn* in the HVOF was too complex for similar FBT estimations to assess particle distribution; however unmelts mostly appeared as circular or nearly circular regions in the microstructure. The microstructure within the unmelt was different from that of the matrix which could affect fatigue initiation due to possible mechanical property mismatch, hence their size, shape and distribution was deemed to be important.

Figure 4.18 shows an optical image of the HVOF lining surface along with the corresponding binarised images showing unmelts. For more consistent results binary images from larger areas (~2mm^2) were produced. As the unmelts were nearly circular, parameters such as the object angle and near neighbour angle (for both object and cell) are not considered here. An FBT measurement showed that the average value of the area of circular unmelts was 1922±800 μm^2. Distribution of their size is quite wide as shown in Figure 4.19 (a). These unmelts covered ~1.1% of the area of the microstructure and majority of them have the r_a of 1.1(nearly circular) as shown in the r_a distribution histogram in Figure 4.19(b). Distribution of

the measured mean near neighbour distance (d_{mean}) for the unmelts is shown in Figure 4.19(c). The average d_{mean} value was 387±159 µm with COV equal to 0.41, somewhat greater than the standard value of 0.36 that indicates an ideally random distribution. Hence the unmelts were believed to have more random distribution than the secondary phase particles (*Sn* and intermetallics) in the RB systems.

4.1.3. Detailed microstructural analysis of *Cu* based bearing systems

The *Cu* based bearing systems consisted of various layers, with additional layers observed in the heat treated specimens. SEM micrographs of the polished LT sections obtained from the RB168 bearing systems are shown in Figure 4.20. Compositions of the different layers obtained from EDX analysis are given in Table 4.6 . For clarification, detailed microstructural and compositional analysis of each of these layers (numbered in Figure 4.20(a)) is presented here separately in a top to bottom hierarchy.

4.1.3.1.*Sn* overlay layer

The *Sn* layer at the top appeared as a white layer in the SEI micrographs of the heat treated and as plated specimens shown in Figure 4.20 (a) and (b) respectively. For both heat treated and non-heat treated specimen this layer appears to be 6±2 µm thick. However the SEI images of the heat treated specimen shown in Figure 4.20(a) indicated another bright white layer over the *Sn* layer (1-2µm) which was found by the EDX analysis to be the SnO_2 formed as a result of heat treatment in air. This layer was not observed in the as plated specimen (non-heat treated).

4.1.3.2.*Ni* layer

The *Sn* overlay layer was electroplated on to a *Ni* layer as shown in Figure 4.20 (a) and (b) (4-6µm thick) which itself was electroplated on a pre-deposited sintered *Cu-8Sn-1Ni* lining layer. The *Ni* layer appeared to be light grey (7±2µm) and EDX analysis showed the presence of up to 3 weight % of *Cu* and *Fe* as foreign elements.

4.1.3.3.*Ni-Sn* interfacial layer

The optical micrograph of the heat treated specimen (Figure 4.20 (a)) showed a very thin granular layer of a dark phase at the interface between the *Sn* and *Ni* layers. However this layer was not prominent in the as plated specimen (Figure 4.20 (b)). A careful observation

of the *Sn-Ni* interface of the heat treated specimen in the SEI image indicated two distinguishable regions (i) a wavy layer along the electroplated *Ni* layer and (ii) granules spreading as globular particles (1-2µm) towards the top *Sn* layer. EDX analysis of both the wavy layer and granules indicated the presence of *Sn* along with *Cu* and *Ni.* When the atomic weight percentages of all the elements were compared, an empirical formula of the type $Cu_x\ Ni_y\ Sn_z$ emerged where the values of x, y and z were found to be 0.21, 5.25 and 16.875 respectively. The values of y and z were in the ratio of 1:1.35. This ratio between *Ni* and *Sn* atoms is very much similar to that in the Ni_3Sn_4 intermetallic compound. Formation of Ni_3Sn_4 type intermetallic compound has been reported by *Mita et al*[7] during a study of solid state reaction kinetics between *Ni-Sn* couples. It was reported that the solid state diffusion reaction between *Ni* and *Sn* layers results in the growth of Ni_3Sn_4 type intermetallics. The low temperature isothermal annealing at 160°C resulted in the formation of granular layer while annealing at 180°C resulted as wavy layer. The micrograph shown here was obtained from the specimen heat treated by the sponsors where specimens were annealed at 180°C for 6 hrs.

4.1.3.3.1Heat treatment of RB168 bearings

It has been reported[7] that *Sn-Ni* couples form a layer of intermetallic compounds at the interface of the materials as a result of an interfacial diffusion reaction during annealing. The thickness and morphology of this layer could be altered by changing heating time and temperature. The top layers of the RB168 systems were a *Sn-Ni* couple that had reacted in a similar way (as seen in Figure 4.20). The nature and morphology of this layer, underneath the top *Sn* layer, could affect subsurface penetration of fatigue cracks during fatigue (an issue that will be discussed further in Chapter 5).

The as received RB168NHT specimens were therefore subjected to a series of anneals at 180, 190 and 200°C for various time intervals from 2 to 72 hours. Optical micrographs of some of the heat treated specimens are shown in Figure 4.21. It is evident that the thickness of the interfacial compound layer increased with increase in the annealing time or temperature. The thickness of the interfacial layer was measured by dividing total area by the total length of the layer as observed in the microstructure of the cross section[7]. The experimental data obtained was in the form of time (hrs) and interfacial layer thickness in microns. Figure 4.22 shows the effect of temperature on the growth of Ni_3Sn_4 intermetallic compound layer formed between the *Sn-Ni* couple in the form of plots between time and layer thickness. The curve is on a log-log base and the slope of the line is considered as a

proportionality constant *k*. This is assumed to be a diffusion[8] controlled growth which obeys parabolic law described as

$l = k(t)^n$ Equation 4-1

The values of *k* and *n* were calculated on the basis of the experimental results and an empirically determined plot is shown as dotted line in Figure 4.22. This curve describes the general growth behaviour on the basis of empirical values of constants *n* and *k*. Similar growth behaviour of *Sn-Ni* compounds have been reported in earlier work[9]in which *Sn-Ni* compound growth was studied in *Ni* and *Sn* rich solders. The *Ni-Sn* overlay layers in the RB168 systems are quite thin which limits the growth of the interfacial layer. A more precise analysis of the growth behaviour of the interfacial compound requires extensive heat treatment experiments especially at various short intervals. However, a full study of the growth kinetics of this layer is beyond the scope of this research and the current analysis was limited to these empirical results. Apart from generalizing further understanding of the growth behaviour of the interfacial layer, the other objective of the heat treatment experiments was to obtain an appreciably thicker layer in order to facilitate nano-indentation for the nanohardness testing described in more detail in Section 4.2.2.

4.1.3.4.Bronze lining layer

The *Cu-Sn* and *Cu-Sn-Ni* phase diagrams[10] are shown in Figure 4.23 (a) and (b) respectively.

Figure 4.23(a) shows a series of complex intermetallic compounds of *Cu* with *Sn*. However considering only the lower portion of the diagram (room temperature), the phases expected to be present were α (solid solution) and ε (intermetallic compound: Cu_3Sn). The alloy studied was a low *Sn* bronze and a considerable portion according to the phase diagram was expected to be *Cu-Sn* solid solution. The amount of *Ni* in this alloy was 1%. It is evident from the ternary diagram of the *Cu-Sn-Ni* systems that most of the added *Ni* forms a solid solution with *Cu.* The single phase nickel-bronze observed in the RB168 lining is thus in line with expected behaviour.

The polished surface of the lining (*LW* plane) was etched using different etching reagents suggested for bronzes[11]. However, a solution of $FeCl_3$ in *HCl* (10g $FeCl_3$+ 200ml *HCl* solution) was observed to etch this lining more efficiently. Figure 4.24 (a) and (b) shows the etched lining surface of the RB168 bearing in heat treated (annealed at 190^{o}C for 6 hrs) (a) and

non-heat treated (b) conditions. The microstructure in both cases shows equiaxed grains of α *Cu*. However, some darker regions near the grain boundaries were deemed to be due to occasional ε compound. The grain size of the heat treated specimen appeared to be somewhat coarser (average grain diameter is 26±5) as compared to the non-heat treated specimen (average grain diameter is 19±7) indicating some grain growth has occurred.

The lining surface was also subjected to compositional analysis using EDX. It is evident from the EDX results (Table 4.6) that the composition of the lining layer is in agreement with the expected composition of *Cu-8Sn-1Ni.*

Table 4.6: EDX compositional results for the RB168 systems

Layer No	Area scanned (mm^2)	% Wt of different elements					Phase identified as
		Cu	Sn	Ni	Fe	O	
1	0.1	N.A	64	N.A	N.A	36	SnO
2	0.5	2±1	97±2	0.1±0.28	N.A	N.A	Sn plated
3	Spots	5±0.5	68±4	25±3	N.A	N.A	Intermetallics
4	0.5	4.7±1.3	N.A	95±2	0.3±0.3	N.A	Ni
5	2	90±1	9±0.6	0.30±0.6	0.4±0.3	N.A	Lining layer

4.1.4. Discussion-microstructural characterization results

4.1.4.1.Al based lining systems

The RB AS20S and AS20 bearing linings have similar populations of secondary particles as observed in the previous AS1241 lining material. The secondary particles in the AS1241 were much more clearly observed in the optical images of the lining surface of the latter as shown in Figure 4.25. For the AS20S/AS20 lining, SEI and BEI images showed the constituent particles more distinguishably and made it possible to use the FBT technique to quantitatively analyse different features of the secondary particles in this system.

A comparison of the important features of the secondary phase particles present in the current and previous[4] lining layers measured via FBT analysis is given in Table 4.7 . Only

Sn particles are common to all three systems and there is a wide variation in their sizes in the three types of lining. The average size of *Sn* particles in the AS20S was found to be finer than that in the AS16 and AS1241 lining. The object angle measured via FBT was along the horizontal (normal to the rolling direction). When the distribution of the object angle of *Sn* particles in the AS20S lining surface was compared with that in the previous AS16 lining, these were found to be mostly aligned at 28^o (an angle along the rolling direction is 90^o) whereas for AS16 these values were mostly 65^o or 27^o indicating a preferred alignment along the rolling direction of relatively coarser *Sn* particles in the systems along the rolling direction. A similar preferred orientation of the *Al* grains of AS16 lining was also observed when the EBSD based grain misorientation angles of all three systems were compared (Figure 4.11). However, both *Sn* particles and *Al* grains in the AS20S lining material did not show any preferred alignment. A similar trend was observed for the intermetallics and *Si* particles in the AS20S lining.

The estimation of clustering of secondary phase particles based upon $COV_{(d)mean}$ calculation showed that the level of random distribution in *Sn* particles was highest in the AS1241 lining compared to that in the AS20S and AS16 lining. The average size of *Si* particles in the AS20S lining was higher than that in the AS1241 lining with approximately similar random distribution. No data for measured features of the intermetallics was available from the previous work for AS1241 and AS16 lining and hence direct comparison with the AS20S lining could not be made. However compared to the *Si* and *Sn* particles present in the AS20S lining, the intermetallic particles had a relatively more uniform distribution and slightly higher object angle.

Most of the *Sn* and *Si* particles were surrounded by *Sn* films in the AS20S lining. The micrograph of the original cast lining material (Figure 4.4(b)) showed an equiaxed *Al* grain structure with *Sn* and other second phase particles distributed along the grain boundaries. These particles reorient themselves and become elongated or broken up during rolling. In addition, the recrystallization of the *Al* grains breaks the regular *Sn* network up and redistributes it as semi reticular particles. The role of *Cu* and *Ni* (work of *J Hogerls*[12]) is to improve the strength of the alloy (by solid solution strengthening) and to form intermetallics of the type $CuAl_2$, $AlNi_3$ and *AlNi*. However up to 1%*Cu* added in the AS20S lining is expected (refer to *Al-Cu* phase diagram in literature review Section 2, Fig 2.1b) to mostly go into solid solution leaving only small amounts to form intermetallics.

Table 4.7: Comparison of various features of different particles measured by FBT for current and previous[4] lining alloys.

Type of particles	Feature	AS20S lining	AS16 lining	AS1241 lining
Sn Particles	Obj Area	27.55±21.85	92±82	40±29
	COV	0.79	0.89	0.72
	Obj Angle	0.65±0.39	0.79±0.41	0.70±0.42
	COV	0.60	0.52	0.59
	Obj AR	1.68±0.41	1.49±0.35	1.48±0.41
	COV	0.24	0.24	0.41
	No of NN	5.5±1.38	5.5±1.47	5.6±1.33
	COV	0.25	0.27	0.24
	Mean NND	30.3±15.32	19±10.6	20.5±8
	COV	0.50	0.56	0.39
Si particles	Obj Area	14.7±14.21	No measurements were made	7.75±6
	COV	0.96		0.77
	Obj Angle	0.64±0.55		0.62±0.38
	COV	0.84		0.61
	Obj AR	1.29±0.27		1.5±0.34
	COV	0.208		0.22
	No of NN	5.52±1.41		5.7±1.45
	COV	0.25		0.25
	Mean NND	43.88±16.48		6.9±2.72
	COV	0.373		0.39
Intermetallics	Obj Area	26.05±16.64	No measurements were made	No measurements were made
	COV	0.64		
	Obj Angle	0.72±0.38		
	COV	0.53		
	Obj AR	1.51±0.42		
	COV	0.28		
	No of NN	5.55±1.25		
	COV	0.22		
	Mean NND	28.88±12.63		
	COV	0.44		

Small amounts of *V* (0.06 % in the AS20S/AS20 lining) are usually added to *Al* alloys for the grain refinement of *Al* matrix and hence to improve the strength by *Hall-Petch* type effects. The EBSD analysis of the *Al* matrix showed that both AS16 and AS20S had comparable grain sizes (with AS20S having slightly larger grain size) while the AS1241 had a coarser *Al* grain structure. Compositional analysis showed that both AS16 and AS20S alloys had 0.25% *Mn* that restricts the recrystallization of *Al* grains during thermomechanical treatments. It was reported[13] that *Mn* forms intermetallics of the type Al_6 *(Fe Mn)* in the form of submicron size dispersoids. These dispersoids retards grain boundary migration and restrict the recrystallization process. In the absence of *Mn* , the recrsytallization effect (taking place during rolling and annealing operations) was evident in the comparatively larger *Al* grain size of the AS1241 lining. Section 6.1 (Chapter 6) will discuss how the alignment of secondary particles may be important with reference to fatigue initiation.

The HVOF coating was designed/expected to distribute very fine *Sn* (at nano scale level) within the *Al* matrix in order to increase the fatigue resistance of the *Al-20Sn-1Cu* alloy. Fine *Sn* particles were observed within splats; however both unmelts (retaining the original dendritic *Sn* distribution[2]) and coarser *Sn* networks (around the unmelts) were also present. Quantitative assessment of the circular unmelt features was carried out for the HVOF spray coated lining which showed that these unmelts were much coarser compared to the secondary phase particles in the RB systems with a wide size range distribution. Apart from these unmelts the microstructure of the HVOF lining showed a large number of scattered pores. Both of these defect populations may affect fatigue behaviour of the spray coated lining.

4.1.4.2.Cu-based lining alloy

The overall microstructure of the *Cu* based system was fairly simple as all the layers studied appeared to be homogeneous in the optical and scanning electron microscope with few secondary particles observed. The major interest lies in the heat treated specimen as the additional interfacial intermetallic layer appeared between the *Sn* and *Ni* overlay layers and grows during annealing.

The thickness and morphology of this layer appeared to change with changing annealing time and temperature. At the same temperature, a rather granular layer appeared for a short time interval of annealing (less then 2 hrs), while a more continuous wavy layer resulted from prolonged annealing. When the temperature was increased, annealing times as short as 12

hrs produced thicker and more continuous interfacial layers. The formation of the initial lumpy layer could be attributed to a rough interface between the joining layers[7].

With the increase in annealing time the diffusion process fills the uneven interface with the intermetallic (Ni_3Sn_4) and subsequent growth results in a more continuous layer. The other effect of the heat treatment process is the formation of a thin *SnO* layer at the surface of the *Sn*. This layer is quite brittle and induces surface roughness to some extent. In the context of fatigue behaviour, the surface layer is always important as any surface inhomogeneities or flaws could result in the initiation of early fatigue damage.

4.2. Mechanical properties

Mechanical properties of various materials were obtained for the bulk materials as well as secondary phase particles observed in the microstructure of various lining alloys. These properties were further used in the fatigue life characterization of bearing components.

4.2.1. Bulk mechanical properties

4.2.1.1.Tensile test properties

Tensile properties of the different layers of all previous (AS16, AS1241) and new (AS20S, AS20, RB168, HVOF) bearing systems were obtained from tensile testing and are shown in Figure 4.26 in the form of true σ-ε curves. The values of σ_t and ε_t are obtained from engineering stress (σ_e) and engineering strain (ε_e) using the relations

$$\sigma_t = \sigma_e(1+ \varepsilon_e) \quad 4\text{-}2$$

$$\varepsilon_t = \ln(1+ \varepsilon_e) \quad 4\text{-}3$$

The summary of tensile test results for each layer is given in Table 4.8. These results also include standard deviation values as tensile tests were performed on 6 specimens from each layer to assess consistency in the data.

AS20S/AS20 monolithic lining layers showed higher values of UTS and 0.2% proof stress than the AS1241 monolithic. However, RB168 lining (bronze lining) showed highest values of tensile properties. Monolithic brazed sheet (3003+4343 layers) showed higher tensile properties than the monolithic *Al* layer. These are used as interlayers for the AS20S and AS20 bearing and flat bar systems respectively.

Table 4.8: Tensile test results for different materials. Data for AS1241 and AS16 systems was obtained from previous work[4].

Material System		Yield point (MPa)	0.2% proof (MPa)	UTS (MPa)	%Elongation
Monolithic Lining layers	AS20S (6 tests)	66±4	79±4	166±5	28±2
	AS20 (6 tests)	65±3	75±6	165±3	30±1
	RB168 (6 tests)	298±13	305±11	360±10	25±4
	AS1241	58±5	72±10	178 ±12	30±2
Monolithic interlayers	Al foil (6 tests)	38±6	44±5	78±7	35±2
	Brazed sheet (6 tests)	47±6	55±4	106±5	30±3
Steel layers	AS20S (6 tests)	470±4	476±8	512±10	14±1
	AS20 (6 tests)	475±7	478±9	504±7	14±2
	AS16	521±19	535±17	678±18	14±3
	AS1241	330±12	344±11	418±21	15±3
	HVOF (3 tests)	205±4	209 ±7	326 ±12	15±2

The AS16 flat bar steel showed higher UTS and proof stress values[4] than AS20S/AS20 flat bar steel layers. The HVOF spray coated steel layer showed the lowest tensile properties if compared with all other RB flat bar steel layers.

The true σ-ε data illustrate the deformation behaviour of each layer in tension and were subsequently used to evaluate the stress and strains developed at the lining surface of the bearings in a three point bend test under different loads using finite element analysis. The tensile properties are dependent upon the amount of deformation brought about during metal working (rolling in the case of the bearing systems). The tensile properties of the monolithic lining, inter and steel layers are expected to be slightly lower than the actual layers present in the bearings, as the latter have been subjected to more deformation during the final stage of bearing manufacturing operation and hence more work hardening is expected.

4.2.1.2.Vickers microhardness test results

A material's elasto-plastic response is most simply evaluated by a uni-axial tensile test performed upon standard tensile test specimens. The current work is related to the evaluation of fatigue performance of a number of multilayered systems for which knowledge of the elasto-plastic response of each layer is needed. However the availability of individual monolithic layers in each system was limited and hence the tensile properties of all materials were not always possible to obtain directly from a tensile test. Moreover, the uni-axial tensile properties of each layer derived from a tensile test may not truly reflect the properties of these layers present within a finished bearing as the latter have gone through a further number of rolling stages prior to finishing. It has been reported[14] that a material's response to micro-indentation could also be used to establish its mechanical properties. This was based upon empirical relations between hardness number and yield stresses which were only true for specific materials.

Variation in the indent sizes under different applied loads was measured and the data was obtained for all layers in the flat bar and finished bearings as well as the monolithic lining and interlayers.

Figure 4.27 shows the variation of the indent size with different load values for all layers from finished bearings and flat bars as well as the monolithic lining from AS20S, AS20, RB168 *Al* foil and brazed sheet (3003+4343 alloy). The data was obtained from the LT plane of all the systems. The lining layers in all these systems seemed to be harder than the interlayers, but the brazed sheet (3003+4343alloys) used as the interlayer in the AS20 system appeared to be closer in resistance to plastic flow (on the basis of load versus indentation size curve shown in Figure 4.27) to that of the AS20S lining. The values of indent sizes against various load values reported in Figure 4.27 for *Al* foil and alloyed foil were obtained by performing the microhardness test on the monolithic layers as the interlayers present in flat bars and finished bearings were too thin (0.03-0.04mm) to give accurate indent sizes especially at higher loads. An attempt was made to get individual data for each of the 3003 and 4343 alloys present in the alloyed foil. As the thickness of 4343 clad alloy was approximately 120µm (as shown in the micrograph in Figure 4.2 (c)) indents free from external constraints could not be made for loads higher than 300g. A careful observation of Figure 4.27 however shows that there is larger scatter in the measured values of the diagonal for loads smaller than 50 g. This is because of

elastic recovery effects becoming significant at lower loads as well as the errors in locating the actual edges of the indentation[15].

For the RB168 systems, it was not possible to get such data for the top *Sn* and *Ni* layers as these were too thin (5-10µm thickness) to be indented by the microhardness indentor. However, the RB168 heat treated *Ni*- bronze lining appeared to be the hardest of all the linings as its load vs. indent diagonal curve is very close to the AS1241 steel curve.

The AS20S and AS20 bearing steel layers show a very similar trend in load vs. indent size curves. The AS16 steel appears to be slightly harder than the AS20S/AS20 steels. The curve for the HVOF steel shows significantly softer behaviour compared to all the RB steels. Measured values of microhardness numbers for different layers are given in Table 4.9.

Table 4.9: Microhardness test results for various materials measured at a load of 50g.

Material Designation	Flat bars			Finished bearings		
	Lining layer	Interlayer	Steel layer	Lining layer	Inter-layer	Steel layer
AS20S	57±8	39±3	182±16	60±3	40±3	190±16
AS20	59±9	47±1	193±16	59±4	43±1	192±14
HVOF spray coated	49±2	N.A	112±3	N.A	N.A	N.A
AS16 (By MM)	43±3	34±6	176±9	48±3	34±6	196±9
AS1241 (By MM)	54±3	35±5	168±11	55±8	35±6	178±11
RB168 (NHT)	N.A	N.A	N.A	158±6	N.A	189±14
RB168 (HT)	N.A	N.A	N.A	161±7	N.A	201±6

4.2.2. Nano-hardness indentation

4.2.2.1.Bulk layer hardness

Results obtained from nano-indentation of the AS20S and AS20 bearing cross-section were in the form of hardness number H_n (load per unit projected area) and the modulus

of elasticity, *E*. Figure 4.28 (a) and (b) shows the location of nanoindents travelling across the lining thickness of AS20S and AS20 bearing towards the backing steel layer with the corresponding H_n and *E* values. A general observation from these results is that the hardness trend in the lining, interlayer and steel backing layer is consistent with the micro hardness test results. Table 4.10 shows the nano-hardness values in *GPa* along with corresponding *E* values. As the interlayer of AS20 consists of 4343 and 3003 layers, where the 4343 is expected to be adjacent to the steel layer, one indent made close to the steel layer showed a significantly lower hardness value compared to the hardness value obtained from a neighbouring indent, also within the interlayer. This is in agreement with the microhardness test results in which the 4343 layer of the monolithic layer seems to be softer than the adjacent 3003 layer. However, a large number of indents are required to confirm this at the same locations which is difficult as one cannot directly view the specimen surface whilst setting the current nanohardness testing machine. The nanohardness values of the HVOF lining are slightly lower than that of AS20S lining with a considerable scatter. The lining layer of the RB168 systems showed higher values of H_n and *E* compared to all *Al* based lining alloys.

The *E* values show a large scatter which is attributed to the displacement noise of the machine which is approximately 3-4 nm. The elastic recovery (strain recovered during unloading) in *Al* and its alloys is very small compared to the plastic depth and is given as the elastic recovery parameter[17]

$$ERP=(h_c- h_f)/h_c \times 100 \qquad 4\text{-}4$$

where h_c and h_f are the maximum and plastic depths. If the amount of noise is incorporated then the error in the slope *S* of the linear portion of the loading unloading curve increases (Fig 3.10, Chapter 3) which leads to a large scatter. If however the corresponding scatter is considered *E* values are within the range of expected values for *Al* and *Al* alloys[16].

In order to check the validity of nano-hardness test results, a comparison between the micro and nano-hardness test results was made. The microhardness numbers are obtained from the following relation

$$H_v = 1.854\frac{F}{d^2} \qquad 4\text{-}5$$

where *F* = load in kgf

d = arithmetic mean of two diagonals

The microhardness test results were therefore converted to *GPa* values by dividing the projected area by the corresponding force in *N*. Table 4.10 also gives a comparison of the results obtained from micro and nano-hardness test. It is evident that the microhardness values are approximately 30% lower than the corresponding nanohardness values. The reason for this discrepancy seems to be the use of contact area for the measurement of nanohardness values instead of the area of the residual hardness impression as used for the microhardness values. The pile up of the material around the contact impression is not accounted for hence the apparent contact area increases[17]. This pile up is very common in elastio-plastic materials (material used here is highly elasto-plastic). Hence, both the hardness and modulus values (obtained from nanohardness testing) are overestimated. The areas of the actual nanoindents were also measured optically and the hardness values based on that area are shown in Table 4.10. These hardness values are lower than the corresponding hardness values obtained from the machine (on the basis of the contact area) which verifies the above argument. A significant difference still remains however between the micro and optically measured nanohardness values which might have arisen due to the shape and calibration effects of the microhardness indenter.

The machine measured E_r values are related to S (the slope of linear portion of loading unloading curve in Figure 3.10) and A (the contact area of the indenter and the targeted material)

$$E_r = \frac{\sqrt{\pi} S}{2A} \qquad 4\text{-}6$$

Using data from the machine, S was worked out and used along with the optically measured A in the above equation to calculate the values of E_r for all layers in the AS20S and AS20 bearings. The optically measured E_r values are lower than the machine measured values but still a large scatter exists.

Although the nanohardness test on the bulk layer did not provide any additional information apart from the modulus of elasticity, its main use was to enable the hardness and elasto-plastic properties of the second phase particles such as *Sn* and intermetallics in the AS20S/AS20 type systems to be estimated. The data for such particles is helpful in assessing their mechanical properties and can be subsequently used in FE modelling to calculate the stresses and strains on these particles within the matrix under the applied loads during initiation and growth of cracks.

Table 4.10: Nano-indentation test results. The unit of all measured values are GPa

Systems	Quantity measured	Lining layer	Interlayer	Backing layer
AS20S bearing	H_v	0.60±0.06	0.41±0.04	1.8±0.4
	H_n (Machine)	0.98±0.13	0.73±0.08	2.5±0.98
	H_n (Optical indent area)	0.74±0.40	0.62±0.09	2.01±0.34
	E_r (Machine)	95.5±21.21	0.53±13.19	187±43
	E_r (Optical indent area)	87.5±20.20	0.59±15.23	177±48
AS20 bearing	H_v	0.63±0.08	0.44±0.06	2.01±0.09
	H_n (Machine)	1.07±0.17	0.98±0.09	2.74±0.94
	H_n (Optical indent area)	0.78±0.09	0.69±0.05	2.3±0.32
	E_r (Machine)	105±14	104±19	172±65
	E_r (Optical indent area)	94.5±24	92.57±17	165±51
RB168 (HT) bearing	H_v	1.79±.2	N.A	1.49±0.5
	H_n (Machine)	4.6±0.97	N.A	2.5±0.9
	H_n (Optical indent area)	3.1±0.43	N.A	1.98±0.34
	E_r (Machine)	188±21	N.A	185±58
	E_r (Optical indent area)	165±23	N.A	176±55
RB1678 (NHT) Bearing	H_v	1.76±.2	N.A	1.84±0.75
	H_n (Machine)	4.1±0.96	N.A	2.8±0.9
	H_n (Optical indent area)	3.1±0.47	N.A	1.98±0.34
	E_r (Machine)	198±21	N.A	184±59
	E_r (Optical indent area)	165±23	N.A	179±55
HVOF Flat bar	H_v	0.60±0.13	N.A	1.2±0.72
	H_n (Machine)	1.08±0.3	N.A	2.8±0.9
	H_n (Optical indent area)	0.87±0.36	N.A	1.98±0.34
	E_r (Machine)	88±13	N.A	104±59
	E_r (Optical indent area)	71±16	N.A	100±34

4.2.2.2.Nano-hardness results for secondary phase particles

For the AS20S lining the sparse distribution of the secondary phase particles was a major hurdle in obtaining successful indentation with the nano-indenter. However, the nano-hardness values reported in Table 4.11 were obtained as a result of sporadic indenting of these particles during systematic bombing raids in the nano-hardness studying. Some of these targeted particles are shown in Figure 4.29.

A large scatter was observed in the measured H_n and E values which indicate the effect of a number of factors which will be discussed under Section 4.2.3. The reported values are based upon the optically measured indent area for consistency with the previous results. It is evident that the intermetallics and *Si* are the hardest particles in the AS20S and AS1241 type linings. For the AS20S systems, the reported values for the *Si* and *Sn* particles were obtained from a few indentations as these particles were quite rare and their chances of encountering the indenter were too low.

Hence their reliability may be questionable where true mechanical behaviour is required, but these results allow a qualitative comparison of the secondary phases. It is also evident that the intermetallics observed in the RB168 system (Ni_2Sn_3) were softer than those observed in the AS20S lining i.e. $AlNi_3$. As the intermetallics in the AS20S lining were mostly encapsulated by *Sn* phase this may have resulted in a large scatter observed in the results. The *Sn* overlay layer in the RB168 systems was found to be softer than the *Sn* particles in the AS20S lining.

In the HVOF systems, the unmelt regions showed lower values of both H_n and E_r compared to those obtained for the matrix. The circular unmelts have a different microstructure from the matrix comprising the dendrite structure of the original powder particles.

Table 4.11: Nanohardness results for various particles. The unit of all measured values are GPa

Lining	Sn		Si		Intermetallics (Unmelts for HVOF)	
	H_n	E	H_n	E	H_n	E
AS1241	0.98±0.3	74±19	2.1±0.43	104±34	2.1±0.32	120±43
AS20S	0.93±0.5	78±26	2.5±.1.2	109±41	2.4±0.6	117±25
RB168	0.48±0.21	54 ±12	N.A	N.A	0.81 ±0.11	51 ±15
HVOF	N.A	N.A	N.A	N.A	0.74±0.3	68±17

4.2.3. Discussion-mechanical properties

4.2.3.1.Residual stresses in multilayered systems

The multilayered systems comprise layers of metals with dissimilar thermal expansion coefficients, hence on cooling these may develop residual elastic stresses in the

component due to differential contraction. Thermal expansion coefficients for medium carbon steel and aluminium are 12×10^{-6} and 23×10^{-6} $^{o}C^{-1}$ respectively[16]. In the bi-layer flat bar with *Al* alloy and steel as the lining and backing layers respectively, cooling from a temperature of 300^{o}C (a possible annealing temperature) results in greater contraction in the *Al* layer than in the backing steel layer. As the thicker steel layer provides constraint to the *Al* layer, the restrained thermal contraction in the *Al* layer results in residual tensile stresses of approximately 10-15 MPa. These values are approximately 15% of the yield stress of the *Al* lining alloy. All fatigue tests are carried out at loads where the *Al* lining undergoes significant plastic deformation and these residual stresses are expected to have a minimal role in affecting the overall failure process. Flat bars when formed into the final bearing shape and then broached may also result in residual stresses, which cannot be easily estimated, however the highly plastic conditions under which the bearing linings are tested are also likely to minimize the effect of any such residual stresses. However any effect of residual stresses must be considered in fatigue estimations and hence experimental strain measurements have been compared with FE estimates as detailed in Section 5.1.5 to account for this.

4.2.3.2.Bulk layer properties

The lining layer of the currently developed AS20S/AS20 systems showed increased values of microhardness and tensile properties compared to the previous AS1241 and AS16 linings. The mechanical properties are sensitive to the microstructure which is very much linked to the composition of the alloy as well as external treatments such as rolling and heat treatment. All current and previous RB systems have been manufactured by similar rolling treatments and the improved mechanical properties of the current systems may be linked to the strengthening due to the presence of *Cu* and *Ni* (solid solution strengthening due to *Cu* and formation of hard intermetallics due to *Ni*) in the current systems. The steel layers for all current and previous RB systems covered a wide specifications range (varying in tensile properties) and this may have resulted in the obvious differences in their tensile test properties observed (e.g. high UTS values of AS16 steels compared to the AS20S steel). In addition variation in the external parameters (i.e. pressure or temperature) during rolling operations (may lead to different amounts of work hardening or annealing during intermediate heat treatments. As detailed information about the rolling and intermediate heat treatment parameters was not available for these systems (due to the proprietary nature of the manufacturing process), therefore further elucidation of the cause of these variations is

difficult. Nonetheless, the importance of establishing the steel backing's mechanical properties has been confirmed by the FE based sensitivity studies discussed in Chapter 5. The final bearing forming operations may also induce work hardening effects and hence the elasto-plastic response of each layer as derived from the flat bar steel and monolithic lining layer may not truly reflect the elasto-plastic response of these layers in the finished bearings. However the relatively small difference in microhardness values of the layers of the finished bearings and the flat bars gives reasonable confidence in using the tensile test data of monolithic lining and flat bar steels during subsequent modelling of the bearing specimens in the 3-point bend fatigue test.

The nanohardness values also confirmed the hardness trend observed in the microhardness values, where the interlayer of AS20S appeared softer than that of the AS20 bearing. The nano indentation within the interlayer was much less affected by constraint effects from the lining and interlayer than the microhardness. The nano hardness test also provided values of the elastic modulus derived from the linear portion of the load versus indent depth curve. A large scatter was observed (compared with expected values) which might be due to the effect of variations in the elastic recoveries as a result of interaction with second phase particles below the surface or due to displacement resolution issues where noise in the displacement measurement can significantly affect the calculated values. The other factor that might have resulted in large scatter is the use of a smaller indentation depth (360nm) for the AS20S lining to avoid interaction of the indenter with any secondary phase particle. Another factor is the size dependent plastic flow behaviour of material at sub-micron level. Microhardness values could increase by a factor of 2-3 if the indentation depth is decreased[18]. This is due to a phenomenon called strain gradient plasticity in which apparent increase in flow stress is attributed to strain gradients accompanied by geometrically necessary dislocations at a density comparable to statistically stored dislocations. These dislocations resist plastic flow at lower indent depths, however at larger indent depths their effect is minimized. Experiments[19] have shown that more consistency in the data could be achieved (for *Al* alloys) for indentation depths greater than 400nm to avoid strain gradient plasticity effects.

4.2.3.3.Properties of secondary phase particles

Both microhardness and tensile testing gave bulk properties of individual layers in each system. However, the fatigue damage occurring at a microscale level in a multiphase material is likely to be sensitive to the mismatch in the mechanical properties of secondary

particles and the matrix. As the microhardness test could not measure the hardness of individual features within the lining layers, the nanohardness or instrumented hardness testing appeared to be the most appropriate choice as much smaller areas in the range of tens-hundreds of nm^2 (and hence secondary particles with areas 8-90 μm^2) could be targeted with loads up to 500mN. However the difficulty of positioning the specimen surface to measure the hardness of a desired region was an obstacle to the easy use of the machine. The targeting of the second phase particles by the nano indenter was based upon a bombing raid approach where indents were set up at specific spacing with the aim that a particle would be sampled. The results obtained for the secondary phase regions in all these systems helps in understanding their mechanical behaviour in terms of nano-hardness values as well as modulus of elasticity. These properties could be further used in explaining the stresses and strains developed in such microstructures under applied loads using any suitable finite or boundary element method.

The secondary phase regions observed were not purely separate entities rather most appeared as mixtures or one phase encapsulating the other. The exact targeting of these secondary regions was challenging; however some of the targeted *Sn*, *Si* and intermetallic particles showed a large scatter in the measured values of H_n and E. The main issues to be considered in obtaining more reliable data are (i) Is the indenter tip lying perfectly within the particle? (ii) What type of constraints are present underneath the particle? The ideal situation is one in which an individual particle indented has enough area to be targeted and the material in its surroundings and underneath is not much different in terms of compliance from the particle. A schematic of this situation is shown in Figure 4.30. In the case of a hard intermetallic or *Si* particle embedded in a soft *Al* matrix, there are possibilities of sinking the particle to some extent into the matrix resulting in an additional measurement *depth of the indent* which affects the calculated hardness value. This means that the reported nano-hardness values of the intermetallics or *Si* particles could be an underestimation. The converse is also true when a soft *Sn* particle is considered to be surrounded by harder matrix (in the AS20S lining for example). In that case, the particle may be considered as fully constrained and the expected hardness value is higher than one obtained from a continuous soft *Sn* layer. This hypothesis is strengthened if the reported values of H_n for *Sn* particles in the AS20S and *Sn* layer in the RB168 system are compared (Table 4.11). The hardness values of the *Sn* layer obtained from the AS20S and AS1241 lining (more constrained) was approximately 40% more than that measured from the continuous layer of *Sn* in the RB168 system with less scatter.

Apart from these issues there could be some other factors affecting the hardness results. The most important one, which is more likely to be prevalent in a heterogeneous microstructure such as the AS20S lining, is the uncertainty regarding the location of different secondary phase particles underneath the targeted particle. Encountering such particles could affect the results if they have a significant mismatch in compliance with the targeted particle.

Despite all these limitations, the results obtained for the secondary phase regions give a good estimate of the mechanical properties relative to the bulk material which have been used in the subsequent finite element modelling of particles to assess stresses and strains under applied fatigue loads.

4.3. Summary

All the characterization results obtained are summarized below:

- The AS20S/AS20 lining consists of widely scattered $AlNi_3$ type intermetallics with finer and fewer *Sn* and *Si* particles with a wide distribution of particle sizes. This lining was harder than AS1241, AS16 and HVOF type linings. Nano-hardness tests showed that intemetallic particles in the AS20S lining were harder and stiffer (on the basis of measured H_n and E values) than *Sn* (in all RB systems).
- The HVOF lining microstructure showed widely scattered circular unmelts which were softer than the matrix (nano-indentation results). The bulk hardness of the HVOF lining was comparable to the AS1241 lining alloy.
- The RB168 Ni-bronze lining appeared to be a continuous phase under the optical and scanning electron microscope. *Sn* and *Ni* layers were clearly distinguishable under the optical microscope. The interfacial intermetallic compound between the *Sn-Ni* layers was found to be harder than the *Sn* but softer than the intermetallic compound observed in the AS20S lining.
- These systems have various layers of different meso-scale properties as well as comprising secondary phase particles of widely varying mechanical properties which may affect microscale fatigue damage initiation. The variation of the mesoscale layer's mechanical properties may well have implications for crack propagation behaviour.

References:

[1] Dana Glacier Vandevell Bearing, Rugby, Warwickshire, UK (private communication) 2004.

[2] Harris, S.J. McCartney, D.G. Horlock, A.J. and Perrin, C. (2000) Mat. Sc. Forum 331, 519.

[3] Gordon England, Independent metallurgist and consultant to the Thermal Spray Coating industry (www.gordonengland.co.uk) 2004.

[4] Mwanza, M. (2004). PhD Thesis, School of Engineering Sciences, University of Southampton.

[5] Mackenzie, J.K (1958). Biomatrica 55, 229.

[6] Yang, N. Boselli, J. Gregson, P.J and Sinclair, I. (1999) J. Microscopy 195, 104.

[7] Mita, M. Kajihara, M. and Krukawa, N. (2005). Mat. Sc. Eng A403, 269.

[8] Wanger, C. (1969). Acta. Metall. 17, 99.

[9] He, M. Kumar, A. Yeo, P.T. and Qi, G.J. (2004). Thin. Solid. Films 462, 387.

[10] Butts, A. (1970). Copper , The Science and Technology of the Metal, its Alloys and Compunds. Hafner. Pubs. Company, USA, 484.

[11] Robert J. R, (1952). Non-Ferous Physical Metallurgy. Pitman. Pubs. Corp, New York, 127.

[12] Hogerls, J. Spaic, S H. (1998). Aluminium 74 (Jahrgang 10), 780.

[13] Polmear, I.J. Light Alloys—the Metallurgy of Llight Metals, R.W.K Honeycomb and P. Hancock, Eds, Pubs. Arnold, 338.

[14] Tabor D. (1951).The Hardness of Metals, London, Oxford at the Clarendon press.

[15] Dieter, G. E. (1988). Mechanical Metallurgy, McGraw-Hill Book Company, 334.

[16] Callister, W. D. (1997). Materials Science and Engineering, 4th Edition, John Wiley and Sons., New York.

[17] Oliver, W.C. (2004). J. Mater. Res 19, 9.

[18] Nix, W. D. (1989). Mater. Trasc. 20A, 2217.

[19] Huang, Qu, Y. S. Hwang, K.C. Li, M. Gao, H. (2004), Int. J. Plasticity, 20, 753.

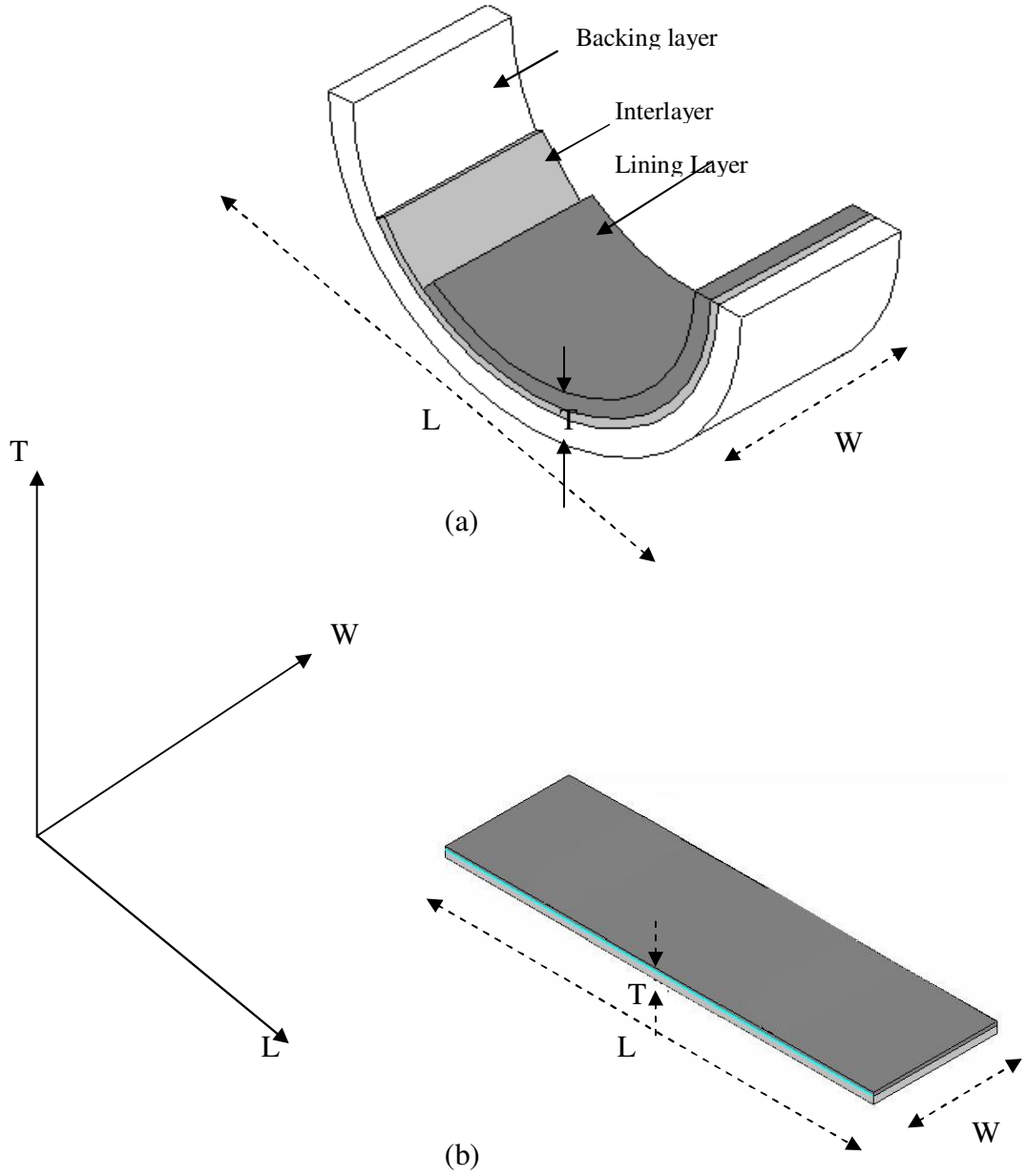

Figure 4.1: Schematics of various surfaces of (a) bearing (b) flat bar specimens subjected to microstructural analysis.

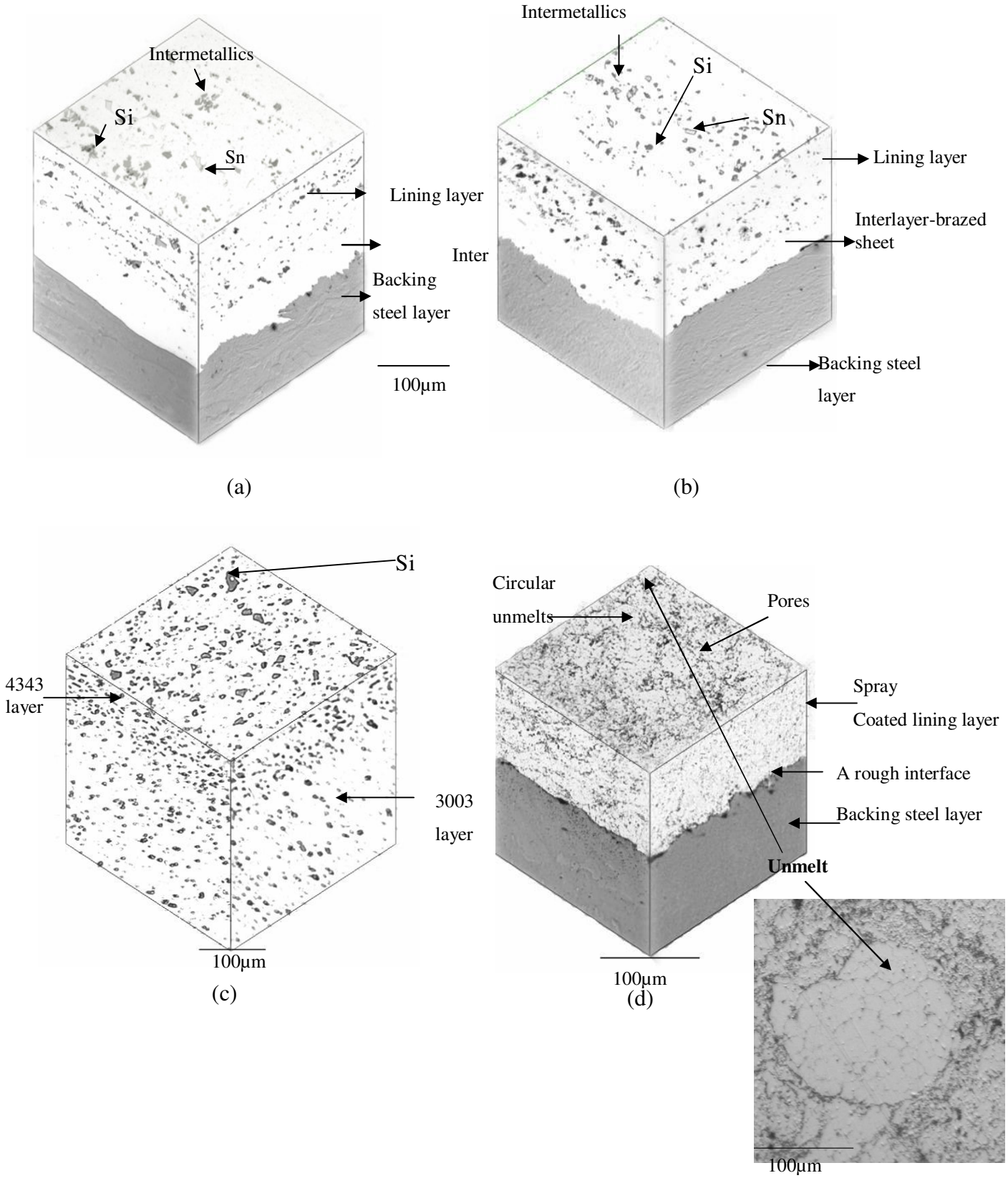

Figure 4.2: Three dimensional optical micrographs of *Al* based systems: (a) AS20S bearing (b) AS20 bearing (c) monolithic brazed sheet and (d) HVOF specimens.

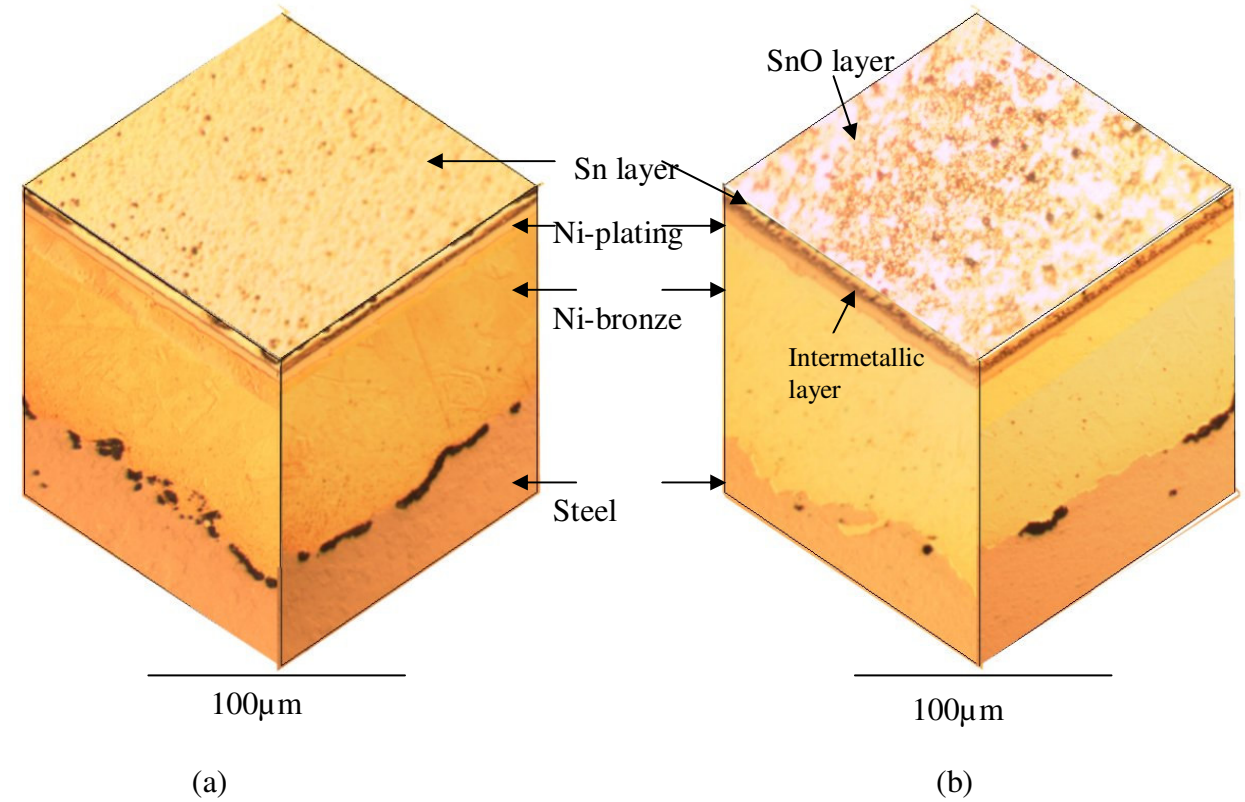

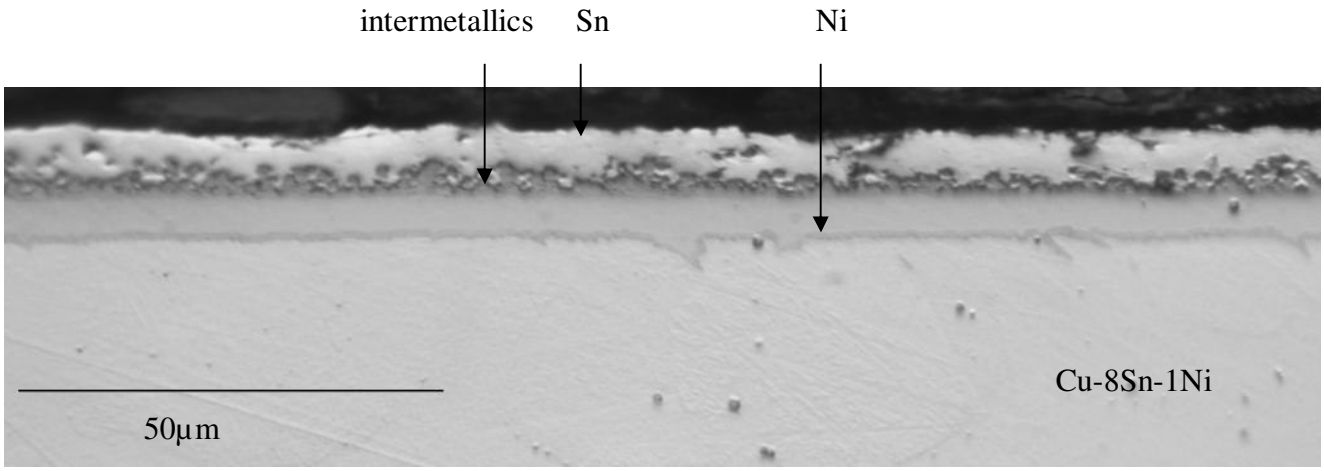

(c)

Figure 4.3: Three dimensional optical micrographs of *Cu* based bearing systems (a) RB168 non-heat treated (b) RB168 heat treated bearing specimens (c) An optical image of the HT specimen showing top layers.

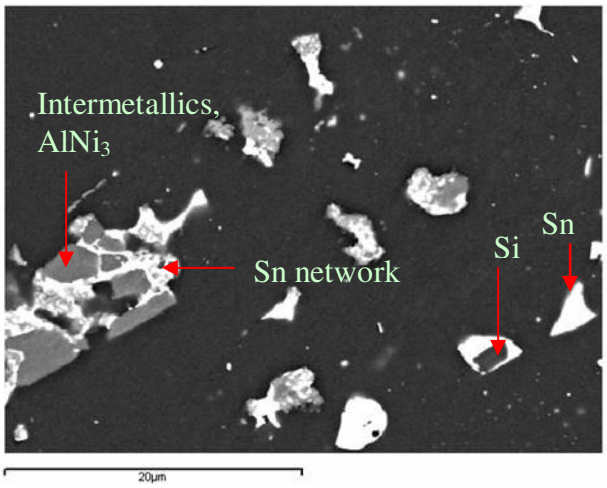

(a)

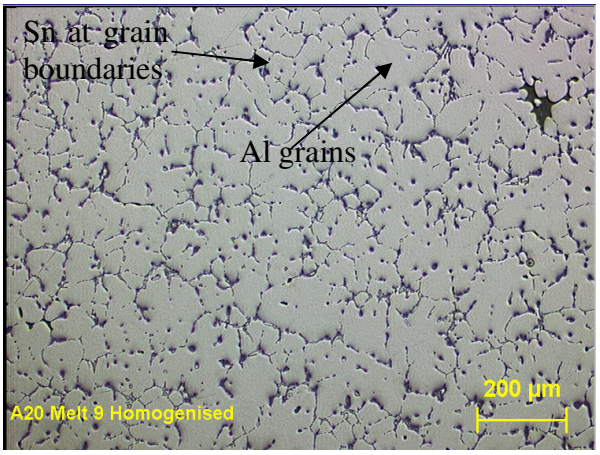

(b)

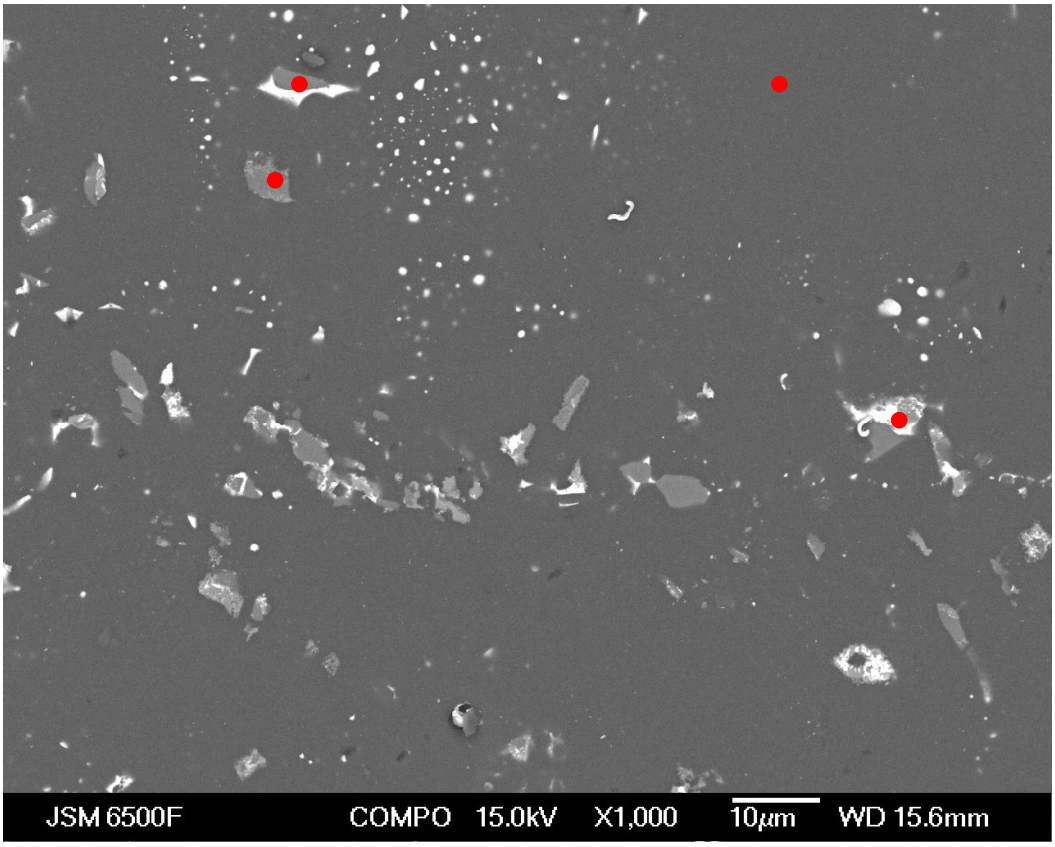

(c)

Figure 4.4: AS20S lining (a) SEM image of AS20S/AS20 bearing lining (b) AS20S lining showing as cast structure (Courtesy DGV). (c) BEI image of the AS20S lining showing various EDX spots on different regions.

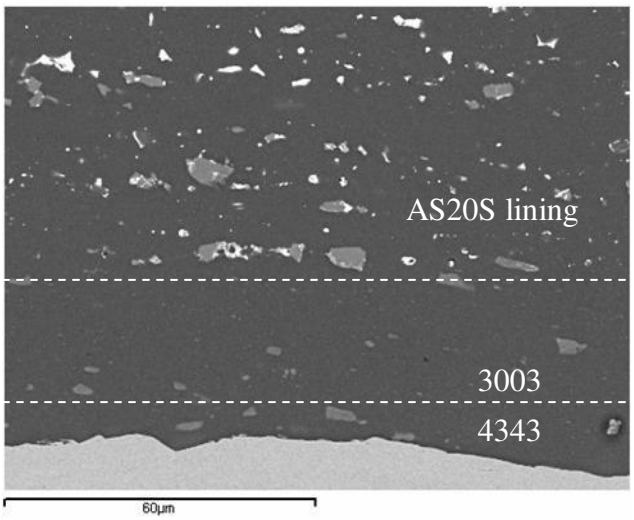

(a) SEM image of interface

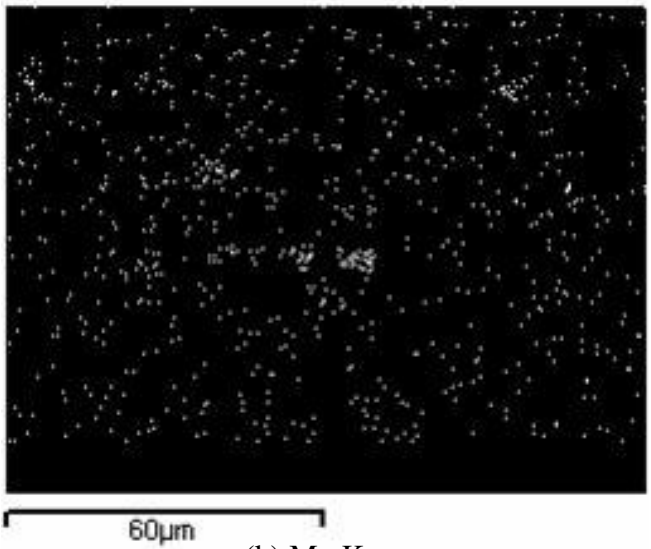

(b) Mn Kα

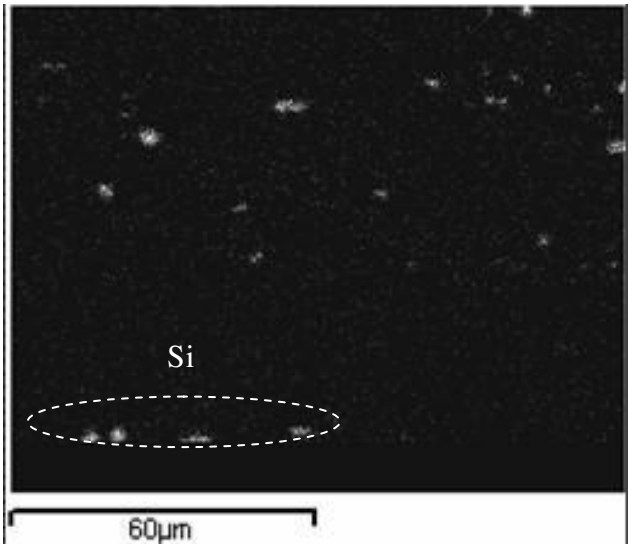

(c) Si Kα

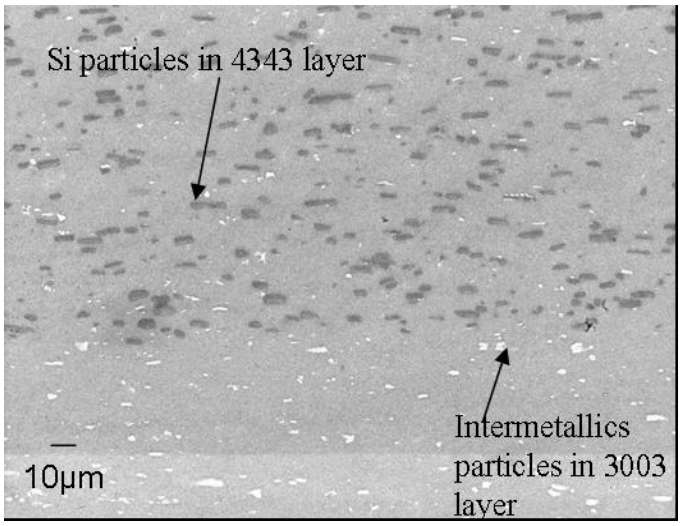

(d)

Figure 4.5: (a-c) Results of the EDX smart area mapping of AS20 bearing interlayer. The white regions in each image shows abundance of the element mentioned below the image. (d) BEI image of the original monolithic brazed sheet.

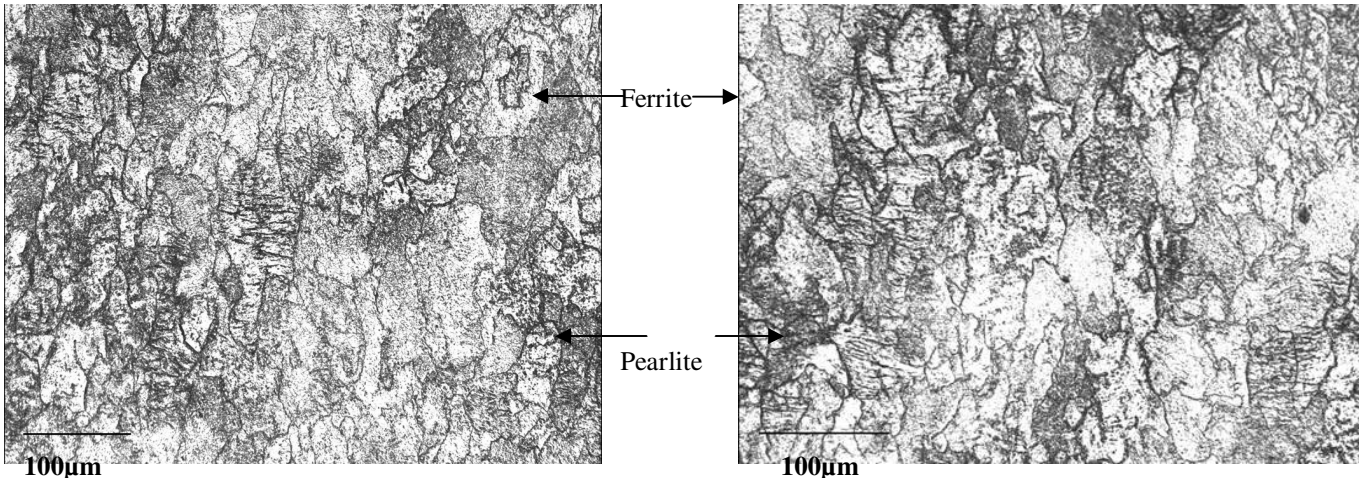

(a) (b)

Figure 4.6: Backing steel layers of the (a) AS20S and (b) AS20 systems.

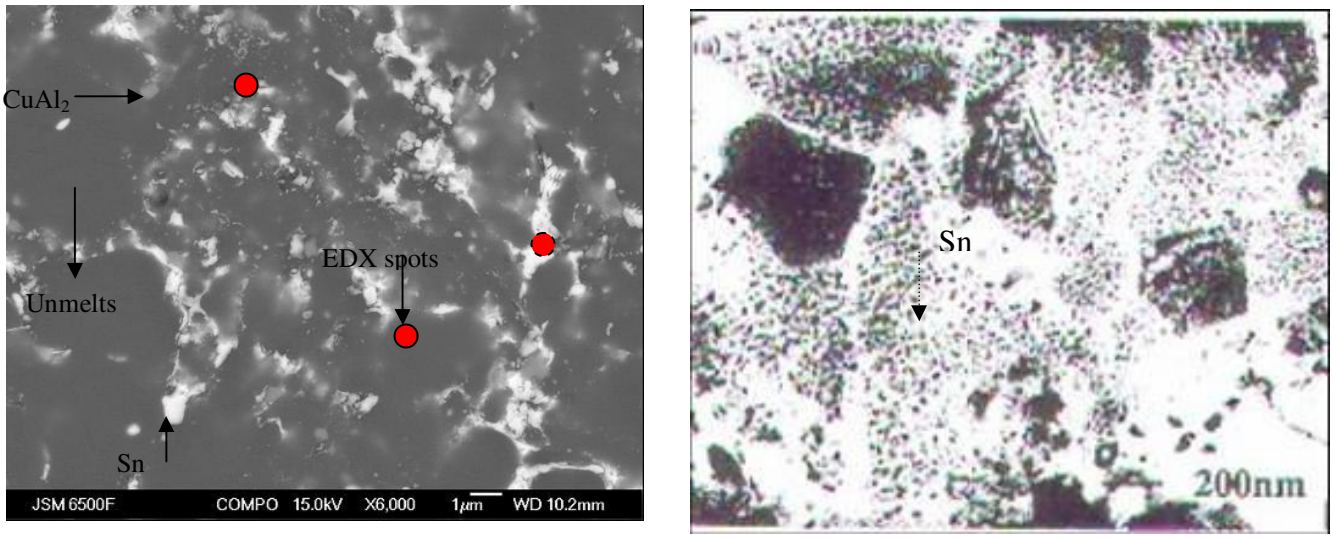

(a) (b)

Figure 4.7: Microstructure of the HVOF lining (a) BEI image of the lining surface (b) TEM image after[2]

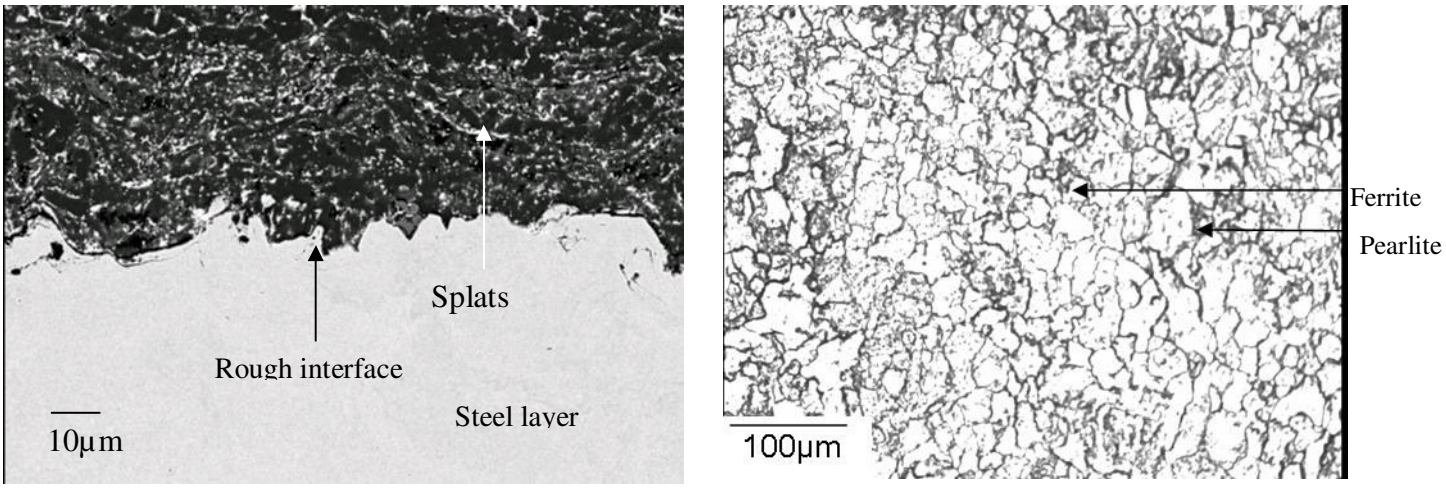

(a) (b)

Figure 4.8:(a) BEI image of the interface between the lining and the backing steel layer (b) Optical image of the backing steel layer of the HVOF system.

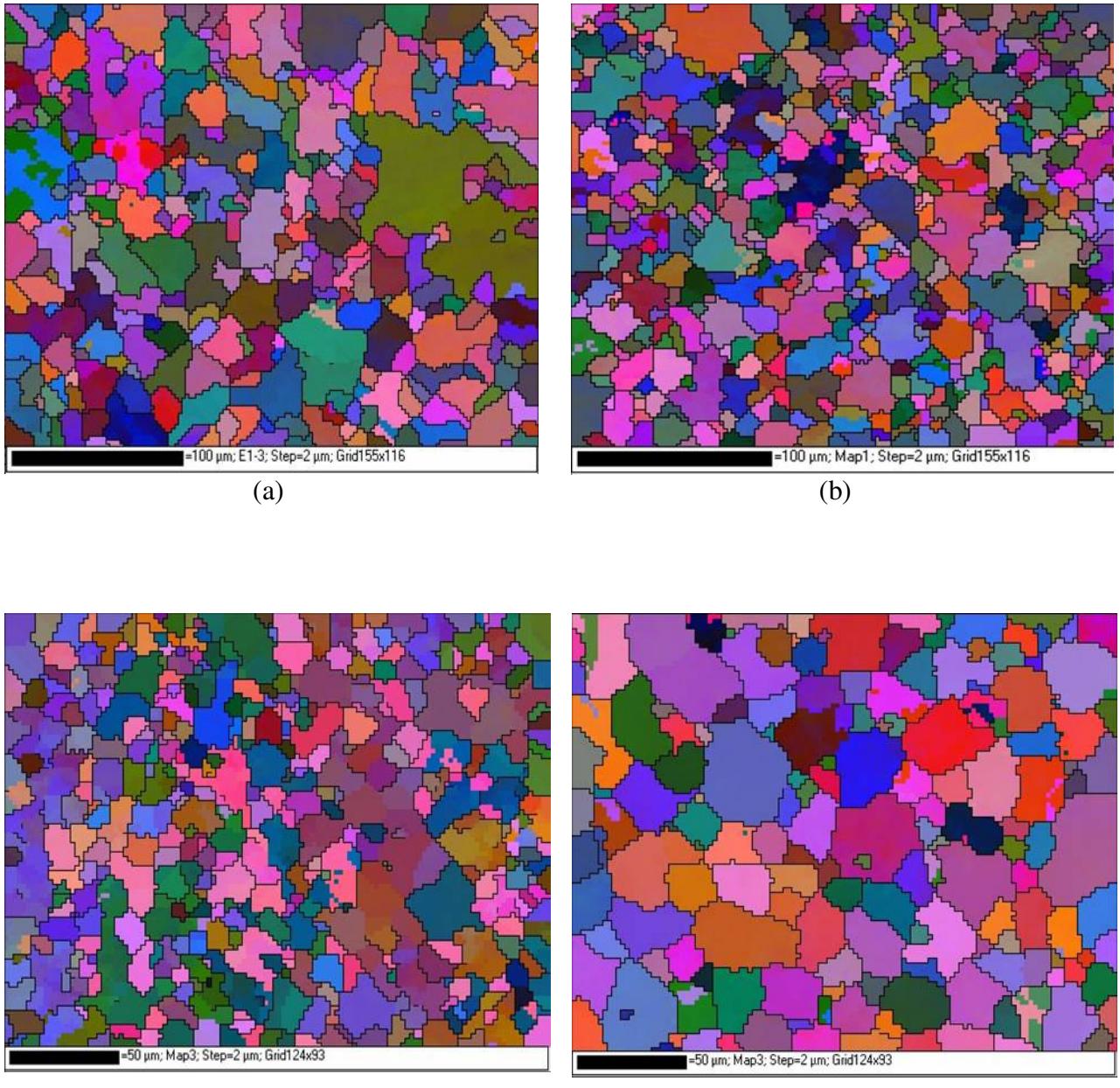

(a) (b)

(c) (d)

Figure 4.9: EBSD map of the *Al* matrix of the LW plane of RB systems linings (a) AS20S (b) AS20 (c) AS16 (d) AS1241[4] systems.

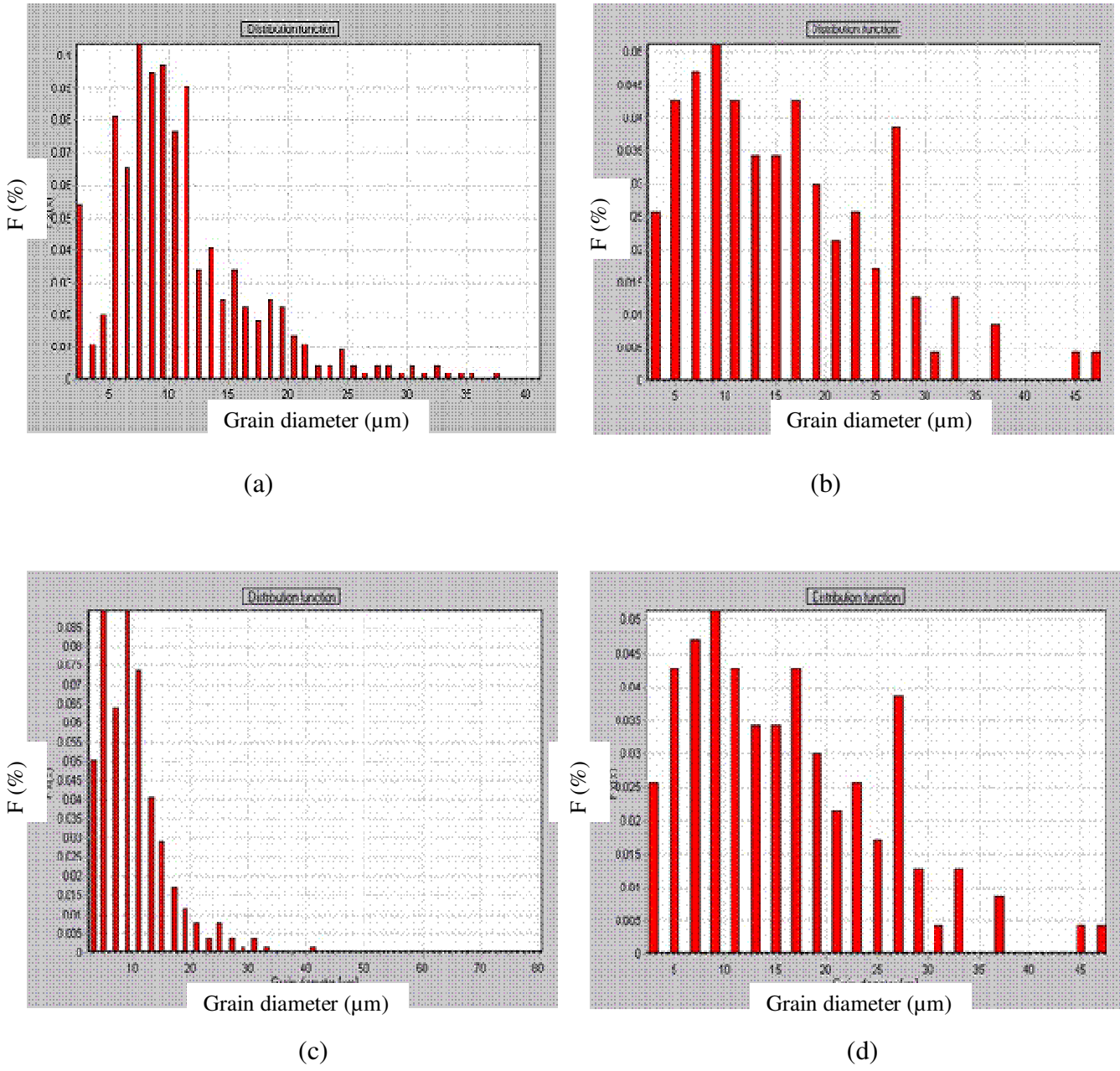

Figure 4.10: Distribution of grain size in the LW plane of the lining surface of (a) AS20S (b) AS20 (c) AS16 (d) AS1241[4] bearings.

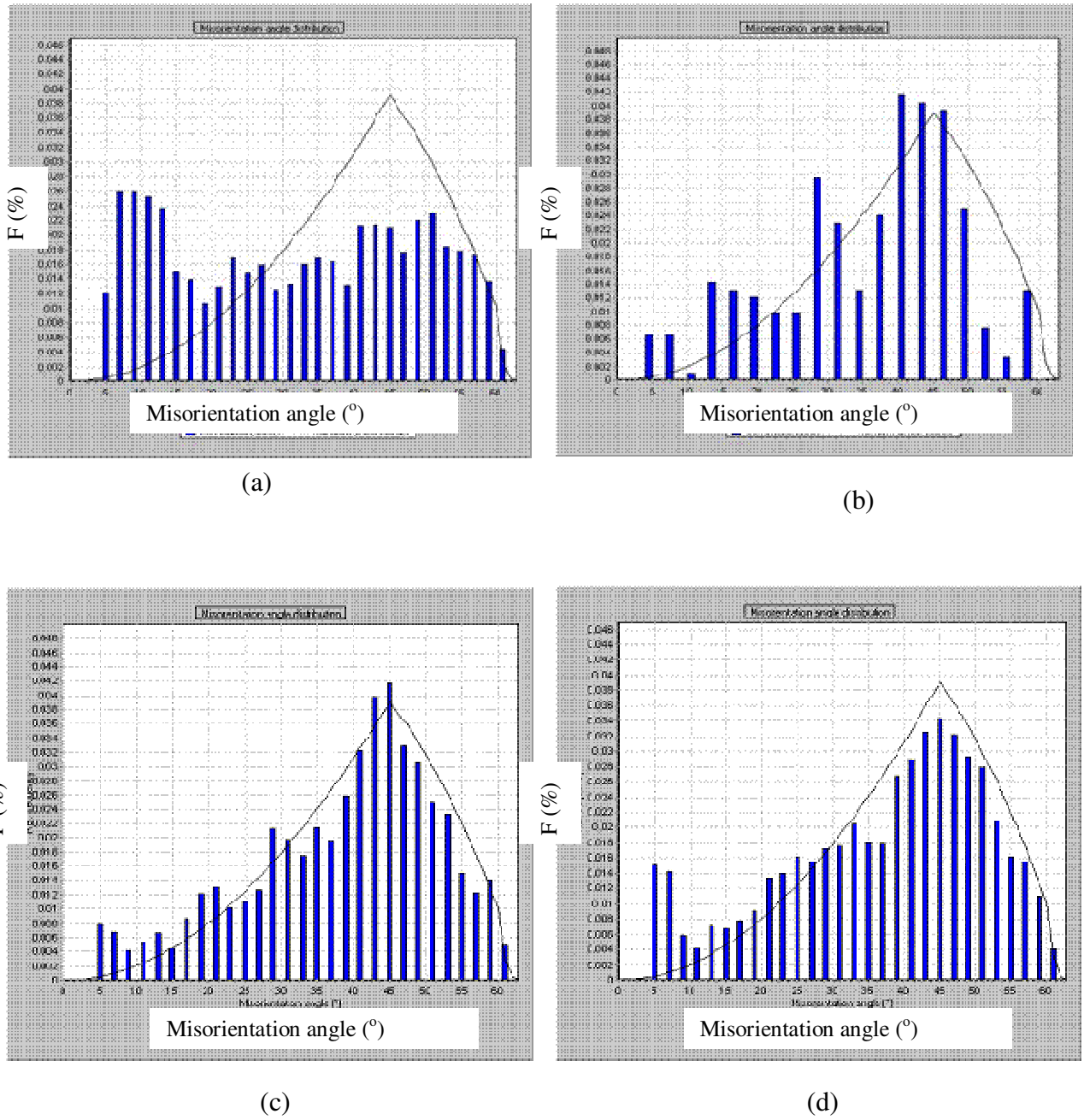

Figure 4.11: Distribution of misorientation angle in the LW plane of the lining surface of (a) AS16 (b) AS1241[4] (c) AS20S (d) AS20 bearings.

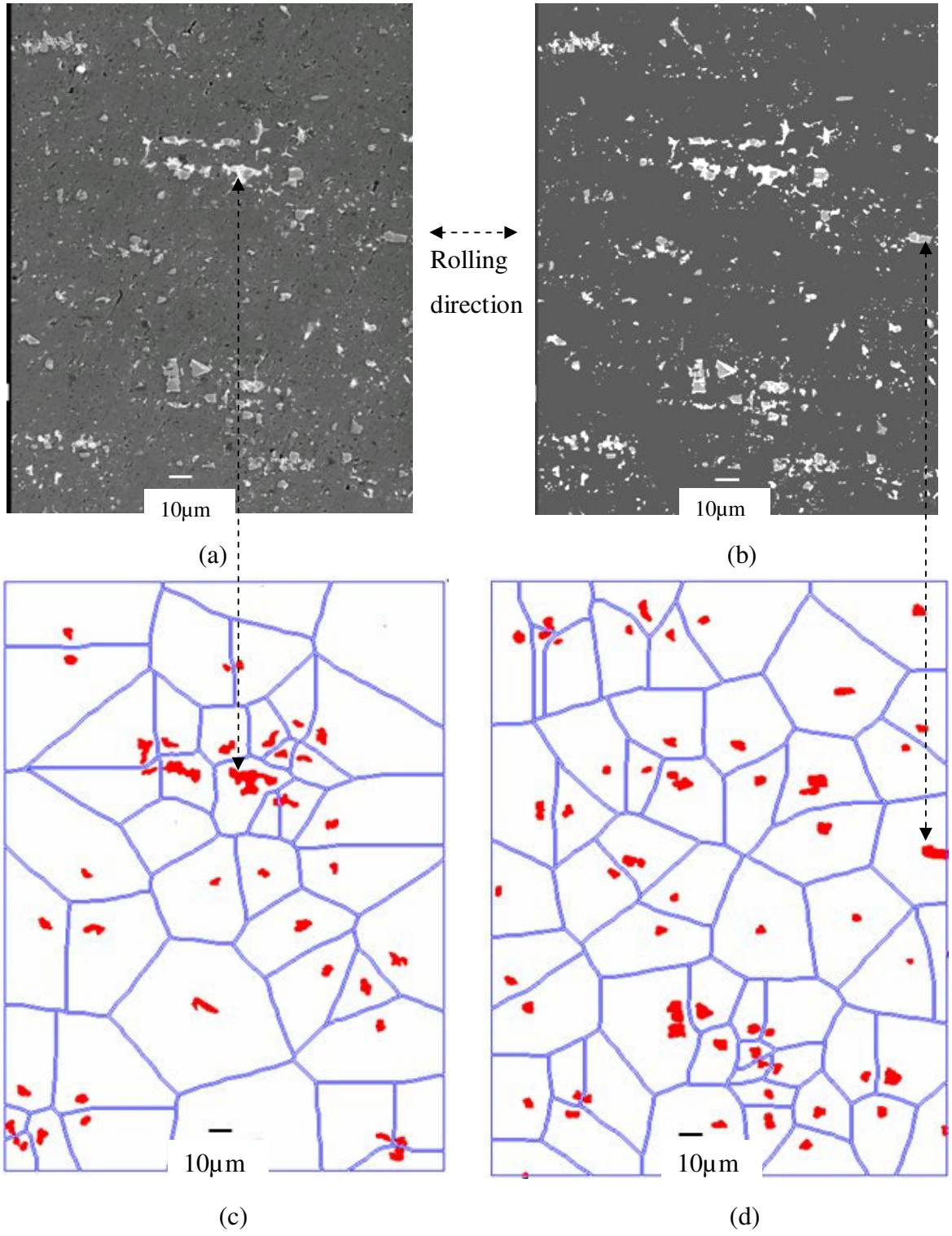

Figure 4.12: Finite body tessellation analysis for AS20S lining: (a) SEI (b) BEI image of lining surface. Binary images showing (c) *Sn* and (d) intermetallic particles.

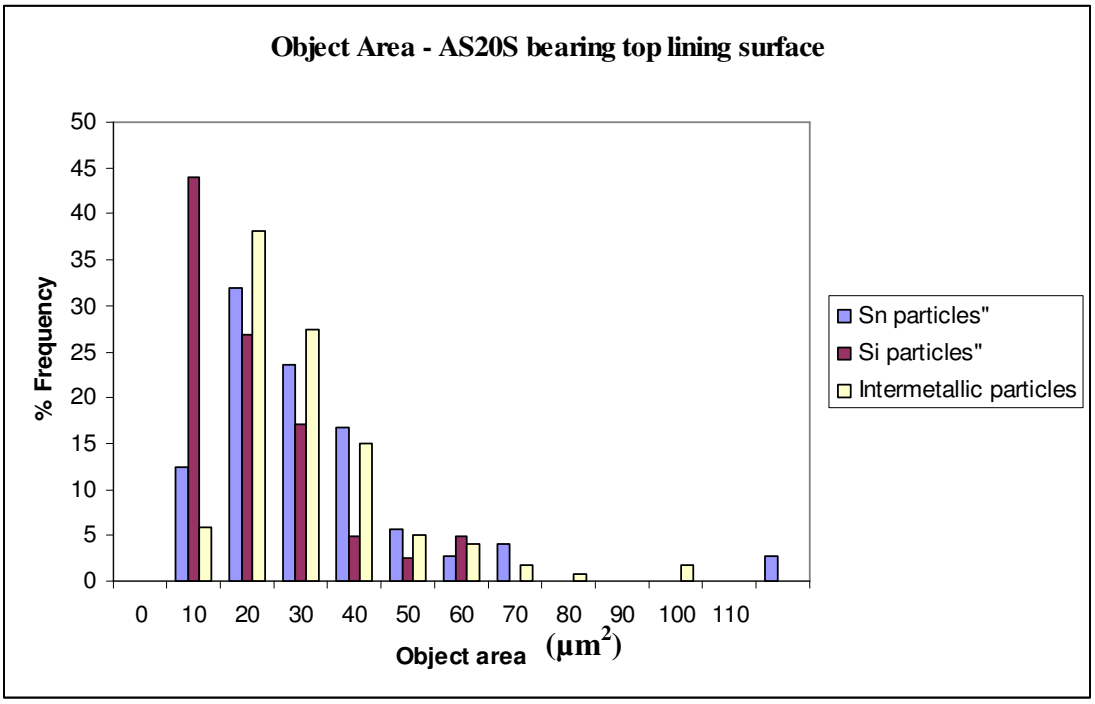

(a)

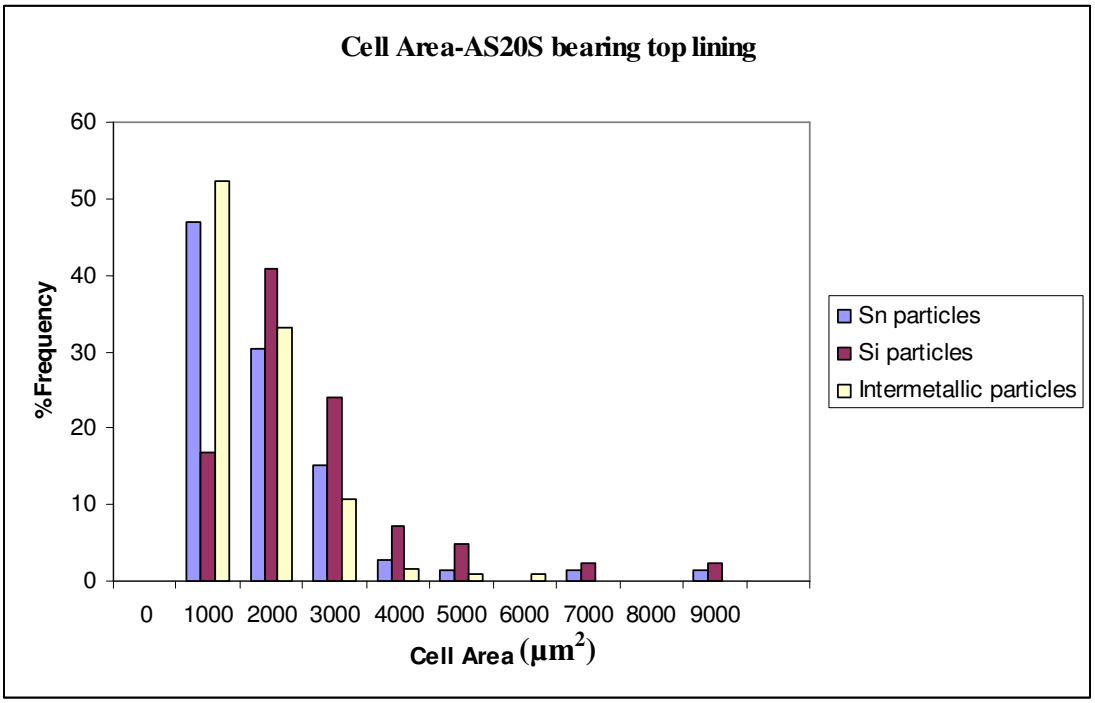

(b)

Figure 4.13: Histogram of *Sn,Si* and Intermetallics showing (a) object area (b) cell area.

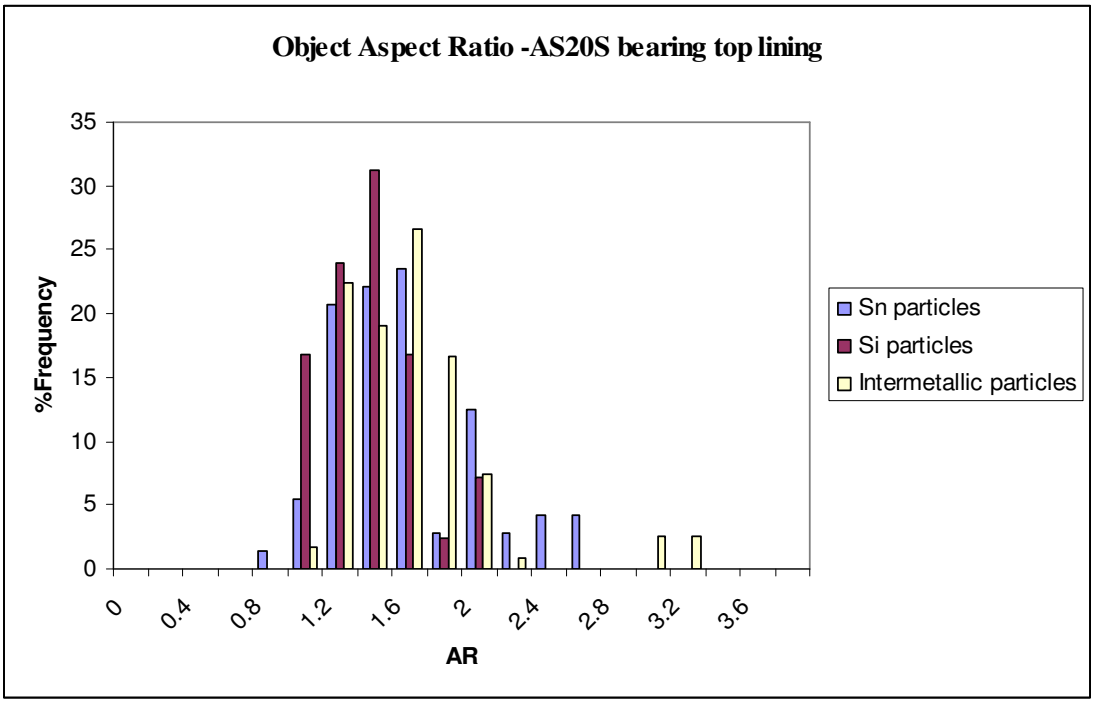

(a)

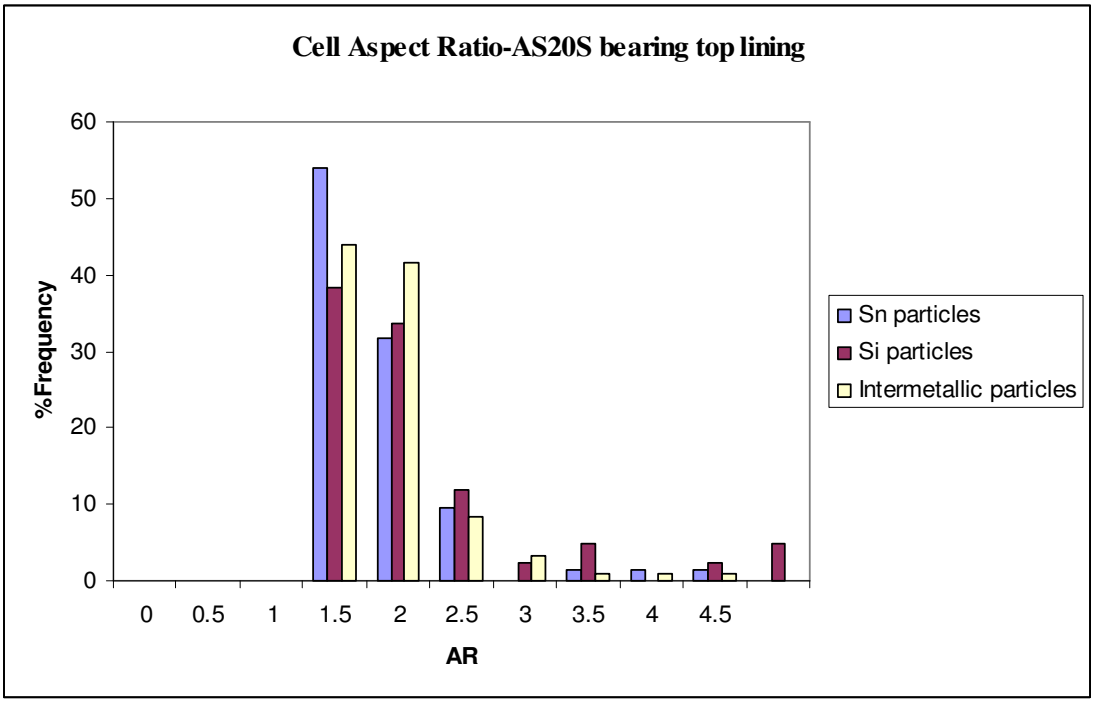

(b)

Figure 4.14: Histogram of *Sn, Si* and Intermetallics showing (a) object aspect ratio (b) cell aspect ratio.

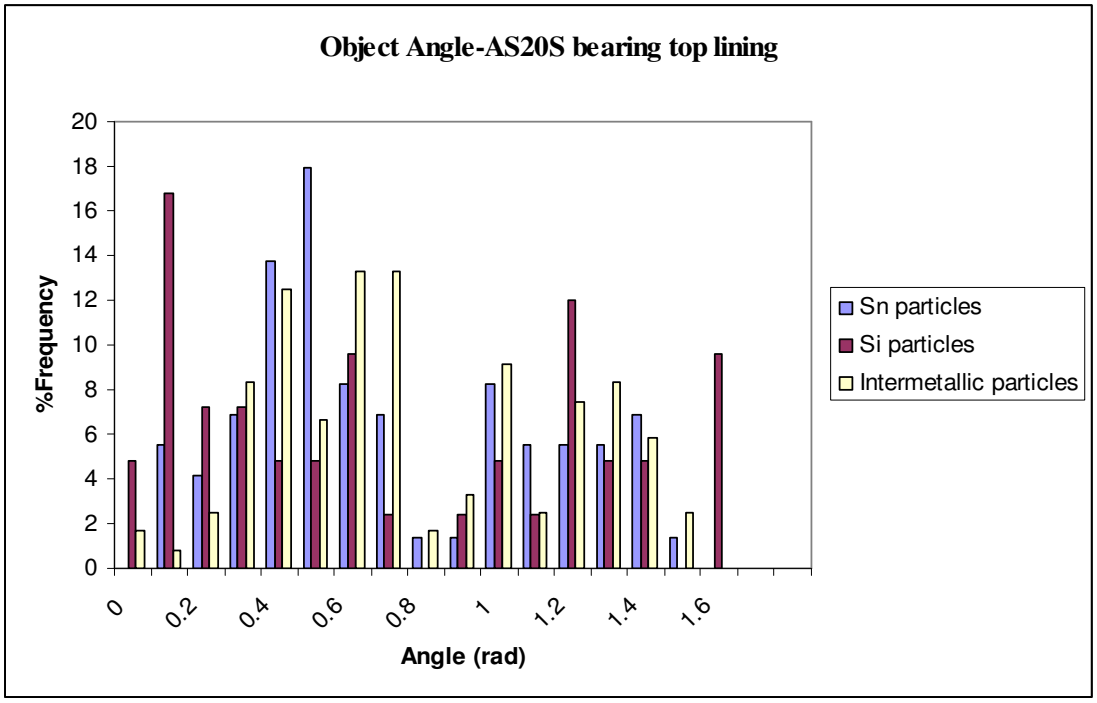

(a)

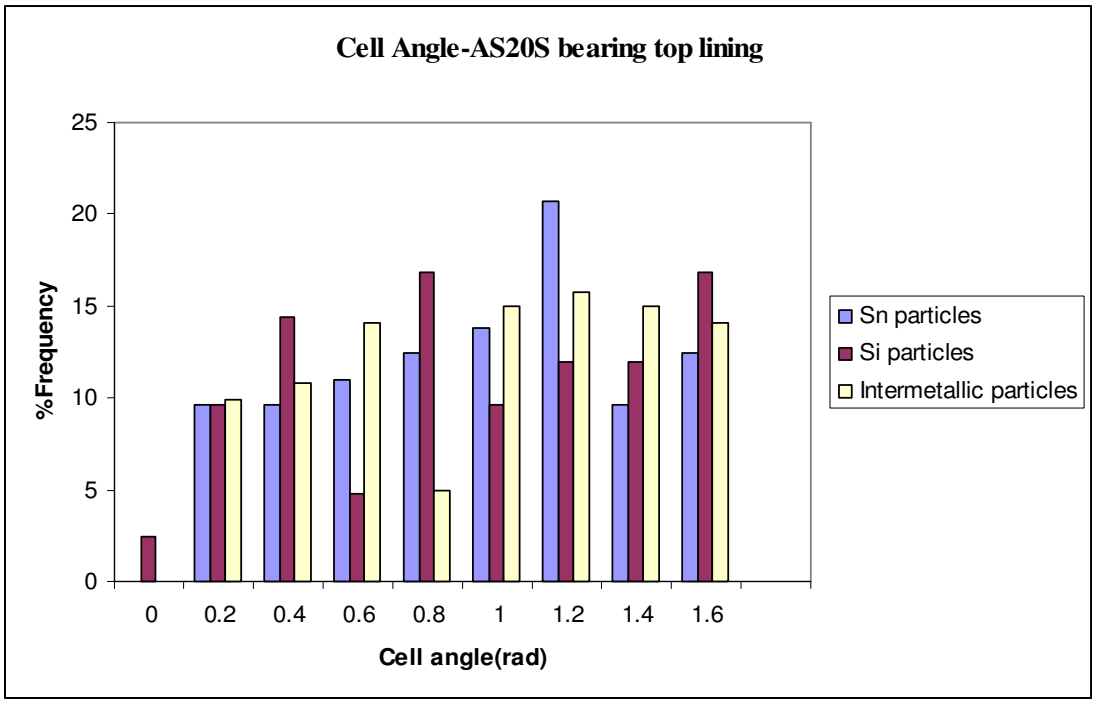

(b)

Figure 4.15: Histogram of *Sn, Si* and Intermetallics showing (a) object angle (b) cell angle.

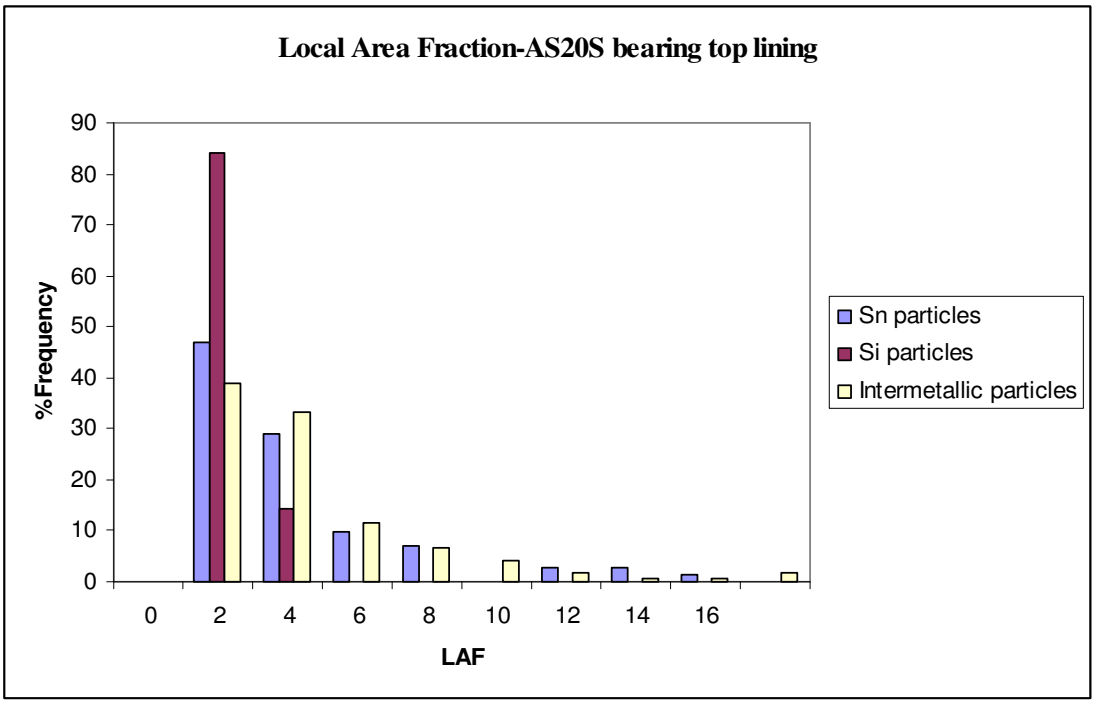

(a)

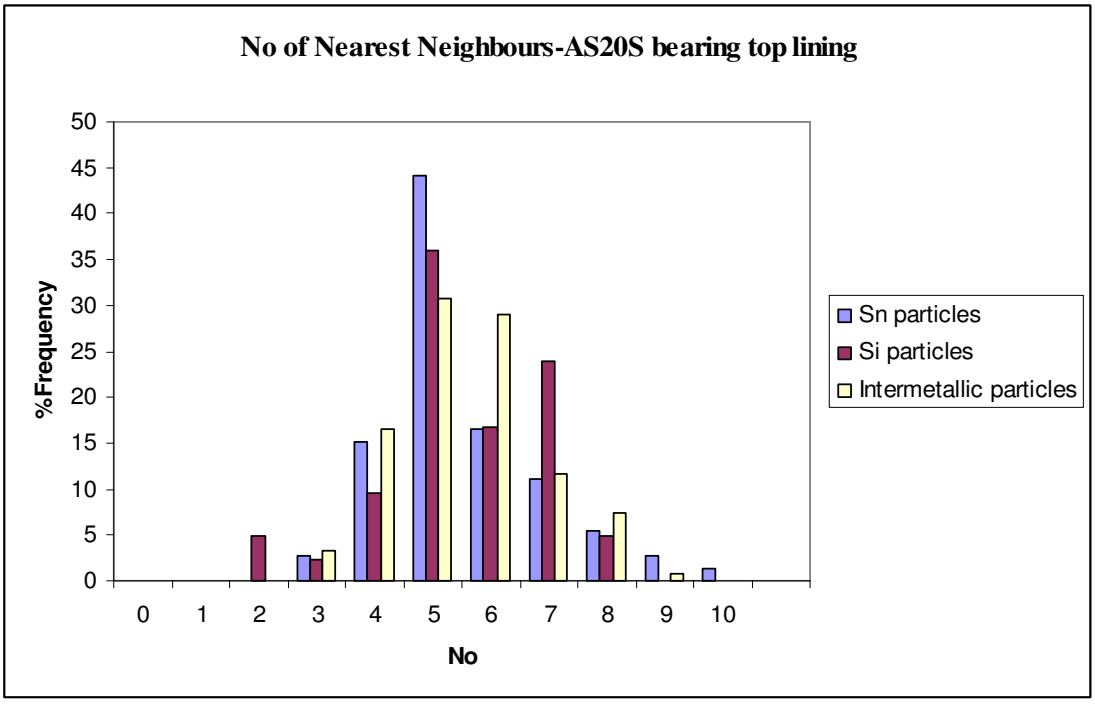

(b)

Figure 4.16**:** Histogram of *Sn, Si* and Intermetallics showing (a) L.A.F (b) No of Nearest neighbours.

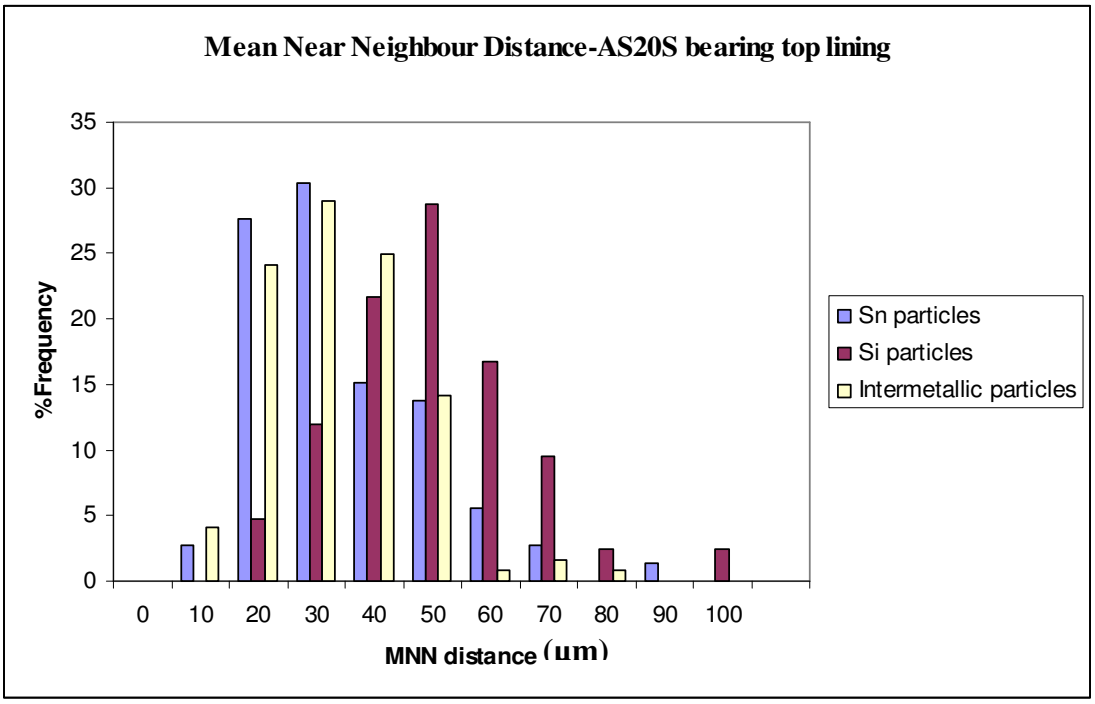

Figure 4.17: Histogram of *Sn* and Intermetallics showing Mean Near Neighbour Distance.

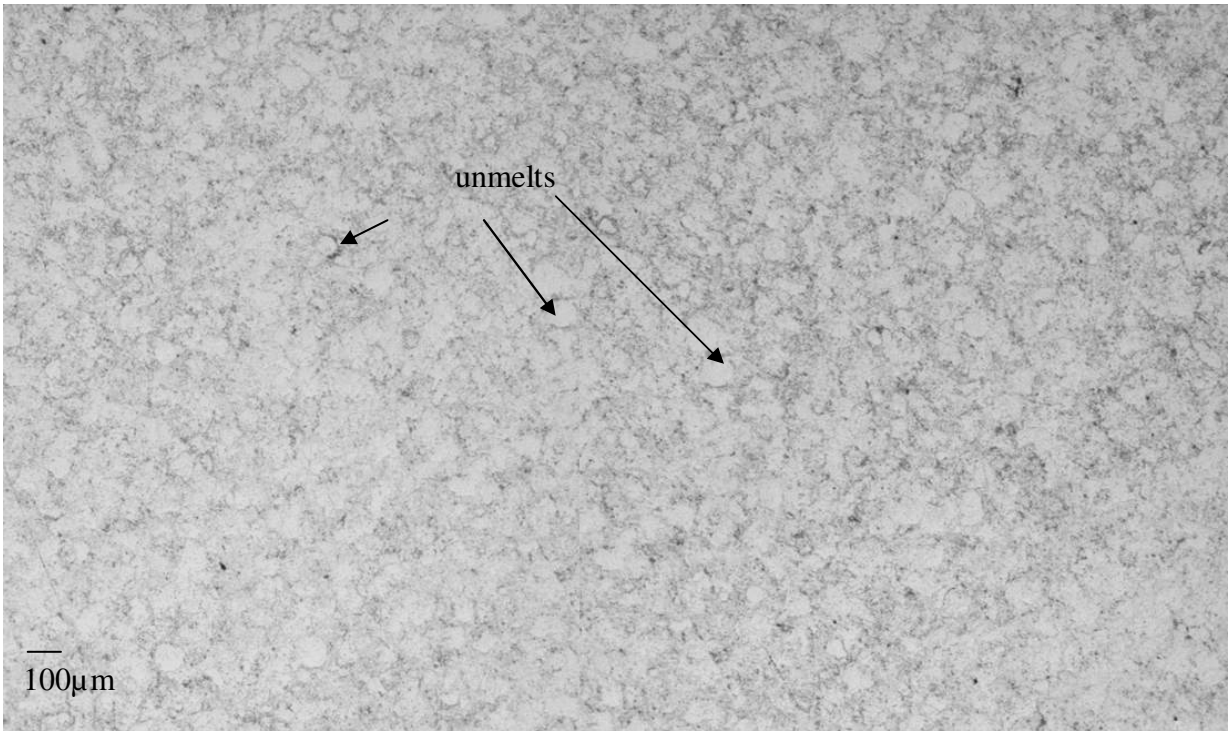

(a)

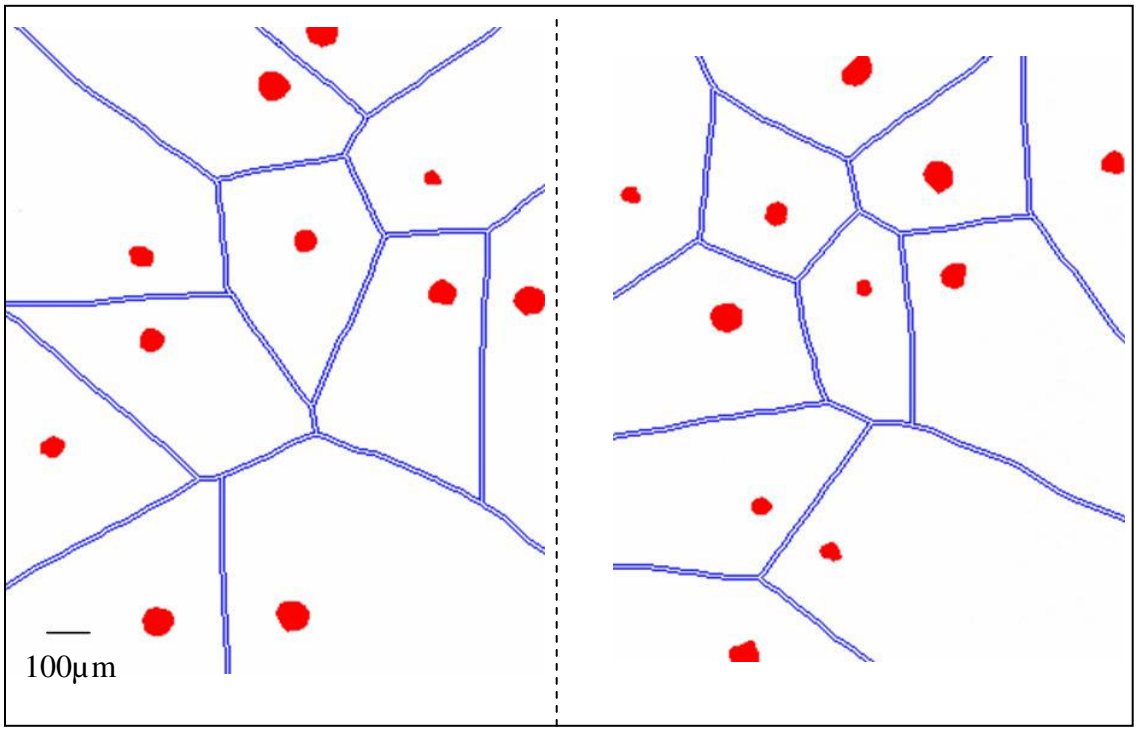

(b)

Figure 4.18**:** FBT analysis of unmelt region in the HVOF surface (a) original image (b) binary images.

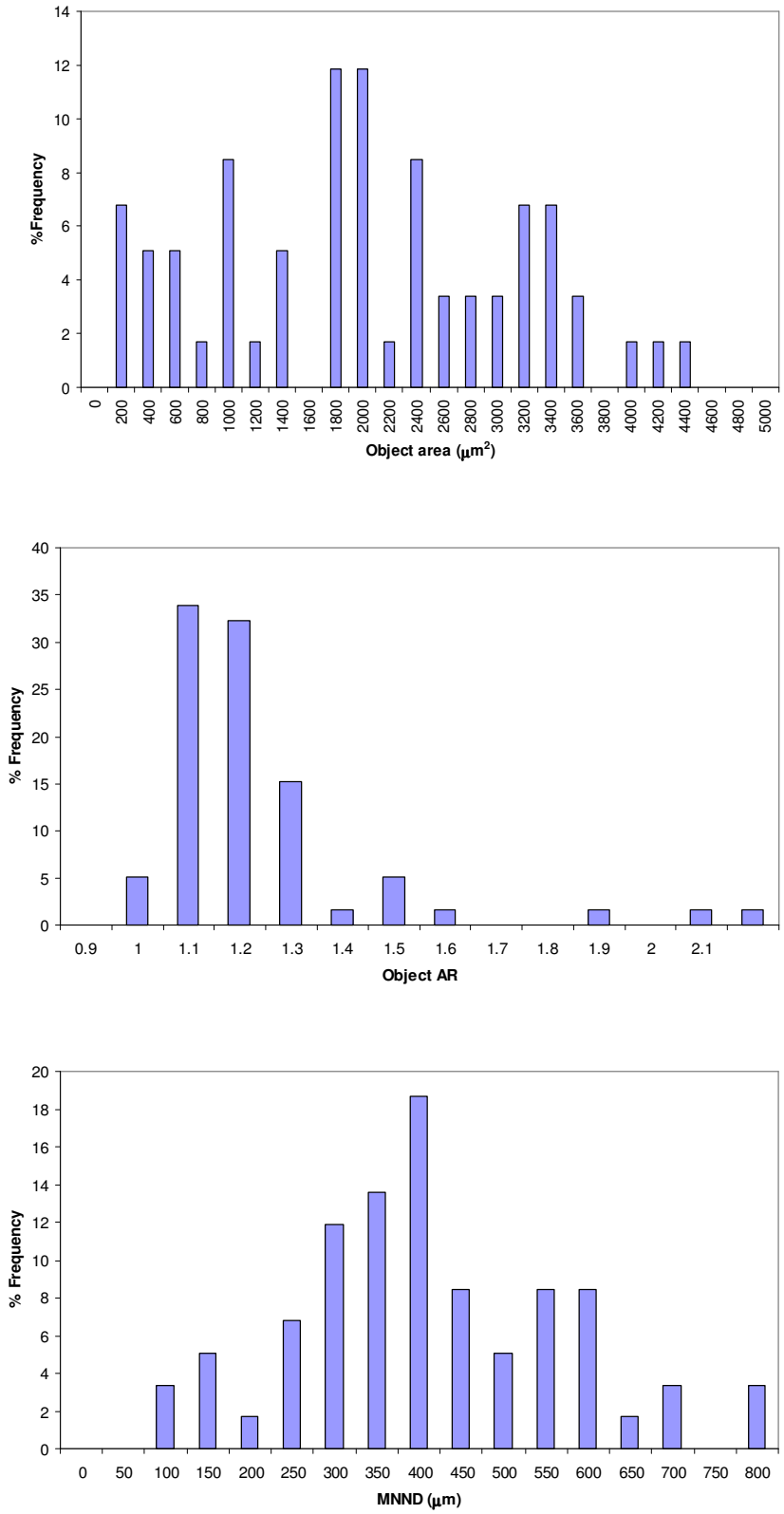

Figure 4.19: Distribution of FBT measured (a) object area (b) object AR and (c) mean near neighbour distance for the circular unmelts observed in the HVOF lining.

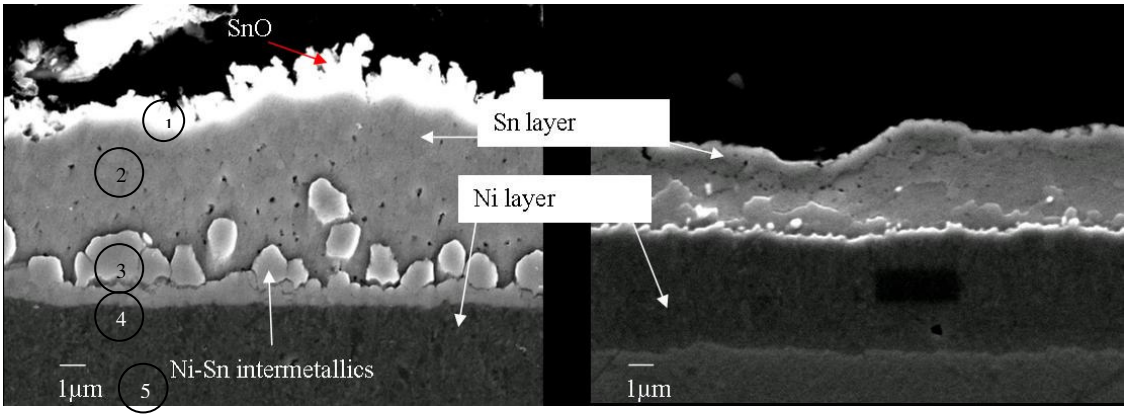

Figure 4.20: SEI images of (a) heat treated and (b) as plated RB168 bearing cross-section showing *Ni* and *Sn* overlay layers electroplated on the surface of *Cu-Sn-Ni* lining layer.

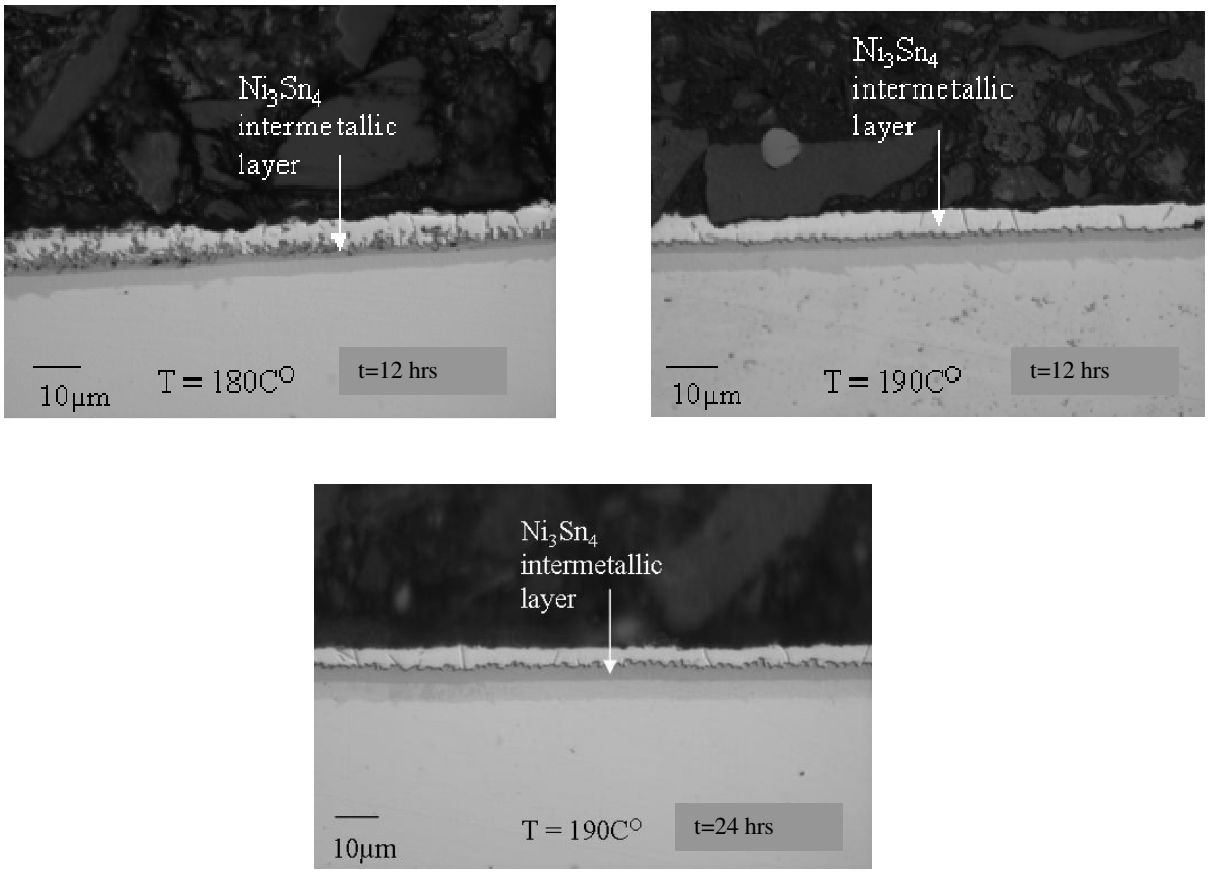

Figure 4.21: Microstructure of the cross-section of RB168 bearing specimen heat treated at different times and temperatures.

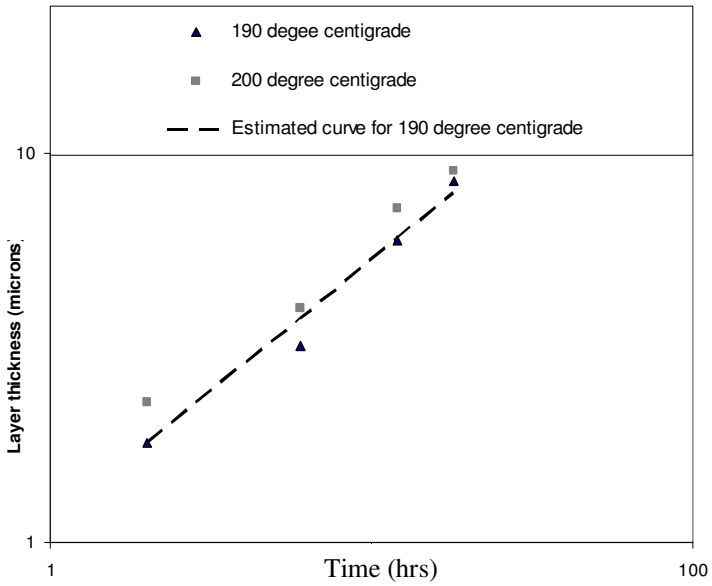

Figure 4.22: Growth behaviour of *Ni-Sn* interfacial compound layer at 190 and 200C^{o}

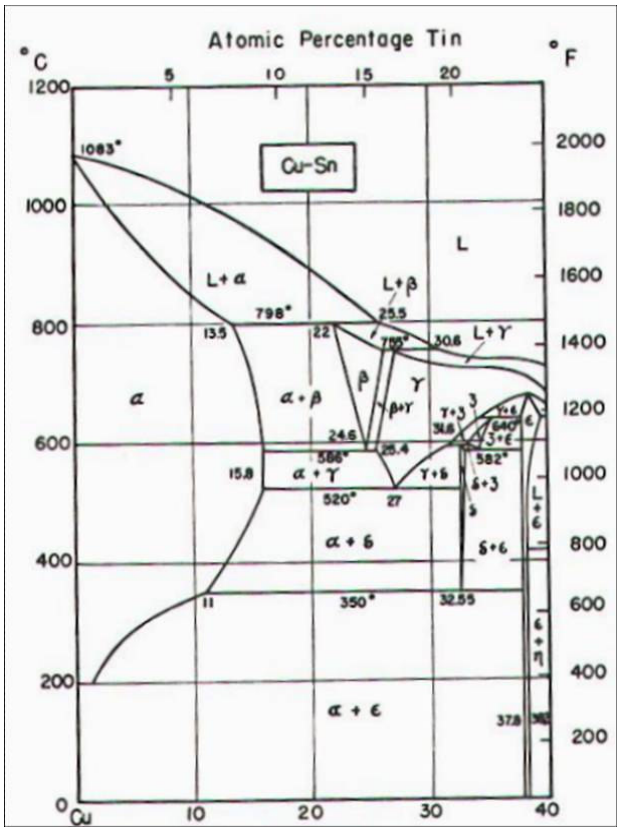

(a)

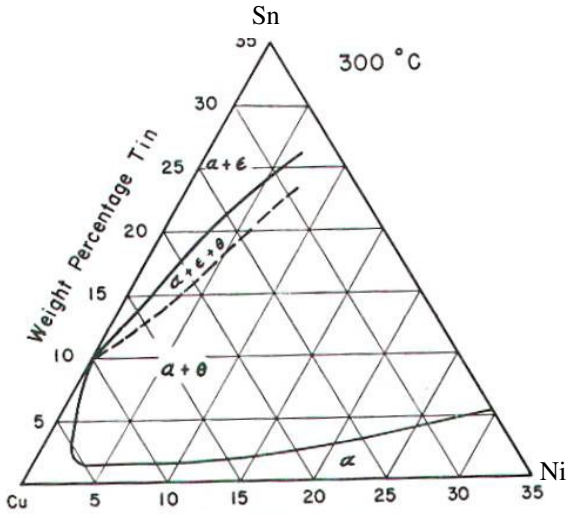

(b)

Figure 4.23 (a) Binary phase diagram of *Cu-Sn* systems (b) ternary diagram of *Cu-Sn-Ni* systems (After[10]).

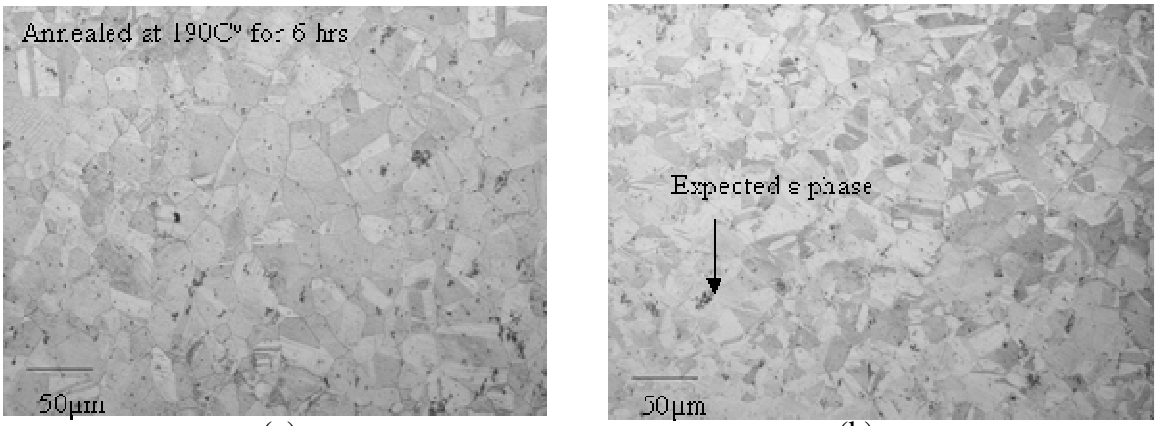

(a) (b)

Figure 4.24: RB168 bearing lining etched surface showing *Cu* grains of (a) heat treated specimen (b) non-heat treated specimen

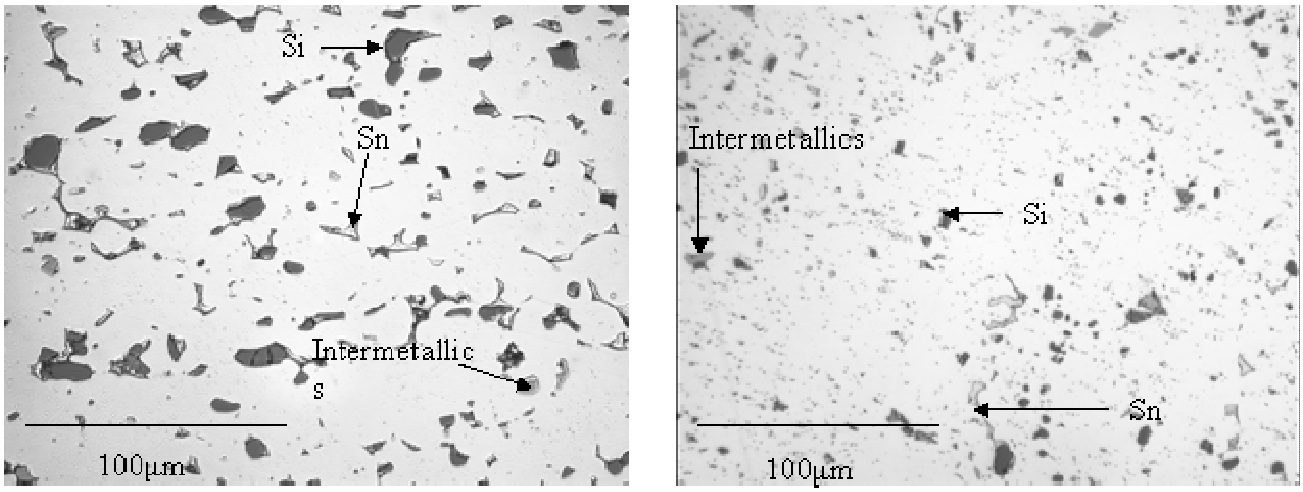

(a) (b)

Figure 4.25: Optical micrographs of the lining surfaces of the (a) AS1241[4] and (b) AS20S bearings.

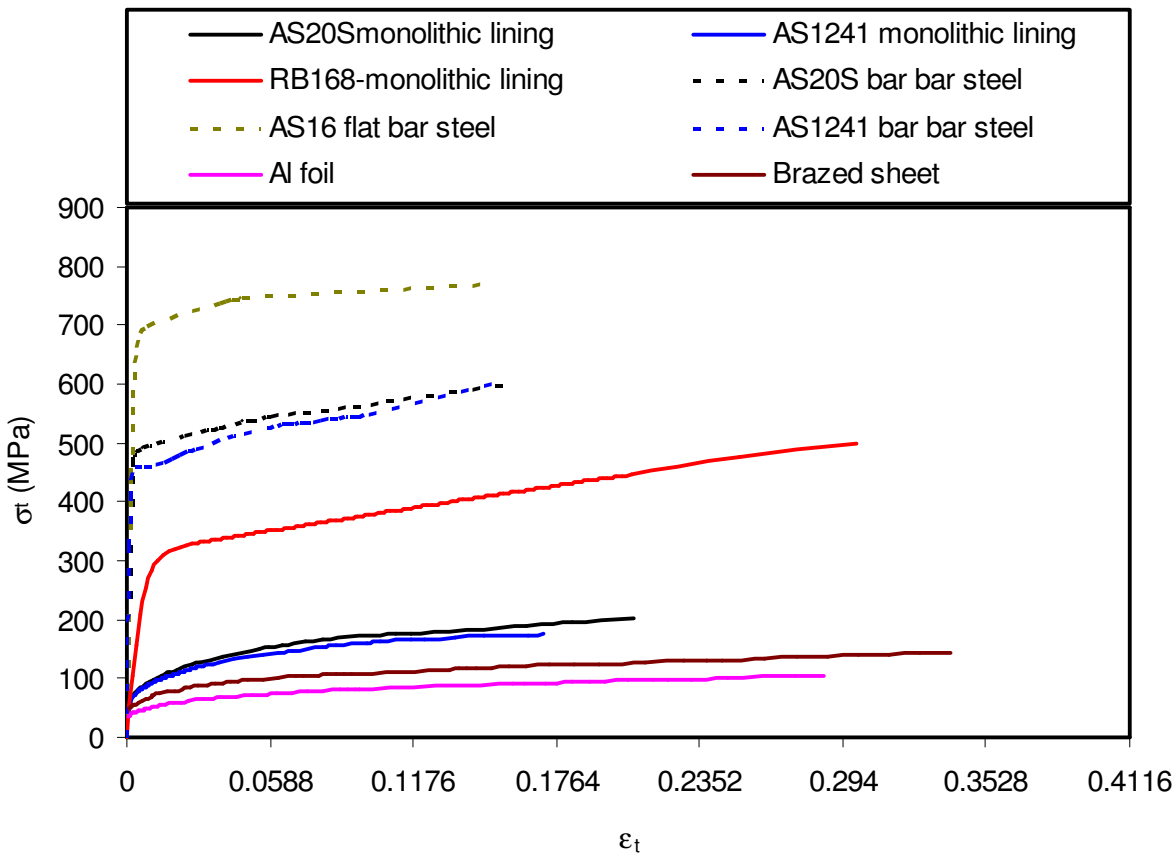

Figure 4.26: True stress vs. true strain curves for the monolithic layers of different systems. Data for the AS1241, AS16 systems and cast *Sn* was obtained from the previous work[4].

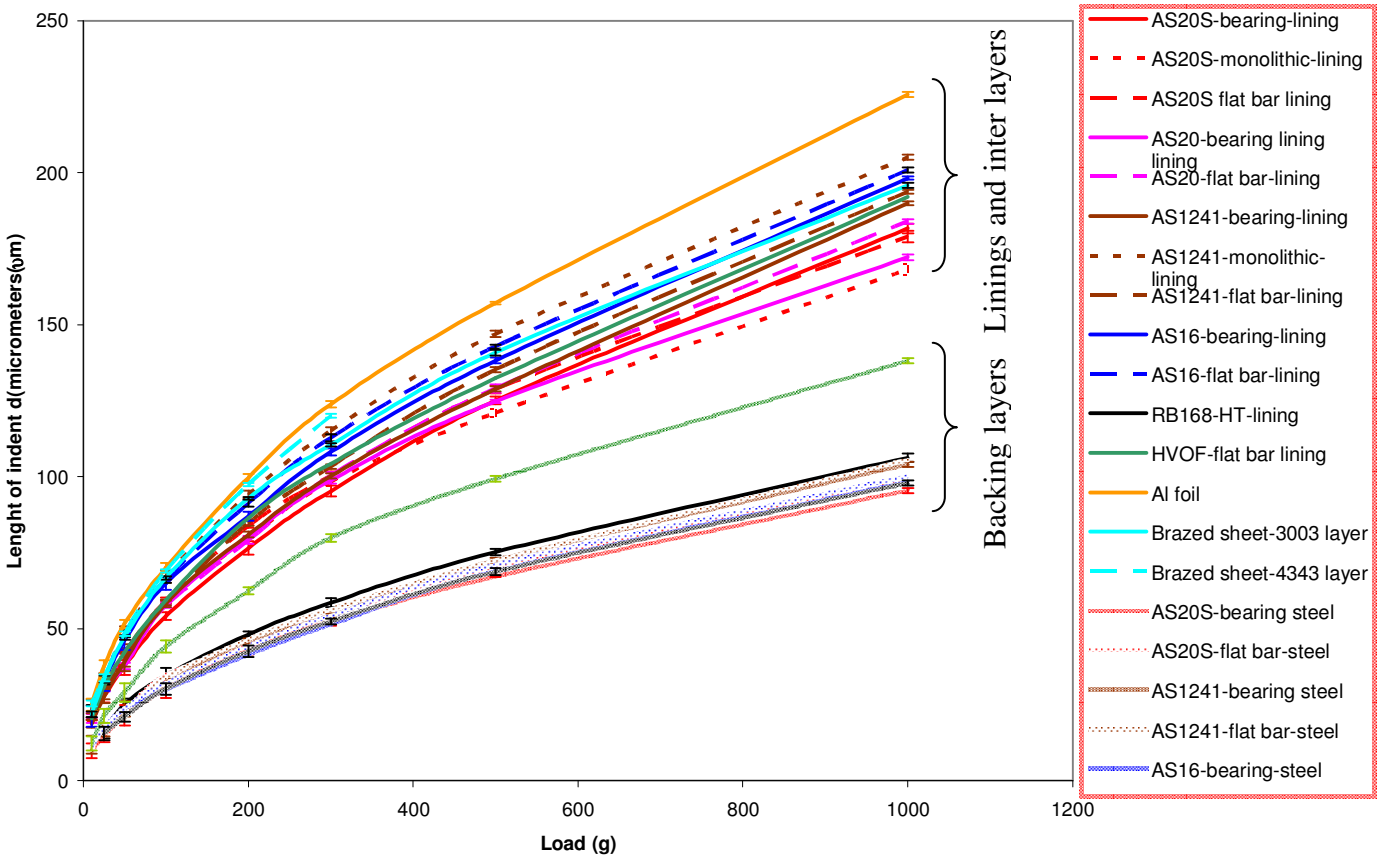

Figure 4.27: Load vs. indent diagonal data for various layers of different systems. Data for AS1241 and AS16 was obtained form previous work[4].

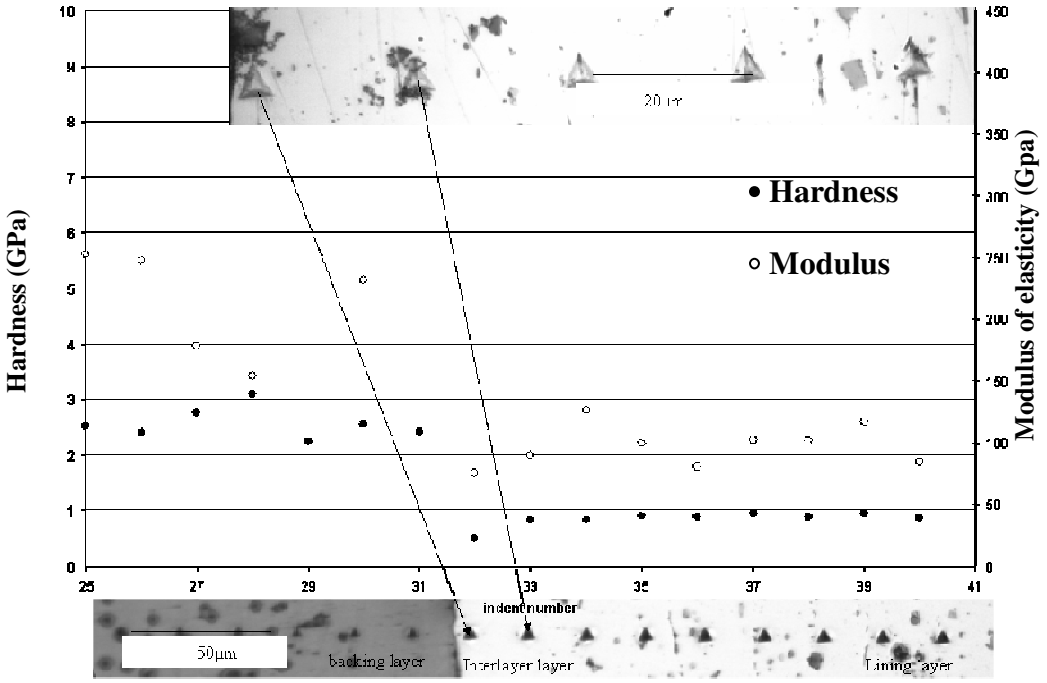

(a)

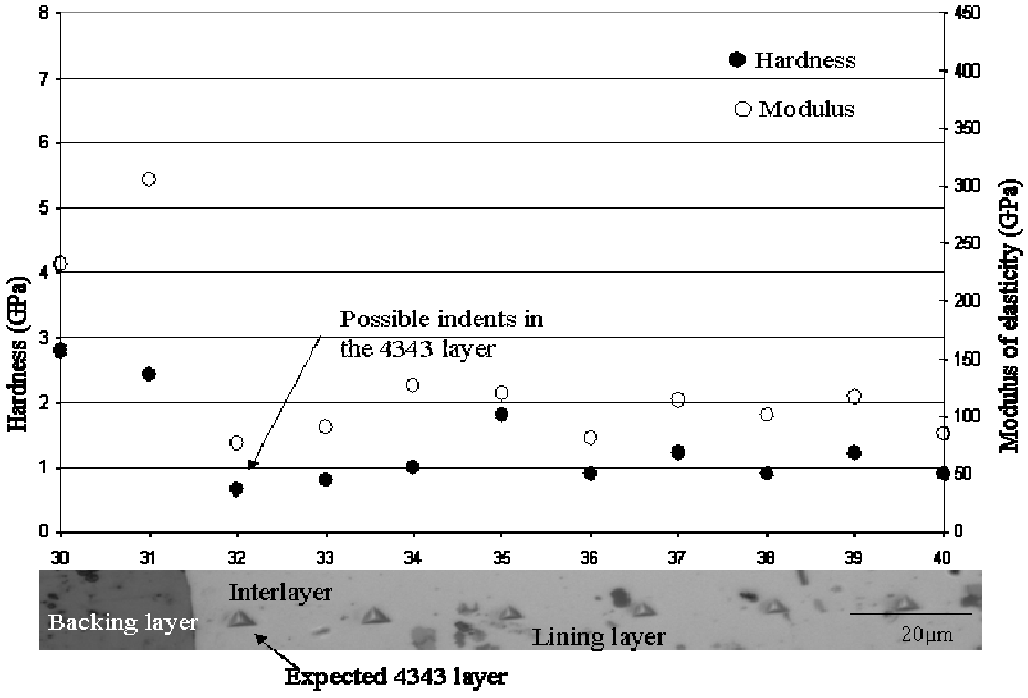

(b)

Figure 4.28: Location of various nano-indents and the corresponding hardness values for (a) AS20S and (b) AS20 bearing systems.

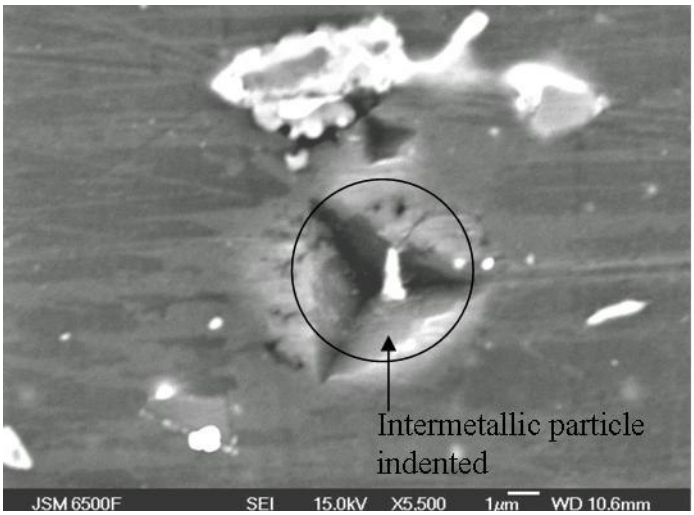

(a)

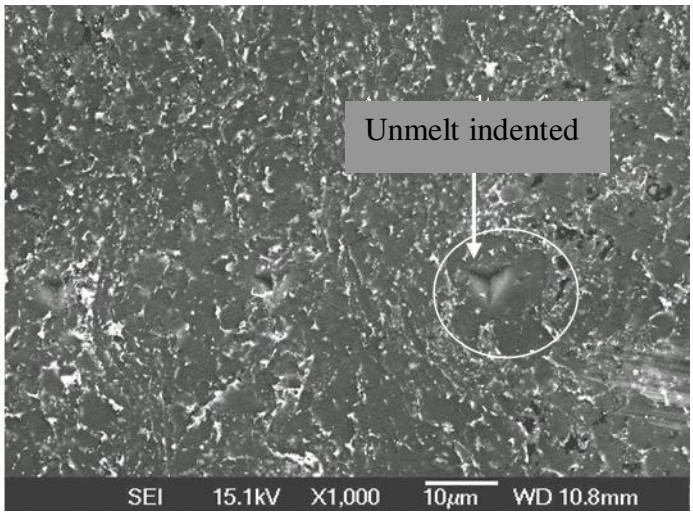

(b)

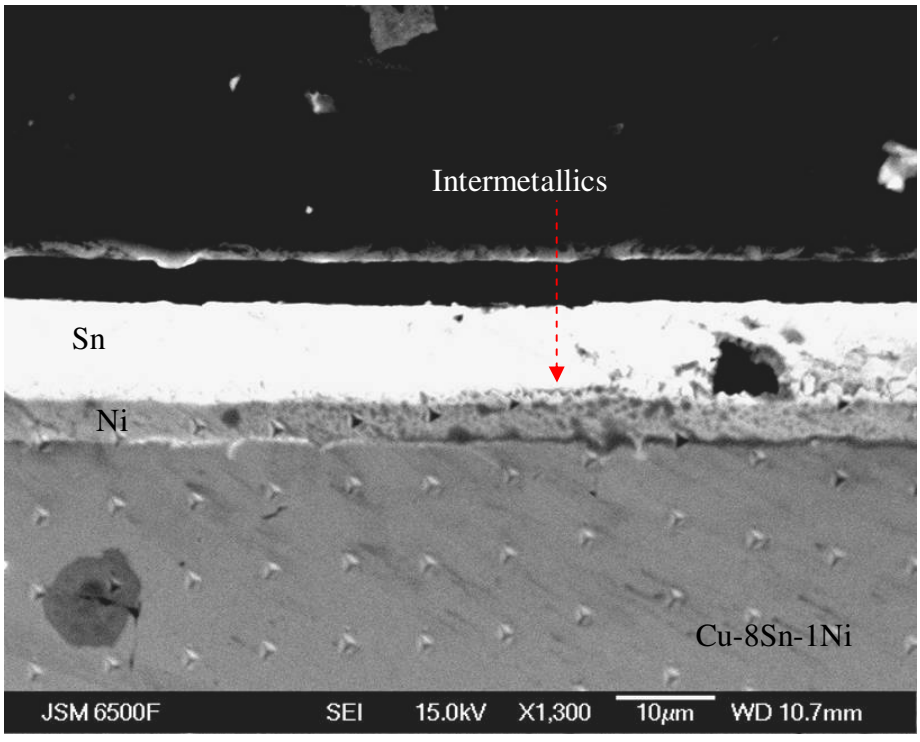

(c)

Figure 4.29: Some targeted secondary phase particles during nano-indentation (a) AS20S lining (b) HVOF lining (c) RB168 overlay layers.

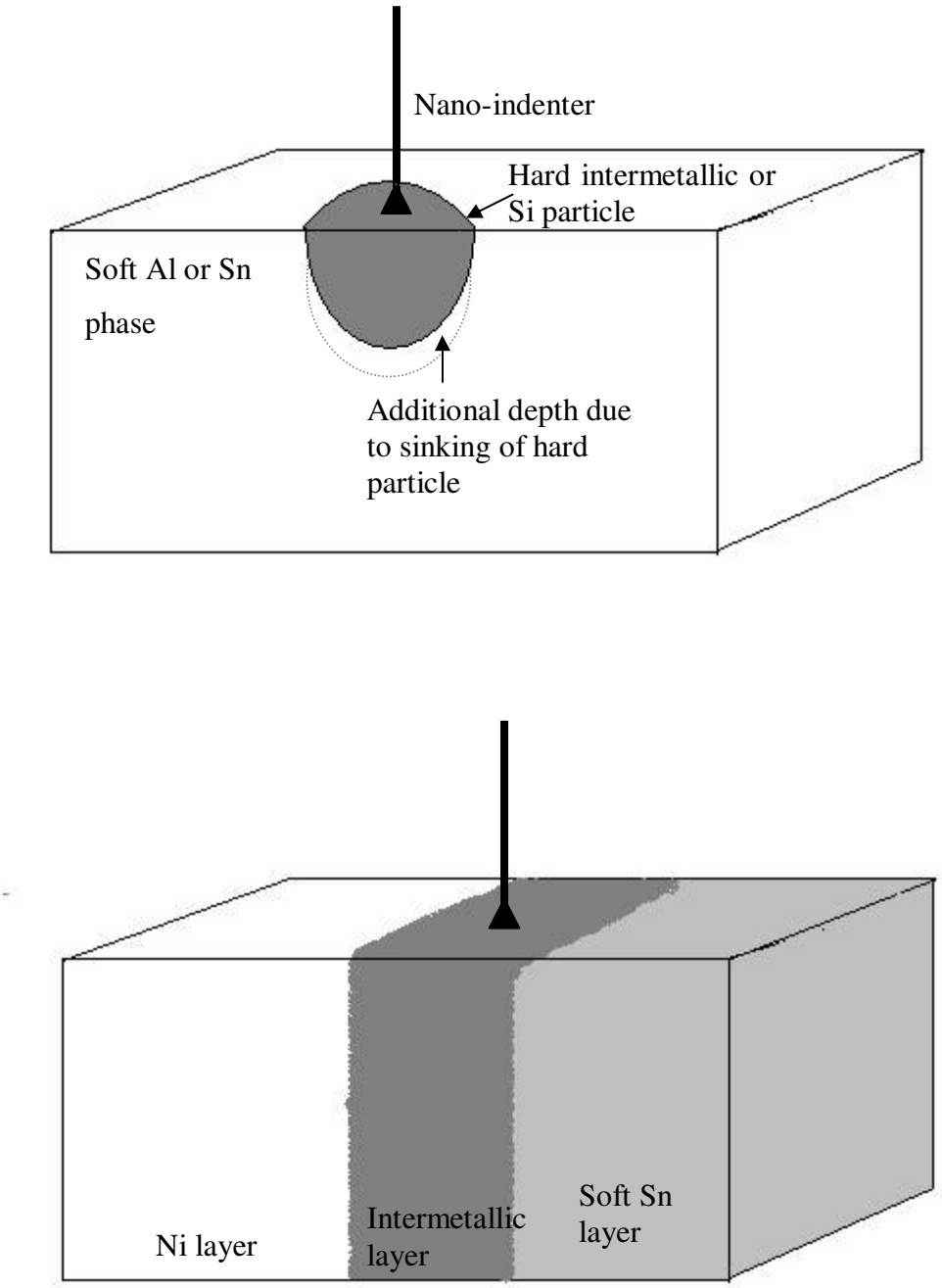

Figure 4.30: A schematic of secondary phase region being targeted by nano-indenter in (a) AS20S lining (b) RB168 interfacial layers between *Sn* and *Ni* overlay layers.

5 FATIGUE TEST RESULTS AND POST FAILURE ANALYSIS

This chapter presents fatigue test results in terms of life time as well as microstructural observations of the initiation and growth of short fatigue cracks. Prior to the analysis of the fatigue test results, a detailed analysis of the stresses and strains developed during a three point bend test have been presented on the basis of experimentally measured strain as well as elasto-plastic finite element analysis.

5.1. Stresses and strains developed in a 3-point bend test

The elasto-plastic behaviour of different materials under applied loads was assessed on the basis of results from simple tensile tests (Section 4.2). This information is required for stress and strain analysis of different multilayered systems in the form of finished bearings and flat bars. As mentioned in Section 3.3, various multilayered bearing and flat bar specimens were subjected to fatigue tests under three-point bend loading conditions. The maximum strains are developed at the free lining surface. In order to compare the fatigue performance of different lining systems, the lining fatigue data was presented as σ-N or ε-N curves. For these systems, the lining layer is significant as the fatigue failure in the finished bearings starts by the formation of small cracks at the free lining surface.

Experimental measurement of stress and strain at the lining surface is not a simple process, especially for specimens with curved surfaces (i.e. bearings). In addition, analytical solutions (based for instance on simple beam theory) for stresses and strains at different locations of the specimen are only applicable for homogeneous, elastic-perfectly plastic materials. For multilayered systems, compound beam theory seems to be an attractive analytical tool but again the materials have to be elastic–perfectly plastic. Therefore, for strain hardening materials, a finite element model to determine the surface 'σ' and 'ε' was originally implemented by *Joyce*[1] in which the elasto-plastic behaviour of different layers of the bearings, (obtained from simple tensile tests) were used. In order to simulate the three point bend test conditions, the bearing specimen was assumed to be fully constrained at the supports (Figure 3.13(a)) while a static point load was applied incrementally at the centre of symmetry of the bearing. A similar load was applied at the centre of symmetry of the flat bar specimen on the backing steel layer. The resultant 'ε_p' values were utilized as the maximum cyclic plastic strain

range '$\Delta\varepsilon_p$' in the subsequent fatigue life assessment curves. Similar modelling approaches were adopted in the current work for different bearing systems with varying materials properties.

Experimentally measured total strains at the free lining surface using an appropriate strain gauge set up in the three-point bend tests were also compared with the modelling strain results and an appropriate correction factor was determined for each system.

5.1.1. Basic assumptions of the FE model

The previously developed ANSYS model[1] was adapted in this research to Version 10. Since both bearings and flat bar specimens were symmetric about the load location, only half models were required. For the flat bars, only the region between the rollers was analyzed as the outer regions were not significantly stressed during the experiment. For all these models, an 8- node quadrilateral plane element (known as plane 82 in ANSYS code) was utilized. These elements can fit to moderately irregular curved shapes and have compatible displacement shapes. Elasto-plastic properties of materials used in the FE analysis were those obtained as true stress- strain flow curves in Figure 4.26. For AS1241 and AS16 systems, the tensile test results were obtained during previous work at Southampton[2] whereas the rest of the tensile test data were obtained during the current programme. In the previous work, no monolithic lining layer was available for the AS16 bearing and hence the data for AS1241 monolithic lining was used in FE modelling for evaluating surface stresses and strains. The brazed sheet mentioned in Table 3.1 is a combination of 4343 and 3003 *Al* alloy used as an interlayer in the AS20 system (Section 3.1).

There was no attempt to simulate fatigue test conditions due to the lack of cyclic mechanical property data. This type of analysis would require the materials behaviour under cyclic loads at different load levels to be established for different individual layers. This was felt to be beyond the scope of this project.

Figure 5.1 shows the stress and strain profiles developed across different layers of the AS20S bearing and flat bar specimen obtained from the FE simulated 3-point bend static test. It is evident from these figures that maximum plastic strain was developed at the lining surface over an area approximately 0.3mm wide. Since maximum stresses and strains developing at the lining surface were to be used for presentation of fatigue lifetime data, the sensitivity analysis for layer thickness and mechanical properties focussed on these parameters.

5.1.2. Layer thickness sensitivity study

It was observed that manufacturing has induced slight non-uniformities in the thickness of different layers in both finished bearings and flat bars. Although the flat bar specimens were obtained from the same long flat bars, the grinding and polishing routes adopted to polish the lining surface of these specimens before fatigue tests caused similar effects. However these variations did not go beyond 0.1 mm from one specimen to the other. In order to study the effects of these variations, the FE model was run both for finished bearings and flat bars for various lining or steel backing layer thickness, while keeping all other geometric parameters constant. In this analysis, the elasto-plastic properties of AS20S steel, *Al* foil and AS20S monolithic lining were used for the backing, inter and lining layers, respectively. For both bearings and flat bars, the values of the lining thickness were varied between 0.15-0.40 mm at a step of 0.05 mm for each model (lining thicknesses of most of the bearings and polished flat bars fall within this range).

The same procedure was adopted for the steel backing layer by varying its thickness from 1.5 to 1.90 mm at an interval of 0.1 mm with constant values for the thickness of the lining and interlayers.

The results were presented in the form of maximum stress 'σ' and plastic strain ranges 'ε_p' developed at the top lining surface versus the applied loads for all these models.

5.1.2.1.Effect of lining layer thickness

Figure 5.2 shows the effect of increasing the lining layer thickness on the maximum lining surface 'σ' and 'ε_p' in bearings and flat bars respectively under the applied load *P*. These curves show no significant variation in the resultant 'σ' and 'ε_p' developing at the lining surface for different lining layer thickness values. The backing steel layer is considerably stiffer than the lining layer, thus the majority of the load is carried by it. However, at intermediate loads between 1500 to 2500 N for bearings and flat bars, increasing lining thickness to 0.4 mm resulted in increased values of the lining 'σ' and 'ε_p'.

A careful observation of the curves in Figure 5.2 (a) show that at a load of 2000 N, a 166% increase in the lining thickness (from 0.15 to 0.40mm) caused a 1 and 10 % increase in the resultant bending 'σ' and 'ε_p', respectively. Similarly in the case of the flat bar specimens (Figure 5.2 (b)), the same increase in the lining thickness resulted in a 2 and 16 % increase in the maximum lining surface stress and plastic strain, respectively. These small variations in the

predicted maximum lining 'ε_p' and 'σ' as a result of changes in the lining thickness are not expected to have a measurable effect on fatigue performance. *Love et al*[3] proposed that decreasing the lining thickness of bearing increases the fatigue strength. This was attributed to the ratio of stress distribution between lining thickness and steel backing approaching the ratio between their modulie. Hence steel being stiffer limits the strains on lining resulting in decreased lining stresses. The work of *Duckworth* and *Walter*[4] experimentally showed that the fatigue resistance of a bearing increases with the decrease of the lining thickness as a result of increase in the cyclic yield stress. This effect could not be assessed through the current modelling results, as the applied load was static. However, slight increase in the lining surface stresses (observed in FE results) as a result of increasing lining thickness is in accordance with the early experimental results shown by *Duckworth et al.*

5.1.2.2.Effect of steel layer thickness

The ratio of the lining layer to the steel layer thickness in all current and old bearing systems lies between 0.15-0.2. It is evident from the load vs. 'ε_p' and 'σ' curves shown in Figure 5.3 that increasing the values of the backing thickness causes a marked decrease in the maximum lining 'ε_p' and 'σ'. The resultant 'σ' and 'ε_p' developing at the lining surface of the finished bearings and flat bars are therefore far more sensitive to the steel backing thickness variations compared to the lining thickness variations.

At the maximum load of 3000 N, a 26% increase in the backing steel layer thickness causes 83% reduction in the lining surface 'ε_p' values. Similarly a 95% reduction in the lining surface 'ε_p' value was observed for a 26% increase in backing steel layer thickness of the flat bar specimen. These results show that the thickness of the steel layer significantly affects the level of stresses and strains developing at the lining surface as compared to that of the lining layer.

The obvious reason for these effects is the constraint supplied by the steel layer at its interface with the lining. In FE modelling, the steel layer is assumed to be bonded perfectly to the lining layer (through an interlayer in the case of most RB systems) and this constraint remains effective during the application of the static load. This assumption may not be perfectly valid during the actual fatigue test as the constraint may not be so rigid at higher loads (especially during cycling loads where the specimen was mechanically fastened in the jig) and

the direct use of the FE data without further experimental validation of the model would not be reliable in characterizing the fatigue behaviour.

5.1.3. Effect of layer mechanical properties

In multilayered systems, the mechanical properties of lining layers, interlayers and steel backing layers vary from one system to the other as different systems use layers of different alloy compositions. A sensitivity analysis based upon the variation in the true σ-ε data for a particular layer (while keeping the same geometrical parameters and material properties data for the remaining layers) was next carried out using the FE model. With the help of this analysis, a quantitative assessment of the variation in the maximum values of the 'σ_t' and 'ε_p' (developing at the lining surface of the finished bearings under applied static loads) was established. Table 5.1 shows the sensitivity matrix for variation in the properties of different layers. The thickness of lining, interlayer and backing layer was taken equal to 0.2mm, 0.04mm and 1.5mm, respectively.

5.1.3.1.Effect of lining layer properties

In order to study the effect of changing the mechanical properties of the lining layer on the developing maximum lining surface 'σ' and 'ε_p', a basic AS20S bearing model was chosen. Using AS20S steel and *Al* foil tensile test data for the backing steel layers and interlayers respectively, the lining tensile properties were changed from those of very soft *Sn* to the hardest AS20S monolithic lining. The effect of change in the lining layer properties on the resulting 'ε_p' and 'σ_t' developing in the bearing and flat bar specimens is shown in Figure 5.4 (a) and (b) respectively.

As the AS20S monolithic was shown to have higher UTS and 0.2% proof stress values compared to other monolithic layers (Table 4.8), the maximum 'σ_t' developing at the lining surface reached its highest value when AS20S monolithic lining layer was used. (assumed as a lining layer in the model). This is because of the higher resistance to deformation for harder layers under the applied bending loads. Consequently the maximum lining surface 'ε_p' developed in case of AS20S monolithic lining reached a lower value than similar results for the brazed sheet, *Al* , *Sn* and AS1241 monolithic layer properties used as the model lining layer. The effect of change in the lining properties is quantitatively described in Table 5.2. It is evident that the AS1241 and AS20S monolithic layers are closer to each other in mechanical properties

compared to the brazed sheet; the replacement of one for the other did not give a significant change in the results.

In the FE based modelling of the 3-point bend test, the presence of possible residual stresses in the lining layer has not been accounted for although it may be considered to effectively reduce the apparent yield stress. However, the results of the lining property sensitivity analysis show that a 10-15% reduction in the yield point has a negligible (1-2% as evident from Table 5.2) effect upon the calculated maximum lining plastic strains, which form the basis of the fatigue analysis.

5.1.3.2.Effect of steel layer properties

The basic AS20S bearing model was used to observe the effects of varying the backing steel layer properties on the maximum lining surface 'σ' and 'ε_p'. Three models were run using the HVOF, AS20S, AS1241 and AS16 flat bar steel tensile properties while using the same geometrical parameters. Among the steel layers, the AS16 flat bar steel showed the highest tensile UTS and 0.2% proof stress. Figure 5.5 shows the plots of calculated maximum lining surface 'σ' and 'ε_p' versus applied loads. The use of AS20S and AS16 steel layers resulted in similar maximum surface stress and strain levels up to a load of 1500 N beyond which the results deviate with the stress and strain values increasing significantly for the systems including AS20S flat bar steel properties. The model using the AS1241 flat bar steel properties initially showed lower maximum surface 'σ' and 'ε_p' than those shown by AS16 up to a load of 2100 N above which the situation was reversed. The effect of the steel layers on the maximum surface 'σ_t' and 'ε_p' is more difficult to explain than that of the lining layers. From the curves shown in Figure 5.5, it is evident that the use of either AS1241 or AS20S steel σ-ε curves at higher loads gives similar maximum surface 'σ_t' and 'ε_p'.

Under the applied fatigue loads, the very thin and comparatively soft lining layer undergoes plastic deformation and hence the experimentally measured 0.2% proof stress ($\sigma_{0.2\%}$) was considered to be important. Figure 5.6 (a) shows the variation of maximum lining σ_t and ε_p as function of the lining $\sigma_{0.2\%}$ values at two different applied loads i.e.2000 and 3000N. A linear variation of both σ_t and ε_p with the proof stress of the lining layer is evident. These relations (best fits) could be expressed as

$$\sigma = a\sigma_{0.2} + b \qquad 5\text{-}1$$

$$\varepsilon = a'\sigma_{0.2} + b' \qquad 5\text{-}2$$

Similarly P vs maximum lining σ_t and ε_p curves shown in Figure 5.2 were approximated by the following equations

$$\sigma = c\ln(P) - d \qquad 5\text{-}3$$

$$\varepsilon = A + eP + fP^2 + gP^3 \qquad 5\text{-}4$$

In all these equations P, σ and ε is the load, maximum lining tensile stress and maximum lining plastic strains respectively. All other symbols were fitting constants. Figure 5.6 (b) shows the effects of varying steel layer stiffness (E) on the lining surface σ_t and ε_p values. For the stiffer steel, more load is carried by the backing layer resulting in lower σ_t and ε_p at the lining surface.

The above analysis was based upon multilayered systems in which all layers were assumed to be adhered perfectly to each other where the applied load acts at a single point. However the modelling results in terms of maximum strains and stresses at the lining surface need to be assessed in the light of direct strain measurements as the experimental conditions and layer bonding may not be as assumed in the model.

Table 5.1: Test matrix for the layer mechanical properties sensitivity analysis

Lining layer: 0.2mm, Backing layer: 1.5mm, Interlayer: 0.04mm

<table>
<tr><th rowspan="2">Model No</th><th colspan="3">Layer type</th></tr>
<tr><th>Lining layer</th><th>Interlayer</th><th>Backing layer</th></tr>
<tr><td>1</td><td>AS20S monolithic</td><td rowspan="12">Al foil</td><td rowspan="5">AS20S flat bar steel</td></tr>
<tr><td>2</td><td>Brazed sheet</td></tr>
<tr><td>3</td><td>AS1241 monolithic</td></tr>
<tr><td>4</td><td>Al</td></tr>
<tr><td>5</td><td>Sn</td></tr>
<tr><td>6</td><td rowspan="6">AS20S monolithic</td></tr>
<tr><td>8</td><td>AS16 flat bar steel</td></tr>
<tr><td>9</td><td>AS1241 flat bar steel</td></tr>
<tr><td>10</td><td>AS20S flat bar stell</td></tr>
<tr><td>11</td><td rowspan="2">HVOF flat bar steel</td></tr>
<tr><td>12</td></tr>
</table>

Various suggestions for amendments in the basic models and appropriate correction factors have been established after experimentally measuring the lining surface strains and comparing these with the predicted strains. The details of this work are presented in the next section.

5.1.4. Summary of the sensitivity analysis

The sensitivity studies based upon the variation of layer thicknesses and mechanical properties show that in either case the dominating effect on the resultant surface stresses and strains is caused by changing the steel layer thickness or mechanical properties.

Table 5.2: Effect of changing mechanical properties of different layers on the maximum lining surface stress and strain. A negative sign indicates a decrease in the quantity.

Change in layer properties	% Increase in the layer UTS	%Increase in the layer 0.2% proof stress	% Change in lining bending 'σ'	% decrease in the resultant top lining plastic 'ε'
Change in lining layer				
AS1241—AS20S mono	6	10	+5	1
Brazed sheet—AS1241mono	46	30	+30	13
Brazed sheet—AS20S mono	55	43	+37	13
Change in steel backing layer				
HVOF flat bar steel- AS16 flat bar steel	63	55	-22	66
AS20S flat bar steel -AS16 flat strip steel	12	32	-23	66
AS1241 flat bar steel-AS20S flat strip steel	38	22.4	+1	+2

The FE predicted lining stresses and strains remain fairly constant over a range of lining thickness (0.2-0.4 mm) within which most of the current and old bearing lining thicknesses fall.

Similar effects were observed by changing the lining properties from the AS1241 to AS20S where the 0.2% σ stress values of both differ by 15%.

In summary the most prominent effect is caused either by changing the properties or the thickness of the steel backing layer. Little measurable effect on the lining surface stresses or strains was observed by changing the properties of the interlayer.

5.1.5. Experimental validation of FE strain predictions

In the FE models of the bearings and flat bars, the maximum plastic strain develops at the lining surface at the plane of symmetry due to the point load that acts at the top of the backing steel layer. This simulation is in accordance with an ideal three point bend experimental set up where the location of the applied load remains at the same point throughout the test and the specimen supports do not move at higher load steps. The FE model follows the deformation behaviour of each of the layers present in accordance with the supplied stress-strain data and calculates the maximum lining 'σ' and 'ε' accordingly by considering the whole specimen as an assemblage of finite elements. In order to evaluate the accuracy of the FE predictions of the total strains, a similar static three point bend test was conducted on all the current and previously studied bearing and flat bar multilayer systems using the strain gauge set up detailed in the experimental methods Section 3.3.4.

In the fatigue life data, the number of cycles is plotted against the maximum lining plastic strain range and hence the maximum lining surface plastic strain was estimated using FE analysis. However in the experimental set up used, it is impossible to separate the elastic and plastic strains accurately. Thus the total strain developed at the lining surface was measured experimentally and compared with the FE predicted total strain.

In order to get more consistent data, total strain readings were obtained from three strain gauges attached to the lining surface (both bearings and flat bars) parallel to each other along the line where maximum total strain i.e. 'ε_t' was estimated in the FE model. The results are presented separately for the bearings and the flat bar specimens.

5.1.5.1.Flat bar strain analysis

Figure 5.7 (a) shows the plots of the maximum 'ε_t' developing at the lining surface measured experimentally and the corresponding FE predictions vs. applied load for all the previous and current flat bar specimens. As the load increases, the ε-load response above a certain load increases indicating the point where the steel is plastically deforming. The flat bars tested beyond a load of 700N showed permanent bending. In case of the HVOF flat bars, the experimental data is less consistent after a load of 600 N which resulted in a large increase in the total strain (Figure 5.7b). From these curves it is evident that the experimental total strain is in good agreement with the FE predicted total strains up to a certain load (about 650 N approximately for the roll bonded and 600 N for the spray coated systems). However at higher loads, the FE predicted strains are lower than the experimental measured total strains for the RB systems. In the case of the HVOF spray coated flat bar, the FE predicted total strain at the lining surface for the corresponding specimen subjected to the strain measurement test was higher than that observed during the experiment (Figure 5.7(b)).

5.1.5.1.1 Possible causes of deviation. The discrepancies between the experimentally measured and FE predicted total strains at higher loads indicates a disagreement between the actual experimental conditions and the simulated three point bend conditions for the flat bars at higher loads. Careful observation of the experimental set up showed a slippage of the supporting rollers from their initial position during the incremental static load steps. This situation is depicted in Figure 5.8(a). The slippage of the roller increases the load span and hence the bending moment caused by the applied load at the centre of the flat bar. Moreover, it should be noted that the load span will also increase without roller slippage for high bending deflection. The simple relation for the bending moment in this case is

$$M = PL/2 \qquad 5\text{-}5$$

where 'L' is the loaded span of the flat bars and 'P' the applied load.

During sliding of the rollers at higher load steps, the length 'L' increases slightly and causes an increase in the bending moment. The increase in the bending moment causes a decrease of the radius of curvature 'R' of the flat bar which is related to the top lining strain[5] by

$$\varepsilon = y/R \qquad 5\text{-}6$$

where 'y' is the position of the point of maximum strain along vertical (along the thickness of the bar)

As the radius of curvature decreases at higher loads, the tensile strain at the lining surface (at the point of maximum load) increases significantly contrary to the strain predicted by the FE model, in which the effect of increase in the load span was not accommodated.

Both the HVOF and RB systems were subjected to the strain measurement experiment under similar conditions and similar effects are present for the HVOF systems as well, but a careful observation of the failed HVOF flat bar showed a clear crack in the vicinity of the strain gauge attached (Figure 5.8(b)). It is obvious that the portion of the top lining surface under the strain gauge is less affected by the applied load than predicted (when cracking occurs at load higher than 600N). In the actual FE model for the corresponding specimen, the lining was assumed to be intact throughout the loading and hence the calculated strains (by FE model) were overestimated.

5.1.5.1.2 Fitting the FE and experimental data

In order to obtain the best compromise between the FE and experimental results the experimentally measured total strains were plotted versus the FE predicted ones in order to identify the discrepancies (Figure 5.9(a)). The 1:1 straight line is the ideal trend line. For the RB (roll bonded) systems, the data points are quite close to the ideal trend line but for the HVOF systems, the data points are significantly lower than the ideal trend line at higher strains. In order to accommodate the FE predicted and experimentally measured total strain results, a polynomial regression analysis was carried out to determine the best possible fit between the FE and experimental results. The corresponding polynomial equations are shown in Figure 5.9(a) along with the curves for each system. Using these polynomial equations, the modified values of the total strain were obtained. Figure 5.9 (b) shows a comparison of the experimentally measured and the corrected values of 'ε_t' vs. applied load. From these curves the corrected values of 'ε_t' (for both RB and HVOF) are now very close to the experimentally measured 'ε_t' values showing that the fitting process has been successful.

5.1.5.2.Finished bearing lining strain analysis

Figure 5.10 shows the experimentally measured and FE predicted total strains vs. applied loads for all the current (AS20S, AS20 and RB168) and previous (AS16, AS1241) RB bearing systems. These curves show that the FE predicted total strains at the lining surface are significantly lower than experimentally measured similar total strains. From these curves it is evident that this difference is more significant at higher loads for all these systems. The

difference between the experimental and FE predicted total strains for the bearings are much higher than the differences observed for the flat bar specimens discussed in the preceding sections.

5.1.5.2.1 Possible causes of deviation

The significant deviation of the experimentally measured 'ε_t' from the FE predicted 'ε_t' indicates that the basic FE model constructed to simulate the three point bend test for the bearing was based upon assumptions which were not true for the actual three point bend experiment. In the FE model, the bearing ends were assumed to be fully constrained at its ends (constraint was applied to all the nodes present at the supporting ends). This assumption restricts the sliding or rotation of the bearing ends even at the higher loads in FE model. However careful observation of the specimen jig indicates a gap of 0.5-0.7mm between the bearings ends lying inside the supporting constraint and the walls of the rectangular groove of the constraint (Figure 5.11). Thus there is a margin for sliding of the bearing ends. As the applied load increases during the static load strain measurement experiment, these ends are no longer rigid and allow the development of additional strain at the point of symmetry where the maximum load acts. As a result the experimentally measured strains are much higher than the FE predicted total strains (i.e. at a load of 2500 N, the experimental total strain is approximately 50% higher than the FE based strain).

In order to improve the simulation of experimental conditions, the original FE model was modified such that the constraint was applied only on one node at the bearing ends (either outer or inner node).

5.1.5.2.2 Fitting the experimental and FE data for finished bearings

Both the experimentally measured 'ε_t' and those from the modified FE models were plotted against each other in order to perform a similar regression analysis as that applied to the flat bars. The polynomial regression analysis resulted in the best fitting curves as shown in Figure 5.12(a). The polynomial equations shown along each curve were used to evaluate the corrected values of the 'ε_t'. These corrected values along with the experimental values are shown in Figure 5.12 (b). At a load of 1500 N, the corrected values of total strain are 20-25% higher than the values obtained from the FE model.

5.1.6. Estimation of correct surface plastic strains

Since the fatigue lifetime curves are based upon the maximum 'ε_p' developed at the top lining surface, a modified value of the 'ε_p' was therefore required. Using the ratio of the FE predicted 'ε_p' to the FE predicted 'ε_t' (for both bearings and flat bars); a corrected value of the 'ε_p' was obtained (by multiplying it with the corrected 'ε_t' obtained from the regression analysis). Figure 5.13 shows a comparison of the FE based 'ε_p' vs. corrected 'ε_p' values for finished bearings and flat bars. For flat bars (Figure 5.13 (b)), both FE based and corrected 'ε_p' values are quite close to each other; however the corrected 'ε_p' values are higher than the FE 'ε_p' values at higher loads. The trend is however opposite to this in case of the HVOF flat bar systems i.e. lower values of modified 'ε_p' are observed than the actual FE predicted 'ε_p',. For the finished bearings the FE based and corrected 'ε_p' values are significantly different (FE based values are significantly lower). These curves show that using the modified 'ε_p' data instead of the original FE predicted 'ε_p' will have significant impact on the fatigue life curve comparison of all the current and previous lining materials.

In the FE model the materials properties used were based upon data obtained from the original monolithic sheets provided and did not account for the presence of residual stresses due to non-uniform contraction of different layers in the multilayered flat bars (during cooling from elevated temperature) as well as in the finished bearings (also due to bending operations and broaching). However, the actual total strain has been measured experimentally and used to validate and correct the FE results; hence this gives more confidence in using the corrected FE based plastic strain results.

5.1.7. Summary of the strain analysis results

The difference between the experimental and FE predicted surface strains are more significant for the finished bearings than the flat bars. The ε_p values evaluated on the basis of the corrected total strain values for the flat bar specimens are not very different from the original values of the FE predicted ε_p. The FE simulated results are valid for loads lower than or equal to 650N. For loads higher than 650 N both original and corrected ε_p values are slightly different (with a significant difference for the HVOF systems). For finished bearings, this difference is large and hence only the use of corrected ε_p values is appropriate unless the original model is modified to incorporate more accurately the experimental conditions. This correlation approach

has been used to produce estimated ε_p values for the bearing systems evaluated here, and is considered to provide an appropriate materials fatigue resistance assessment parameters.

5.2. Fatigue test results

Fatigue test results from both interrupted and uninterrupted 3-point bend tests have been presented here in the form of total life curves for both bearing and flat bars. Observations of microstructurally short fatigue crack initiation and growth have been carried out on interrupted flat bar tests using acetate replication approaches. Failed specimens were also examined using the optical and scanning electron microscope in order to investigate surface and subsurface crack morphologies.

5.2.1. Lifetime results

Total life of a component is usually expressed in terms of number of cycles versus applied stress or strain. The lining surface stress and strain values used for the construction of *S-N* or *ε-N* type curves for bearings and flat bar specimens are those obtained from elasto-plastic FE model after implementing the experimental corrections described earlier. Table 5.3 and 5.4 give the details of fatigue tests conducted on different bearing and flat bar specimens during current work.

5.2.1.1.Fatigue life on the basis of stress and average pressure

Laboratory fatigue life data was first obtained in the form of σ_t-*N* where σ_t is the maximum lining surface tensile stress developed in a 3-point bend test. The rig test data in the form of S'-*N* was obtained from DGV where S' was calculated from the pressure exerted on the bearing lining during an accelerated rig test based upon a projected area. The loading conditions in a three point bend fatigue test are however different from those in the accelerated rig test and hence σ_t-*N* type data are not directly comparable with the rig test results. In order to compare the laboratory lifetime curves with the rig test data, the contact pressure P_{av} exerted on the backing layer of the bearing was considered comparable equivalent to the S' value presented in the rig test data. This contact pressure was based upon the contact area of the loading roller and the applied load as shown in Figure 5.14 (a)

Figure 5.14 (b) shows fatigue life curves for the AS20S and AS20 bearing obtained from rig test data as well as laboratory based 3-point bend test data on the basis of FE simulated and corrected maximum lining σ_t and calculated P_{av} exerted through the loading roller. It is

evident that curves from the rig test data fit well with the laboratory data in the form of P_{av}-N for the tested AS20S and AS20 type bearing specimens. However the applied loading levels for the 3-point bend test data led towards higher applied pressures and lower lifetimes but the two approaches exhibit reasonable overlap between lifetimes of 10^6-10^7 cycles. The lifetime data based upon σ_t-N was not so close to the rig test results as the lining tensile stresses developed during the three point bend test are dependent upon the elasto-plastic behaviour of the layers present in a complex way (Section 5.1) and may not be linked directly to the simple mechanism implied by the applied average pressure but may be considered to define the local fatigue failure conditions at the lining surface more accurately. The compatibility of the rig test and 3-point bend test data (in the form of P_{av} N) gives confidence in the use of these laboratory based 3-point bend fatigue analyses in explaining fatigue failure processes relevant to the rig test specimens, which are closer to engine loading conditions.

5.2.1.2.Fatigue life based upon maximum plastic strain

Fatigue life is conventionally expressed as *S-N* curves. Such data is useful when dealing with components which undergo low cycle fatigue (LCF) and when the applied stress level does not go beyond the elastic limit. The specimens under current investigation i.e. the bearings and flat bars are composed of a number of layers in which the materials of each layer differ in their mechanical properties i.e. yield point and UTS. Under the fatigue load levels chosen (1800-2000N), the FE predicted maximum stresses developed on the lining surface are within the range of 90-110MPa which is considerably higher than the yield point (~50-60MPa) of the lining layer used in all the bearing and flat bar systems. The fatigue lives of both finished bearings and flat bars were therefore evaluated on the basis of a strain life approach as considerable plastic deformation is encountered in the lining surface under the load levels applied. According to *Joyce's*[1] work on similar systems, if the fatigue life is presented on the basis of maximum top surface stress, the plastic deformation of the specimen will not be accounted for. This was indicated when attempts to fit modified *Basquin* curves[6] on the σ-life data resulted in deviations between different specimen geometries (i.e. bearings and flat bars). Here the ε- life representation, suggested by *Coffin and Manson*[7] seemed to be more appropriate and hence has also been implemented for fatigue life characterization.

To reiterate, the failure criterion for the lifetime fatigue tests was 0.3 and 0.5 mm deflection (from the initial maximum position) in the direction of the applied load for bearings

and flat bars respectively. These criteria were established in previous research and were used here to allow better comparison across all material multilayered systems. For the HVOF spray coated system, only flat bar data was obtained as finished bearings of this system were not available for testing. The results for both finished bearings and flat bar systems are discussed in more detail in the following sections.

Fatigue life data for the current bearing and flat bars tested in air and oil under 3-point bend loadings is presented in Table 5.3 and Table 5.4. The fatigue life of all *Al* based current and old bearing systems is shown in Figure 5.15 in terms of number of cycles to compliance failure as defined earlier, N_f versus the maximum lining surface plastic strain amplitude $\Delta\varepsilon_p/2$ predicted by the corrected FE model after fitting the experimental and FE predicted total strain data (reference to Section 5.1.5).

In this figure, the data for the AS16 and AS1241 bearings tested in air and oil during previous research[2] is also presented; as corrected $\Delta\varepsilon_p$ values for these systems have been evaluated during the current research on the basis of the FE predicted and experimental $\Delta\varepsilon_t$ values. As the experimental results of ε_t showed some scatter, this is reflected in the corrected $\Delta\varepsilon_p$ values, and is incorporated in the fatigue life data in the form of error bars, giving a more realistic picture of the life time behaviour of each individual system.

If the fatigue lifetime results for all the current and previous *Al* based bearing systems are compared on the basis of the modified data, the intrinsic lining materials fatigue resistance of the AS20S/AS20 bearings appears to be much better than that of the AS16 and AS1241 systems under both ambient and oil environments. The AS20S and AS20 systems do not appear to show different fatigue resistance on the basis of the data obtained. On the basis of these comparisons, the interlayer does not seem to affect overall lifetime significantly.

Changing the environment from ambient to oil does not have any significant effect on the fatigue resistance of the AS20/AS20 systems although this was observed for the previously tested AS1241 specimens.

Fatigue lifetime curves for all *Al* based flat bar specimens on the basis of corrected $\Delta\varepsilon_p/2$ values are shown in Figure 5.16. The order of various systems on the basis of increasing fatigue resistance is AS1241→AS16→AS20S. HVOF results are very scattered but appear to show a comparable behaviour to both best and worst performing RB flat bars.

The effect of orientation on AS20S and AS20 lifetimes in which applied tensile stress was parallel and perpendicular to the rolling direction were also compared.

Table 5.3: Fatigue lifetime test results of multilayered bearings

Specimen type	**Environment**	**Maximum $\Delta\varepsilon_p$ at lining surface (corrected)**	**No of cycles 'N' (Ambient)**	**No of cycles 'N' (oil)**
AS20S	Ambient and oil	0.00289	3221926	N.A
AS20S	Ambient and oil	0.003213	5499823	N.A
AS20S	Ambient and oil	0.003968	661367	3760008
AS20S	Ambient and oil	0.004426	437646	379022
AS20S	Ambient and oil	0.004954	358152	365452
AS20S	Ambient and oil	0.005566	286618	379022
AS20S	Ambient	0.006316	173241	156743
AS20S	Ambient	0.007224	161381	230864
AS20S	Ambient	0.008318	155464	N.A
AS20S	Ambient	0.011355	107450	81857
AS20	Ambient and oil	0.003247	4215815	N.A
AS20	Ambient and oil	0.004091	3604904	N.A
AS20	Ambient and oil	0.004616	649116	3919678
AS20	Ambient and oil	0.005236	437712	N.A
AS20	Ambient and oil	0.005982	283053	N.A
AS20	Ambient and oil	0.006912	250989	412380
AS20	Ambient	0.008071	206982	234566
AS20	Ambient	0.009531	134146	107604
AS20	Ambient	0.011427	107637	66375
AS20	Ambient	0.017272	69976	68009
Bronze Bearings				
RB168NH	Ambient	0.00403	399292	N.A
RB168NHT	Ambient	0.00446	256863	N.A
RB168NHT	Ambient	0.00489	99255	N.A
RB168NHT	Ambient	0.00534	77823	N.A
RB168NHT	Ambient	0.00583	68133	N.A
RB168HT	Ambient	0.00403	306814	N.A
RB168HT	Ambient	0.00446	336971	N.A
RB168HT	Ambient	0.00489	336971	N.A
RB168HT	Ambient	0.00534	666539	N.A

Table 5.4: Fatigue lifetime test results of multilayered flat bars

Specimen Type	Orientation	Maximum $\Delta\varepsilon_p$ at lining surface (corrected)	No of cycles 'N'	Comments
AS20S	Parallel	0.002302	912924	Failed
AS20S	Parallel	0.0026	863210	Failed
AS20S	Parallel	0.003057	925179	Failed
AS20S	Parallel	0.0034	723659	Failed
AS20S	Parallel	0.006383	139743	Replication
AS20S	Perpendicular	0.002302	1021950	Failed
AS20S	Perpendicular	0.0026	883269	Failed
AS20S	Perpendicular	0.003057	895638	Failed
AS20S	Perpendicular	0.0034	803698	Failed
AS20S	Perpendicular	0.004383	148688	Failed
AS20	Parallel	0.0028	612458	Failed
AS20	Parallel	0.002302	745263	Failed
AS20	Parallel	0.003057	561364	Failed
AS20	Parallel	0.004383	243371	Failed
AS20	Parallel	0.0054	308662	Failed
AS20	Parallel	0.0046	512453	Failed
AS20	Parallel	0.006226	78562	Failed
HVOF	N.A	0.0031001	194473	Failed
HVOF	N.A	0.0035321	517000	Failed
HVOF	N.A	0.006488	119020	Failed
HVOF	N.A	0.005677	79512	Replication
	N.A	0.006177	111944	Replication
	N.A	0.003632	215202	Failed
	N.A	0.002134	78192	Failed

There is no measurable difference in the lifetimes exhibited by specimens in either orientation (although this was observed in the AS16 where a more pronounced directionality in the microstructure was observed).

A comparison of fatigue life of AS20S bearings (the systems proving best fatigue resistance among all RB *Al* based systems) with the currently developed RB168 bearing specimens (in both heat treated and non-heat treated conditions) is shown in Figure 5.17. It is

evident that as received RB168 specimens (non-heat treated) showed a similar fatigue life trend to the AS20S/AS20systems. Fatigue resistance of the RB168 heat treated specimens was however observed to be somewhat more than the non-heat treated specimens and showed the best overall performance.

5.2.2. Effect of specimen geometry on fatigue life

Figure 5.18 shows a comparison of the fatigue life of finished bearings and flat bar specimens on the basis of the corrected ε_p-$N_.$. It is noted that the lifetime data for both specimen geometries (considering all current and previous systems) is in good agreement except some discrepancy observed in the AS20 system (which might be due to experimental scatter and could be overcome by performing more tests). This gave confidence that specimen geometry and loading differences have been adequately accounted for in the analysis. The failure criteria used for the finished bearings and flat bars during current and previous research was based upon the similar level of lining surface damage (cracks) of both geometries. The similar life time trend of the two specimen geometries hence supports the assumed failure criteria adopted for the two different geometrical shapes.

The lining surface of the finished bearings and flat bars were examined after the designated failure criteria were achieved and in each case it was found that it was long cracks coalesced together to form a dominant crack that caused gross failure. The deflection in the bearing was monitored during cycling in load control. It was observed that 90 % of the compliance deflection occurred at ~ 95% of N_f.

5.2.3. Behaviour of short fatigue cracks

The comparable fatigue life behaviour of both bearing and flat bar geometries gave confidence in using flat bar specimens for replication studies to analyze initiation and growth of short fatigue cracks in more detail.

For more detailed analysis of the initiation and growth behaviour occurring, large area replication (~360 mm^2) of the flat bars obtained from AS20S, AS20, and HVOF spray coated systems was carried out during interrupted fatigue tests at the same plastic strain level (ε_p=0.0060±0.0004). RB168 systems were not available in the form of flat bars hence the detailed analysis of short fatigue crack initiation and growth is limited to the *Al* based systems. The local stress and sample parameters for these observations are shown in Figure 5.19.

AS20S/AS20 flat bars were tested in tensile orientations parallel and perpendicular to the rolling direction. As similar lifetime trends were observed for two orientations (Figure 5.16), hence the detailed initiation analysis was only carried out for specimens tested in tensile orientation parallel to the rolling direction. The values of σ_t have been calculated by the elasto-plastic FE model whereas the ε_p values were obtained after multiplying the FE predicted values with an appropriate correction factor (reference to Section 5.1.5). The other parameter indicated in the diagram is the yield stress σ_y of the lining layer of AS20S/AS20 as obtained from a tensile test upon the monolithic lining layer. The σ_y value for the HVOF system used is one obtained for the AS1241 monolithic layer as no monolithic layer for the HVOF system was available. The HVOF lining showed approximately similar microhardness values to those shown by the AS1241 lining.

The overall flat bar surface of each system was defined in a two dimensional coordinate system in order to investigate the micro-crack fields developing at the lining surface. In this coordinate system, the X-axis lies along the length of the loading span and the Y-axis along the width of the flat bar (the width of the replicated surface) normal to the tensile stresses σ_t developed at the lining surface. The dominant cracks observed on the lining surface of the failed flat bars lay more or less parallel to the Y-axis.

The distribution of stresses calculated by the corresponding FE model (Figure 5.1) shows that the value of $\sigma_{gradient}$ within an area of 2 mm (where cracks were observed) were 4.5 and 6 MPa/mm for the AS20S/AS20 and the HVOF spray coated systems respectively. The corresponding ε_p gradient values were 0.0012 and 0.001/mm indicating that both stresses and strains do not vary much within the area (~1-2mm) where short fatigue cracks initiate and grow. However appropriate stress or strain values have been used for particular crack locations in all subsequent analyses.

5.2.4. Short crack initiation

The presence of second phase particles was evident from the microstructural characterization of the lining layers of both RB and HVOF spray coated systems (Reference to Section 4.1.1). The second phase regions observed in the HVOF spray coated system were circular unmelts surrounded by *Sn* rich areas with very few intermetallics whereas in the AS20S/AS20 lining, *Sn*, *Si* and intermetallic phases were observed. It is an established fact that inclusions and secondary phase particles are common sites for crack initiation[8]. Previous studies

by *Mwanza*[9] on similar *Al* plain bearing alloys (AS16) have shown that the size and shape of both *Sn* and *Si* affected fatigue crack initiation. However the size, shape, distribution and mechanical properties of these particles may vary from one system to the other giving rise to different initiation mechanisms in different alloys.

For RB168 systems, specimens in the form of flat bars were not available and hence short crack initiation and growth results via acetate replication were not conducted. The surface analysis of short cracks for this system was only confined to a qualitative microstructural investigation of surface and subsurface crack morphologies.

5.2.4.1.Crack initiation in AS20S/AS20 lining

Fatigue testing on the flat bar specimens was interrupted frequently during the early stages of life, every 500 cycles, in order to track crack initiation events. Cracks were observed on the AS20 lining surface after 17000 cycles whereas in the AS20S lining, initiation was observed after 27000 cycles. Figure 5.20 (a) and (b) show optical images of the replicas obtained from the AS20S and AS20 flat bar lining surface which exhibits some crack initiating regions. It is evident from these micrographs that crack initiations is related to the breaking or decohesion of secondary phase particles. However, the exact nature of the initiating particle is still difficult to assess even after careful observation of the optical micrograph of the replica. As discussed in Chapter 4, the microstructural features in the AS20S/AS20 lining were hard to distinguish optically especially in the regions where clusters of *Sn* and intermetallics were observed with *Sn* regions mostly encapsulating the intermetallics.

In order to observe the crack initiating secondary phase particles in more detail using the FEG-SEM, a flat bar AS20S specimen was subjected to a number of fatigue cycles (~20000 at a plastic strain of 0.0062) that resulted in discernable fatigue damage on the lining surface by OM. The BEI images shown in Figure 5.20 (c &d) reveal that cracks initiate preferentially within the cluster of *Sn* and intermetallic regions in which both cracking of intermetallics as well as decohesion of *Sn* and intermetallic interfaces was observed. Figure 5.20(e) presents a large low magnification area obtained from a fatigued AS20S lining indicating some other low strain (ε_p= 0.0055-0.0060) crack initiating regions showing a similar trend. A quantitative assessment of various features of fatigue initiating particles is given in detail in chapter 6.

5.2.4.2.Crack initiation in the HVOF spray coated lining

The microstructural dependence of crack initiation in the HVOF spray coated flat bar lining is somewhat difficult to observe as features such as *Sn* particles are expected to be distributed at a finer scale. These finer features made it difficult to assess replicas of the coating surface during an interrupted fatigue test. Figure 5.21(a) shows the replica obtained from an HVOF coating which does not show particularly distinct microstructural details. More useful information was obtained by investigating the surface of the flat bar specimen subjected to 500 fatigue cycles at a plastic strain of 0.004 in the SEM to observe small cracks initiating from various regions. The purpose of testing the HVOF specimen at a plastic strain lower than that of the AS20S specimen was to get as many initiating sites as possible which otherwise would have been difficult as cracks in the HVOF lining grow very fast at higher plastic strains. Figure 5.21(b & d) show the BEI and SEI images obtained from a low ε_p region (0.0030—0.004) of the failed HVOF coated surface in which a crack seems to be initiating from the interface between circular unmelts present in the microstructure and the surrounding matrix. There was some evidence of crack initiation from the pores scattered throughout the microstructure as evident from Figure 5.21(c). These pores were also observed to surround the unmelt regions and it was difficult to judge the exact cause of crack initiation at these unmelt interfaces.

5.2.5. Short crack propagation behaviour

In order to study the lining surface growth behaviour of short fatigue cracks, AS20S/AS20 and HVOF flat bar specimens were subjected to load levels that gave similar maximum plastic strain levels (0.0060±0.0004) for a better comparison. In all systems short fatigue cracks (of the order of 5-10μm) initiated and grew finally coalescing to form longer cracks (of the order of 1-2mm) which subsequently coalesced to similar macro cracks until the gross deflection failure occurred. Intermittent replication was used to monitor the growth behaviour of cracks in each system.

5.2.5.1.Surface short crack growth behaviour of *Al* based systems

Figure 5.22 shows typical regions showing individual crack growth in all three systems at the same ε_p level. Cracks in the AS20S lining appeared after N/N_f ~ 20% and propagated independently (unaffected by each others presence) for a significant time fraction of life after which they coalesced to form larger cracks. The same trend was observed in the AS20

lining (both linings have the same microstructure, just the interface differ) although the cracks appeared earlier compared to the AS20S system. For the HVOF system, cracks of length ~1mm appeared on the surface after the first few loading cycles, however the cracks shown in Figure 5.22 (c) are typical of those obtained from a region further away from such long cracks to allow observation of typical individual crack growth. HVOF cracks initially propagate at a faster rate compared to the RB systems at the same ε_p level.

The general behaviour of surface short crack growth for the AS20S, AS20 and HVOF lining is shown in Figure 5.23 in the form of *da / dN* versus *projected crack length* curves. These curves reveal the growth behaviour of different cracks at different crack lengths during lifetime. It is evident that propagation behaviour of individual cracks in the AS20S and AS20 systems is similar. Small cracks grow steadily during early stages of the fatigue life. The peaks in the curves show a sudden increase in the growth rate when two cracks coalesce together as a result of which the apparent length of the crack (*projected length* in this case) under observation increases dramatically. In the lining surface of both AS20S and AS20 systems, most of the coalescence events occur in the latter part of the lifetime to form dominant cracks. Dominant cracks within the region where maximum bending (σ~ 105MPa) acts finally coalesce leading to the failure of the specimen. In both systems, small cracks also emerged in the neighbourhood of the narrow maximum ε_p band (~1.5 mm wide), but they did not show any significant growth due to shielding effects from neighbouring cracks.

The crack growth behaviour of the HVOF spray coated systems is different from that observed in the AS20S lining. Cracks initiating from numerous sites grew faster during the early lifetime (first 4000 cycles) and coalesced to form big cracks. One crack shown in Figure 5.24 was a typical crack which achieved a length of ~ 1.4mm during the first 1000 cycles (actually it grew to a significant length when viewed after the very first cycle). However the short cracks which emerged during the first 1000 cycles coalesced quickly to form longer cracks the further growth of which was slower during the rest of the life time. The overall growth rate of the HVOF cracks after their early coalescence is extremely sluggish compared to those of the AS20S/AS20 systems resulting in comparatively similar life times.

5.2.5.2.Crack growth characterization on the basis of ΔK versus *da/dN*

Crack growth behaviour is usually expressed in terms of stress intensity range at the tip of a crack due to a far field tensile stress versus the growth rate of the crack. ΔK values for

the growing cracks were calculated from the *Scott and Thorpe*[10] equation as given below assuming the crack geometry shown in Figure 5.25 (a).

$$K_s = [M_{f(0)}\{1-\frac{0.3a}{W}\}\{1-(\frac{a}{W})^{12}]+[0.39E(k)\{\frac{a}{W}\}^{12}\sqrt{c/a}\}]\frac{\sigma_{\max}}{E(k)}\sqrt{\pi a}$$

$$M_f = [1.21-0.1\{a/c\}+0.1(a/c)^4]\sqrt{\frac{a}{c}} \qquad 5\text{-}7$$

$$E(k) = [1+1.47\{a/c\}^{1.64}]^{1/2}$$

where

a = half crack length

W = width of the specimen

c = crack depth

σ_{max} = maximum applied tensile stress

$M_{f(0)}$ = correction factor allowed for semi-elliptical crack shape

$E(k)$ = elliptic integral of second kind

ΔK is the difference in the K values at maximum and minimum values of the far field tensile stress. The σ_{max} and σ_{min} values were calculated from the FE model for each system. In this work the value of a/c is difficult to assess from surface observations and hence the crack is considered to be of a semi-circular shape. However this assumption is only valid until the cracks remain uncoalesced. With successive coalescence, the a/c ratio increases (Figure 5.25 (b)) and the crack shape is no longer semi-circular. Therefore, the ΔK calculations for coalesced cracks will be less valid and the a/c ratio needs to be corrected. The values of σ_{max} developed at the lining surface of the AS20S/AS20 and HVOF system were 105 and 110 MPa and the σ_y is 55-60MPa. Hence the short cracks are growing under highly elasto-plastic conditions and LEFM conditions clearly do not apply well. Nonetheless the analysis is done to provide a correlation parameter that takes account of local lining stresses and to compare different systems investigated during similar work on AS1241 and AS16[2].Figure 5.26 (a) shows da/dN versus ΔK curves for cracks growing in the AS20S, AS20 and HVOF spray coated linings. All three curves show considerable scatter. As the lining materials are microstrucurally inhomogeneous in all three systems, there is significant variation in the da/dN values for three systems. The variation in the growth rate due to second phase particles in the AS20S lining is evident from Figure 5.27 (a). It is clear that as the crack approached secondary phase (which

was either *Sn* or intermetallics) there was a sudden decrease in its growth rate from $1x10^{-5}$ to $9.1x10^{-6}$ mm/cycle. The growth rates of cracks in the AS20S and AS20 systems appear similar but in the HVOF lining, initial crack growth rates are faster than in the AS20S/AS20 systems (Fig 5.26(a)) but decrease till the end of the lifetime. As the surface crack length increases, the values of the subsurface crack depth *c* are expected to approach the lining thickness. The lining thicknesses were 200-400 μm in both AS20S/AS20 and HVOF systems and as cracks approached a surface length (2a) of ~1.1 –1.3mm (Figure 5.23), the value of *c* (based upon semicircular assumption, a/c=1) reaches the value of the lining thickness. As the subsurface crack is retarded or shielded by the harder steel layer as shown in Figure 5.26 (b), the observed crack growth rate falls (Figure 5.26(a) and Figure 5.23). However prior to this the growth rate of the HVOF cracks is significantly higher than that of the AS20S/AS20 cracks due to quick growth and many coalescence events taking place.

5.2.5.3.Projected crack tip spacing vs. *da/dN*

Figure 5.28 shows the relation between projected spacing between the tips of two cracks and their individual growth rates. It is evident that the growth rates of most of cracks significantly increase as soon as their tip spacing is reduced. The curves plotted are for cracks observed in both low and maximum ε_p regions. There were multiple initiating sites because the initiating particles (usually intermetallics and *Sn* for AS20S/AS20 lining and pores or unmelts for the HVOF) were observed to be scattered throughout the microstructure. In such microstructures cracks initiating from different regions interact with each other differently. Many collinear type interactions were observed in both the AS20S and AS20 lining throughout the lifetime in which the growth rate of the crack under consideration instantly increases as obvious from Figure 5.28(a). Crack tips of many small cracks in the HVOF system were observed to be shielded due to parallel overlap of the tip of a long crack growing at a faster rate (Figure 5.28 (b)). This type of shielding was also observed in the AS20S and AS20 systems although mostly in the low ε_p regions.

5.2.5.4.Crack fields

. Figure 5.29-Figure 5.30 show the evolution of the crack fields in a 2-D coordinate system developed during a fatigue test at different life time intervals from multiple sites for the AS20S and HVOF spray coated lining. For the AS20S the cracks appearing at N/N_f = 20% grow consistently with some coalescence events occurring in the high ε_p region. The small cracks

developed in the low ε_p region were mostly shielded as evident from. Figure 5.29. Finally at $N/N_f = 90\%$, small collinear cracks have formed a dominant crack leading towards the failure of the specimen.

Crack fields in the HVOF systems are shown in Figure 5.30 at different life times. Many more cracks were observed on the surface at a lifetime fraction significantly smaller than that of the AS20S systems. Early coalescence observed in the HVOF ($N/N_f = 10\%$) resulted in the formation of big cracks dominating the local area and arresting the tips of many small cracks even in the high ε_p region. Although the number of cracks observed in the low ε_p region (0.0035-0.004) was more than observed in the AS20S/AS20 lining, their further growth was retarded due to the fast growing and coalescing cracks in the high ε_p region.

5.2.5.5.The tortuosity of crack tip trajectory

In the two dimensional coordinate system applied to the lining surface of the flat bars, the position of the tips of individual cracks were measured in order to trace their trajectories throughout the microstructure. These positions were measured at different lifetime fractions in order to observe the level of tortuosity in their path. In Figure 5.31, the crack tip trajectories have been shown in such a way that their displacement along the horizontal (parallel to the applied maximum σ_t) gives an indication of the tortuosity. The origin of each crack is also shown in the same diagrams. Crack tips were observed to be displaced frequently away from normal to the applied σ_t which shows that the advancing front of the short cracks are microstructurally attracted or repelled by certain microstructural features such as *Sn* / intermetallics (Figure 5.27). This behaviour was observed for both the AS20S and AS20 systems which indicate that cracks are highly sensitive to local microstructure. The level of tortuosity observed in the trajectory of the HVOF short crack tips was slightly higher than that observed in the AS20S/AS20 systems. The measurement of tortuousity was obtained by the following formula

$$Tortuosity = a_{actual}/a_{projected}$$

where a stands for crack length. The higher the value of the above term, the more tortuous the crack is. For a number of cracks growing from different regions, this value was calculated for different systems at the initiation, mid and end of fatigue life. The averaged values are given in Table 5.5. For the RB168 system, measurements were only taken from the failed surface of bearings. It is clear that the HVOF lining showed highest level of tortuosity

compared to all other systems although the tortuosity level in the AS20S/AS20 type linings was comparable.

Table 5.5: Measured values of crack tip tortuosity

Lining type	Tortuosity
AS20S	1.7±0.32
AS20	1.6±0.38
HVOF	1.8±0.41
RB168-NHT	1.2±0.33
RB168-HT	1.3±0.15

5.2.5.6.Surface crack morphology of RB168 overlay layer

The surface layer of the RB168 non- heat treated specimen was a *Sn* layer (*SnO* in the case of the heat treated specimens), and the cracks shown in Figure 5.32 are portions of dominant cracks developed during fatigue lifetime tests. Both *Sn* and *SnO* are continuous materials with no secondary phase regions apart from some inhomogeneities in the form of pores (which was more evident from the unpolished surface of heat treated finished bearings), hence the observed cracks had a straight trajectory.

Figure 5.32(b) and (d) show the coalescence of two dominant cracks for non-heat treated and heat treated specimens respectively. The measured tortuosity values of a number of dominant cracks (Table 5.5) as well as small cracks from low ε_p regions were somewhat lower compared to similar measurements for the *Al* based linings. Hence, the surface growth behaviour of the short fatigue cracks in case of the RB168 overlay layers appears to be much simpler than that of the RB and spray coated *Al* based linings.

5.3. Subsurface crack growth in the layered systems

Optical micrographs of fatigue cracked AS20S, AS20 finished bearings and HVOF flat bar (at a nominal maximum plastic strain of 0.0011 and load ratio of 0.1) sectioned perpendicular to the surface are shown in Figure 5.33. These images show the difference in the crack propagation routes through the layers of the specimen in the AS20S, AS20 and HVOF systems. The crack in the case of the AS20S (Figure 5.33(a)) seems to be deflecting within the

Al interlayer. The crack behaviour of the AS20 bearing (Figure 5.33(b)) under the same loading conditions appeared different from that observed for AS20S bearing. The crack in this case seemed to propagate through the lining layer and deflects at the steel/interlayer interface. As the interlayer of the AS20 system itself is complicated (composed of 3003 and 4343 alloy discussed earlier), with the thinnest 4343 layer adjacent to the steel layer it may be that the crack has deflected in the very thin 4343 interlayer region. The microhardness test on the thin 4343 layer of the monolithic brazed sheet showed lower hardness number values than that for the core 3003 layer. This seems to be in agreement with prior work on crack shielding[12] in which the crack traveling from harder 3003 layer is deflected within the softer 4343 layer. However the BEI images (Figure 5.33(c)) obtained from the region where the crack deflects reveals crack penetration deep into the backing layer. Careful observations of the BEI images of the failed AS20 bearing at the interlayer also show detachment of the very thin 4343 layer.

An optical micrograph of the HVOF fatigue tested specimen indicating crack propagation through thickness is shown in Figure 5.33 (d). There is no interlayer present and the crack deflected and bifurcated at the steel/lining interface as it approached from a softer lining towards the harder steel layer. The crack after passing through the lining layer has propagated along the interface between lining and the surface. This reflects poor interface strength.

Figure 5.34 shows micrographs of the cross-section of failed bearing specimens of RB168. The dominant crack in both heat treated and non-heat treated specimens appeared to be penetrating deep into the steel layer. Cracks for both types of specimens did not show any deflection during subsurface growth between different layers. The Ni_3Sn_4 intermetallic layer formed at the *Sn-Ni* interface is stiffer (E=51 ±15GPa) than *Sn* (E=45GPa) as is obvious from nano-hardness test results (Section 4.2.2) as well as reported by *Luhua et al*[11]. The observed slightly increased fatigue resistance of the heat treated specimen could be attributed to the presence of harder intermetallic layer between the very thin *Sn-Ni* layers that might have restricted the subsurface penetration of the fatigue crack to some extent, however observations of crack growth behaviour in these very thin top surface layers is challenging.

5.4. Summary of the results

The fatigue behaviour of different multilayered systems has been studied on the basis of a plastic strain life approach. Crack initiation and growth observations have been

carried out on interrupted flat bar tested samples. Fatigue life studies of the finished bearings based upon the curves plotted between N and corrected ε_p values showed that the AS20S and AS20 bearing systems have a better fatigue resistance compared to that of the previous AS1241 and AS16, a comparable behaviour to the bronze bearing systems (in the non-heat treated condition). However, RB168 bearing system in annealed conditions showed much better fatigue resistance compared to all the *Al* based systems. Comparable lifetime trends were observed when the corrected ε_p –N data was plotted for two specimen geometries (i.e. bearing and flat bar) which indicates that the different established failure criteria for each geometry are comparable. In the flat bars, the lifetimes of the HVOF system were very scattered but slightly higher than the AS1241 and AS16 RB flat bars. However the lifetime data for the AS20S and AS20 flat bars seemed to be close to the best lifetimes shown by the HVOF flat bars and more consistent.

Microstructurally short fatigue cracks appeared on the AS20S and AS20 flat bar lining surface after 20% and 15% life time respectively whereas cracks instantly appeared on the surface of the HVOF lining (after only 5% life time) although the surface plastic strain levels for all three systems were estimated to be similar. For the AS20S lining surface, cracks appeared to be initiating from the clusters of *Sn* and intermetallics mostly by cracking of the *Sn*-intermetallic interface or the intermetallics themselves, whereas for the HVOF spray coated systems, decohesion of circular unmelts were observed to be the crack initiating sites. In the lining layer of the AS20S and AS20 flat bars, individual growth of single cracks was more evident and crack coalescence and shielding was only observed after a significant proportion of the lifetime. For the HVOF spray coated system, cracks were observed to be growing from the first few loading cycles and retarded the further growth of many small neighbouring cracks in both high and low strain regions. Surface cracks on the RB168 (both heat treated and non-heat treated condition) overlay layer were quite straight compared with the *Al* based systems. The measurement of the location of crack tips showed that a similar level of tortuosity existed in the AS20S and AS20 lining as cracks in both linings exhibit similar microstructural sensitivity in short crack growth behaviour (both linings have the same microstructure). However, the trajectories of the HVOF crack tips appeared slightly more tortuous than that of the other two systems, indicating a different scale of microstructural sensitivity in crack growth behaviour. The lowest tortuosity of the crack path was observed in the RB168 system in *Sn* and *SnO* overlay layer.

Cracks in the case of the AS20S system appeared to be deflecting within the *Al* interlayer whereas for the AS20 system, the cracks were observed to be deflecting within the narrow strip of 4343 layer of the brazed sheet (the latter appeared to be comparatively softer during microhardness testing). In case of the HVOF spray coated system, the penetration of the dominant crack through the lining layer resulted in deflection at the lining and backing layer interface with observed debonding at some locations. Subsurface trajectory of cracks in the RB168 bearing showed some evidence of crack deflection along the lining-backing interfaces. However, there were clear evidences of crack penetration into the harder steel backing layer.

References:

[1] Joyce, M. R. (2000). PhD thesis, University of Southampton, UK.

[2] Mwanza, M.C. (2004). PhD thesis, University of Southampton, UK.

[3] Love, P. P, Forrester, P. G. Burke, A. E. (1953). Proc. Inst. Mech. Engrs. Automobile Division, 2.

[4]Duckworth, W. E. and Walter. G.H. (1956), Int. Conf. Fat. Metals, 582

[5] Hibbeler, R.C. (1997). Mechanics of Materials, 3rd Edition, Prentice Hall Int. Pubs.

[6] Basquin, O.H. (1910). Proc. ASTM 10, 625.

[7] Manson, S.S. (1954). Behaviour of Materials Under Conditions of Thermal Stress, National Advisory Commission on Aeronautics: Report 1170.

[8] Kunio, T. Shimizu, M. Yamada, K. and Sakura. (1981).Int. J. Frac 17, 111.

[9] Mwanza, M.C. Joyce, M.R. Lee, K.K. and Reed, P.A.S. (2003) Int. J. Fat. 25, 1135

[10] Scott, P.M. and Thorpe, T.W. (1981). Fat. Eng. Mater. Struct 4, 291.

[11] Luhua, X. John, H.L. (2005). Thin Solid Films xx, 5.

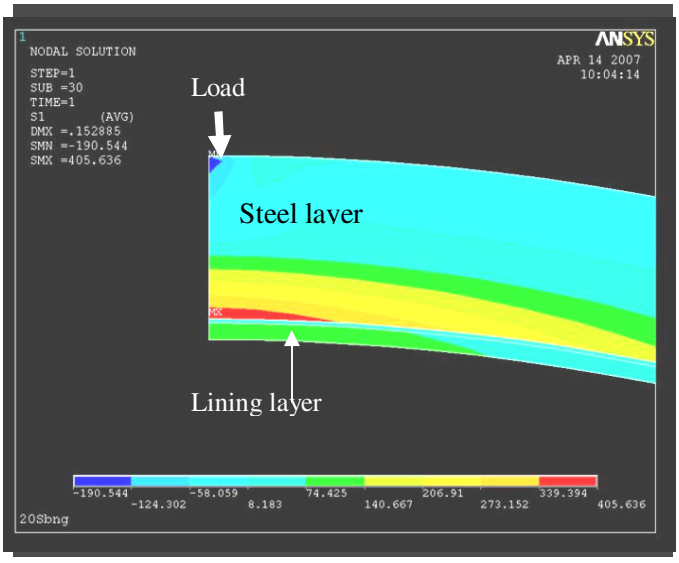

(a)

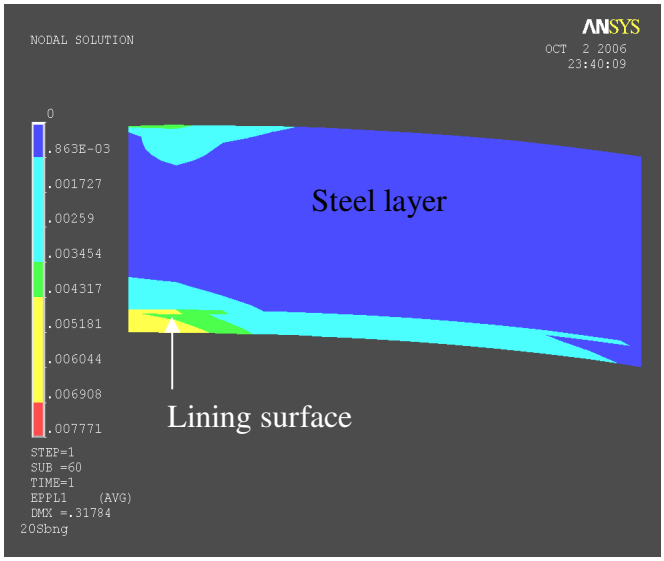

(b)

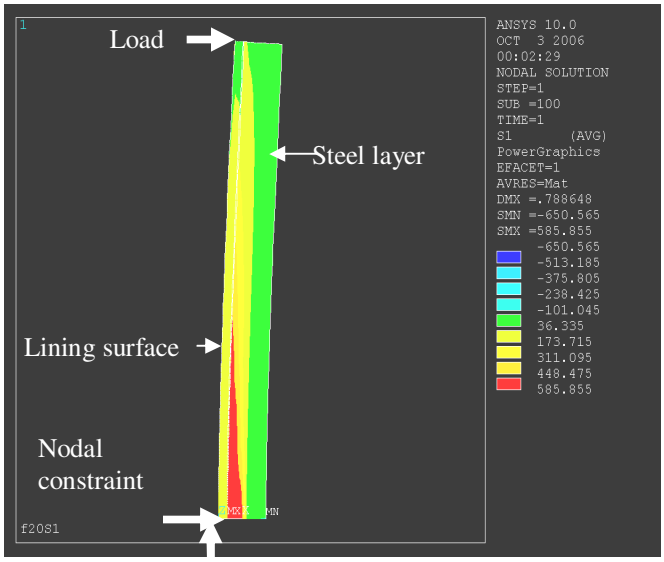

(c)

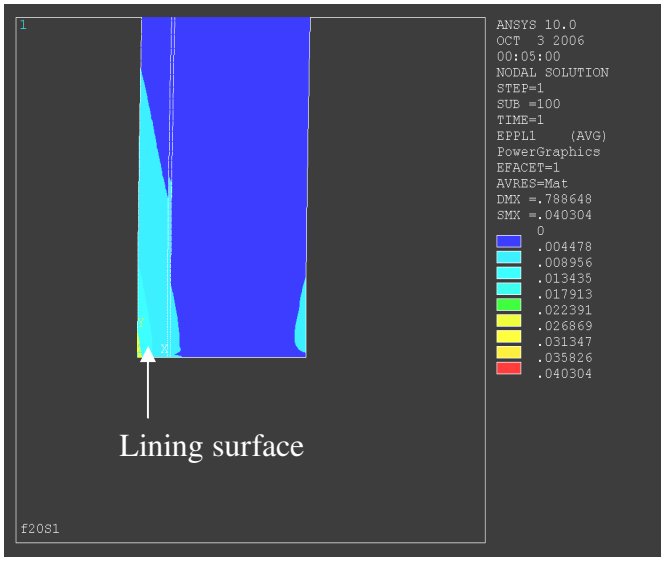

(d)

Figure 5.1: FE simulated stress strain profiles through different layers developed under three point static bend test for the AS20S (a) bearing tensile stresses (b) bearing plastic strains (c) flat bar tensile stresses (d) flat bar plastic strains.

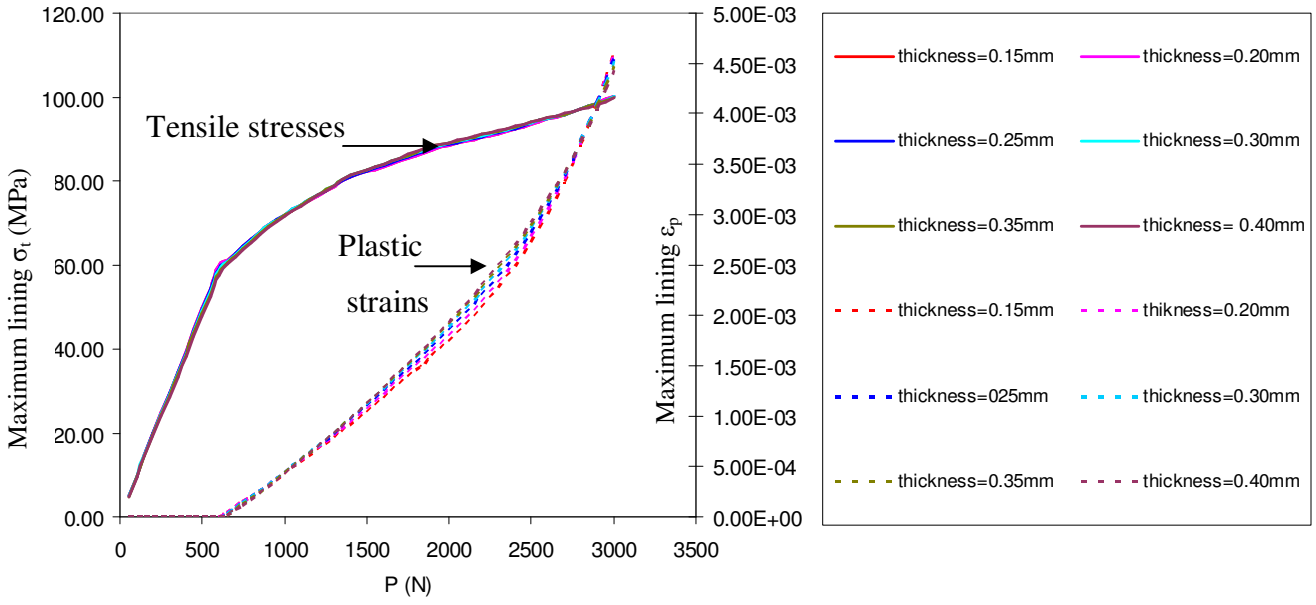

(a)

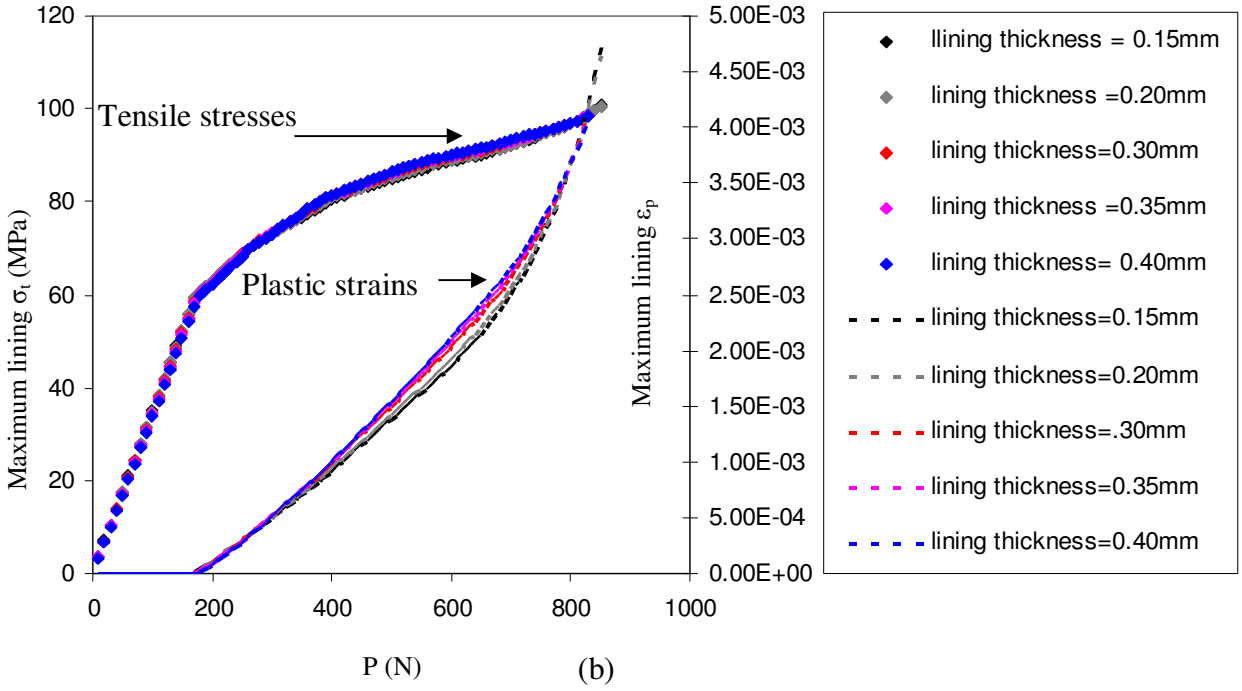

(b)

Figure 5.2: Effect of lining layer thickness on maximum lining surface tensile stress and plastic strain for (a) bearing and (b) flat bar specimen. AS20S monolithic lining, *Al* and AS20S flat bar steel elasto-plastic properties have been used for lining, inter (0.04mm thick) and backing layers (1.5mm thick) respectively.

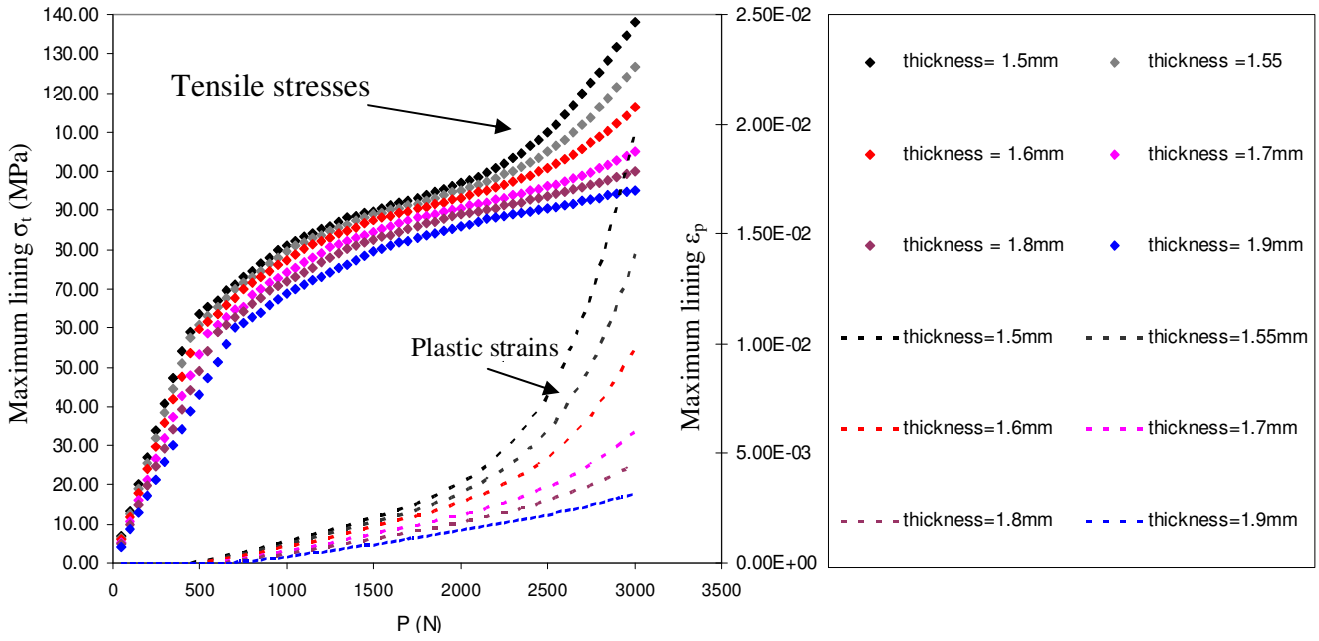

(a)

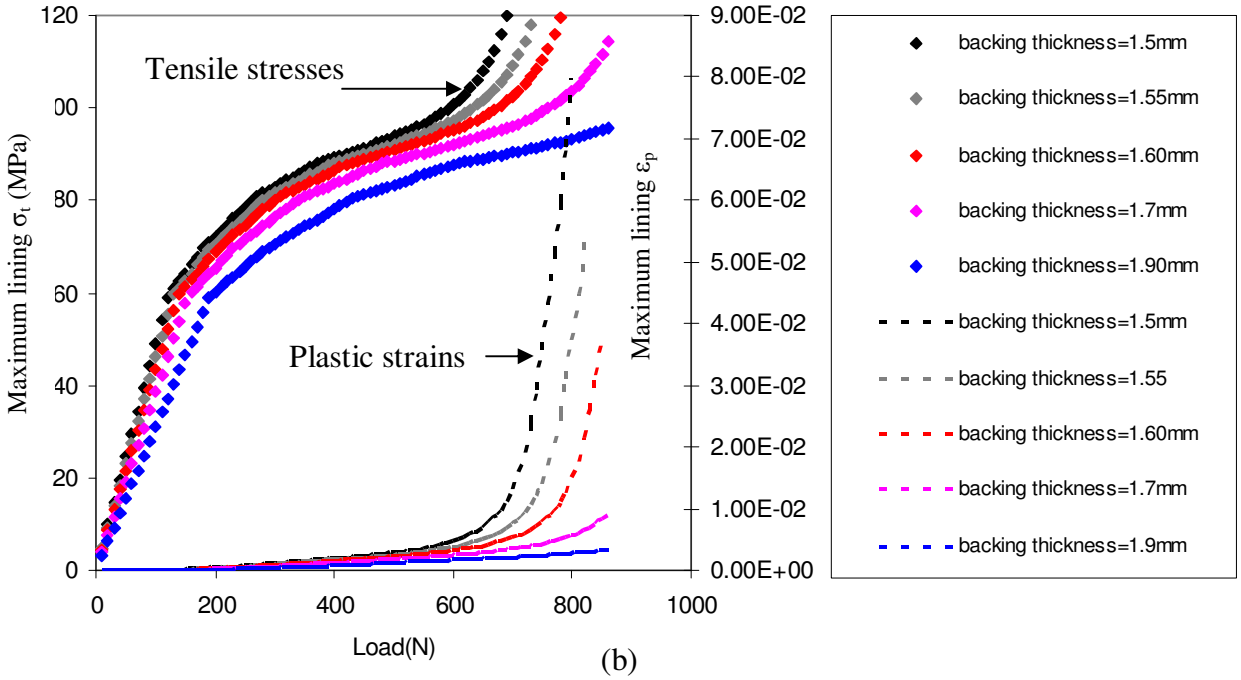

(b)

Figure 5.3: Effect of backing layer thickness on maximum lining surface tensile stress and plastic strain for (a) bearing and (b) flat bar specimen. AS20S lining, Al foil and AS20S flat bar steel elasto-plastic properties have been used for lining (0.3mm thick), inter (0.04mm) and backing layers respectively.

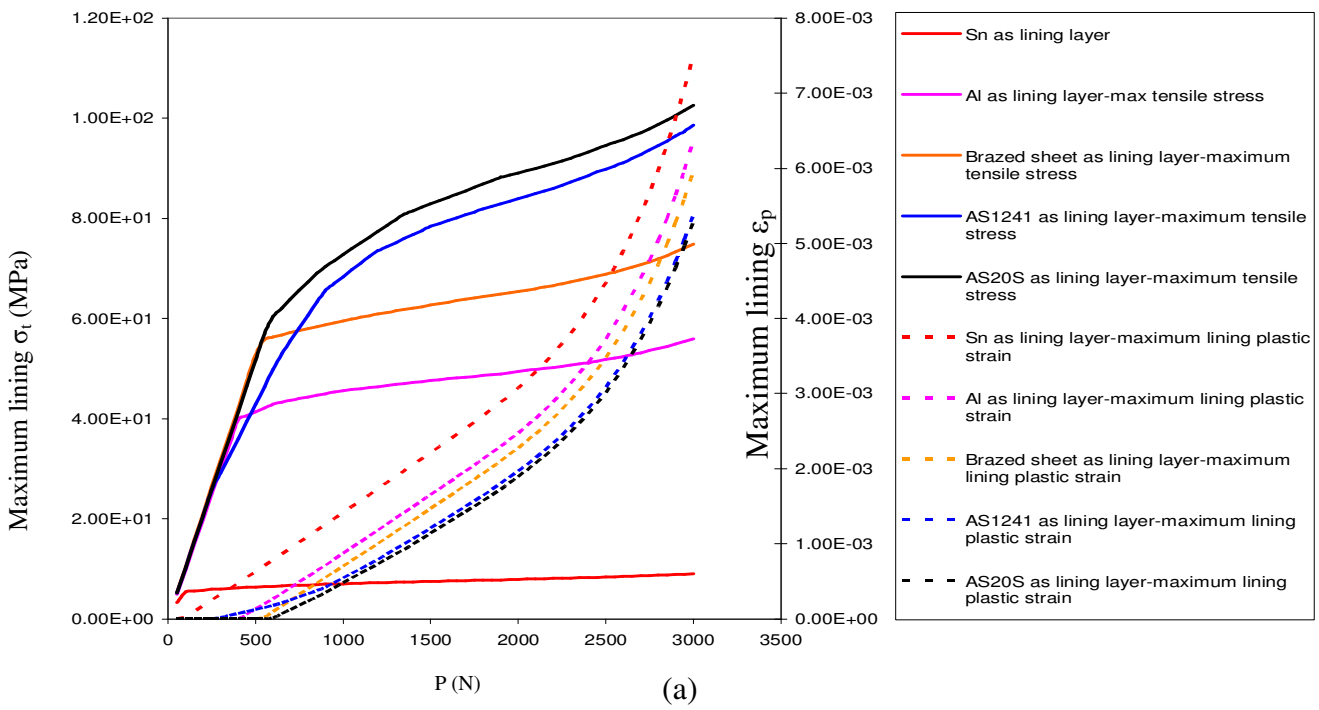

(a)

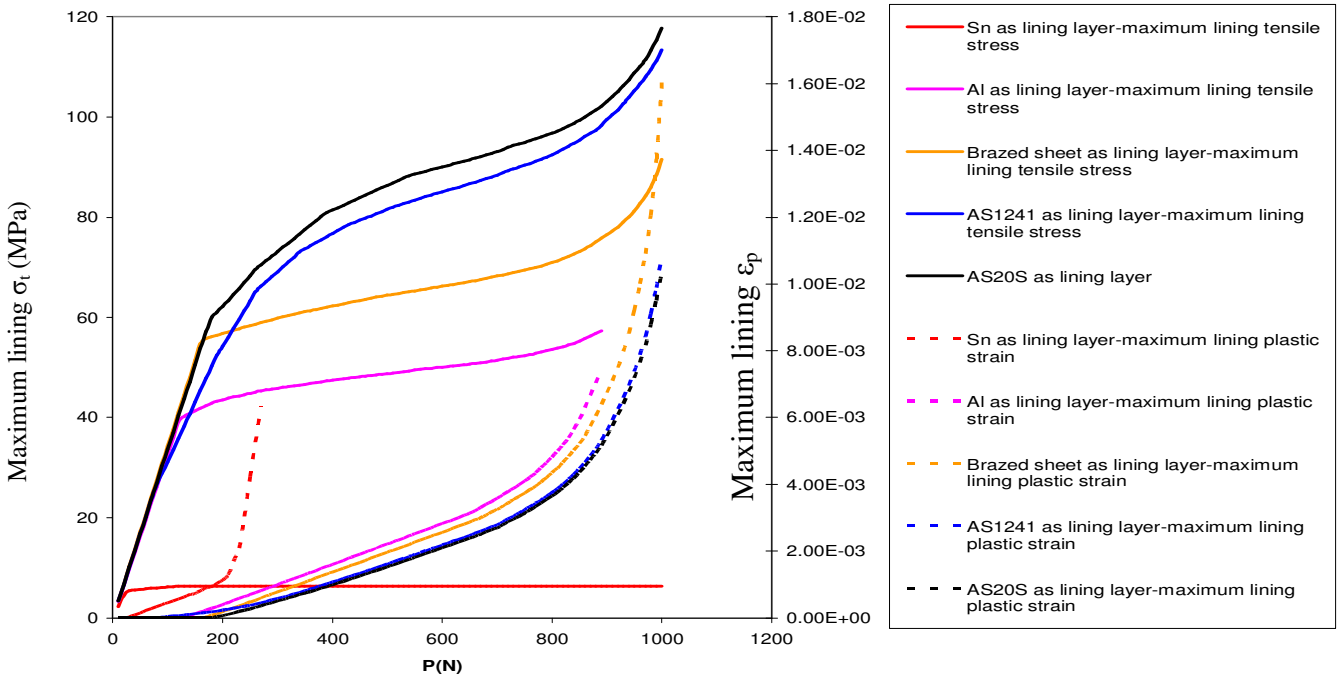

(b)

Figure 5.4: Effect of variation of lining layer tensile properties on the lining surface stresses and plastic strains for (a) bearing (b) flat bar specimens. AS20S flat bar steel (1.5mm thick) and *Al* foil (0.04mm thick) were used as backing and interlayers respectively (lining = 0.2mm thick).

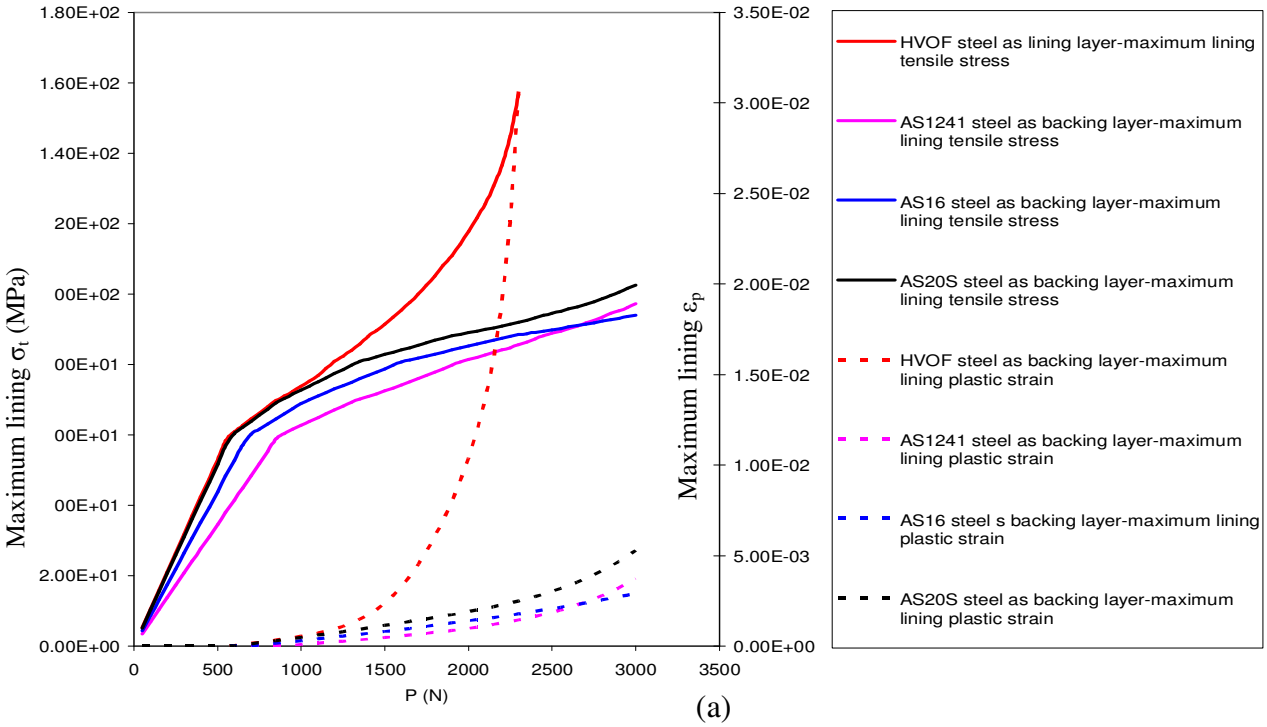

Figure 5.5: Effect of variation of backing layer tensile properties on the lining surface stresses and strains for (a) bearing (b) flat bar specimens. AS20S monolithic lining (0.2mm thick) and *Al* foil (0.04mm thick) were used as lining and interlayers respectively (backing =1.5mm thick).

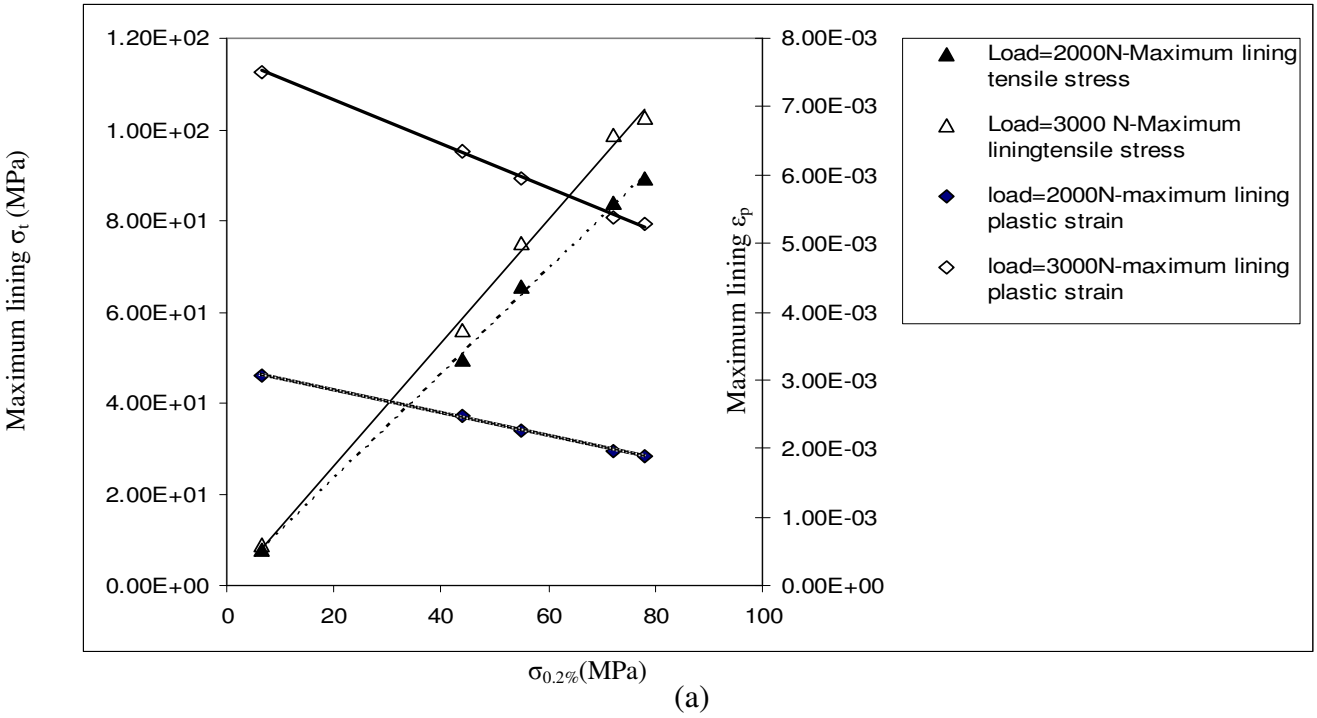

(a)

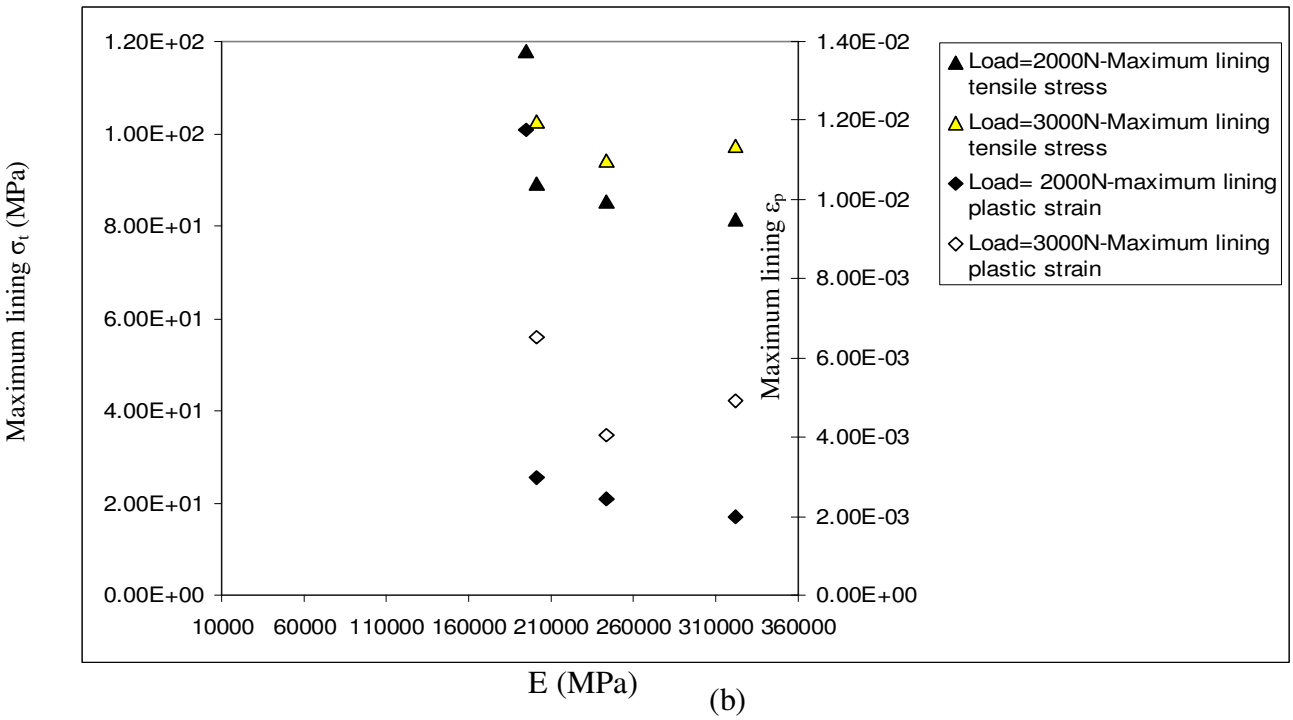

(b)

Figure 5.6: Effect of varying (a) lining $\sigma_{0.2\%}$ (AS20S steel as backing layer) and (b) steel backing *E* (AS20S monolithic as lining layer) upon lining surface stresses and strains. Thicknesses of lining, inter (*Al* foil) and backing layer are 0.2, 0.04 and 1.5mm respectively.

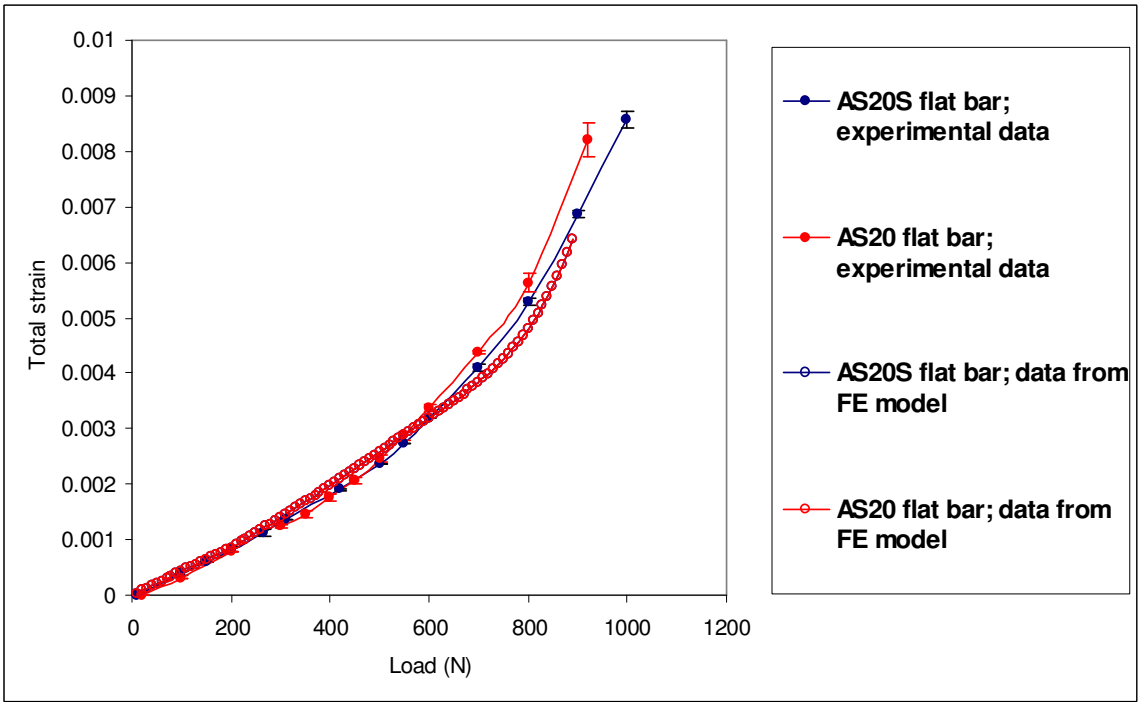

(a)

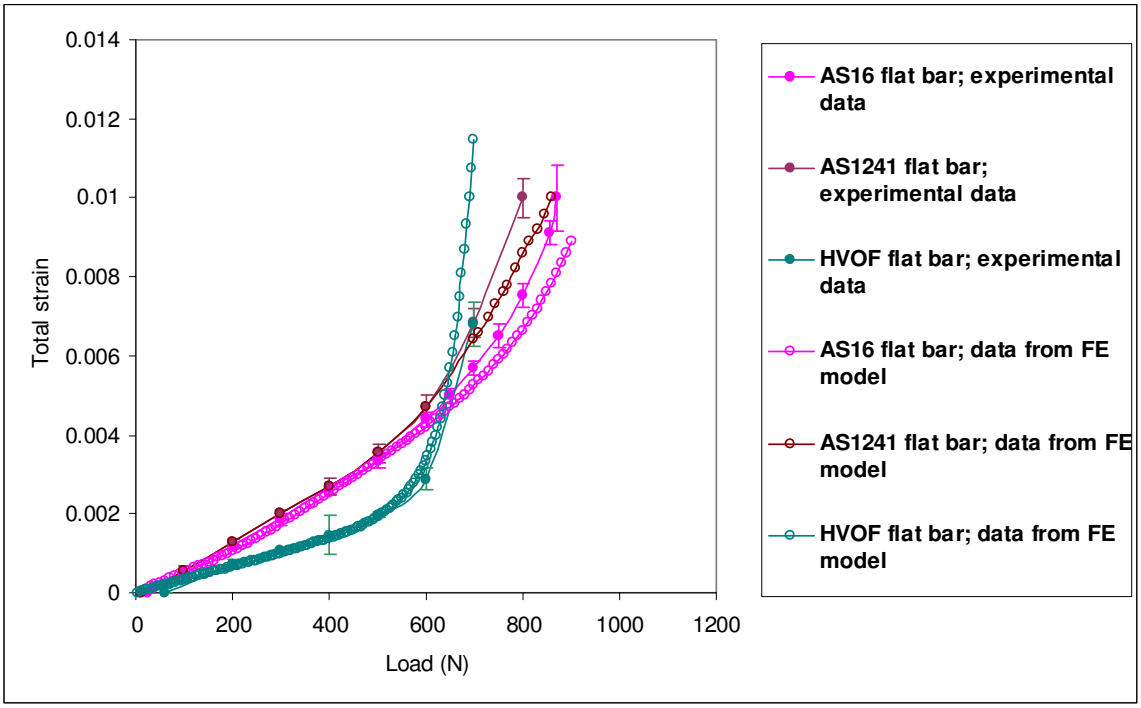

(b)

Figure 5.7: Load vs. total strain curves for flat bars/strips (a) current flat bar systems (b) previous flat bar systems.

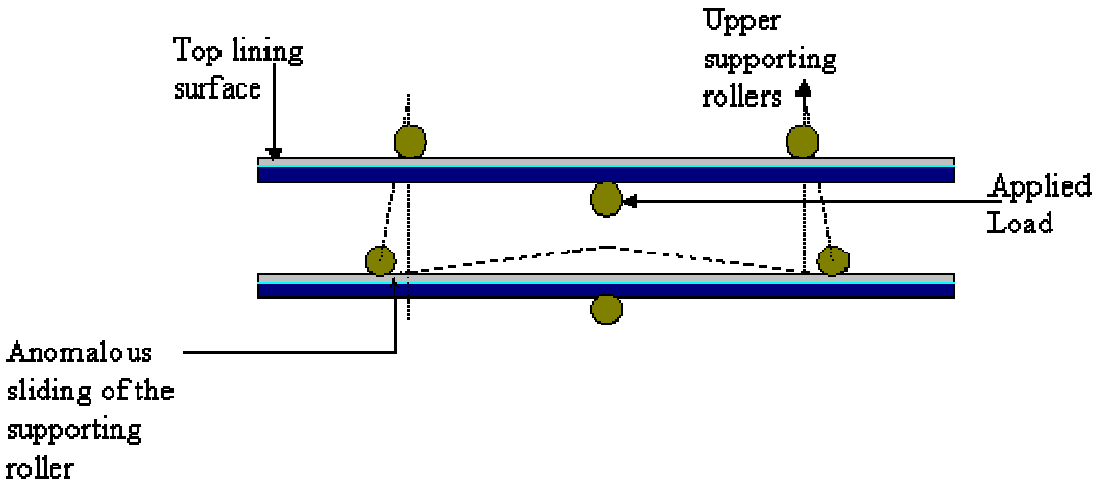

(a)

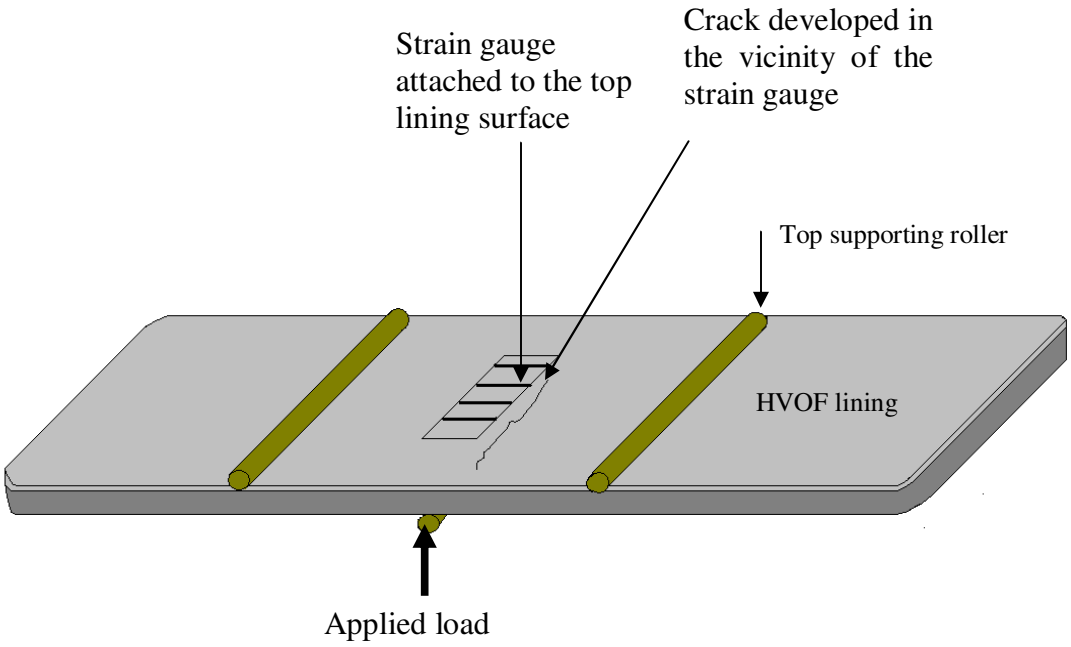

(b)

Figure 5.8: (a) Geometrical representation of the possible sliding of the roller during the lining strain measurement experiment. (b) Cracks developed in the vicinity of the attached strain gauge on the lining surface of the HVOF flat bar specimen.

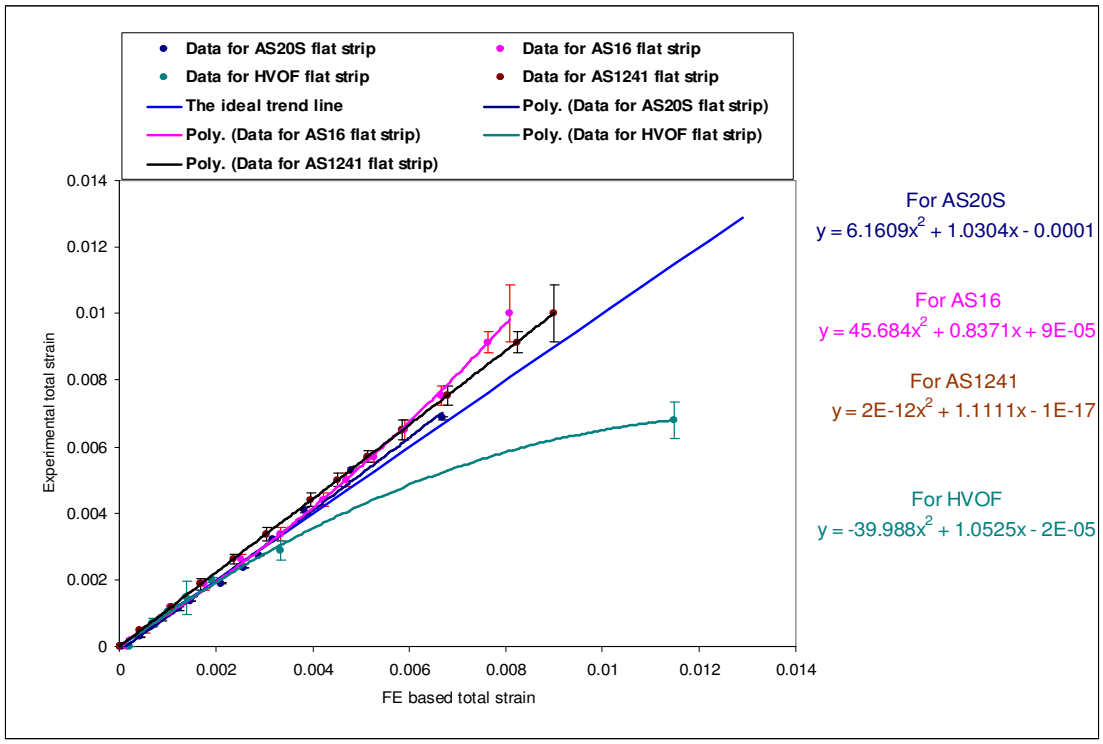

(a)

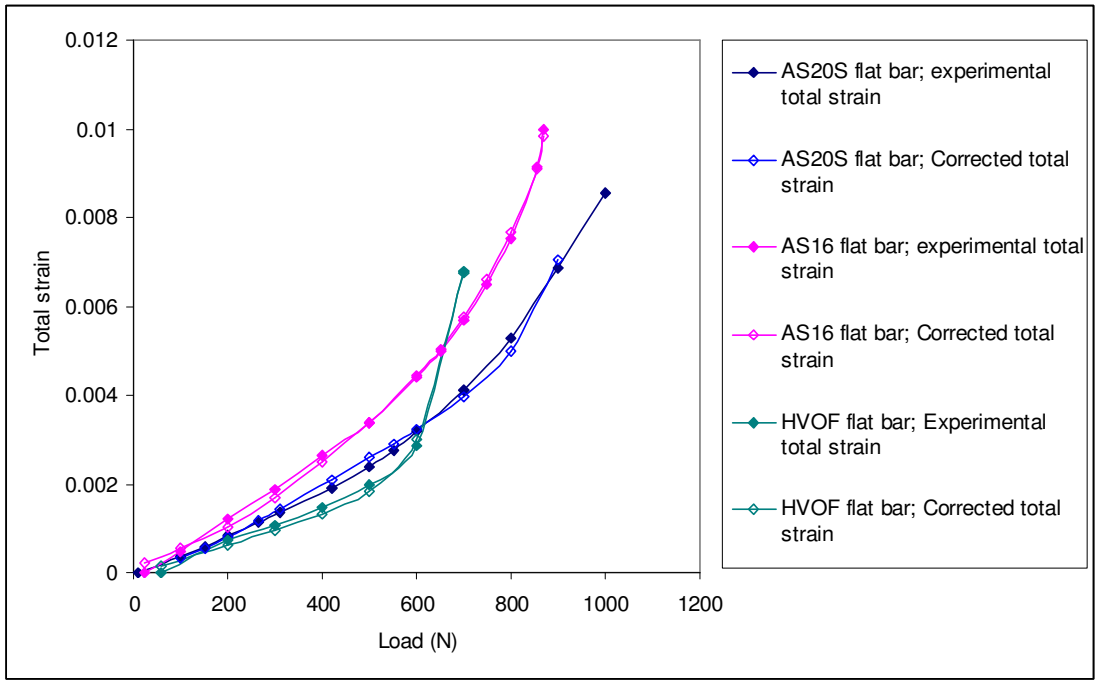

(b)

Figure 5.9. (a) Experimental total strain data vs. FE predicted total strain data for flat bar (b) Experimentally predicted vs. corrected values of the maximum lining total strains.

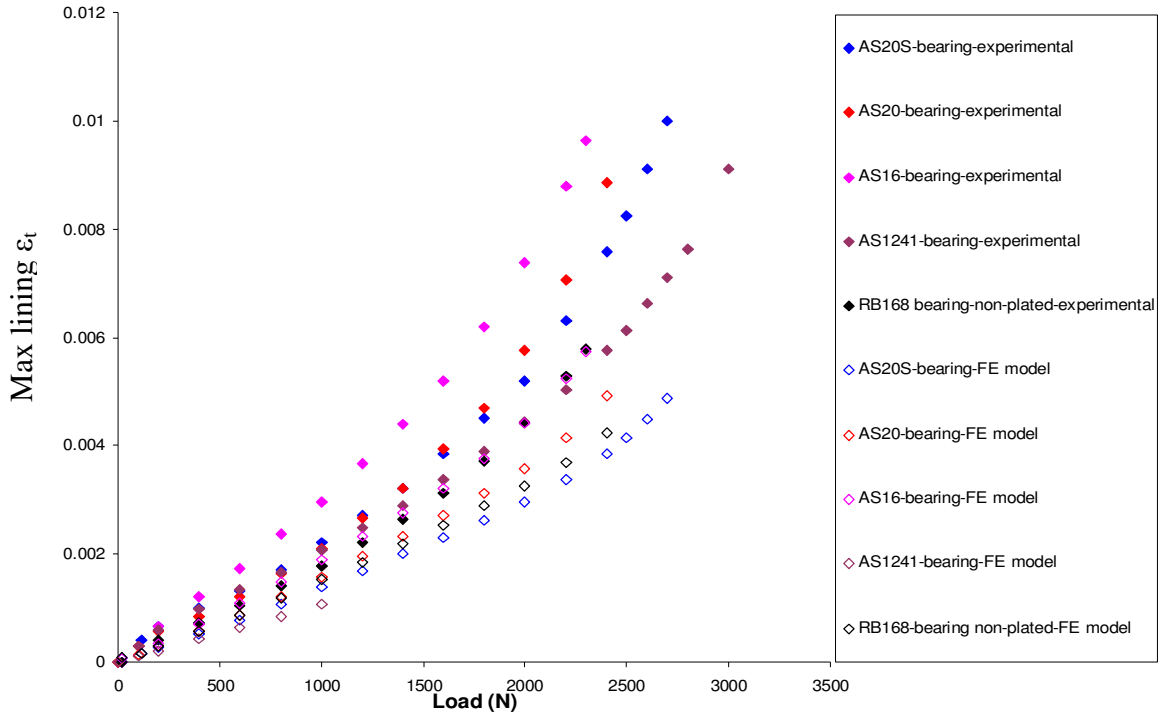

Figure 5.10: Load vs. experimental and FE based total strain data for all previous and current bearings.

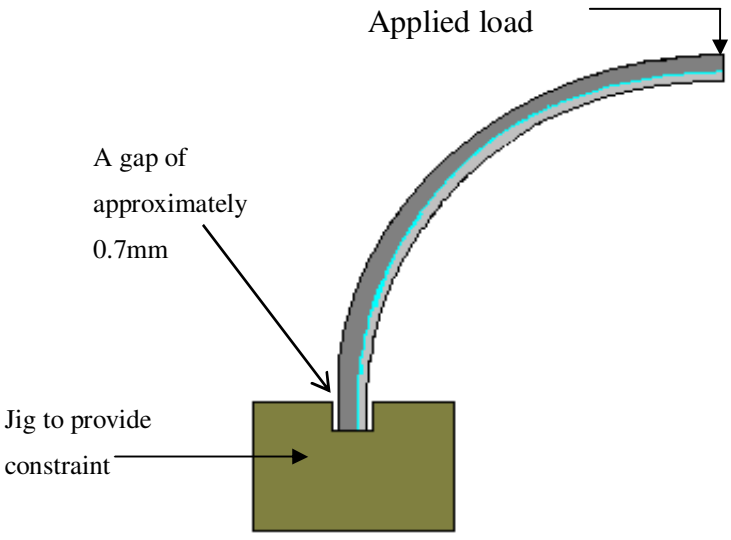

Figure 5.11: Bearing end in the specimen jig during three point load (a) FE based bearing model showing fully constrained end.

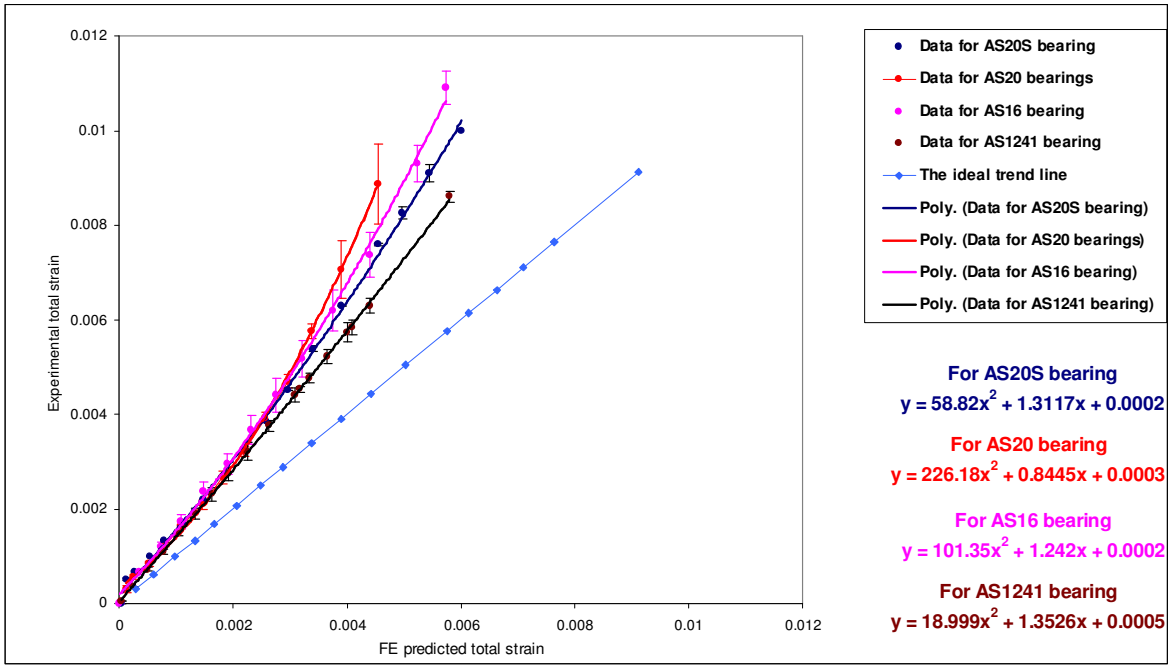

(a)

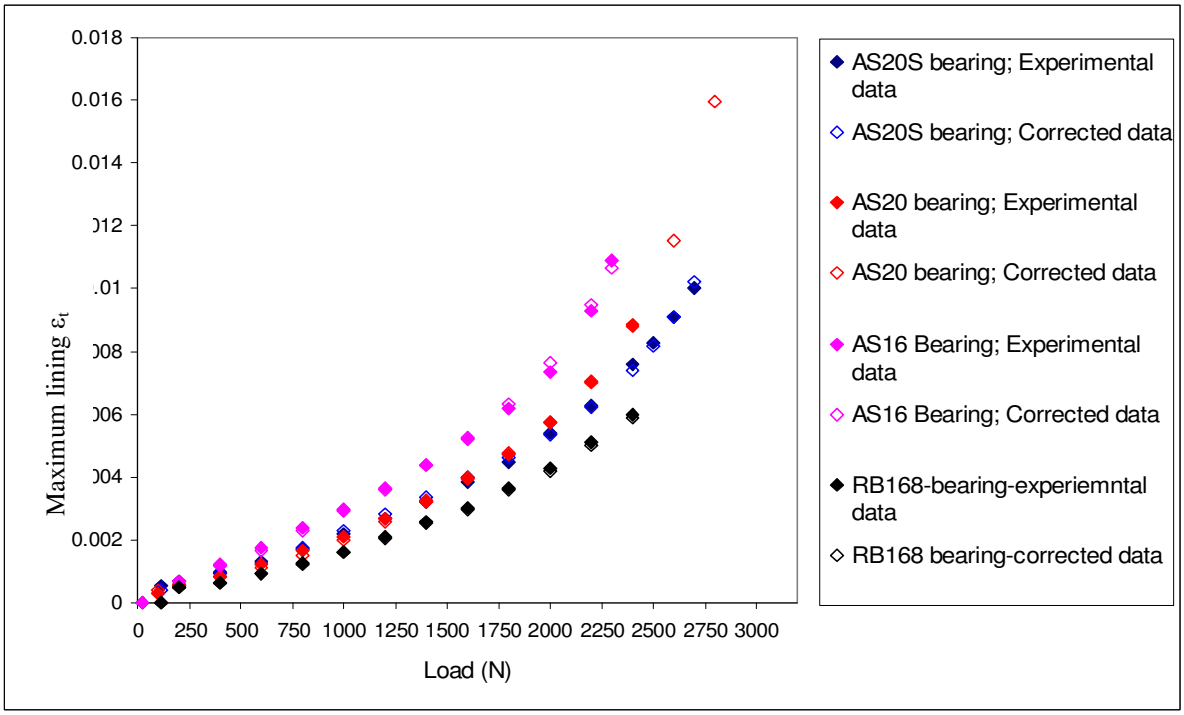

(b)

Figure 5.12:(a) Experimental vs. FE predicted total strain values for bearing systems (b) Load vs. experimental and corrected values of maximum lining surface total strains.

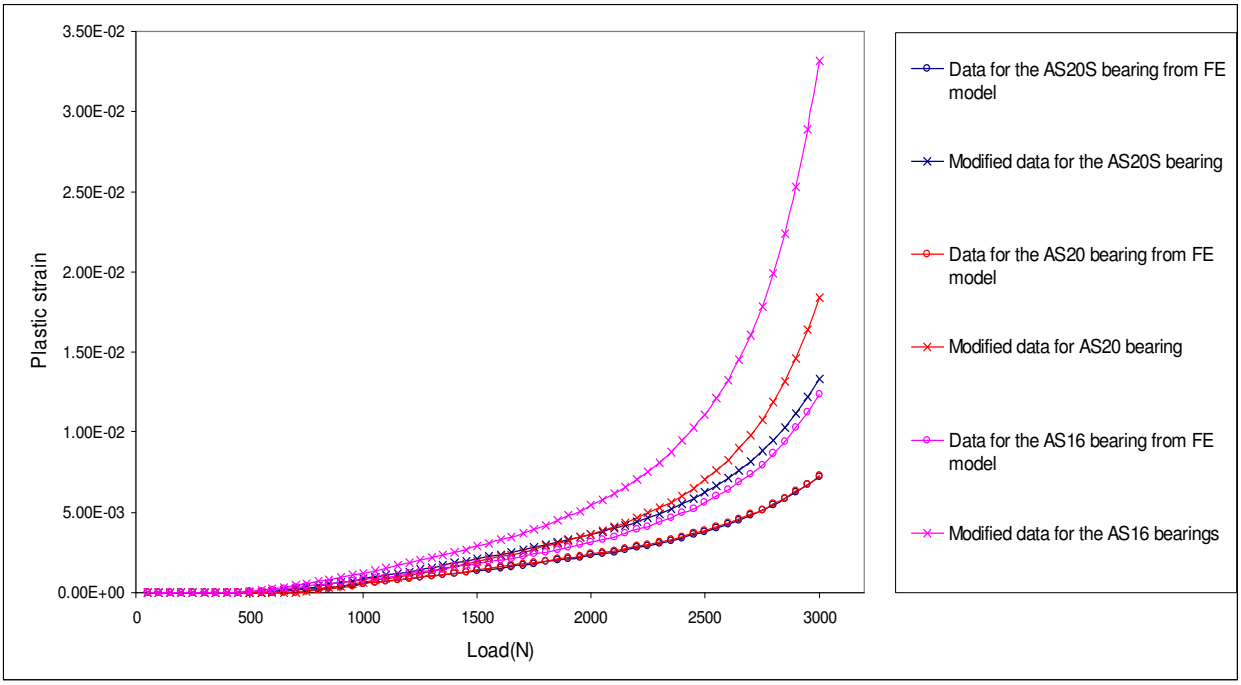

(a)

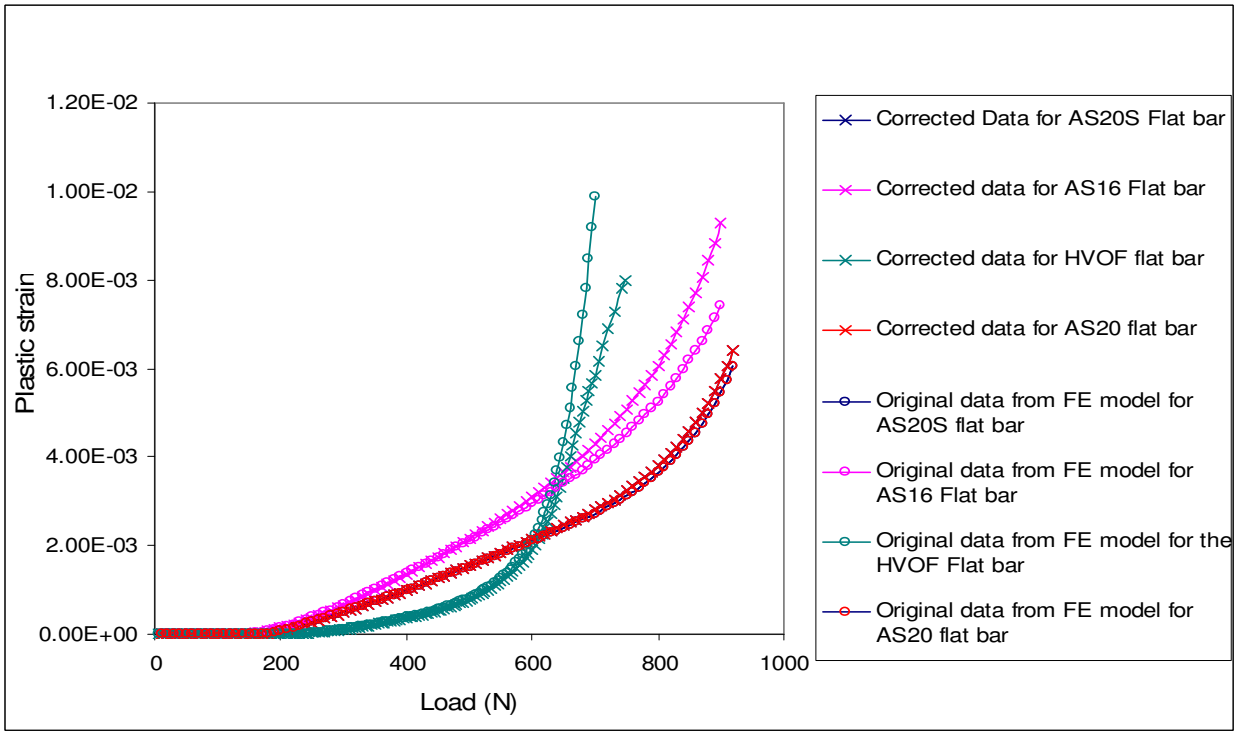

(b)

Figure 5.13: Comparison of the FE predicted and corrected values of max lining ε_p for (a) finished bearings (b) flat bars.

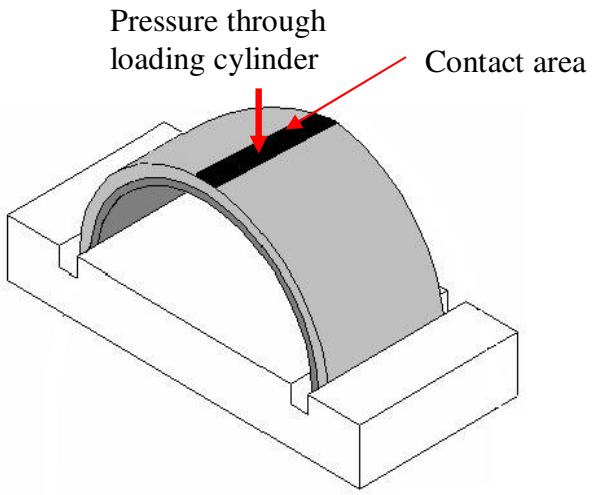

(a)

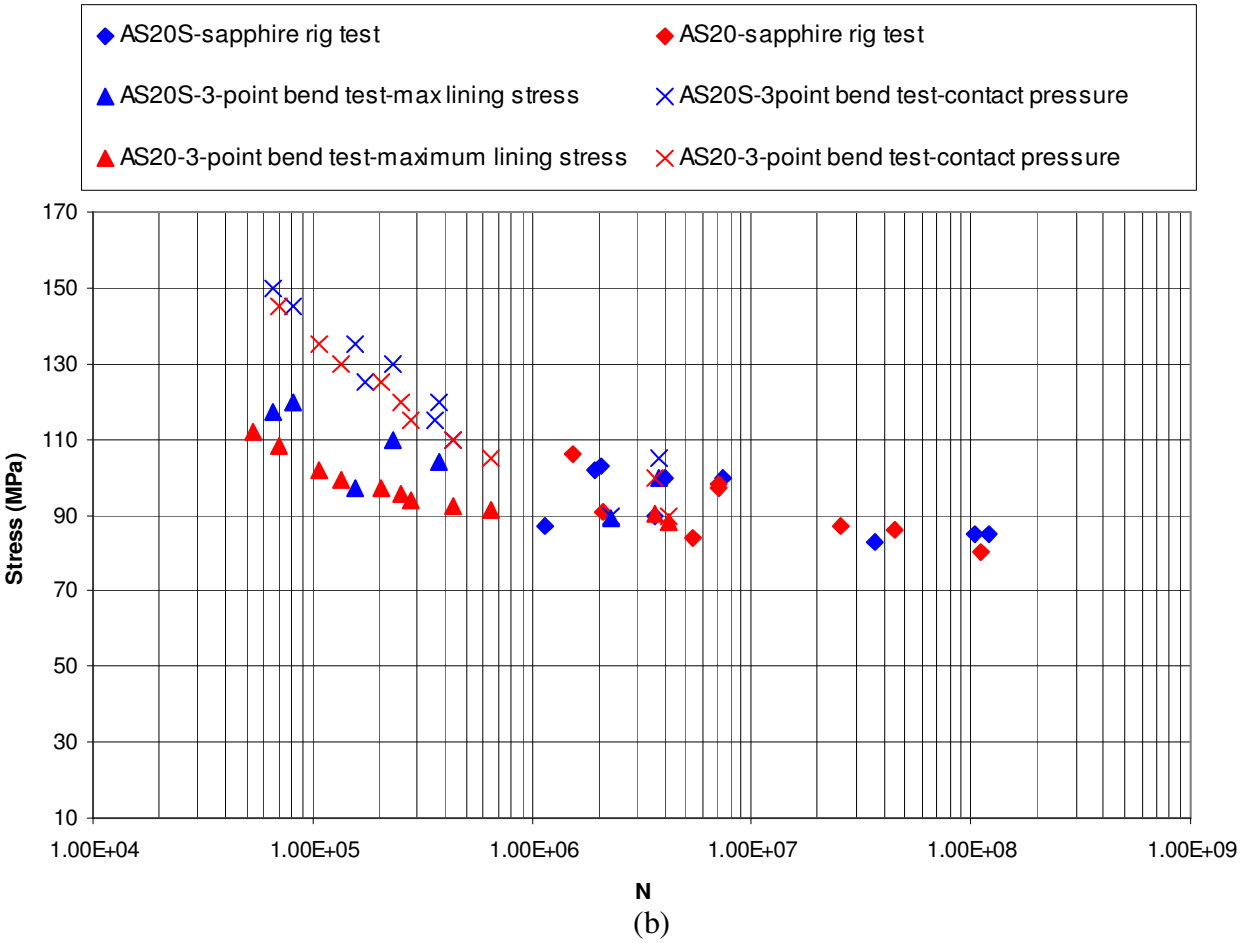

(b)

Figure 5.14: (a) Loading roller-bearing contact area at the backing layer of the bearing (b) Fatigue life of AS20S and AS20 bearing specimens in the form of *S-N* and P_{av} –*N* compared with the fatigue data from accelerated rig test.

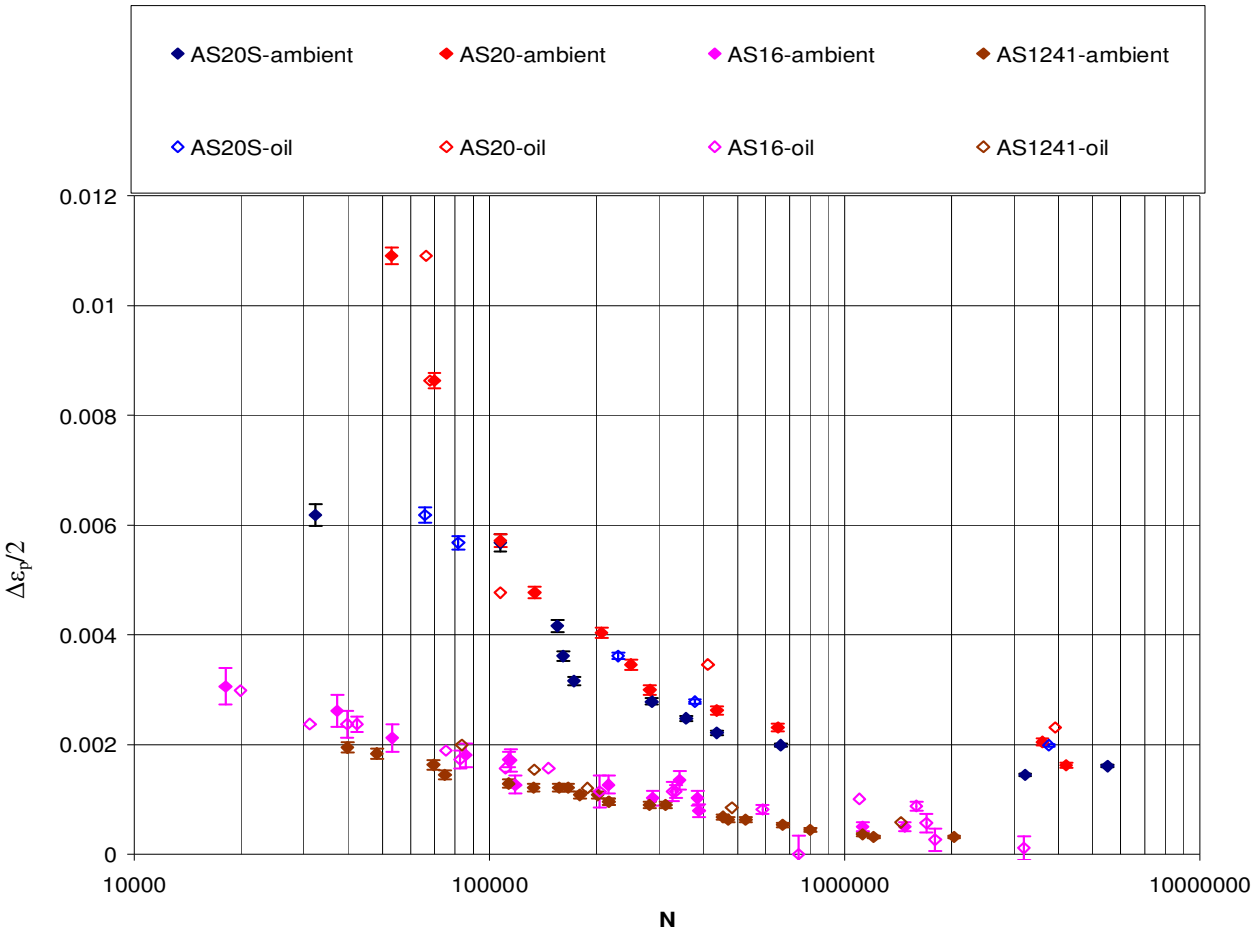

Figure 5.15: Fatigue life of all current and previous bearing specimens in the form of $\Delta\varepsilon_p$-N under ambient and engine oil environment. Plastic strain amplitude values are FE based validated by experimental strain results.

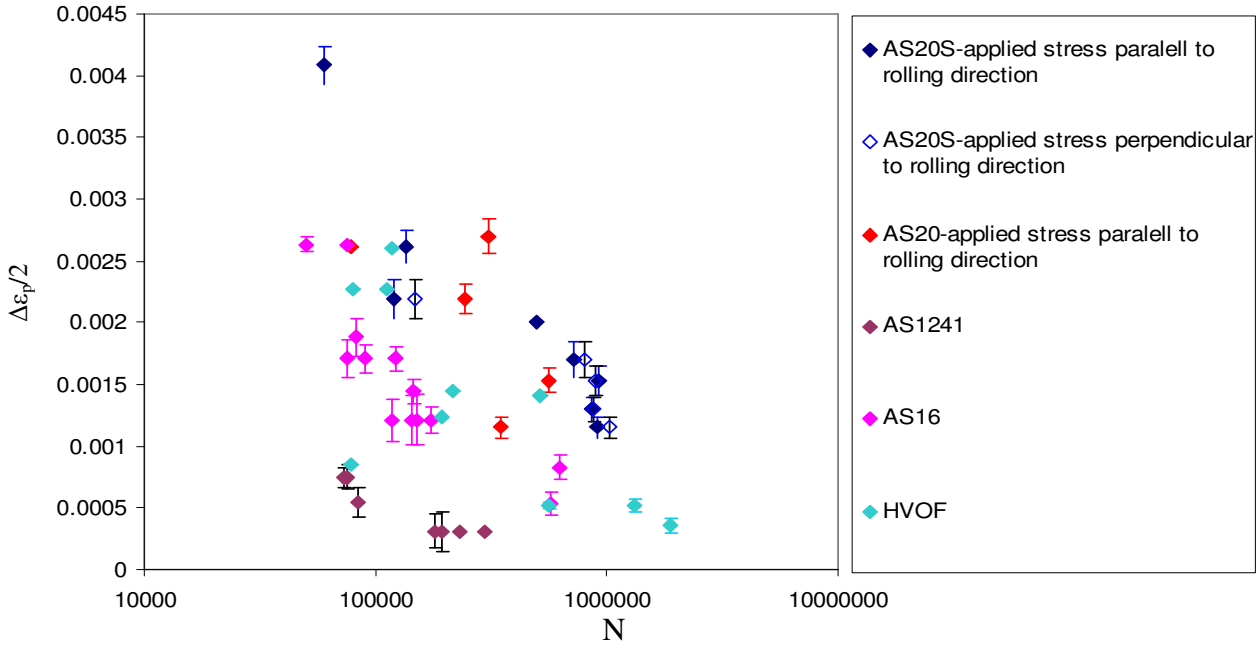

Figure 5.16: Fatigue life of all previous and new *Al* based flat bar specimens compared with the spray coated flat bar specimens in the form of $\Delta\varepsilon_{p/2}$-*N*. Data for the AS1241 and AS16 some of the HVOF systems was obtained from previous research.

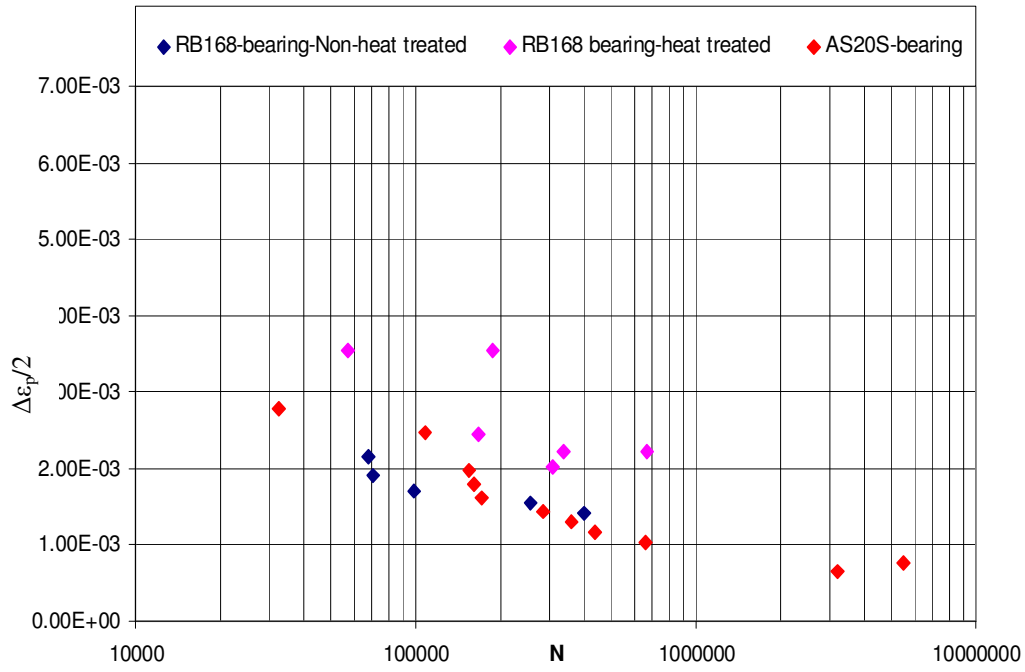

Figure 5.17: A comparison of fatigue lifetime results for the RB168 and AS20S bearing systems in air. Plastic strains amplitude values were based upon elastoplastic FE model validated through the experimental strain measurement at the bearing lining surface.

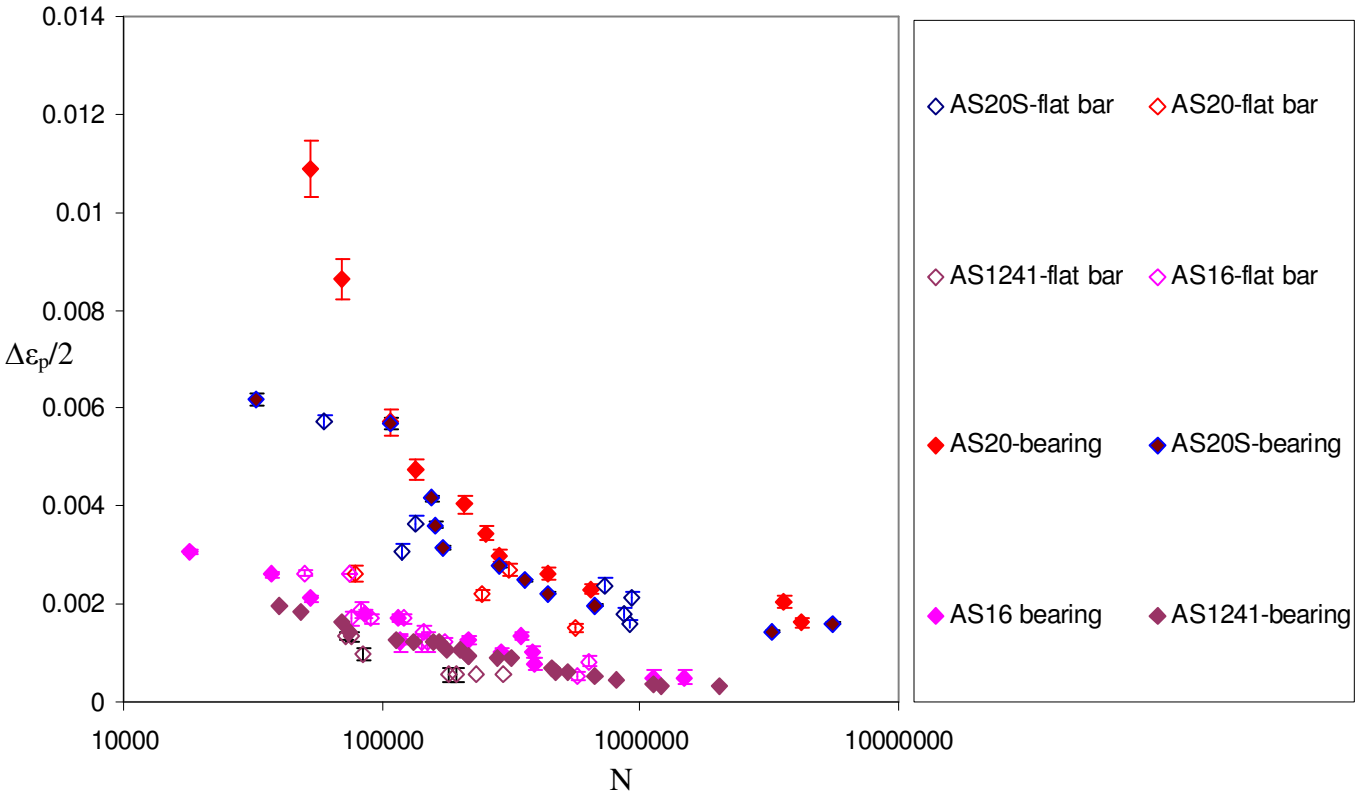

Figure 5.18: A comparison of fatigue life of RB bearing and flat bar specimens. All data for the AS16 and AS1241 was obtained from previous research.

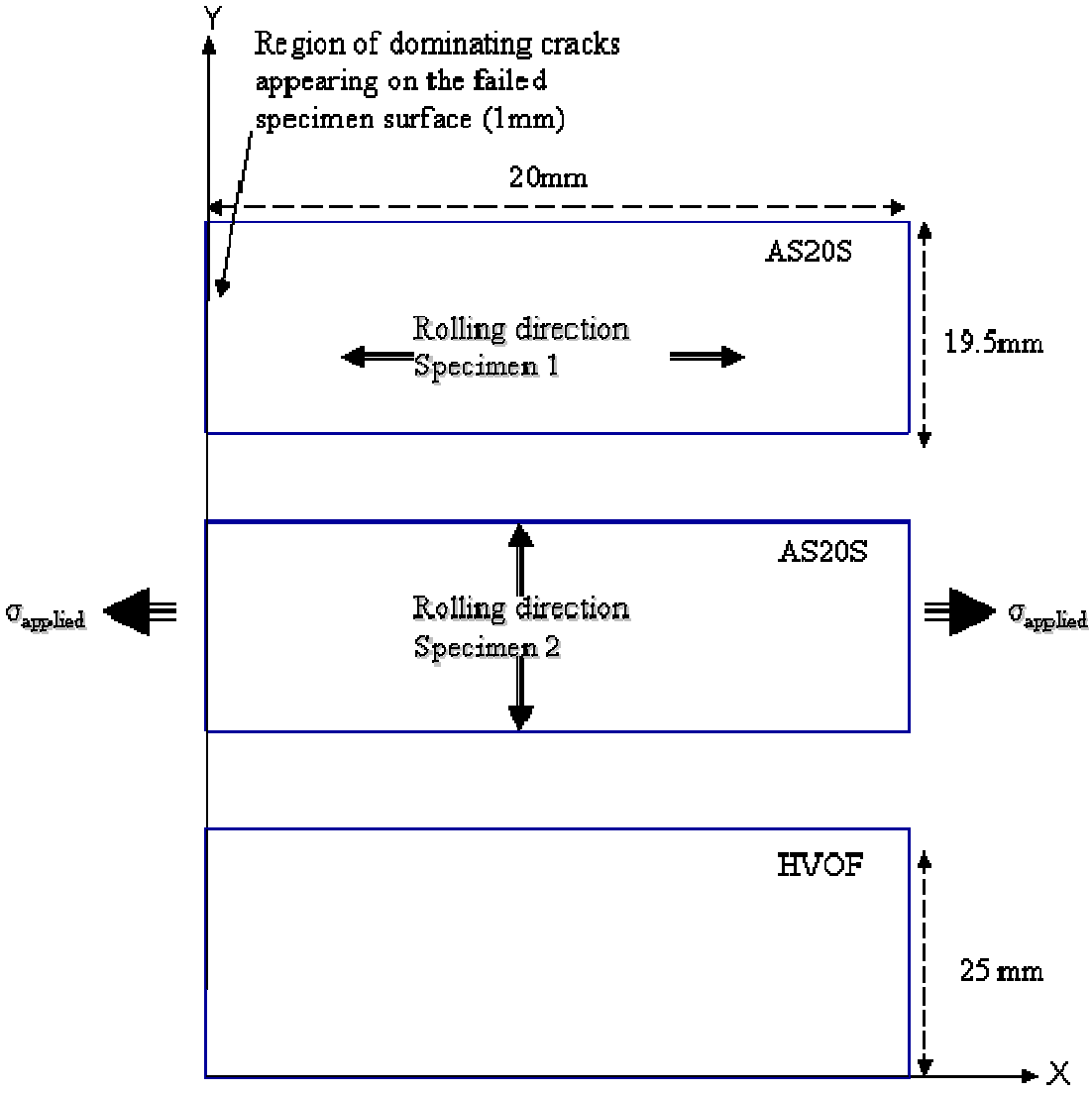

Parameters for AS20S/AS20 system

σ_{max} = 105 MPa

σ_{min} = 29.816 MPa

σ_y = 59 MPa

Width = 19.5 mm

Load span = 40mm

Parameters for HVOF system

σ_{max} = 110 MPa

σ_{min} = 15 MPa

σ_y = 56 MPa

Width = 25 mm

Load span = 40mm

Figure 5.19. Method of defining a two dimensional coordinates systems on the flat bar lining surface to study the crack fields.

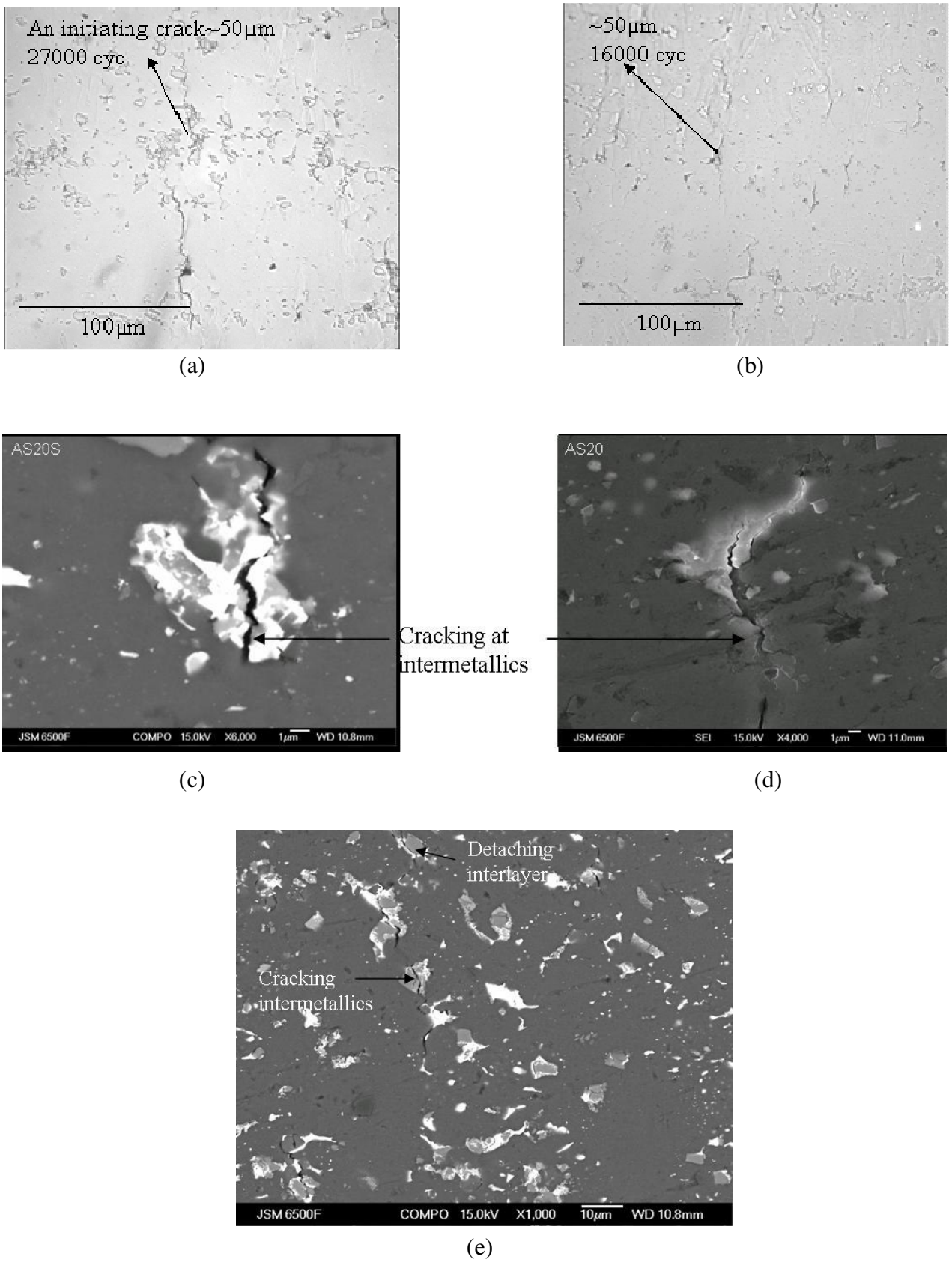

Figure 5.20: Optical micrograph of the surface replicas of (a) AS20S (b) AS20. BEI images (c) AS20S (d) AS20 lining surface (e) BEI image from larger area of AS20S lining surface.

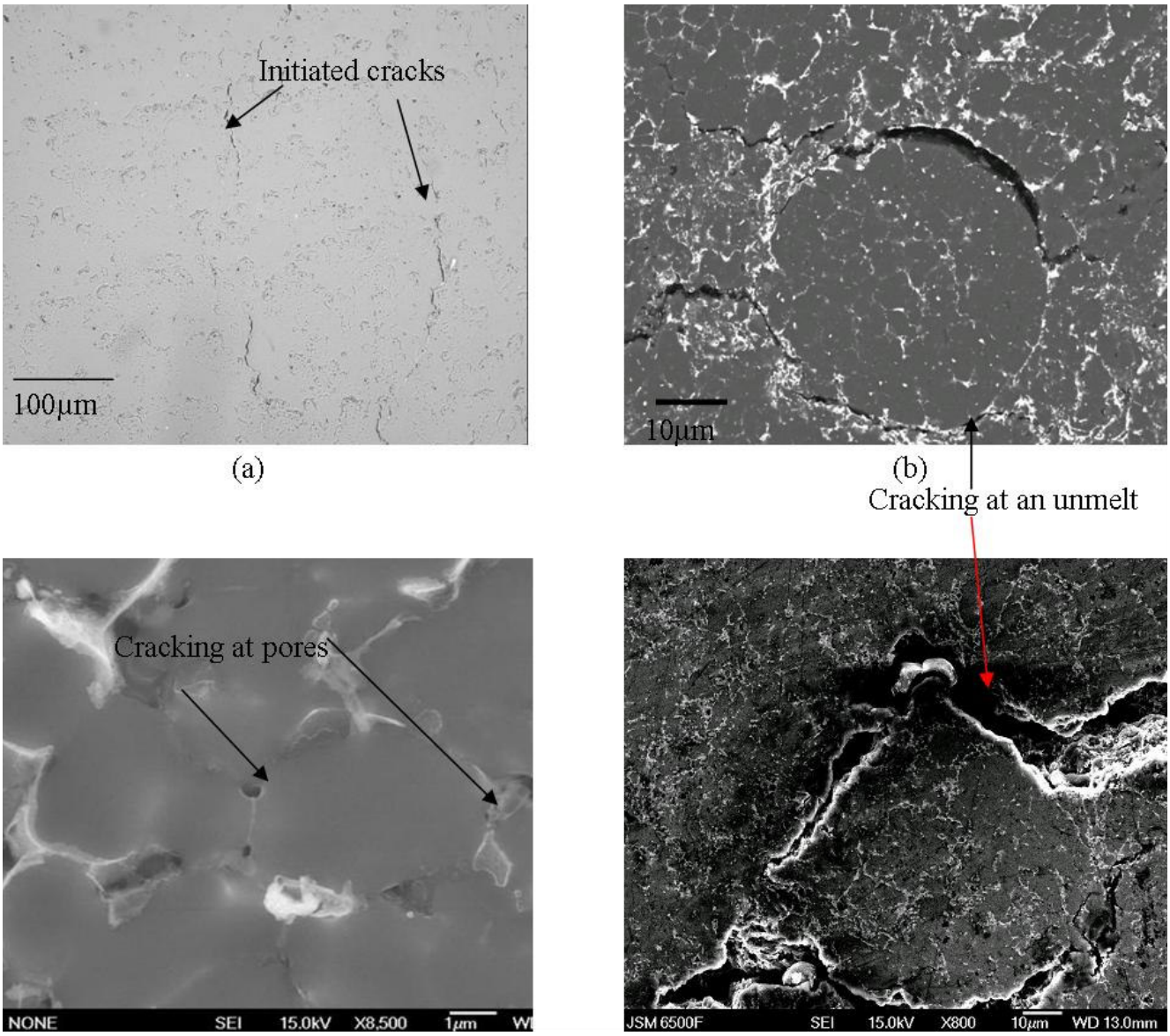

Figure 5.21: (a) Optical image of the replica from HVOF flat bar (b) BEI and (d) SEI images of crack initiating from unmelt. (c) Crack initiating from pores surrounding unmelts.

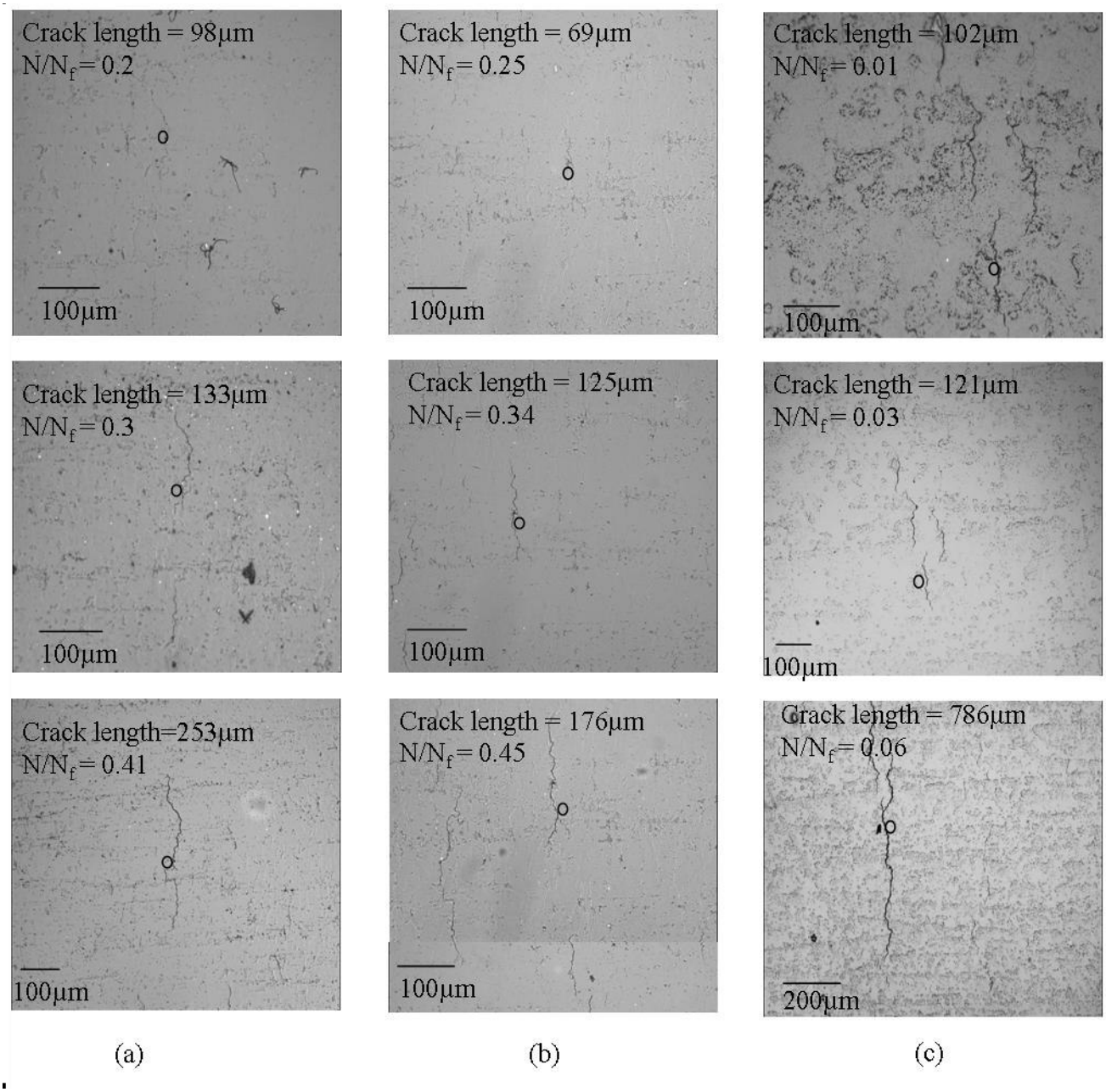

Figure 5.22: Lining surface crack growth behaviour. Optical images of surface replicas of (a) AS20S (b) AS20 (c) HVOF lining at different life time intervals. Typical crack shown by red marks.

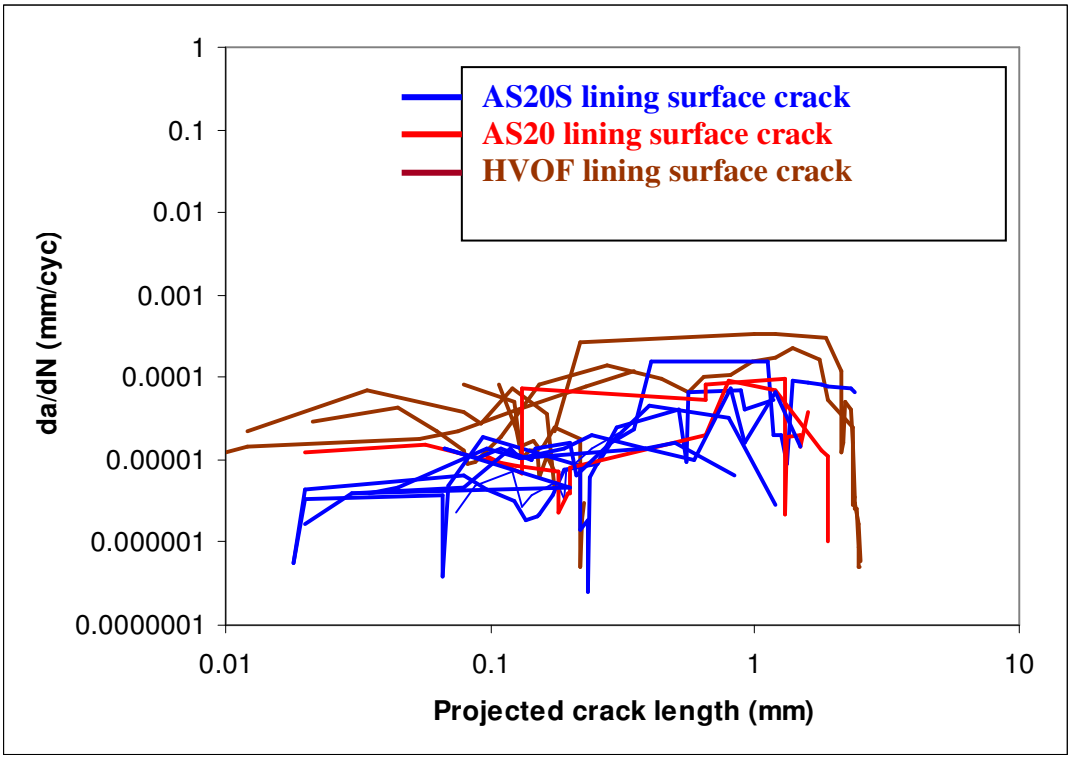

Figure 5.23: Lining surface crack growth behaviour of AS20S, AS20 and HVOF flat bar systems at a constant maximum ε_p of 0.0064±0.003. da/dN vs. Crack length data was produced from optical images of the lining surface replicas during interrupted fatigue tests.

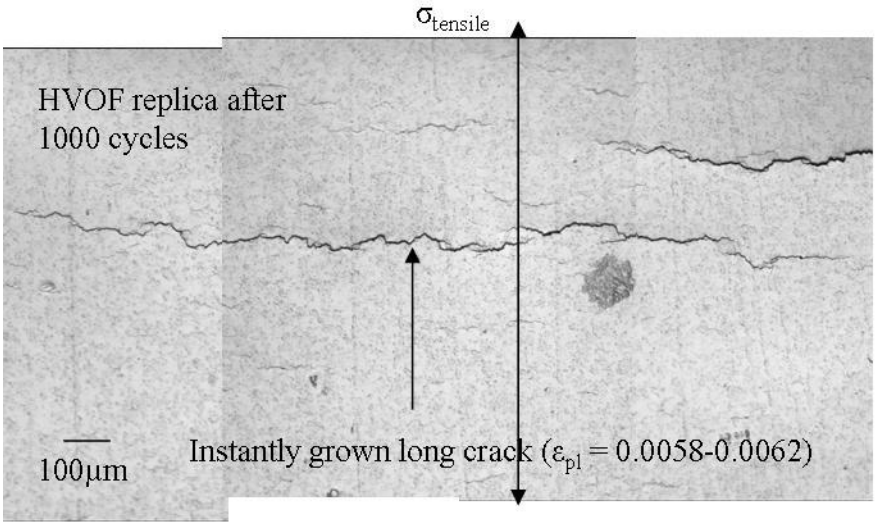

Figure 5.24: Optical micrograph of the HVOF replica showing instant emergence of very long cracks.

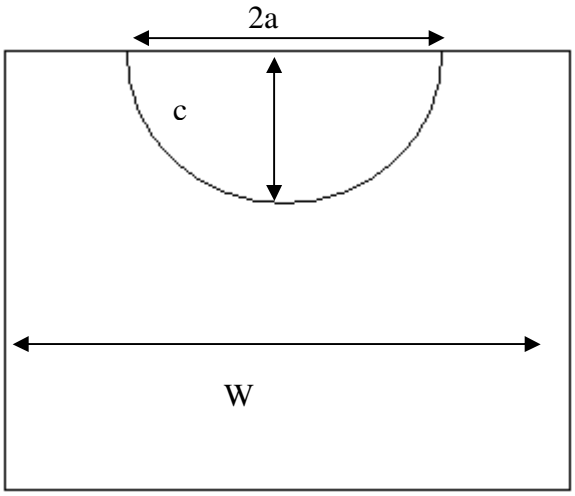

(a)

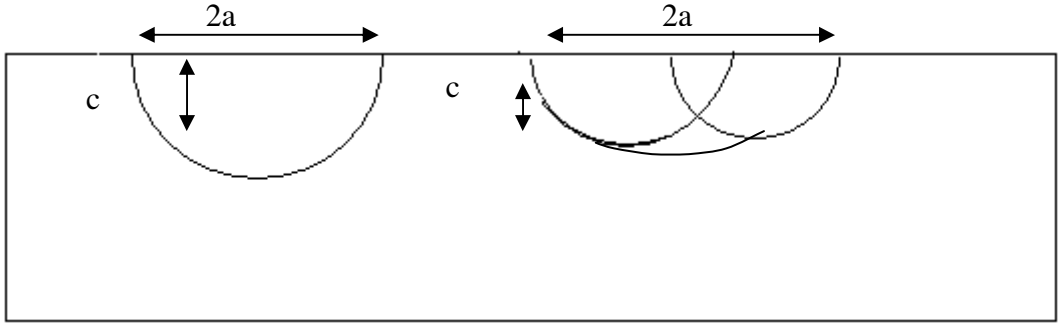

(b)

Figure 5.25 (a) Crack geometry used for short crack ΔK calculations from Scott and Thorpe equation (b) Increase in a/c value with coalescence of cracks.

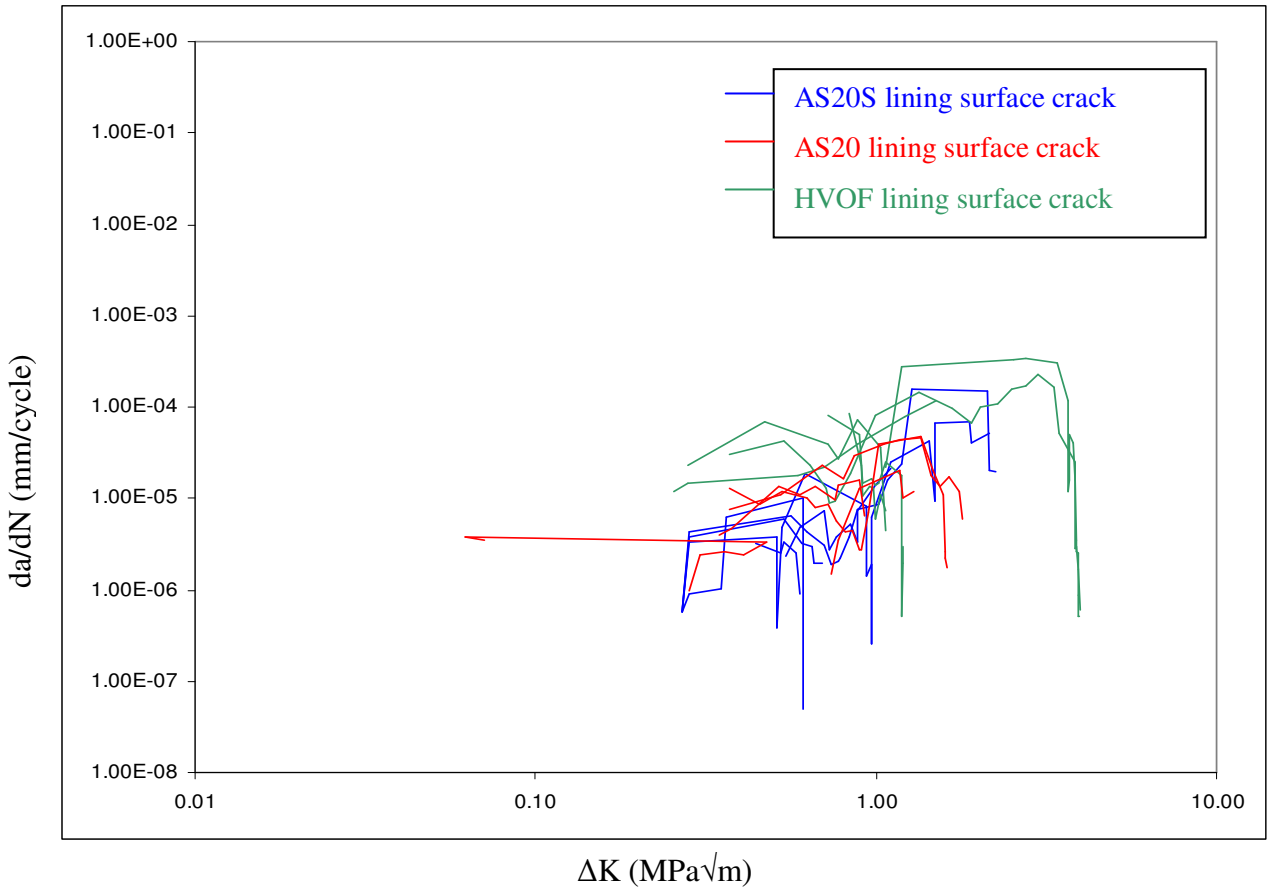

(a)

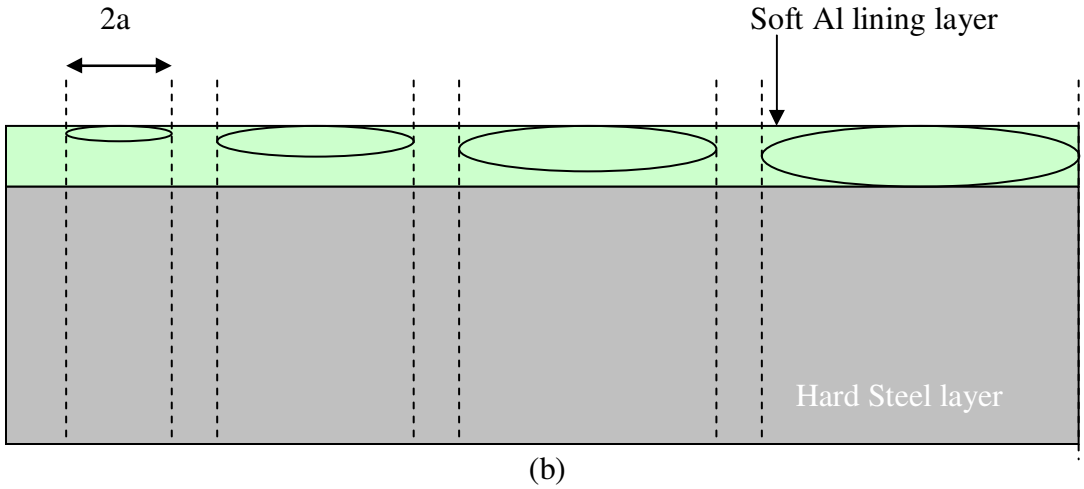

(b)

Figure 5.26:(a) *da/dN* vs *ΔK* of various cracks in the high strain region of the flat bar specimens of all three systems (b) A geometrical representation of subsurface retardation of crack due to a harder backing layer.

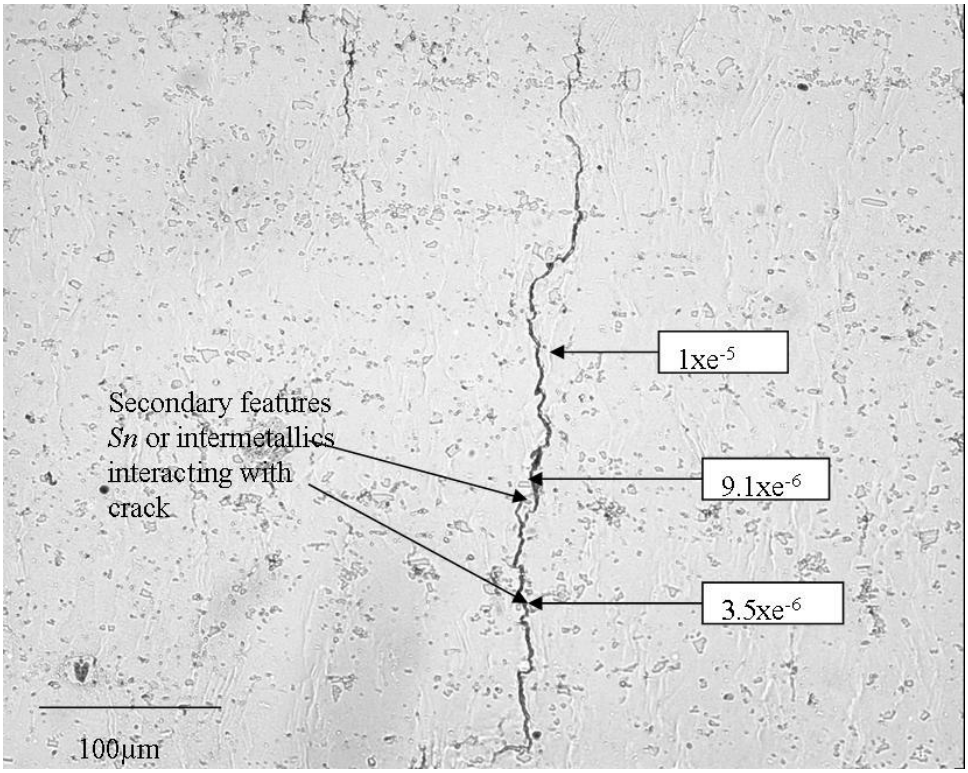

(a)

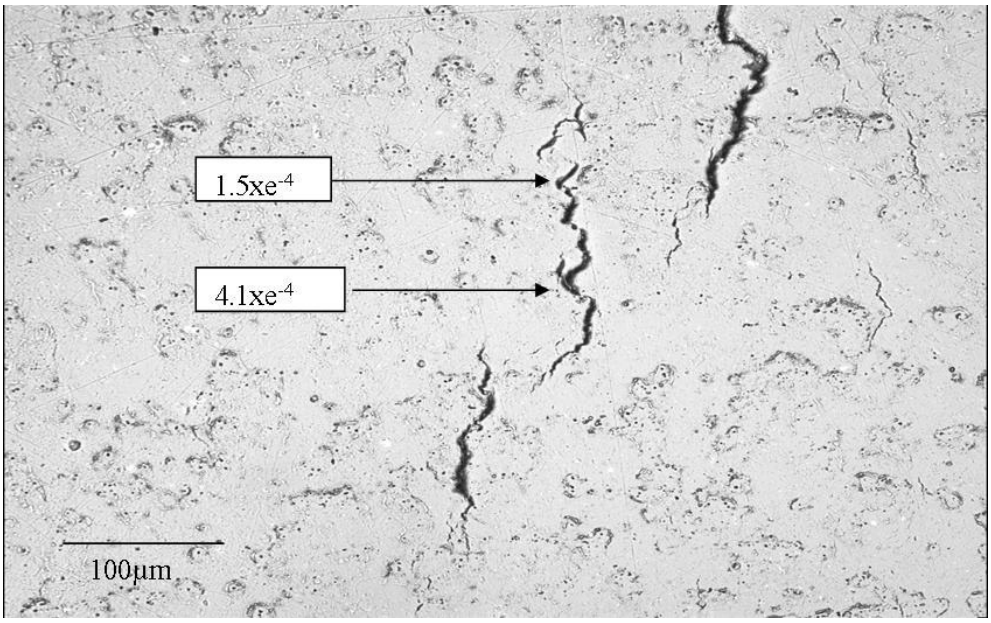

(b)

Figure 5.27: (a) Variation of da/dN surface cracks at different locations of (a) AS20S and (b) HVOF lining surface.

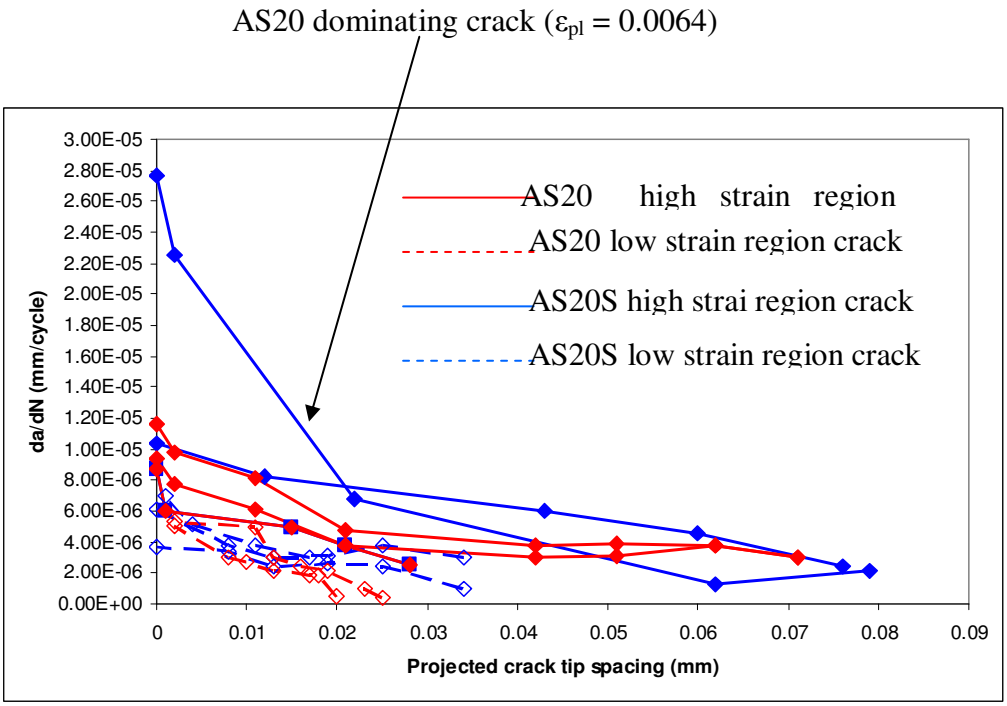

(a)

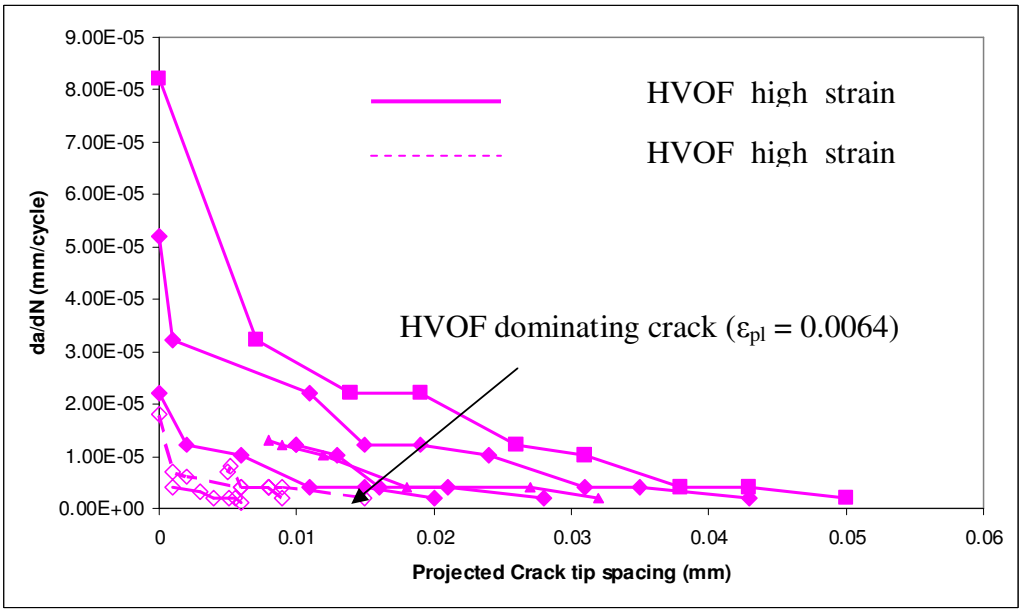

(b)

Figure 5.28: Crack tip spacing vs. *da/dN* characteristics of (a) AS20S/AS20 (b) HVOF flat bars systems.

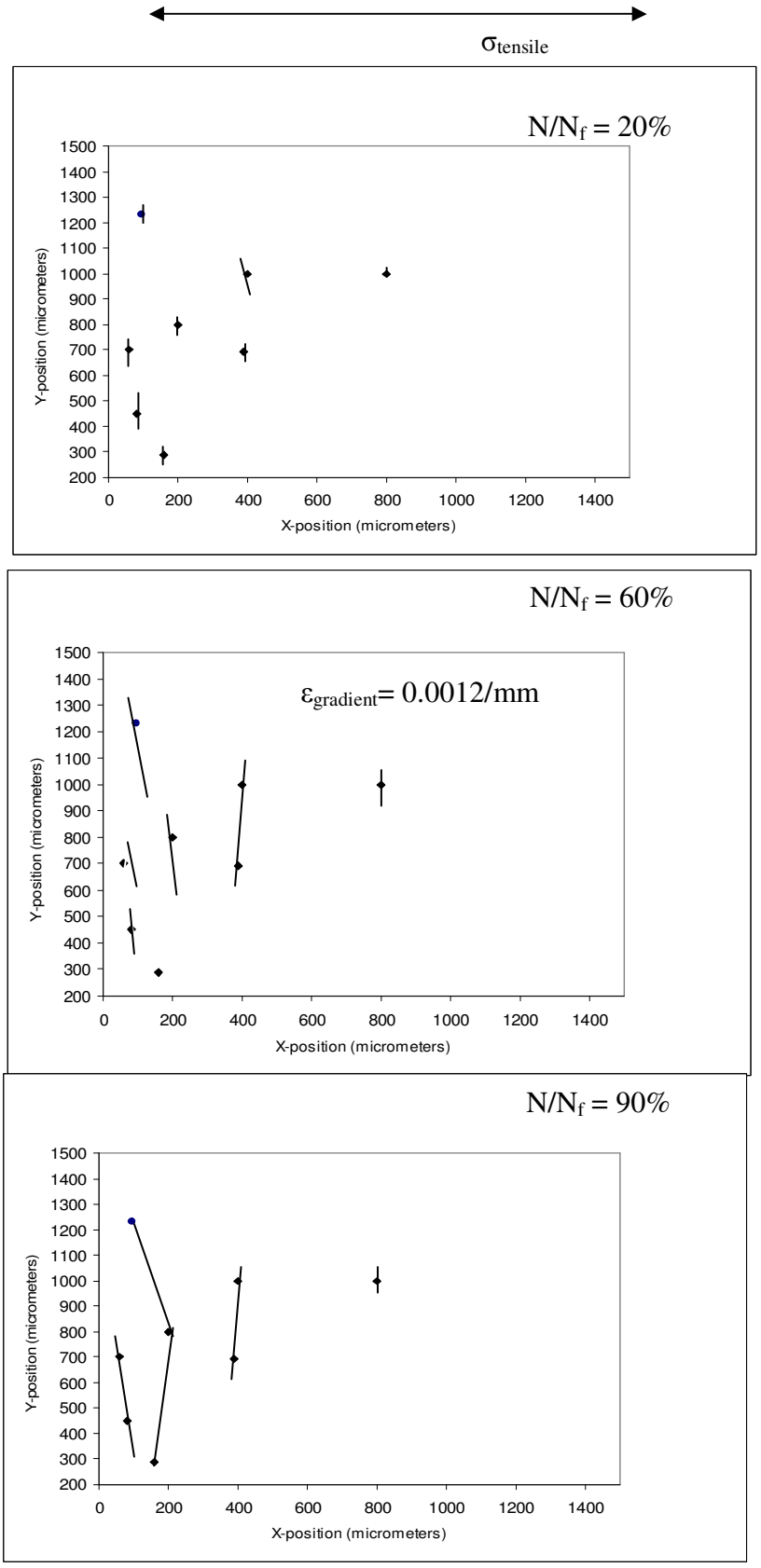

. Figure 5.29: Short fatigue crack interactions at different life time fractions for AS20S lining.

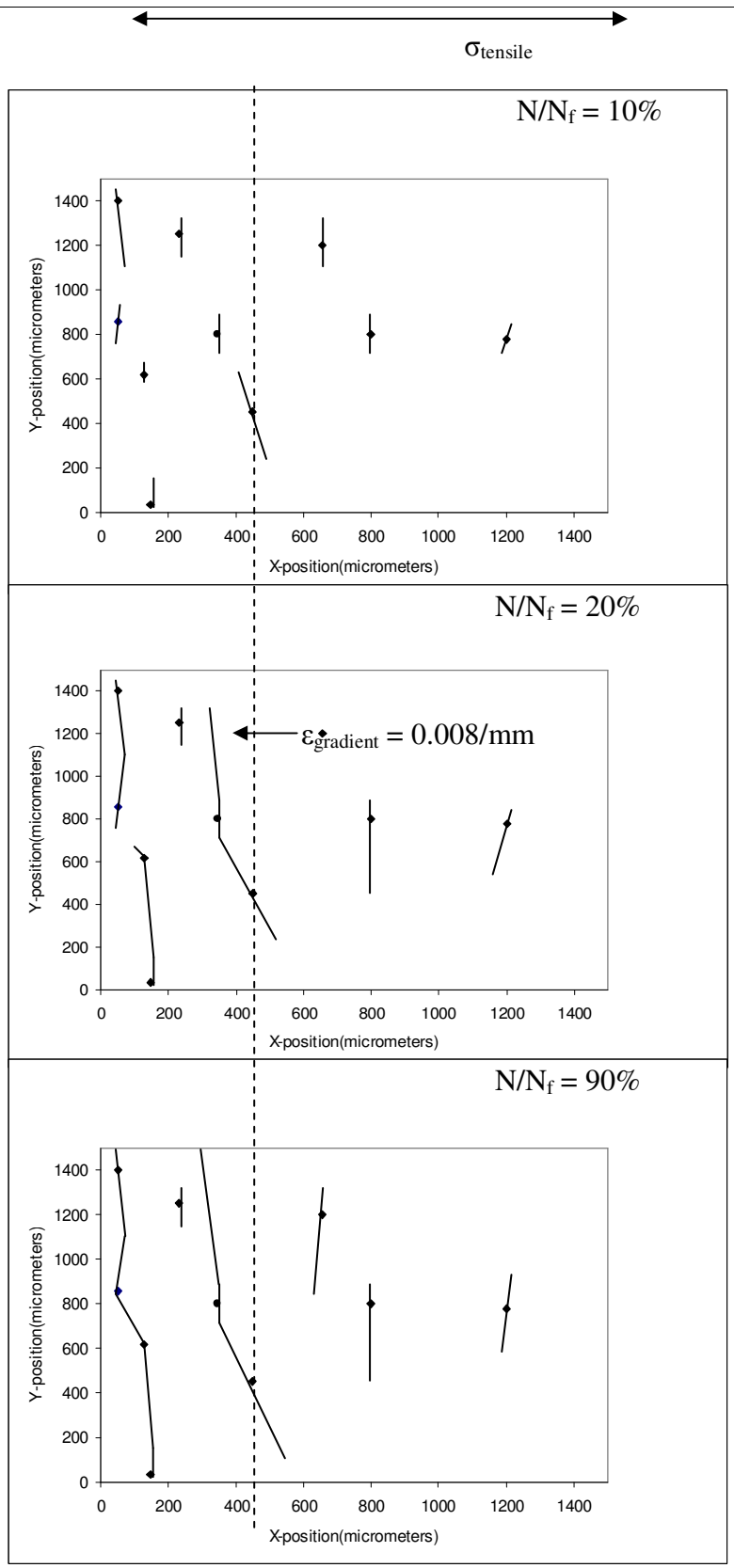

Figure 5.30: Short fatigue crack interactions at different life time fractions for the HVOF lining.

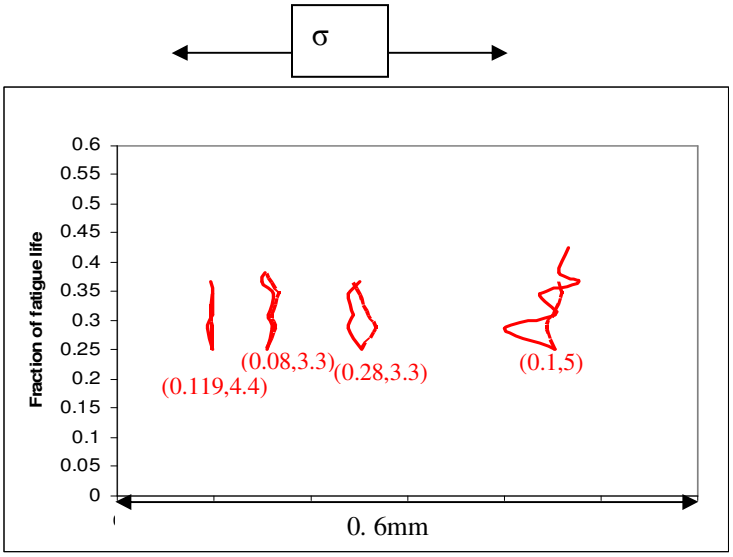

(a) AS20S System

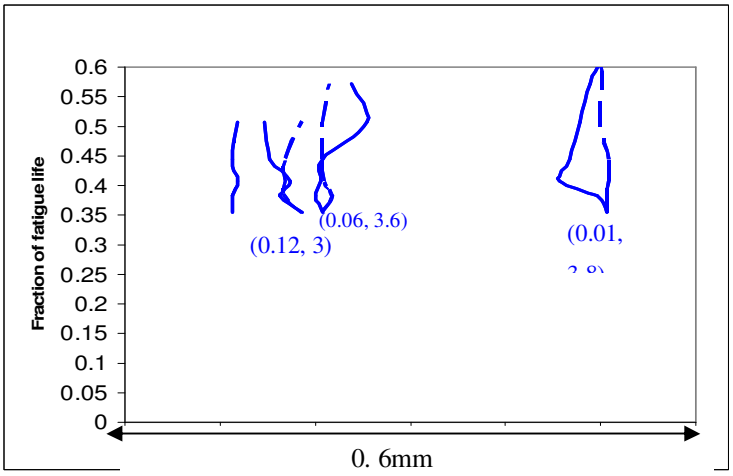

(b) AS20 systems

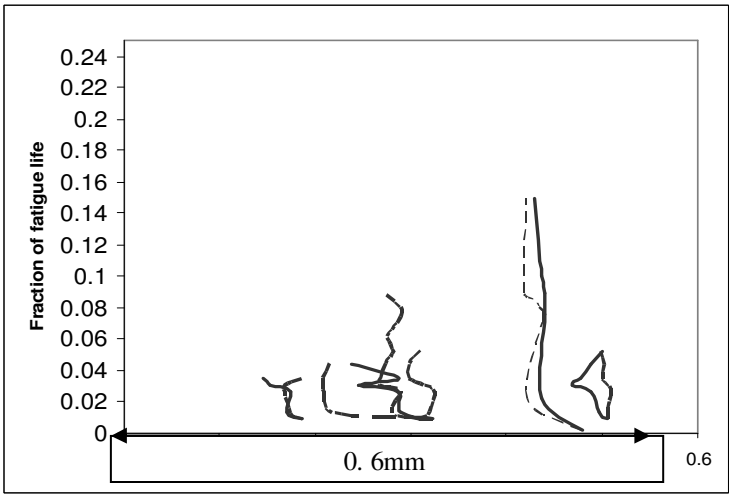

(c) HVOF system

Figure 5.31: A 2-map of surface crack tip trajectories in all *Al* based linings.

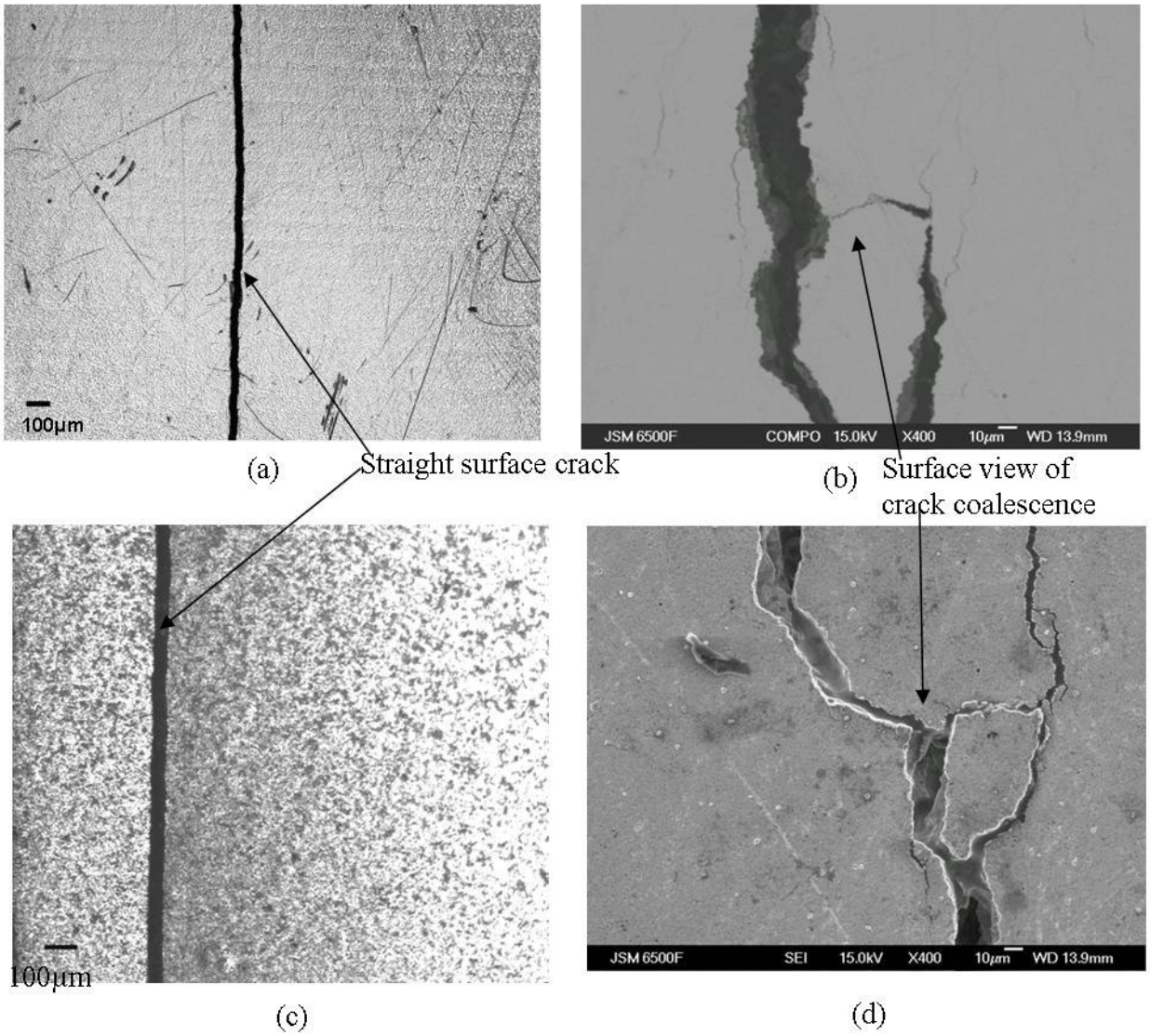

Figure 5.32: Surface morphology of cracks in RB168 (a and b) non-heat treated (c and d) heat treated specimen.

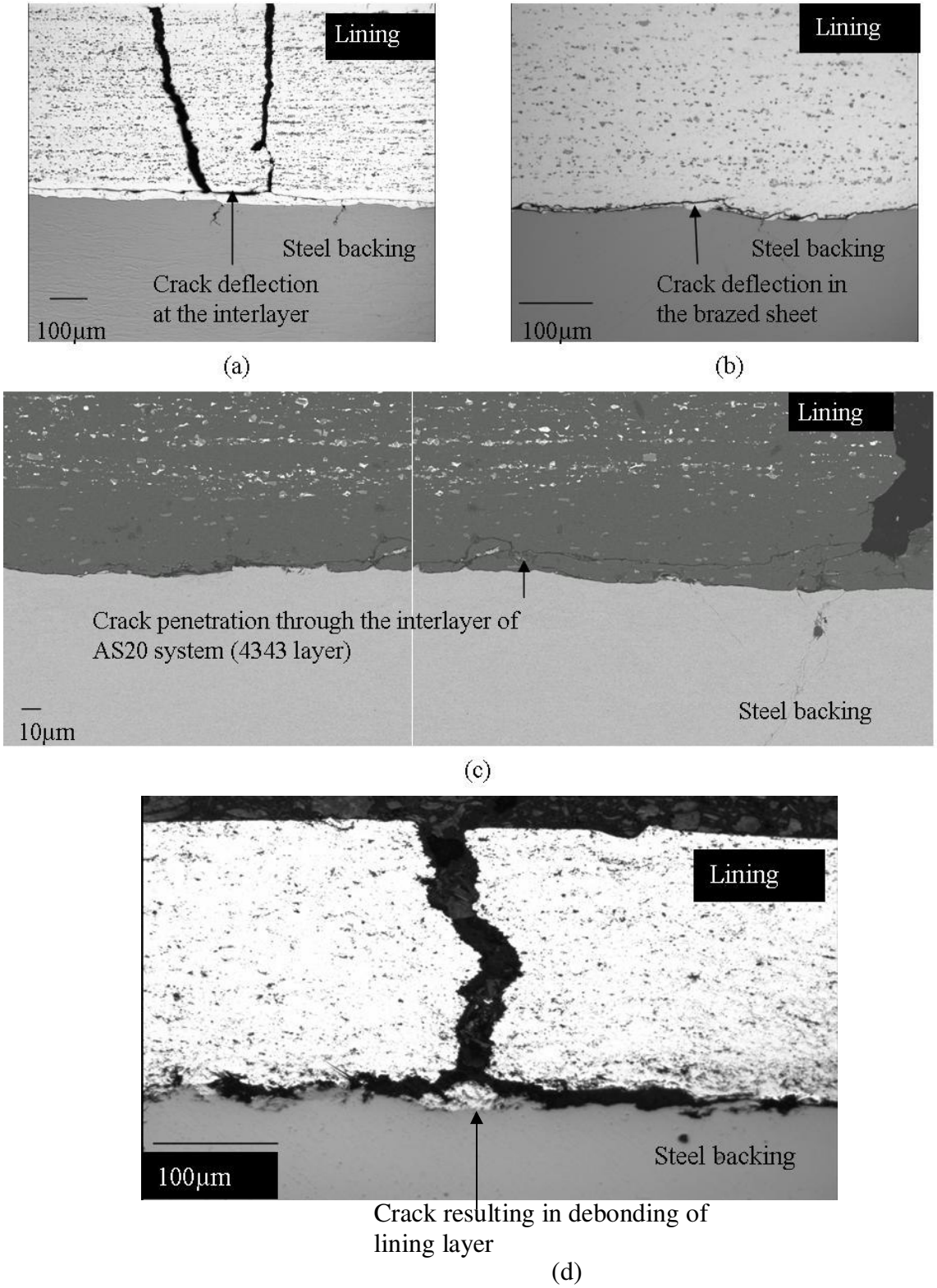

Figure 5.33: Micrographs showing subsurface penetration of fatigue cracks in (a) AS20S bearing (b) AS20 (c) AS20 BEI image (d) HVOF flat bar.

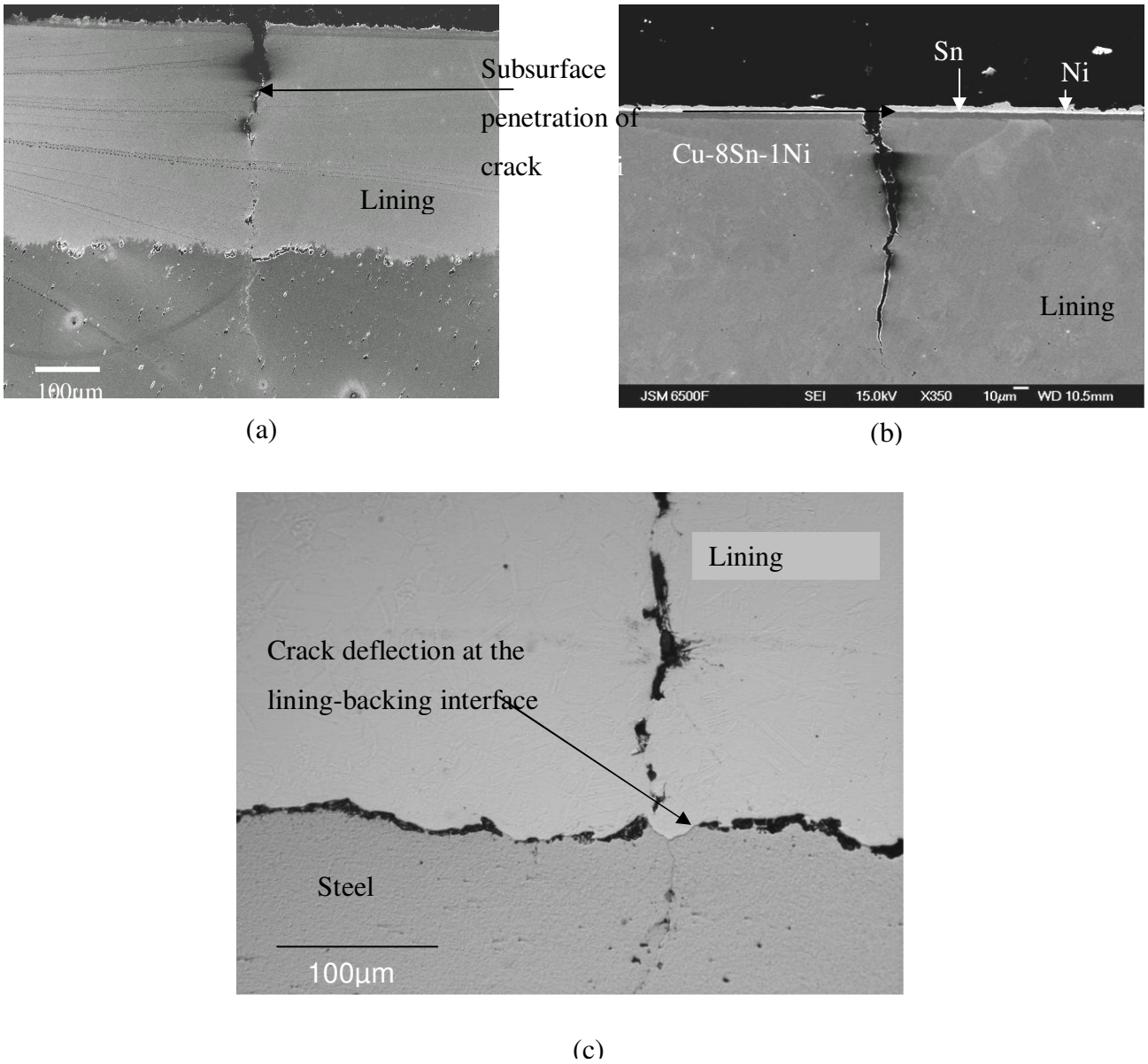

Figure 5.34: Subsurface crack trajectory in the RB168 (a) heat treated (b) non-heat treated specimen. (c) Crack penetrating into the steel backing. Both specimens tested at maximum estimated lining plastic strain of 0.003.

.

6 FURTHER ANALYSIS AND DISCUSSION

Experimentally observed differences in the fatigue lives for various finished bearings systems have been further analysed in the context of initiation of microstructurally short fatigue cracks (Chapter 2, Section 2.3) on the lining surface of the flat bar specimen and their subsequent growth behaviour leading towards gross failure according to a predefined criterion (Chapter 5, Section 5.2).

6.1. Microstructural fatigue damage initiation

Two basic types of lining alloys were investigated during the current work (i) *Al* and (ii) *Cu* based alloys. The *Al*-based AS20S/AS20 lining (in the tri-layer system) showed distinct secondary phase particles; whereas the other *Al* based lining (bi-layer) deposited by the HVOF process showed unmelt powder particles in the optical and SEM images. The *Cu* based lining known as the sintered bronze bearing alloy did not show distinguishable second phase particles under the optical and electron microscope. Micro-scale fatigue damage initiation analysis for the *Al* based bearing was carried out quantitatively whereas for the *Cu* based systems only some qualitative explanations can be given as the specimens available were not in a suitable geometrical shape to be subjected to surface replication during fatigue testing.

6.1.1. Short crack behaviour observed in previous Al bearing alloys

Figure 6.1(a) presents the fatigue initiation period at the lining surface observed for different systems compared with the subsequent growth period until failure in the flat bar specimen geometry. As evident from Figure 6.1 (a), a significant proportion of the observed fatigue life of the RB multiphase *Al* based systems is spent in the initiation of short fatigue cracks. It has been reported by *Barter et al*[1] that a significant proportion of fatigue life is taken up by the short crack regime (<1mm in length) and hence a material's microstructural aspects controlled by processing parameters and compositions are important in designing against fatigue initiation. Extensive work on fatigue initiation by *Goldsmith et al*[2], *Bowls*[3] and *Kung et al*[4] has concluded that microstructurally short fatigue cracks initiate at inclusions and secondary phase particles depending on their sizes. The tests in the present research are highly accelerated compared to service conditions where much longer lifetimes are observed and hence initiation

processes are expected to dominate overall fatigue lifetimes to an even greater extent. Hence a focus upon fatigue initiation processes has a great relevance to bearing design.

Experimental observation of fatigued linings has confirmed that fatigue initiation in the alloys under investigation was highly microstructurally dependent (Figure 6.1 (b-d)). For a clear understanding of the fatigue resistance of these alloys, microstructurally short fatigue crack growth behaviour must be explained in terms of fatigue initiation (where cracks form) and subsequent growth.

A quantitative assessment of crack initiation behaviour in the AS16 and AS1241 lining was carried out during previous research by *Mwanza et al*[5] in which an adaptive numerical modelling technique was implemented to classify the initiating particles using FBT features. The microstructure of these alloys was complex with a large number of *Sn* (AS16) and *Si*(AS1241) particles present along with few $CuAl_2$ type intermetallics. The *Sn* and *Si* particles were identified as the potential fatigue initiation sites in the AS16 and AS1241 linings respectively. The adaptive numerical analysis was implemented on the *Sn* particles in the AS16 and *Si* particles in the AS1241 lining (focusing on the particles initiating fatigue as well as those not participating in initiation). It was concluded that *Sn* particles associated with fatigue crack initiation in the AS16 lining were larger than average, had high aspect ratio and were aligned with their major axis perpendicular to the tensile axis. Subsequent microstructural modelling based upon elliptical inclusions showed that high hydrostatic stresses were developed at those regions of high curvature at the ends of the axis perpendicular to the global tensile axis and hence where the *Sn*/matrix interface appeared to be highly strained due to mismatch between the compliance of two phases (where the *Sn* was considerably more compliant than the *Al* matrix). On the other hand, *Si* particles associated with the crack initiation in the AS1241 lining were larger than the average, and had their major axis aligned parallel to the tensile axis. Since *Si* particles are less compliant than the *Al* matrix ($E_{Si} > E_{Al}$), crack initiation also occurred by decohesion of the *Si/Al* interface again at the region of maximum hydrostatic stress, which this time occurred at the sharp ends of particles aligned parallel to the tensile axis.

6.1.2. Particles observed in the AS20S lining

The AS20S lining is similar to the AS1241 lining in that both have *Sn* and *Si* particles in common although their volume fractions are higher in the AS1241 (*12%Sn and 4% Si*) than that in AS20S (6.5% *Sn* and 2.5% *Si*). In addition, the presence of small amounts of

Cu, Ni and *Mn* in the AS20S lining gave rise to the formation of intermetallics of more complex compositions ($AlNi_3$+$AlNi_4$+$CuAl_2$ type) than those observed in the AS1241 ($CuAl_2$). However the average particle size of *Sn* in the AS20S lining was much less than that in the AS16 lining (Table 4.7). This refinement in particle size and number was partly based upon the earlier work on AS16 and AS1241 to reduce the relative tendency to fatigue initiation. The current FBT analysis showed a slightly larger *Si* particle size in the AS20S lining compared to the AS1241, but the overall *Si* content in the AS20S lining was much less than that in the AS1241 lining producing a sparse distribution of *Si* particles. The most prominent feature of the microstructure of AS20S lining was the existence of *Sn* mostly surrounding intermetallic particles (very rarely *Si* as the latter were very occasional particles). In some regions, *Sn* also appeared to completely encapsulate intermetallic particles or clusters of intermetallic particles.

6.1.2.1.Analysis of various features of crack initiating particles

An AS20S flat bar specimen with polished lining surface was subjected to a 3-point bend fatigue test applying the same plastic strain amplitude (0.0064±.0002) as that applied to the study of their growth behaviour through replication (Section 5.2.3). In this instance the specimen was subjected to a certain number of load cycles (20% of the observed fatigue life) so that an appreciable number of short fatigue cracks (2-10µm long) were clearly observable under the optical microscope. However due to difficulties in distinguishing between *Sn* and intermetallic regions (Section 4.1.2), the cracked lining surface was observed under the SEM in order to scan a large area (4 mm^2) that showed short fatigue cracks initiating from aggregates of *Sn* and intermetallics which were not easily distinguishable from each other.

During a detailed analysis of early short cracks, three different types of crack initiating regions were identified in the SEI images (i) individual intermetallic particles ($Al\ Ni_3$ type) cracking (ii) *Sn* layers detaching from intermetallic particles (iii) *Sn* particles de-cohering from the matrix. Binary images consisting of each type of initiating and non-initiating particles were constructed for the FBT analysis using the same method as that described in Section 4.1.2.4 of Chapter 4. Various features such as object area A, object angle θ, mean near neighbour distance d_m and object aspect ratio r_a were calculated for each particle in the binary images of the initiating and non-initiating particles. All these geometrical features have been explained in Figure 3.7.

Table 6.1 shows all measured features for each type of initiating and non-initiating particle population. The number of each type of particle have also been given in the same table.

It is evident from this table that both initiating intermetallic and *Sn* particles had an average size higher than the average size of non-initiating particles. Detaching *Sn* layers were thinner than non-detaching *Sn* layers. The values of d_{mean} show that both initiating *Sn* and intermetallic particles were more widely scattered compared to non-initiating particles of the same type. The measured object angle and object aspect ratios did not show any observable differences between the initiating and non-initiating particles.

To understand the trend in a given particle population, distributions of all these measured features are shown in Figure 6.2 and Figure 6.3 in the form of histograms. These histograms show the frequency of initiating and non-initiating particles occurring for different values of the measured features. Apart from the object area distribution shown in Figure 6.2 (a), which shows a trend towards initiating for the coarser *Sn* and intermetallic particles, the other histograms showed a fairly random distribution of the measured features for different entities.

Table 6.1: FBT measured feature for various short crack initiating particles in the AS20S lining (number of particles in brackets)

	Intermetallics		Sn particles		Sn layers	
Features	Initiating (293)	Non-initiating (333)	Initiating (98)	Non-initiating (345)	Initiating (167)	Non-initiating (334)
Object Area(μm^2)	45±29	24±15	37±12	17±15	17±10	21±11
Object AR	1.50±0.41	1.5±0.39	1.62±0.37	1.6±0.47	1.97±0.59	1.93±0.66
Object Angle(rad)	0.8±0.46	0.86±0.41	0.93±0.50	0.95±0.38	0.50±0.39	0.93±0.39
d_{mean} (μm)	66±25	43±23	130±64	56±32	62±29	82±43
Total area fraction	0.008	0.0096	0.0023	0.0041	0.0032	0.0018

Figure 6.3 (b) shows that d_{mean} for all three types of crack initiating particles were higher than those of non-initiating particles. The object angle (angle between the direction of tensile stress and the particle major axis) distribution for the *Sn* and intermetallic particles is quite random (Figure 6.3(a)); however the object angle of the initiating or detaching *Sn* layers

was lower than that of the non-initiating *Sn* layers. The majority of the detaching *Sn* layers were aligned at an angle of 28° while non-detaching *Sn* layers were mostly aligned at 53° with respect to the tensile axis.

6.1.2.2.Short crack initiation observed in the HVOF lining

As shown in Figure 6.1(a), the crack initiation life of the HVOF lining was very short (about 1/20th of the RB systems at comparable lining plastic strain amplitude). Hence to distinguish the micro-scale initiation phase from the growth phase (which is comparable to the RB bearings) was quite challenging. However the HVOF flat bar tested at lower plastic strain (0.003) showed clearly that the most prevalent fatigue initiation sites were de-cohesion of the circular unmelts left during the spray coating process. However, detailed observations under scanning electron microscope proved that, some cracks were also potentially initiating from pores scattered throughout the microstructure (Chapter 5). As these unmelts were mostly circular (r_a~1), their object area and mean near neighbour distance were considered to be important features. FBT measurements of the object area of the crack initiating unmelts showed that their average area was 1723µm^2, which is higher than that of the non-initiating unmelt region valued at 1241µm^2. In addition, the d_{mean} values of the initiating unmelts were not much different from the non-initiating unmelts.

6.2. Micromechanical study of initiation

In this section initiation behaviour that accounts for 15-20 percent of the overall fatigue life of the AS20S lining will be examined in detail with the help of analytical and numerical modelling in the light of observed fatigue initiation phenomena. Fatigue initiation at the microscale level in a multiphase *Al* alloy such as AS20S/AS20 (as well as previously investigated systems) could be attributed to high stresses and strains at various microstructural locations developing under the applied load. More detailed analysis of the hydrostatic stresses developed around secondary phase particles with different compliance from the matrix is presented in the work of *Nutt* and *Needleman*[6] in which it is hypothesized that a crack initiates (due to interfacial decohesion of the secondary particles) when the hydrostatic component of the matrix stress state reaches a critical value. This hypothesis was confirmed by *White* and *Clyne*[7] who experimentally observed void nucleation sites along particle-matrix interfaces where the hydrostatic component of the applied tensile stress was highest.

Both analytical and numerical modelling was carried out in order to understand the nature and intensity of various types of stresses and strains within and around the particles. The AS20S lining consists of second phase particles of widely varying mechanical properties such as extremely compliant *Sn* particles (though these were rare), hard and stiffer *Si* and intermetallic particles. The behaviour of these embedded secondary particles under the applied load is therefore expected to be very different. On the other hand, the HVOF system has two distinguishable regions (matrix and circular unmelts) which are similar to each other in mechanical response (Section 4.6, nano-hardness test results).

The whole analysis was carried out using three types of modelling approaches, namely :

i Bi-material linear elastic modelling (both analytical and numerical analysis)

ii Bi-material non-linear elasto-plastic analysis (numerical modelling)

iii Tri-material non-linear elasto-plastic analysis (numerical modelling)

The main objective of using these different approaches was to examine the changes in simulated results when a simple bi-material linear elastic model was extended to a tri-material non-linear elasto-plastic model. The analysis was carried out for both AS20S and HVOF type linings.

Table 6.2 gives various properties of different materials along with the relative proportions of each constituent phase to be used in the subsequent modelling work.

Table 6.2: Various elastic properties used in the modelling work. Values highlighted were obtained from nano-hardness test results explained in Chapter 4

Phase	Lining type	Relative proportion (% volume fraction)	E (GPa)	ν
Al	AS20S	98	87±21	0.33
Sn		1.3	42	0.36
Al_3Ni_4		2.01	120±40	0.17
Circular unmelt	HVOF	2.5	68±17	0.33

Thus the effectiveness of a simple analytical model to predict the real stresses and strain fields in a complex multiphase alloy will be assessed.

6.2.1. Analytical approach

Analysis of elastic fields of an ellipsoidal inclusion embedded in a mechanically homogeneous material has been carried out by *Eshelby*[8] assuming linear elastic behaviour for

the inclusion and the matrix. In this analysis it was assumed that the inclusion undergoes a transformation (ε^t) represented by the strain tensor such that it does not fit in into its previous space. According to *Eshelby*, if a homogeneous elastic inclusion undergoes a "stress free" strain, then uniform stress and strain fields are set up within the constrained inclusion. The stress σ within the inclusion and constrained strain ε^C are related to each other as

$$\sigma = C_M\left(\varepsilon^C - \varepsilon^T\right)$$
$$\varepsilon^C = S\varepsilon^T \qquad 6\text{-}1$$

Where ε^C-ε^T is the misfit strain, C_M is the stiffness tensor of the material and S is a constant tensor that could be calculated from the aspect ratio of the inclusion and the Poisson's ratio of both matrix and inclusion. *Eshelby* results could be used to model stresses and strains within a particulate composite.

For the analysis of stresses within the current systems (AS20S and HVOF), it was assumed that these multiphase alloys would behave as bi-material particulate composites in which hard (intermetallics in the AS20S) and soft (unmelts in the HVOF system) particles are embedded in a mechanically homogeneous and isotropic matrix. The applied stress (σ^A) of 110 and 105 MPa was chosen for the AS20S and HVOF systems which were evaluated for the lining layer of these systems by an elasto-plastic 3-point bend FE model described in Chapter 5. These values of σ^A chosen were the estimated values of the maximum lining stresses acting during the fatigue initiation tests on AS20S and HVOF flat bar specimens. The assumed shape of the model and direction of σ^A is shown in Figure 6.4.

The results of the *Eshelby* analysis for the AS20S and HVOF systems are shown in Figure 6.5 in terms of variation in the particle and matrix stresses with the particle aspect ratio (r_a). Under applied load, a load transfer to the stiffer phase is evident in either case, with higher stress experienced in the matrix containing soft *Sn* particles than the *Sn* particles, while the opposite is observed for the matrix containing hard intermetallics. The dominant crack initiation mechanism appeared to be due to breaking of intermetallics or decohesion of the *Sn* film around the intermetallics in the AS20S lining. This can be explained in terms of the compliance mismatch between the *Al* matrix and the intermetallics, leading to significant load transfer to the intermetallics. These seem to be more brittle than *Si* (which has a similar compliance mismatch) since the intermetallics crack rather than decohere as the *Si* particles do. The increased compliance mismatch between the low stiffness *Sn* and stiff intermetallic may lead to

preferential decohesion of the *Sn* film due to local stress concentration effects. For the HVOF systems, Figure 6.5(b) shows that the maximum tensile stress within the matrix is high and remains fairly constant with increasing r_a of the unmelts within which the stresses are lower. The *E* value used for the unmelts was slightly lower than the HVOF matrix. Therefore a compliance mismatch between the unmelt and its surrounding matrix though not very significant, might have caused the experimentally observed detachment of unmelts from the matrix.

6.2.2. Numerical Modelling

The FE analysis of stresses and strains within the multiphase AS20S lining system was initially applied to (i) the bi-material linear elastic analysis for validation purposes and then extended to (ii) a bi-material and (iii) a tri-material elasto-plastic analysis. The important parameters calculated from the FE analysis are the maximum tensile stresses (σ_t) within the particle and the matrix, maximum hydrostatic stress (σ_{hyd}) within the matrix and surrounding *Sn* film and maximum plastic shear strain (ε_{shear}) in the matrix. The principal tensile stress is represented by σ_t, whereas σ_{hyd} at a point is the hydrostatic pressure due to all stress components.

6.2.2.1.Linear elastic FE analysis

Finite element analysis of the assumed elastic bi-material model (used in the *Eshelby* calculation of stresses) was carried out for a meaningful comparison of analytical and numerical results. Using the same material constants under exactly the same loading conditions, the parameters such as σ_t, σ_{hydro}, and ε_e were calculated by an Ansys code. Figure 6.6 (a) shows the meshed bi-material model in which a hard intermetallic particle was assumed to be embedded in a soft *Al* core. Along a 40 mm longitudinal dimension a 0.1 mm elongation was applied that gave a strain of 0.22% which produced an average stress in the systems ~110MPa in the AS20S lining. A similar stress level was used during the *Eshelby* analysis. The volume fraction (V_f) used in the model was consistent with that obtained from FBT measurements given in Table 6.2 Figure 6.7 shows the contour plots of σ_t and σ_{hydro} from which the maximum values within the particle and at the particle-matrix interface can be identified. The σ_t developing in the hard particle (intermetallic) is higher than that in the surrounding matrix which is in line with the results of the *Eshelby* analysis. Similarly, the development of high σ_{hydro} at the interface of

particle and matrix where the radius of curvature of the particle is minimum indicates a possible decohesion mechanism of the intermetallic particle, as observed experimentally. The results of the linear elastic FE analysis are presented together with the respective *Eshelby* results in Figure 6.8 as variations of σ_t in the particle and matrix with particle r_a. These results are not expected to agree perfectly since the *Eshelby* analysis was adapted to 2-D (from original 3-D), however they are sufficiently close to give more confidence in using either of these models to predict the stress distributions within any other type of particulate composite or multiphase alloy with known elastic properties of the matrix and the particle.

6.2.2.2.Elasto-plastic FE analysis

The *Eshelby* approach as well as the linear elastic FE analysis predicted the elastic response of the matrix and an embedded elliptical particle under the applied load. During fatigue loading, all layers within a multilayered bearing have different mechanical responses as was evident from the calculation of stresses and strains within different layers based upon the elastoplastic static 3-point bend test simulation. For an applied load of 900 N, the calculated maximum tensile stresses in the lining layer of all systems irrespective of the specimen geometry were above the yield stress of the lining layer (in excess of 70MPa which is > σ_y~60MPa). The lining layer itself consisted of an *Al* matrix containing *Sn*, *Si* and intermetallic particles. Both *Al* and *Sn* deform plastically. However in the FE analysis, intermetallics and *Si* particles were assumed to behave in a purely elastic manner. This assumption may not be a true reflection of the mechanical behaviour of intermetallics, however fatigue initiation observations showed early breaking of internmetallics which indicates that they were brittle. In order to explain the phenomenon of crack initiation, the FE model was built to simulate two different types of conditions;

(i) A bi-material elasto-plastic model: A hard elastic particle embedded in a soft elasto-plastic core (Intermetallic in *Al* matrix)

(ii) A tri-material elasto-plastic FE model with a hard elastic particle surrounded by a soft elasto-plastic layer, all embedded in a soft elasto-plastic matrix. For the elasto-plastic analysis, the materials flow curves obtained by standard tensile tests (Figure 6.9) were used as elasto-plastic input data for the materials behaviour.

6.2.2.2.1 Bi-material elasto-plastic FE model

The bi-material linear elastic FE analysis was extended to a bi-material elasto-plastic FE analysis in order to evaluate the particle and matrix σ-ε fields under conditions closer to the real deformation behaviour.

As the E value for the embedded intermetallic particle measured by nano-hardness tests was subjected to significant scatter, a sensitivity analysis was carried out by varying this value between 80-160 (measured value averaged at 120±40) in order to see the effects of this on resulting stress and strain fields in the matrix and the particle. Figure 6.10 shows that varying the E value within experimental scatter (r_a =3, particle major axis parallel to tensile axis) has a rather small effect on the both maximum tensile and hydrostatic stresses in the particle and matrix, respectively. However the plastic shear strain in the matrix appears to increase significantly with increasing particle E value. Hence elasto-plastic FE results in terms of particle and matrix stresses are less sensitive to the variation of the particle elastic modulus.

It was observed during statistical analysis of fatigue initiation in the AS20S lining that the particle size of the intermetallics was linked to short crack initiation. FBT analysis of the size distribution showed that relatively coarser individual intermetallic particles were predominantly cracking or detaching from the matrix. For the FE analysis, the particle V_f was varied from 2-5% (average value 2.5%) in order to examine its effect on critical stresses and strains. The major axis of the elliptical particle was assumed to be aligned in the direction of the applied stress. Figure 6.11 shows that increasing the particle V_f increases the predicted σ_t, σ_{hydro} and plastic ε_{shear} in the system. When V_f was increased from 2 to 5%, the tensile stress in the intermetallic particle was increased by approximately 28% whereas the hydrostatic stress at the particle-matrix interface was increased approximately by 16%. This could be attributed to the fact that as the particle size increases, more load is transferred to it generating higher σ_t within the particle giving rise to its breakage and higher σ_h stresses at the particle-matrix interface due to a severe compliance mismatch between soft matrix (*Al* in this case) and hard particle. Crack initiation at the interface could be either due to the predicted high hydrostatic stresses or the high plastic shear strain.

6.2.2.2.2 Tri-material elasto-plastic FE analysis

In the AS20S lining, apart from microscale fracture of intermetallics, the detachment of *Sn* layers from hard intermetallics (or *Si* particles occasionally) was quite evident.

Sn itself is softer than intermetallics or the *Al* matrix. The σ-ε flow curve for *Sn* shown in Figure 6.9 reflects the behaviour of cast *Sn* under a normal tensile test which is expected to be softer than one present as a coating around the hard particles in the A20S lining as the latter form has emerged as a result of rolling and heat treatment operations during bearing manufacture and will have less casting defects. Therefore the use of elasto-plastic data of cast *Sn* may not reflect the true mechanical behaviour of *Sn* layers in a tri-material FE model. However the purpose of this model was to understand the distribution of microfields of stresses and strains at various locations of a tri-material system comprising materials of widely varying mechanical properties that may explain the possible causes of fatigue initiation in the AS20S lining (Figure 6.1(b)). Figure 6.12 shows the distribution of σ_t, σ_h and plastic ε_s in the tri-material FE model representing an intermetallic coated with *Sn* layer in the AS20S lining. The "hard particle-quite soft layer-intermediately hard matrix" gives rise to a complex assembly of three materials, the response of which under applied stress/strain has to be carefully examined before attempting to link it with observed fatigue initiation process. Thus, a parametric investigation was carried out to study the sensitivity of stresses and strains to the thickness of surrounding *Sn* layer, the aspect ratio r_a of the layered particle and its orientation.

In the 2-D meshed FE model, the ratio of the embedded intermetallic particle to the matrix was kept fixed (according to the FBT measured V_f =2%) and the thickness of the encapsulating *Sn* layer was varied as a percentage of the particle major axis from 0 to 10% (since within the microstructure of the actual sample, the thickness of the encapsulating *Sn* layers was observed to be falling within that range).

Figure 6.13(a) shows how the variation in the thickness of *Sn* layer affects the predicted σ_t, σ_{hydro} and plastic ε_{shear} in the tri-material system provided that the particle major axis remains aligned with the tensile axis and r_a (major axis/minor axis) is equal to 3. It is evident that higher tensile stresses develop within the particle when practically no *Sn* layer is present. Under that situation the stresses within the matrix were found to be approximately 11-14% lower than in the particle. With the introduction of the encapsulating *Sn* layer, the maximum tensile stresses within the particle drops to some extent and achieves a relatively constant value for layer thicknesses up to 10% of the particle major axis. The tensile stresses within the matrix and the *Sn* layer fall too, with gradual increase in the *Sn* layer thickness but remain fairly constant at a level ~12 and 20% lower than the particle stresses respectively. In order to explain the observed fatigue initiation in the light of FE predicted tensile stress trends, a

situation could be imagined in which a very hard and less compliant intermetallic particle is surrounded by an extremely compliant *Sn* layer, the load carrying ability of which is negligible compared to the surrounding *Al* matrix (c.f. flow curve of *Sn* shown in Figure 6.9). As far field stress is applied to the *Al* matrix (intermediately hard) which was no longer in direct contact with the stiffer and less compliant intermetallic, most of the strain is borne by the matrix resulting in higher stresses in the particle. Maximum stresses therefore develop when no *Sn* layer is present and this explains the fracturing of individual intermetallic particles as observed experimentally due to a comparatively higher load carried by them.

The variation of the predicted hydrostatic stress at the layer-particle and layer-matrix interface is also shown in the Figure 6.13(a). It is evident that for *Sn* layer thickness of 1-3% of the particle major axis (equivalent to 3-4 μm thickness), the estimated hydrostatic stresses were higher than those estimated for layer thicknesses higher than these values. This explains the detachment of 3-5μm thick *Sn* layers during investigation of fatigue initiation observations. The variation of plastic shear strain in the matrix and *Sn* layer is shown in Figure 6.13(b). In the absence of a *Sn* layer, the matrix adjacent to the particle showed the highest value of plastic shear strain which falls significantly in the presence of *Sn* layer and within which its value decreases as its thickness increases.

Figure 6.14(a) shows the effect of varying the particle major axis orientation relative to the axis of the applied stress while keeping the r_a and layer thickness constant at 3 and 0.05a respectively (a = particle major axis). It evident that variation in the particle orientation gives rise to a complex combination of tensile and hydrostatic stresses in all three materials. When no *Sn* layer is present, the tensile stresses in the particle remain approximately 10-12% higher than the matrix for orientations 0-45^o after which these values fall to achieve the same stress level as in the matrix. The trend of tensile stresses in the presence of *Sn* layer becomes more complex. Both particle and matrix tensile stresses are maximum when the particle lies at an angle of 15^o to the tensile axis. However the particle stresses were much lower than the stresses in the matrix when the particle is aligned at an angle greater than 30^o. Moreover the change in the orientation from 0-90^o does not seem to be affecting these types of stresses in the layer. The hydrostatic stresses at the particle-*Sn* layer interface did not appear to be affected much by the variation of the particle angle. The hydrostatic stress at the *Sn* layer matrix interface were minimum for extreme orientations (θ=0^o and 90^o).

Plastic shear strain values (Figure 6.14b) in the *Sn* layer are maximum under both extreme situations (particle parallel and perpendicular to the tensile axis). The high values of plastic shear strain in the *Sn* layer compared to the matrix might have caused crack initiation in the *Sn* layer. The other reason for the detachment of *Sn* layer from the matrix may be the presence of high hydrostatic stresses in the matrix[6].

Figure 6.15 shows the combined effects of variation in the thickness of *Sn* layer and the orientation of the embedded elliptical intermetallic particle upon all the measured parameters keeping particle aspect ratio constant. The particle tensile stresses are maximum when no *Sn* layer is present and it is aligned along the tensile axis. Although the object angle measured could not be verified from the FBT measurements of crack initiating particles, as the object angle of those particles was fairly randomly distributed among initiating and non-initiating particles, however, the majority of the intemetallics appeared to be fracturing without an outer layer or when partially encapsulated within a *Sn* layer. The FBT measured object angle of non-initiating *Sn* layers was ~53-56^{o} when the layer thickness was 10% of the particle major axis (equivalent to a thickness of 2 micron in the actual microstructure). It is evident that minimum hydrostatic stresses in the matrix and *Sn* layer occurred at an angle of 60^{o} which is fairly consistent with the FBT measurement, as higher values of hydrostatic stresses in the matrix or the *Sn* layer are deemed to be the cause of debonding of the *Sn* layer from the matrix. Maximum plastic shear strain appears to be occurring within *Sn* layer when the particle was aligned perpendicular to the tensile axis with *Sn* layer thickness 7-10% of the particle major axis.

Figure 6.16 shows the effect of variation in the r_a of the embedded particle coated with a *Sn* layer of 4% of the particle major axis upon various measured features. As shown in Figure 6.16 (a), the tensile stresses within the particle as well as the surrounding matrix appear to be minimum when the particle r_a was 1. At $r_a < 1$, both *Sn* layer and the matrix show higher values of tensile stresses than in the hard intermetallic (the intermetallic particle could be imagined as aligned perpendicular to the tensile axis). At $r_a > 1$, the tensile stress in the layer and the matrix drops whereas within the hard intermetallics it appears to rise. The variation of the hydrostatic stresses at the layer-particle and layer matrix interface shown in Figure 6.16 (a) appears to be less affected by the change in the r_a; however it is evident that these stresses were higher at the particle-layer interface and lower at the layer-matrix interface when $r_a<0.5$. Plastic

shear strain within the *Sn* layer decreases significantly as the particle r_a increases. However no significant effect was observed on the plastic strain intensity in the matrix (Figure 6.16(b)).

The combined effect of variation in the r_a and the thickness of *Sn* layer are shown in Figure 6.17 in the form of 3-D curves. Maximum tensile stresses in the particle are created when its r_a is high and when no encapsulating *Sn* layer is present. Similarly the hydrostatic stresses in the layer-matrix and the layer-particle are high when the r_a of the particle is higher than 1 (particle aligned perpendicular to the tensile axis). This seems to be in agreement with the early FE modelling results to explain the fatigue initiation in the AS16 lining[5]. It was observed that maximum hydrostatic stresses existed at the minimum radius of curvature of *Sn* particle when it is aligned in a direction perpendicular to the tensile axis and caused decohesion from the surrounding matrix. The situation is not as simple in the tri-material model, however higher hydrostatic stresses in the matrix and *Sn* layer explains the detachment of *Sn* layer from either the matrix or the hard intermetallic particle.

6.2.3. Optimum geometry for maximum fatigue resistance

The FBT measured features of the AS20S lining microstructure did not show a well defined trend in the measured features related to the shape of the crack initiating particles compared to the previous AS16 and AS1241 lining and hence the linking of these features to micromechanical results was not a trivial task. FE modelling results did not present a simple relation between various measured features for different particles. However the effect of variation of two parameters simultaneously (layer thickness and particle orientation/ particle angle) on the stresses and plastic strains as presented in the form of 3-D curves in Figure 6.15 and 6.17 was observed to be helpful in estimating optimum size ranges and shapes. A minimum level of these values was reckoned to be the norm for defining particle geometrical features with optimum resistance to mechanical damage.

According to experimental observations most of the breaking intermetallics were individual i.e without an outer *Sn* layer or with a partial *Sn* layer. The failure of hard and brittle intermetallics was the result of high tensile stresses created within them due to a far field tensile stress. An individual intermetallic particle least favourable for breaking has a size of 24±15 μm (Table 6.1) and is aligned 40-60^o with the tensile axis (Figure 6.14(a)). *Sn* layers least likely to detach are those more than 8% of the particle major axis (>3 μm thickness in the actual microstructure) as the values of maximum hydrostatic stress and plastic shear strain are

minimum beyond these limits. Similarly *Sn* layer and the matrix experience minimum hydrostatic stresses when the particle is aligned at an angle 55-60^o with respect to the applied tensile axis (Figure 6.15 (b)). If the aspect ratio is considered, it is evident from Figure 6.17 (a) that a relatively globular intermetallic particle (r_a~1) with *Sn* layer thickness of 8-10% of the particle major axis has minimum tensile stresses under the applied load and hence is less prone to breaking or crack initiation. A *Sn* layer with r_a ~2 and thickness more than 8% of the particle major axis has minimum hydrostatic stresses under the applied load and hence is less prone to decohesion or debonding from the matrix or the adjacent intermetallic particle (Figure 6.17 (b)).

Size, morphologies and distribution of the secondary phase particles within the microstructure are dependent on a number of factors which are related to their composition, manufacturing techniques as well as a combination of various parameters used during mechanical working of the bearings and intermediate heat treatment. With the knowledge of optimum particle sizes and shapes, microstructural goals can be defined for one or more of these manufacturing and processing parameters to be adjusted to form an alloy with best resistance to fatigue initiation.

6.3. Surface short crack growth behaviour

The detailed analysis of the surface short cracks was carried out only for the *Al* based alloys as the bronze bearings were not available as flat bars to apply surface replicating techniques.

6.3.1. Crack tip characterization

Both tips of a short crack advance after initiation provided that there is no shielding effect from a neighbouring large crack or from any secondary particle. Crack growth rate is sensitive to the local microstructural features as the advancing crack tips may interact differently with different secondary phase particles. The AS20S lining microstructure is complex as both *Sn* and intermetallics occurring together offer different compliance conditions to the advancing crack tips. Experimental observations showed that crack tips were seeking clusters of *Sn*. *Sn* particles in the AS20S lining are softer than the intermetallics and mostly encapsulate them. It is probable that the local stress conditions as a result of mismatch in the mechanical properties of the two phases might have accelerated the crack growth as soon as its tip arrived at such a soft cluster or retarded when it arrived at hard intermetallic particle.

6.3.2. Plastic zone calculation, crack coalescence and shielding

The fast growth rate of a crack observed when its tip approaches the tip of another collinear crack is the result of the interaction of the plastic damage ahead of their tips. The size of the plastic zone developed ahead of a crack tip during cyclic deformation is dependent upon the values of ΔK and σ_y (of lining layer in this case) and is given by *Rice*[9]

$$r_c = 0.318\left(\frac{\Delta K}{2\sigma_y}\right)^2 \qquad 6\text{-}2$$

This formula is a simple estimation of the plastic zone ahead of a crack tip in an isotropic material.

When two collinear cracks approach each other, their plastic zone sizes r_c can be considered the coalescence zones and as soon as the crack tip spacing is comparable to the r_c, growth rate increases until the cracks coalesce.

During previous work by *Joyce*[10], crack interactions were classified into three types namely collinear, parallel and oblique (Figure 6.18). In his work, the tips of two cracks were considered to interact with each other in one of the above mentioned ways. For simplicity of the FE model, he assumed that the tip of one of the cracks was stationary (crack not growing at all) while the tip of the growing crack was considered to be advancing gradually towards the corresponding tip of the stationary crack. In the FE modelling approaches used to characterize their interaction, collinear cracks showed an increase in the driving force of the crack tip advancing towards an assumed stationary crack. This happens as the lobes of the converging plastic zones appear to deform towards each other forming an annular plastic zone. As the tip further advances, the region between two tips becomes entirely plastic that results in coalescence. Similar plastic zone deformations have also been reported by *Kaung and Chen*[11]. Parallel cracks were modelled in such a way that their axis of symmetry is normal to the applied load. The vertical crack spacing was kept constant. Using an appropriate FE model it was shown that the initially growing crack was shielded by the larger free crack (a larger plastic zone existed ahead of the free crack). As the length of the growing crack was further increased its driving force ($J_{growing}$) increases and at the same time the driving force of the free crack seemed to be reduced. When they achieve equal size, their driving forces become comparable. The converging lobes of their plastic zones are distorted towards each other giving rise to high

stresses. Further increase in the length of the growing crack overtakes the free crack and continues to grow at the expense of the free crack driving force (which is entirely shielded) while a large plastic zone exists ahead of the growing crack. The cracks interacting obliquely showed a complex behaviour in which both shielding and coalescence mechanisms were observed. Assuming similar growing and stationary cracks (but with oblique orientation), the crack tip driving force seemed to be increased at the converging tips but to a lesser extent than the collinear cracks (greater spacing between cracks due to vertical alignment and hence plastic zones did not merge to the same extent.). Upon further increase in the length of the growing crack the driving force at the closing tips seemed to reduce indicating a shielding mechanism. These tips appeared to be deflecting towards each other without further propagation normal to the far field applied stress.

These modelling results are now considered in terms of the experimental observations of the surface crack growth in the three types of linings.

Crack fields at different lifetime intervals are shown in Figure 6.19-6.21 for all three lining systems with calculated plastic zone sizes at each crack tip. It is evident that in the maximum ε_p region, most of the AS20S/AS20 lining surface cracks interact in a collinear way after a significant fraction of fatigue life and form dominant cracks (Figures 6.19-20). A few cracks in the surrounding low ε_p (0.0055—0.0060) were observed which showed a parallel interaction with the cracks in the maximum ε_p region and hence did not show measurable growth.

Crack fields developed in the HVOF lining are shown in Figure 6.21 which reveals many short cracks emerging form both maximum and lower ε_p regions. However most of the cracks in the lower ε_p region are shielded by the cracks in the high ε_p region due to the large number of cracks and hence the greater number of parallel interactions. Parallel and oblique interaction was also observed within the narrow strip of maximum ε_p region of the HVOF lining. There is no obvious difference in the propagation behaviour of short cracks between the AS20S and AS20 lining surfaces; however the formation of dominant cracks was observed to be quicker in the AS20 specimen resulting in shorter total lifetime at similar ε_p level. This could be a reflection of the expected scatter in lifetimes at this ε_p range arising from the location of individual initiation sites giving rise to somewhat differing coalescence behaviours.

The plastic zone size values calculated by Equation 6.2 and the modelling of crack interactions is based upon the isotropic properties of the bulk materials and hence does not account for the secondary particle's interaction with the crack tips where the differing mechanical properties of the particles may be expected to give rise to local shielding, deflection or accelerated crack growth. A model that could incorporate both the microscale interaction of the crack tip with embedded secondary particles with different properties from the matrix and the more mesoscopic interactions of crack fields with overlapping, collinear, oblique or parallel interactions could provide a better basis for assessing an optimised microstructure for this regime of fatigue failure. Another key requirement in setting up such a model would be the ability to predict appropriately the distribution of initiation sites for a given particle population, in order to set up the appropriate microcrack fields, to which the mesoscopic crack growth modelling could then be applied. However, development of such a complex multiscale modelling approach was beyond the scope of this research. A more modest approach is outlined in the following section.

6.3.3. Crack growth modelling and fatigue life prediction

Qualitative analysis of the short fatigue crack growth helped in understanding individual crack growth behaviour as well as their interaction in the form of coalescence and shielding. Modelling of short crack growth behaviour therefore requires a robust description of individually growing short fatigue cracks.

In order to explain short crack behaviour numerically, various stages involved during their early growth such as coalescence with similar growing cracks as well as shielding effects of a neighbouring crack must be defined and quantified or estimated. For a multiphase alloy such as the AS20S lining, each individually growing short crack interacts with secondary phase particles (*Sn*, *Si* or intermetallics) of varying mechanical properties. A detailed crack tip characterization is therefore quite challenging. The problem is further complicated with particles having sparse distributions and irregular morphologies. Before adopting any methodology for simulation of short crack growth behaviour in order to generalize towards a total life prediction, various approaches used in the previous work are here briefly reviewed. *Soboyejo et al* [12] working on medium strength pressure vessel steel (with martenstic microstructure) evaluated the interaction of coplanar semi-elliptical cracks. They concluded that before any contact, coplanar cracks grow almost independently. When they coalesce their stress intensity factor

increases, instantly after which a rapid transfer to a single elliptical crack occurs. Such FE based data was observed to be in good agreement with the experimental crack growth data.

Chen et al[13] has carried out a detailed experimental and numerical analysis of microstructurally short fatigue cracks emerging during fatigue testing of 2124 *Al* alloy composite reinforced with *SiC* whiskers. They subjected experimentally observed events of crack coalescence and arrest to statistical analysis (Monte Carlo simulations) in order to define probability of crack arrest, crack growth and coalescence. *Lefebvre*[14] has reported his work on short fatigue crack simulation in the 2024-T351 based material in conjunction with the metal inert gas (MIG) welding process. It was observed experimentally that crack initiation was linked with two kinds of defects: interdendritic defect (~10-50 microns) and gas porosity. Based upon measured distributions of defect sizes related to short crack initiation and their mutual interactions (coalescence and arrest), a crack propagation model based upon the *Hobson*[15]approach and on a microstructure sensitive approach based upon continuous dislocation distribution method were used which represented fatigue behaviour of these materials quite well.

A direct implementation of any short crack growth modelling technique to the current RB AS20S type lining is not simple as a large number of short cracks should be merging during the fatigue test in order to get a best possible estimation of their growth behaviour prior to their forming dominant cracks. As presented earlier (Chapter 5), short crack initiation events at a maximum lining stress level of 105MPa (Max ε_p=0.006±0.0004) in the AS20S lining were observed to be approximately 20/mm^2 at N_f~20%. Some of the initiated cracks coalesced immediately with the neighbouring initiating cracks. The main challenging aspect for the application of any crack initiation simulation method is the randomness in the distribution of the shape of initiating and non-initiating particles. This was evident from the FBT measured features such as object angle and object aspect ratio (Section 6.1.2.1) showing no specific trends. The only feature relevant to the initiation was the particle size (coarser particles more prone to initiation) which itself showed a wide size range. In order to derive any empirical relation for crack growth modelling, some further assumptions are necessary to make the procedure simpler.

6.3.3.1. Semi-empirical modelling approaches

In the *Hobson*[15] model where short crack growth is characterised in a continuous material with well defined grain boundaries, it is assumed that crack growth rate is proportional to the distance between the advancing crack tip and an approaching grain boundary.

$$\frac{da}{dN} = C_1\left(\frac{n}{2}D - a\right)^{1-\alpha} a^{\alpha} \qquad 6\text{-}3$$

C_1 and α are constants; D is the grain diameter and n is the number of grain spacings.

In order to obtain constants such as C_1 and α some fitting with experimental data is required and this approach was developed by other researchers including *Grabowski* and *Yates*[16], *Bomas et al*[17] and *Lefebvre*[14]. Based upon experimental data for the material in question they defined boundary conditions in the model (in terms of maximum and minimum spread in the growth rate). They derived upper and lower growth bounds from experimental data and assumed a linear growth of cracks between grain boundaries (i.e. α =0 in equation 6-3 in order to simplify *Hobson*'s original model). After the short crack regime, a *Paris* law was assumed to occur.

6.3.3.2.Objectives of the current model

The purpose of the crack growth modelling was to investigate how effectively the experimentally measured *da/dN* versus ΔK data, obtained for the growth of microstructurally short fatigue cracks in the AS20S lining (Refer to Chapter 5, Section 5.2.5.2) could be used to estimate the total fatigue life of AS20S flat bar specimens tested at various plastic strain amplitudes. In this application of the *Hobson* model it was assumed that the spacing of hard particles was equivalent to the grain size term in equation 6-3 for the crack barrier spacing.

6.3.3.3.An overview and basic assumptions

A two dimensional schematic view of the cracked lining surface of the flat bar specimen is shown in Figure 6.22 (a). This shows the surface damage condition (for a specimen defined as failed according to the compliance criterion explained in Chapter 3) with a number of dominant cracks that have developed throughout the lifetime. It is also evident that the damaged area lies in a narrow surface strip (19.5×1.5mm). The specimen was tested at a maximum lining stress of 105 MPa, which was an intermediate value in the overall load spectrum used in the

fatigue life experiments. The average length of the dominant cracks calculated was 5±3 mm. By back tracking, the growth history of each of these long cracks was determined using replicas (obtained during interrupted fatigue testing), assessing the number of coalescence and shielding events in each region. These coalescence and shielding events have been shown in Figures 6.18-6.21. The schematic of the simulated microstructure is shown in Figure 6.22(b) which shows small intermetallic particles scattered throughout the microstructure along with some coarse intermetallics with a potential to initiate cracks. Experimental study of short crack initiation showed that the average fatigue initiation life was 20% of the observed total life of a specimen at this stress level. For the modelling work, the crack growth behaviour (determined experimentally) of the lining of AS20S flat bar specimen tested at $\Delta\varepsilon_p$ =0.006 in the form of *da/dN* vs. ΔK data was used. The values of ΔK were obtained using the *Scott* and *Thorpe* equation (explained in Section 5.2.5.2) assuming small uncoalesced cracks of halfpenny shape with a/c ratio equal to 1 up to a surface length of 0.4mm. However, as the surface crack length increased due to coalescence, the a/c ratio thereafter varied as *a*/0.4 (as the lining thickness was approximately 0.4mm) To simulate the growth behaviour of the short fatigue cracks, the following assumptions were made.

- In order to simplify the model, it was assumed that all cracks were initiated at $N = 0.2N_f$ (based upon experimental observation on initiation at $\Delta\varepsilon_p$=0.006). Subsequently interaction between these initiated cracks was considered. There were some short cracks of the order of 5-8µm appearing after this period. These cracks immediately coalesced (with collinear cracks) and resulted in an increase in *da/dN*. Other cracks of the same size order were arrested (those parallel to the growing cracks) due to the shielding effects of neighbouring cracks and did not grow. For growth simulation, only the cracks initiated in the early stage were considered and their coalescence with similar cracks was accounted for.
- For the modelling of initiation, the most prominent fatigue initiating particles i.e. the intermetallics and layered intermetallics were considered. This was further simplified by representing all such particles as a single population in the simulated microstructure as the growth behaviour does not depend on whether the crack was initiated from an individual intermetallic or intermetallic encapsulated with a *Sn* layer. The d_{mean} value between the particles retarding a growing crack was used as a distribution factor. These values based on FBT measurements have been given in Table 6.1.

- Initial size of the short cracks was assumed to be of the order of the average diameter of the particle (individual or layered intermetallic) participating in the initiation process. This size was approximately 5 microns.
- The growth data used in this work was in the form of *da/dN* vs ΔK relationships. In order to model crack growth in the AS20S lining, retardation in the crack growth was linked to interaction with hard intermetallics. These hard intermetallics, scattered throughout the microstructure (considering their average distribution) were assumed to act as barriers to growth (as do the grain boundaries in the *Hobson* model). It was hard to find a large number of individually growing short cracks without interaction with any other entity such as a second phase particles or neighbouring crack. However, within various dominant crack regions, a limited number of small individually growing cracks (2-3 in each of the 6 regions) was observed to be growing in a continuous matrix during the very early stage of fatigue life 0.2-0.3N_f). Average experimental growth behaviour of such cracks was as approximated by the following equation.

$$\frac{da}{dN} = (C_1)\Delta K + C_2 \qquad 6\text{-}4$$

Where C_1 and C_2 were empirically derived constants valued at 4×10^{-5} and 3×10^{-4} mm/cycle respectively.

- Using experimental data of *da/dN* obtained during interrupted fatigue testing, upper and lower bounds of the growth rate were derived as shown in Figure 6.23. There was a large scatter in the these bounds, however the best possible fit is shown in this figure that incorporates ΔK levels from very low to higher values. These upper and lower bounds indicate the peaks (due to crack coalescence) and drops (due to crack interaction with intermetallics) in the growth rate of short cracks.
- After initial fast growth, the growing crack is assumed to encounter a hard intermetallic particle (a non-initiating intermetallic particle). This retards crack growth (a fall in the growth rates is observed experimentally and shown in Figure 5.27). Figure 6.24 shows the schematic of assumed crack growth behaviour up to the average length of 5mm. This diagram explains how the growing crack encounters the intermetallic particles (drop in *da/dN*) and a similar collinear crack (rise in *da/dN*). Total life includes initiation life as well as a 10% life observed experimentally when practically no surface crack growth could be measured because of subsurface shielding effects. The spacing between the

intermetallic particles was derived from FBT measurement (44±15 μm). The average number of coalescence and shielding events (measured from dominant crack regions) were utilized to simulate the growth behaviour of a crack up to 5mm. Within the total crack growth of 5mm, 4 such coalescence events were incorporated (based on the average value obtained from various dominant cracks observed across the whole damaged surface). It should be noted that after achieving a length of 1-1.5 mm, the microstructural barriers i.e. the intermetallics, were assumed to be no longer effective and hence a *Paris* growth law was estimated. However experimentally, this regime was very hard to achieve as a similar neighbouring crack usually coalesced resulting in a rapid increase in growth rate. For crack growth simulation, ΔK levels were obtained for various lengths of cracks up to 5mm total length at a far field applied stress of 105 MPa using the *Scott* and *Thorpe* equation. Corresponding values of *da/dN* were obtained using Equation 6-4 (upper and lower growth bounds defined by curves in Figure 6.23). Number of cycles during each growth step was calculated by integrating Equation 6.4 and all these cycles added to initiation life as well as 10% of the total fatigue life observed (which accounted for the remaining life of the specimen prior to the final failure criterion, during which surface growth ceased due to subsurface shielding effects, although some sub-surface crack growth continued to give final failure). All these life intervals were summed to get an estimated life of the specimen. For comparison with the experimental fatigue lifetime curves, the values of $\Delta\varepsilon_p$ corresponding to applied $\Delta\sigma$ (and hence ΔK levels) were used.

6.3.3.4.Sensitivity of the model

The sensitivity of the above model was investigated based on the variation in the following parameters.

- Applied $\Delta\varepsilon_p$ levels were varied from 0.003-0.012 (by changing applied σ level)
- Spacing between intermetallic particle retarding crack growth was varied from 25 to 80 μm.
- Changing the initiation life from 15 to 25% of the observed fatigue life.

6.3.3.5.Results and discussion

Figure 6.25 shows the comparison of experimentally obtained fatigue life results of AS20S flat bar specimens in the form of $\Delta\varepsilon_p/2$-N curve with the results obtained from crack growth simulation at three different particle spacings used (at various plastic strain levels). It is evident that the estimated fatigue life data points on the basis of experimentally observed average particle spacing (d_{mean}=44μm) fall closer to the experimentally measured life time curve at higher plastic strain amplitude values. At lower plastic strain amplitudes, these data points showed lower estimated fatigue life compared to the experimentally observed results. The estimated lifetime data was derived for the flat bar specimen tested at a plastic strain amplitude of 0.0030 which is an intermediate value in the plastic strain amplitude range used for all tests. The possible reason for this discrepancy at higher and lower plastic strain amplitudes is the delay in the initiation process at lower plastic strain amplitudes. A similar effect was observed in the previous research by *Edward and Yang*[18] and *Suresh*[19]. *Lefebvre*[14] simulating a single crack growth model in his work on MIG weld fusion zone found that the modelling results gave a reasonable approximation of the parent alloy at higher stress levels. However, the data diverged at lower stress levels which was attributed to the increasing fatigue initiation life at the lower stress levels which was fitted to a fixed proportion of the lifetime in the current situation.

Variation in the fatigue initiation life from 15%-25% of the observed total life of the specimen resulted in the corresponding scatter in the lifetime axis, however this scatter could not account for the discrepancy between experimental and modelled fatigue life predictions at very low plastic strain levels.

The fatigue life of the AS20S system was observed to be sensitive to the applied stress and hence the plastic strain level. Figure 6.26 (a) gives a comparison of the fatigue initiation life times of the AS20S flat bar specimens at various plastic strain levels. It is evident that the initiation time interval approximately increases by 12 times when plastic strain amplitude is reduced to one half. Comparison of the lining fatigue initiation life of the AS20S system with the previous AS16 and AS1241 flat bars is shown in Figure 6.26 (b). It is evident that the initiation life of the AS20S is much higher than the previous RB *Al* based linings. This improved resistance to fatigue initiation has contributed to the overall observed fatigue resistance of the AS20S lining. However, for a more precise estimation of the total fatigue life on the basis of da/dN vs. ΔK data, empirical growth laws must be derived from experimental results at low plastic strain levels in order to account for the increased fatigue initiation life.

In this analysis, when particle spacing was decreased to 25 µm (i.e. the number of barriers to advancing crack tip increased), the estimated fatigue life appeared to be higher than the fatigue life estimated at d_{mean} =44 (experimentally observed spacing) and 80µm as shown in Figure 6.25. A good agreement between the experimental and simulated curve at lower plastic strain amplitude is evident. This means that increasing the number of barriers to advancing crack results in frequent drops in the growth rate that has accounted for (to some extent) the delayed initiation in the AS20S systems at lower plastic strain amplitude.

6.4. Subsurface crack growth

Crack deflection mechanisms during interaction with layers of different mechanical properties i.e. elastic modulus and yield strength have been extensively studied by early researchers. For bimetal layers, it was argued by *Suresh et al*[20] on the basis of a micromechanics approach that when a crack reaches an interface from a softer layer, cyclic slip in the harder layer becomes difficult and the crack deflects as it seeks a material with lower resistance to fracture, the crack deflection causing a reduction in the crack tip driving force and hence results in the crack arrest. *Suresh et al*[20] and *Joyce*[21] studied subsurface crack growth behaviour in tri-metal layers using FE analysis. These models showed enhanced crack tip driving force as the crack reached the softer interlayer from a relatively harder lining and penetrates until shielding and a propensity for deflection becomes apparent due to the influence of hard steel backing.

6.4.1. Effect of interlayer

6.4.1.1.RB systems

In the current work, effects upon subsurface deflection of the crack were investigated with two different interlayers pure soft *Al* (AS20S) and a harder brazed sheet (AS20). The thickness of both layers was of the order of 40 microns. A magnified schematic view of the failed AS20S and AS20 systems along with their layer architecture is shown in Figure 6.27. The deflection mechanism of the crack at the *Al* interlayer in the AS20S bearing is in agreement with the early work by *Joyce*[21] according to which the fatigue crack entering from a harder AS20S lining to the softer *Al* interlayer penetrated and then deflected in the interlayer due to the shielding effect of the harder backing layer. The AS20 system had the more complex interlayer (3003+4343) which was harder than the pure *Al* foil in most of the RB systems. Within the brazed sheet, the 4343 layer (adjacent to steel layer) was found to be softer than the

3003 layer. As the subsurface crack tip approaches the 3003 layer there is an increase in the crack tip driving force as 3003 was still softer than the AS20 lining. This driving force further increases when the crack tip interacts with the even softer 4343 layer. But the thickness proportion of the 4343 layer was approximately 10% of the whole brazed sheet (total thickness 0.04mm) and hence the SEM images seemed to (and are likely to) show the interlayer as detaching directly from the backing layer. It was however difficult to prove via SEM observations that the crack deflected within the very thin 4343 layer as this was not distinctly clear even at very high magnifications.

6.4.1.2.Spray coated system

For the HVOF system, the penetrating crack detached the coating completely as soon as it approached the interface. The failure at this point is considered to be due to a poor interface between the coating and the backing layer. This means that the grit blasting technique used prior to coating did not give the required mechanical strength to the bond between the lining and steel layers and there might be some pre-existing damaged regions at the interface. A similar phenomenon was evident during surface strain measurement (Section 5.1.5.1) of the HVOF specimen during a static 3-point bend loading when the observed total strain was much less (~ 15-40%) than predicted by the corresponding FE model, which assumed the interface to be perfect.

6.5. Performance of RB and HVOF systems

AS20S and AS20 linings appeared to be more resistant to the initiation and growth of fatigue cracks with delayed coalescence to form dominant cracks which resulted in an overall increased fatigue life. HVOF flat bars on the other hand showed instant crack initiation, fast initial growth and coalescence to form longer cracks but slower growth of the coalesced cracks until the final failure. This latter phenomenon although means the HVOF lining appeared comparable to the RB systems in overall fatigue life predictions; however there are critical issues of the lining detachment from the backing layer (observed from the cross-sectional view of the failed specimen) and hence the simple laboratory lifetime estimations and surface crack growth behaviour is not a guarantee of the comparable performance of the HVOF bearing during actual engine operation. The integrity of the bonds between the lining layer, interlayer

and backing layers of the RB systems keeps them intact even after the subsurface penetration of the cracks.

The purpose of the much stronger interlayer used in the AS20 bearing was to restrict the subsurface crack penetration by reducing the crack tip driving force (as compared to softer *Al* foil in the AS20S system), however no beneficial effect was observed on the overall lifetime of the bearing as the crack was actually observed to penetrate the brazed sheet and to deflect within the very thin 4343 layer. FE based sensitivity analysis showed that variation of interlayer properties had no effect upon the surface stress and strain conditions while keeping the lining and interlayer of same material. This led to similar initiation and crack growth behaviour in both AS20S and AS20 systems.

6.6. Bronze bearings

The bronze bearings (RB168) systems were provided at the end of this research programme and the results provided correspond to the limited number of specimens tested. The lining layer of the RB168 bearing specimen (*Ni*-bronze) was microstructurally homogeneous in both heat treated and non-heat treated conditions compared to the *Al*-based lining in the AS20S system which showed a complex multiphase microstructure. The bronze lining layer in the RB168 bearing systems was much harder and stronger than the conventional *Al* lining used in the AS20S system, however the *Sn* overlay layer was significantly softer. No preferential crack initiating regions were observed in the microstructure of the *Sn* overlay layer in the RB168 bearing system. The surface of the failed specimen and tortuosity level shows that the crack once initiated (most probably from surface inhomogenities such as pores) follows a straight trajectory. This trajectory was not as straight in the heat treated specimen as evident from the measured higher value of tortuosity which could be linked to a rougher lining surface in the heat treated condition. The material underneath the *Sn* overlay was quite hard (*Ni* layer), but the thickness of both layers is so small that no crack deflection at the *Sn-Ni* interface was observed using current techniques. The harder *Ni* layer might have resisted the subsurface crack penetration to some extent; however the crack once penetrated grew towards the harder steel layer. There is a slight evidence of crack deflection at this stage; however the crack appeared to deeply penetrate into the steel layer at the end of life.

Despite the higher strength of the *Ni*-bronze, the total fatigue life (in lining ε_p terms) of non- heat treated RB168 bearing was comparable to that of the AS20S system. However on the

basis of observed fatigue life, the annealed specimen (at 190C^{o} for 6 hrs) was more fatigue resistant than both AS20S and RB168 bearing system. There were no differences in the crack routes when microstructures of the surface and cross-section of failed RB168 system in both conditions were observed. The Ni_3Sn_4 intermetallic layer formed (by consuming both *Ni* and *Sn* layers) at the *Sn-Ni* interface is stiffer (E=52 ±15GPa) than *Sn* (E=45GPa) as obvious from nano-hardness test results (chapter 4). Similar results have been reported by *Luhua et al*[22]. The observed increasing fatigue resistance of the heat treated specimen could be attributed to the presence of harder intermetallic layer between the *Sn-Ni* interface that might have resisted the subsurface penetration of the fatigue crack to some extent in the very early stages of crack growth. Subsurface crack deflections in such thin overlay layers are hard to compare via conventional sectioning approaches to interrupted tests on half shell bearings.

References:

[1] Barter, S.A. Bishop, .B. and Clark, G. (1991) Air craft materials report 125, AR-006-618, Department of defence, defence science and technology organization, Aeronautical research laboratory Melbourne, Australia.

[2] Goldsmith, N.T. Clark, G. and Barter, S.A. (1996). Eng. Failure. Anlys 3, 191.

[3] Bowls, C.Q. and Schijve, J. (1973). Int. J. Fat. Frac 9, 171.

[4] Kung, C.Y. and Fine, M.E. (1979), Metallurg. transc A10A, 603.

[5] Mwanza. M., Joyce, M.R. Lee, K.K. Syngellakis, S. and Reed, P.A.S. Reed. (2003), Int. J. Fat 25, 1135.

[6] Nutt, S.R. Needleman, A. (1987) Scripta. Met 21, 705.

[7] Whithouse and A.F. Clyne, T.W. (1995) Acta. Met 43, 2107.

[8]Eshelby, J.D. (1957) Proc.Roy. Soc A241, 376.

[9] Rice, J.R. (1967). Special technical publication: Philadelphia: ASTM , 415, 247.

[10] Joyce, M.R. (2000). PhD thesis, University of Southampton, UK.

[11] Kaung, K.H. and Chen, C.K. (1999). Fat. Frac. Eng. Mater. Struc 22, 742.

[12] Soboyejo, W.O. Kishimoto, K. and Smith, R.A. (1988). Fat. Frac. Eng. Mater 12, 167.

[13] Chen, E.I. Lawson, L. and Meshi, M. (1995). Metal. Mater. Transc 26A, 3163.

[14] Lefebvre, F. (2003). PhD thesis, University of Southampton, UK.

[15] Hobson, P.D. (1982). Fat. Eng. Mater. Struc 5, 323.

[16] Grabowski, L. and Yates, J. R. (1992). Int. J. Fat 14 (4), 227

[17] Bomas, H. Linkewitz, T. and Mayr, P. (1996). Fat. Fract. Eng. Mater. Struc. 19 (2/3), 299

[18] Edward, L and Yang, Y.H. (1994). Acta. Metall. Mater 42, 1413.

[19] Suresh, S.(1998) Fatigue of materials, second edition, Cambridge university press.

[20] Suresh, S. Y. Sugimuera, Tschegg, E. K. (1992). Scripta. Metall. Mat 27, 1189.

[21] Joyce, M.R. Reed, P.A.S. and Syngellakis, S. (2003). Mat Sc and Engg A342, 11.

[22] Luhua Xu, John, H.L. Pang. (2005). Thin. Solid. Films 20, 5.

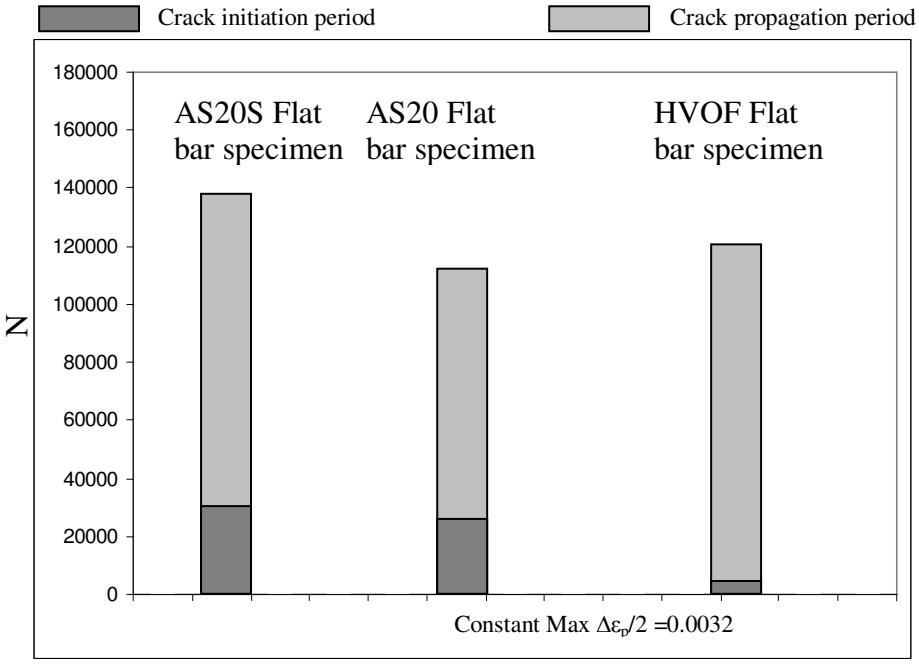

(a)

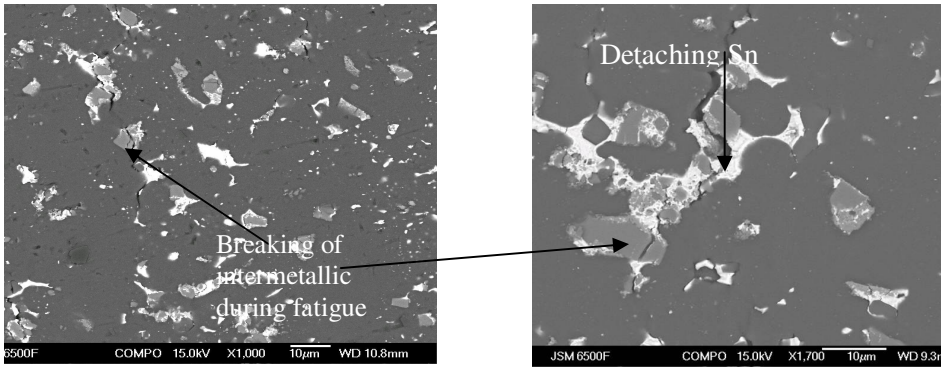

(b) (c)

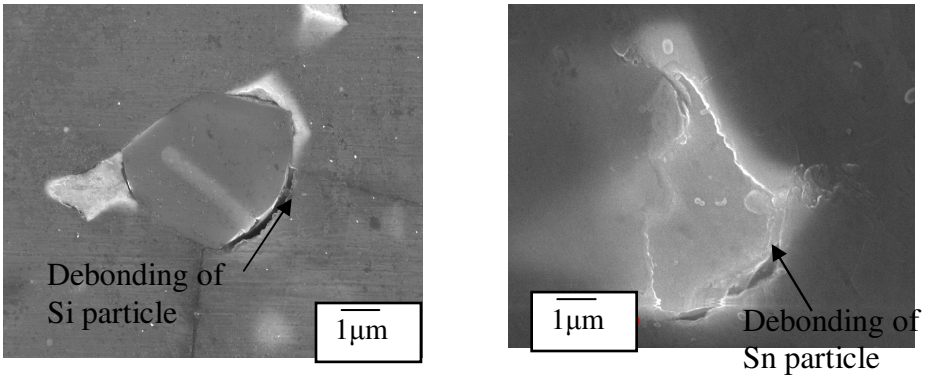

(d) (e)

Figure 6.1: (a) A comparison of fatigue initiation and growth lifetimes of different systems. Fatigue initiation in (b & c) AS20S (d) AS1241 and (e) AS16 lining[5]

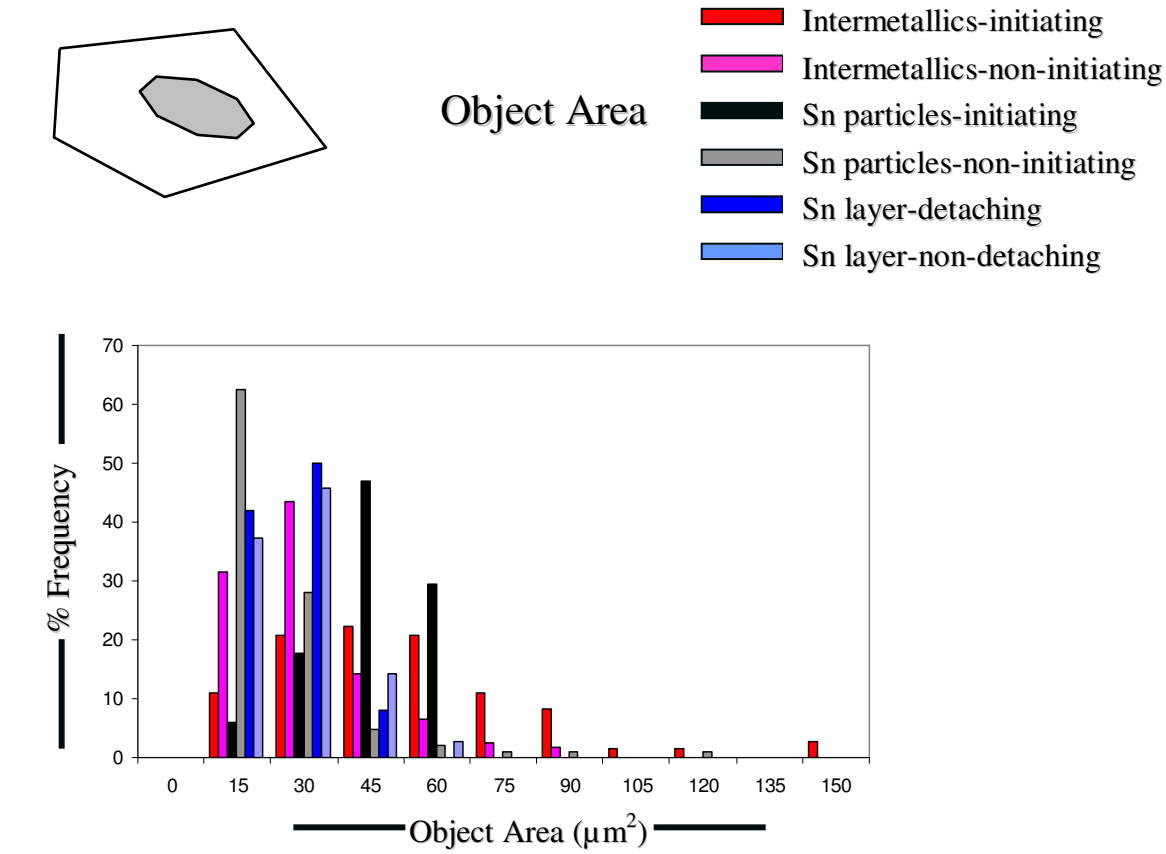

(a)

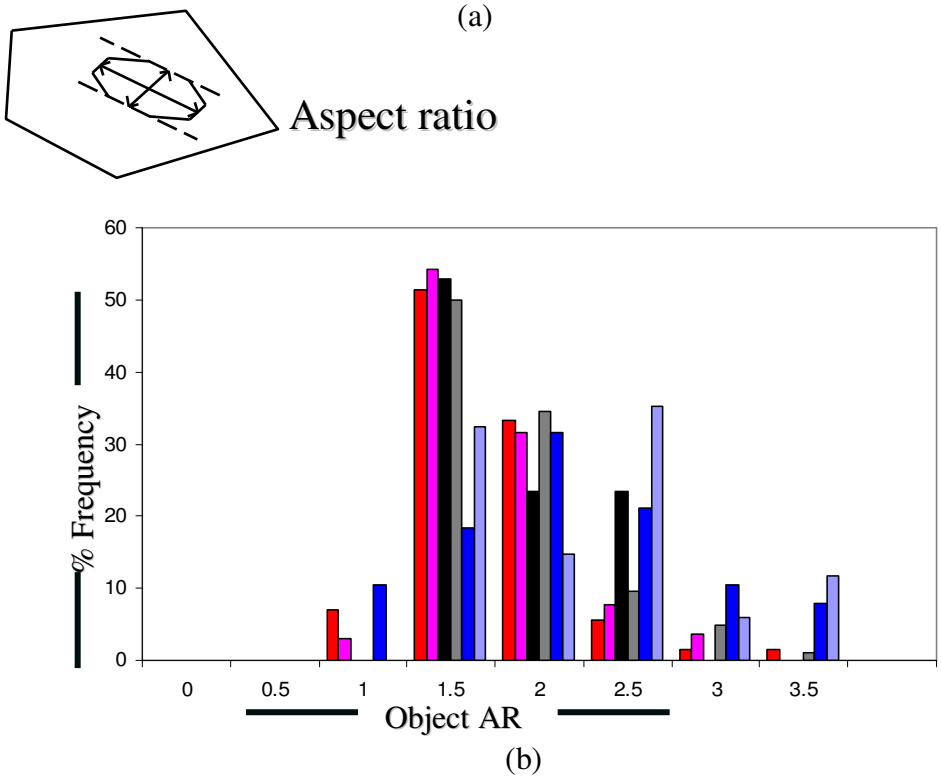

(b)

Figure 6.2: FBT measured (a) object area (b) aspect ratio of short crack initiating particles.

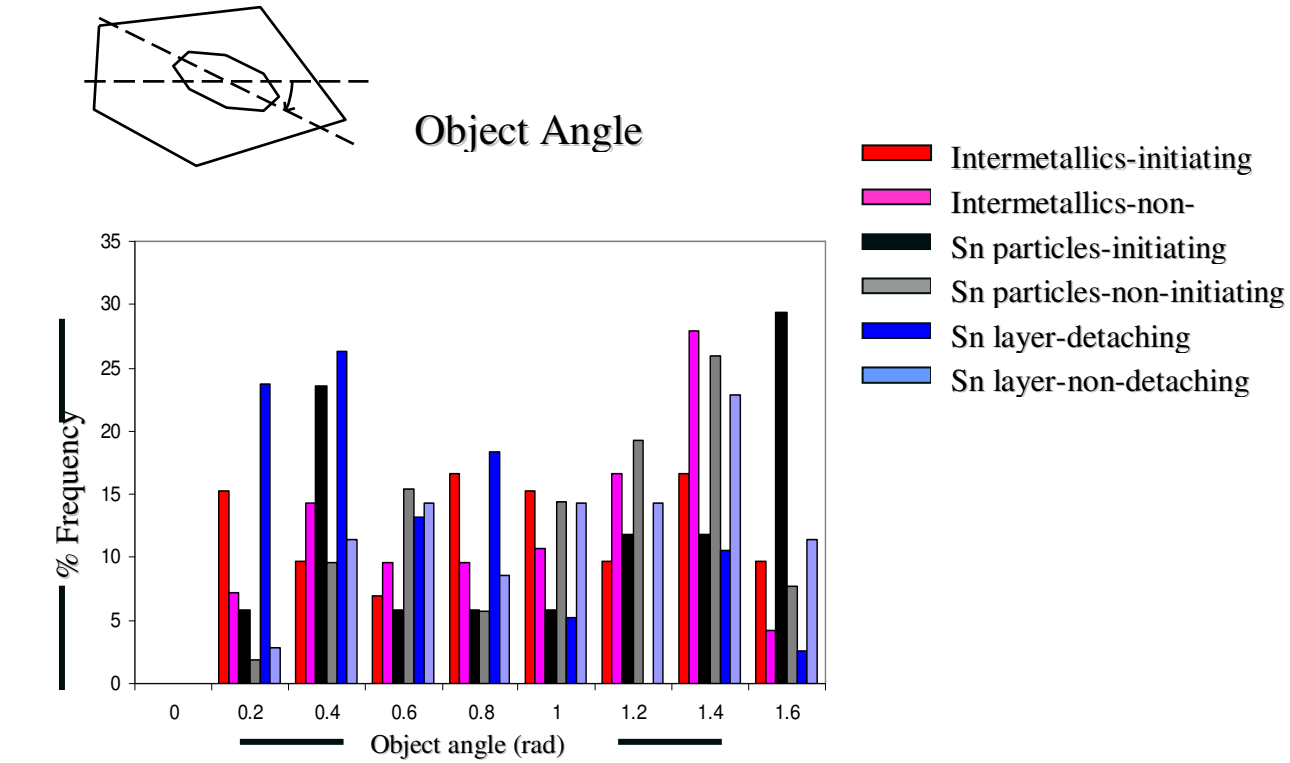

(a)

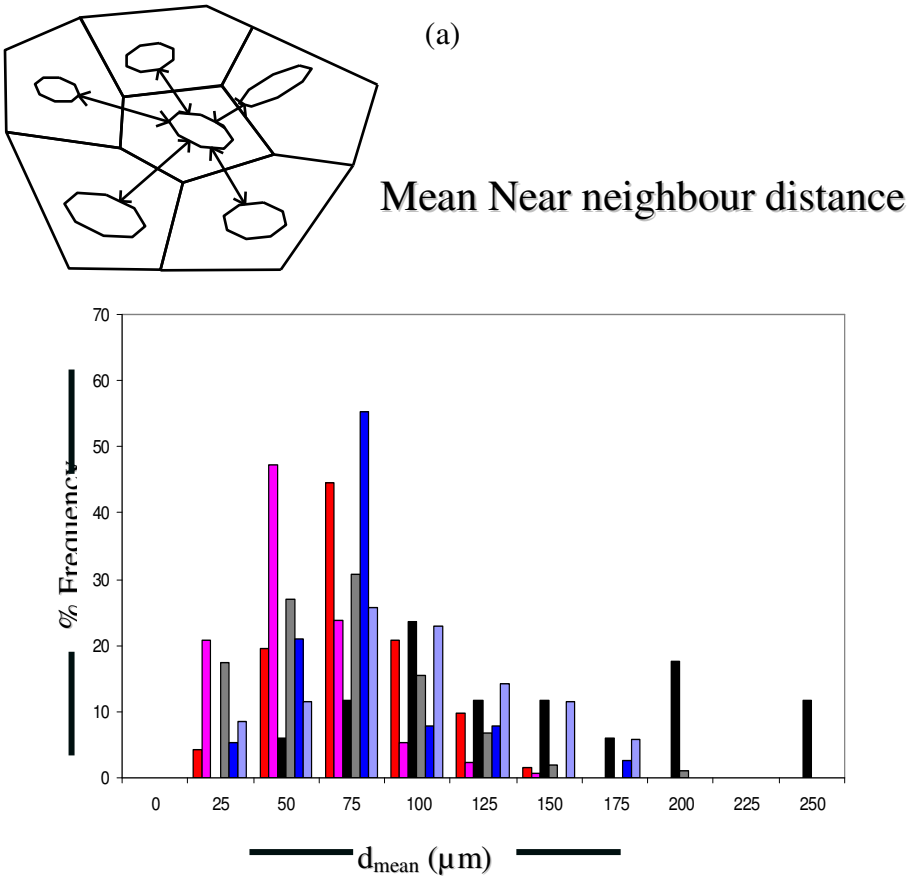

(b)

Figure 6.3: FBT measured (a) object angle (b) and d_{mean} of short crack initiating particles.

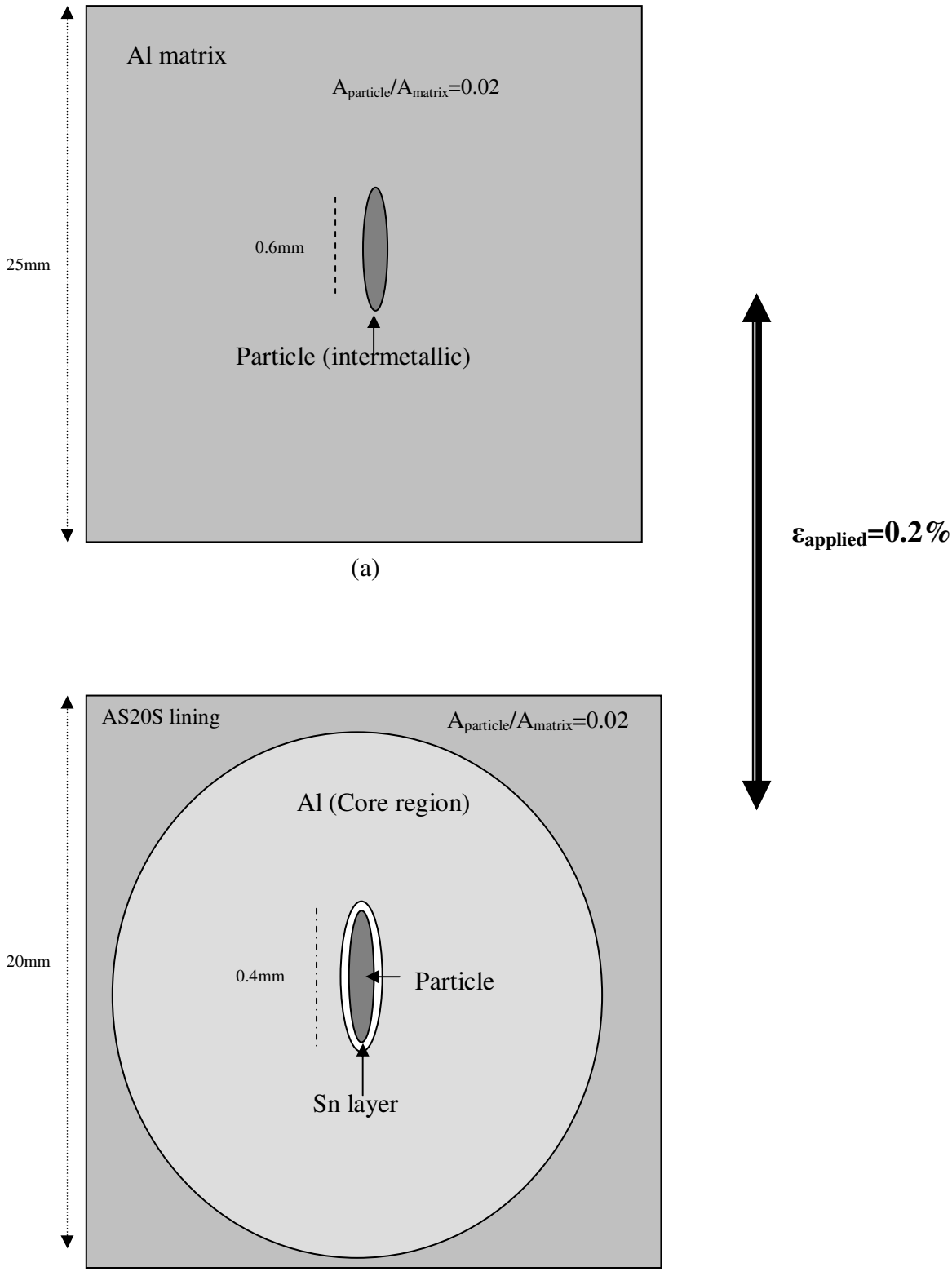

Figure 6.4: A schematic of the geometry of (a) bi-material model used in analytical and numerical modelling (b) elasto-plastic tri-material model used for numerical modelling.

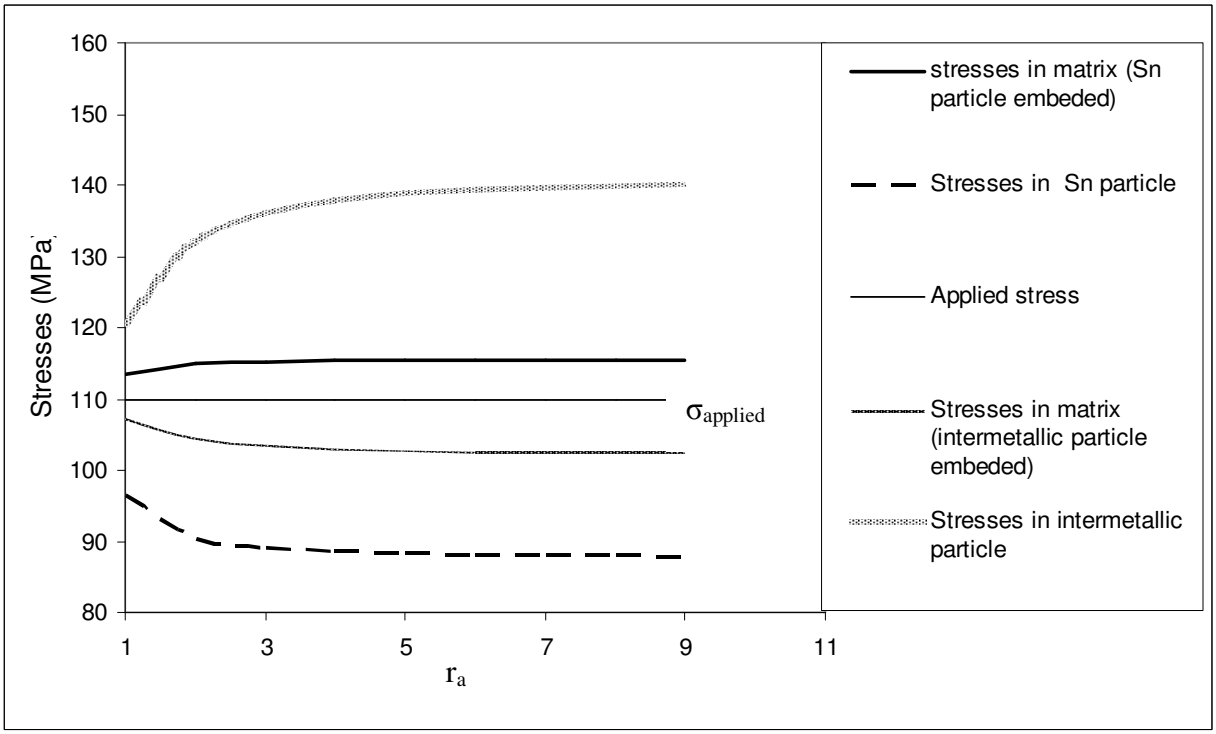

(a)

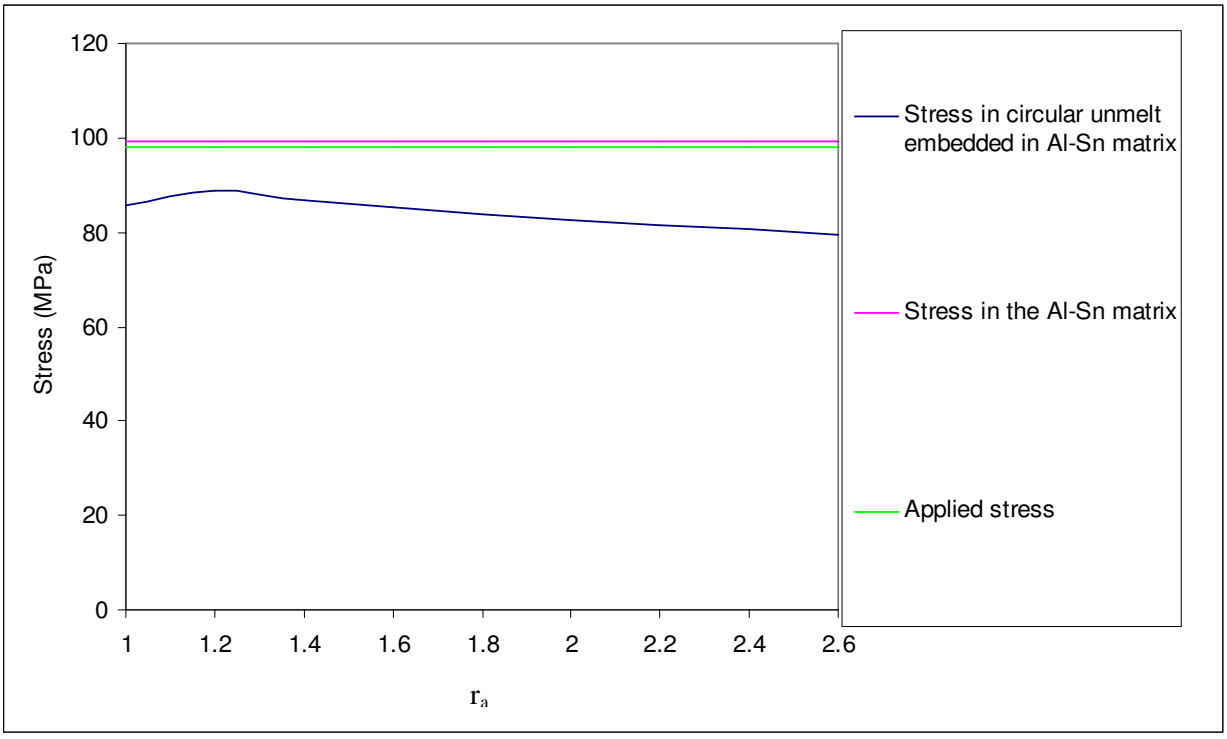

(b)

Figure 6.5:Variation of particle and matrix stresses calculated by Eshelby analysis for the bimaterial model used for (a)AS20S lining and (b) for HVOF lining with the particle r_a.

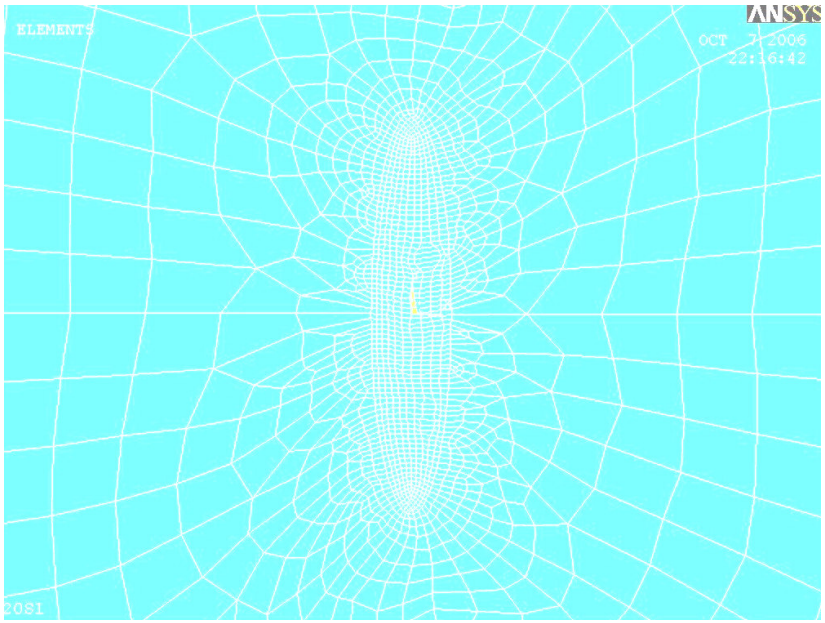

(a)

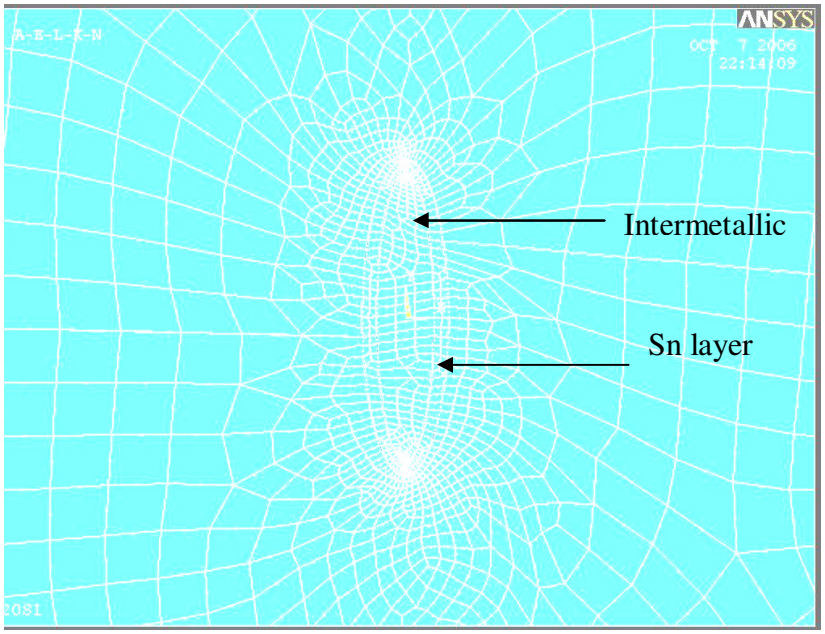

(b)

$\varepsilon_{applied}$ =0.2%

Figure 6.6: A 2-D meshed geometrtrical model of (a) a simple intermetallic and (b) a layered intermetallic particle embedded in Al matrix.

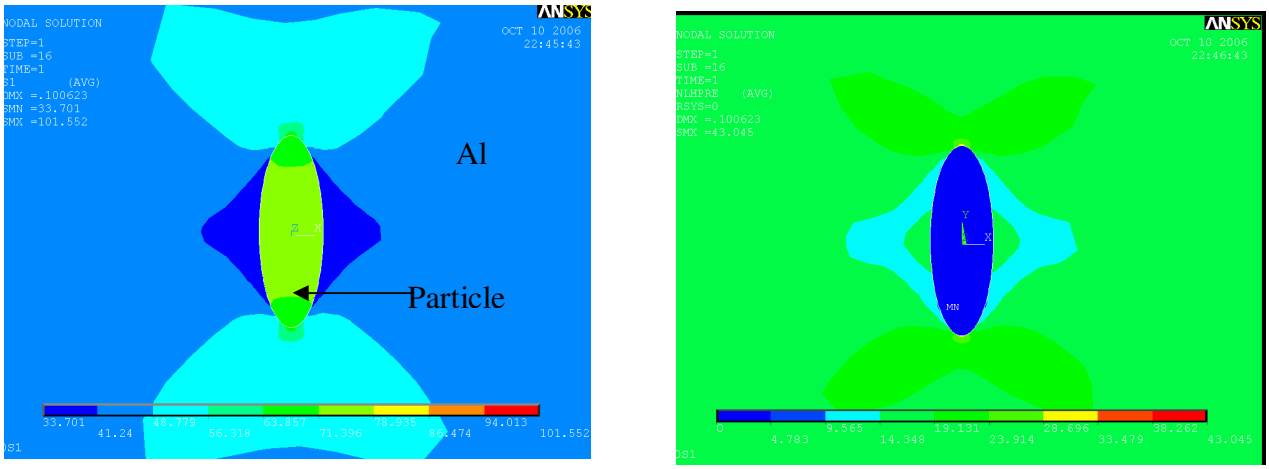

(a) (b)

Figure 6.7: FE predicted (a) tensile and (b) hydrostatic stresses in a bimaterial linear elastic model for the AS20S type lining

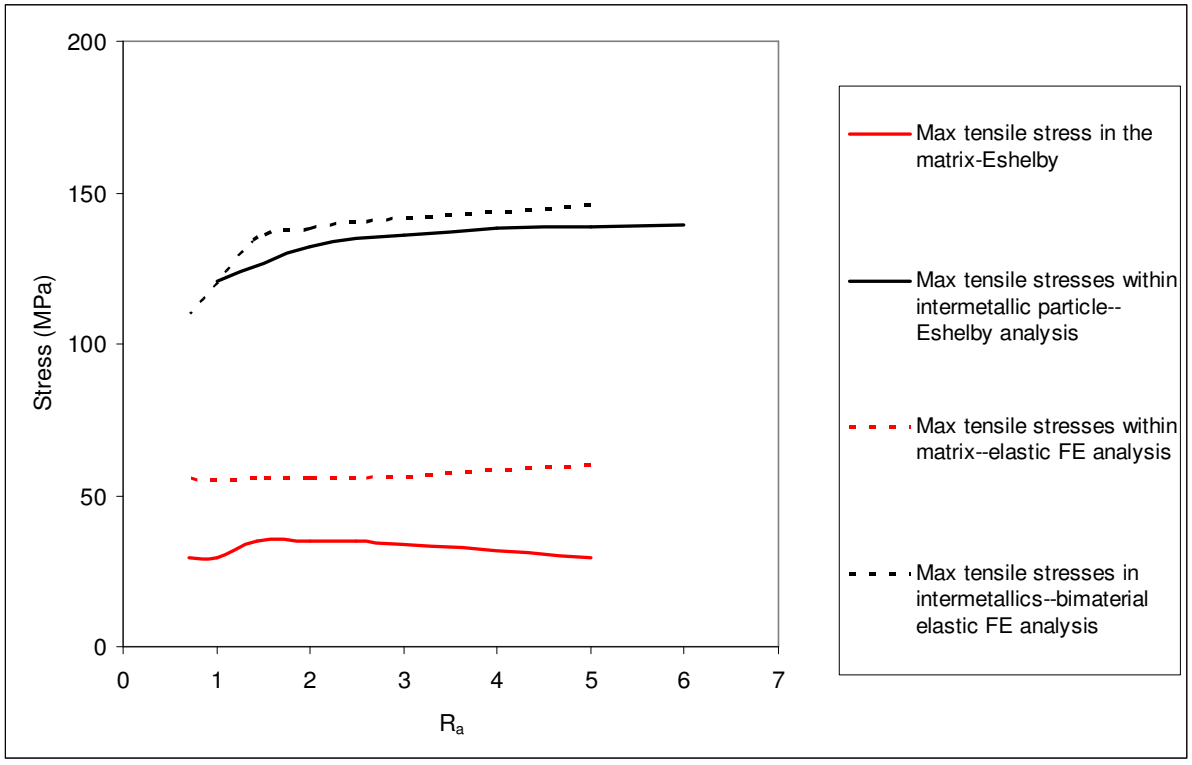

Figure 6.8: FE and Eshelby predictions of maximum tensile stresses in a bimaterial linear elastic model.

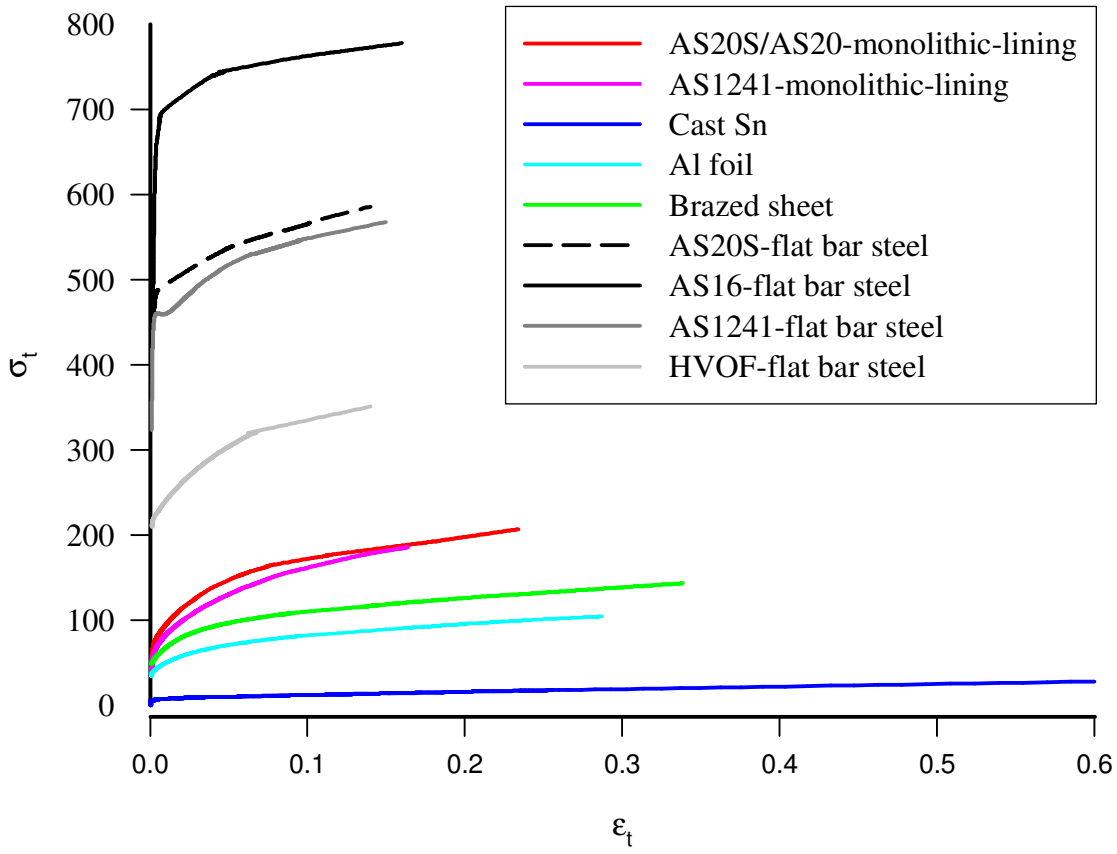

Figure 6.9: General σ-ε behaviour of all layers used. Data for AS1241, AS16 systems and *Sn* was obtained from previous work at Southampton[5].

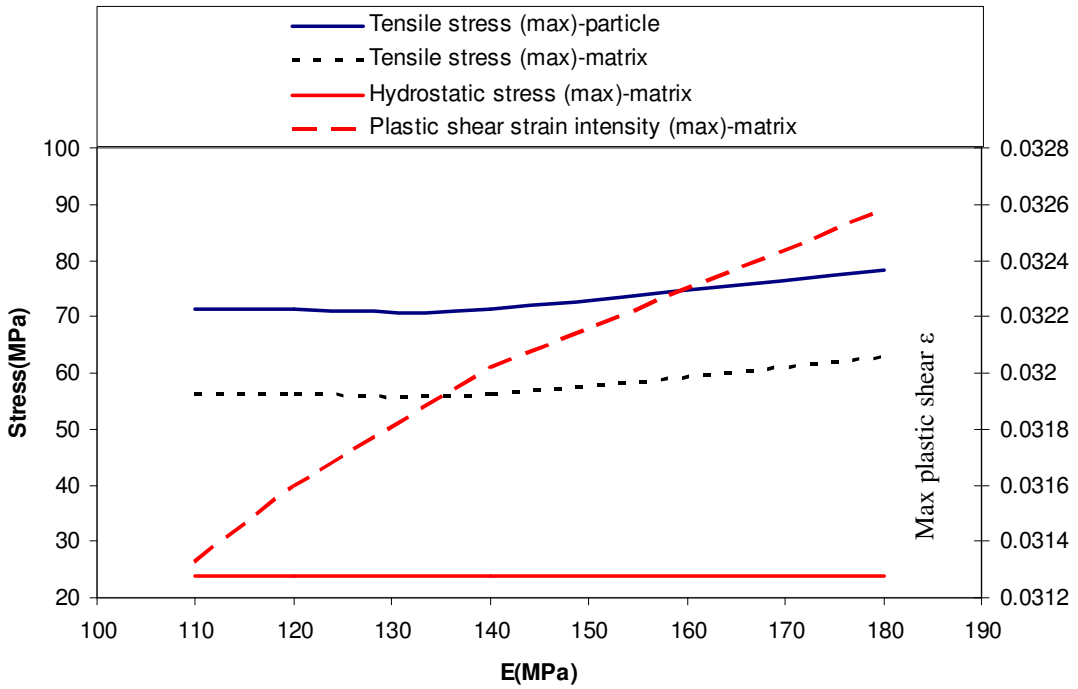

Figure 6.10: Effect of variation of elastic modulus of the embedded intermetallic particle on the resultant σ-ε in the intermetallic particle and the matrix of AS20S lining simulated by elastoplastic bimaterial FE model.

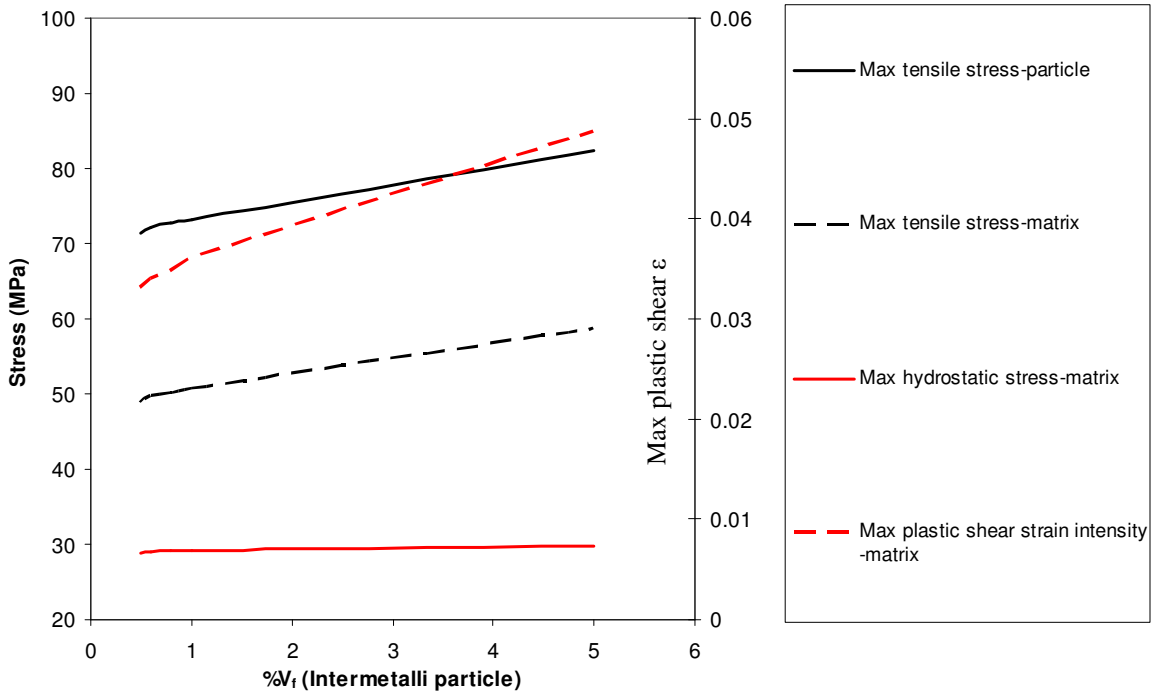

Figure 6.11: Effect of variation of volume fraction of the embedded intermetallic particle on the resultant σ-ε in the intermetallic particle and the matrix of AS20S lining simulated by elastoplastic bimaterial FE model.

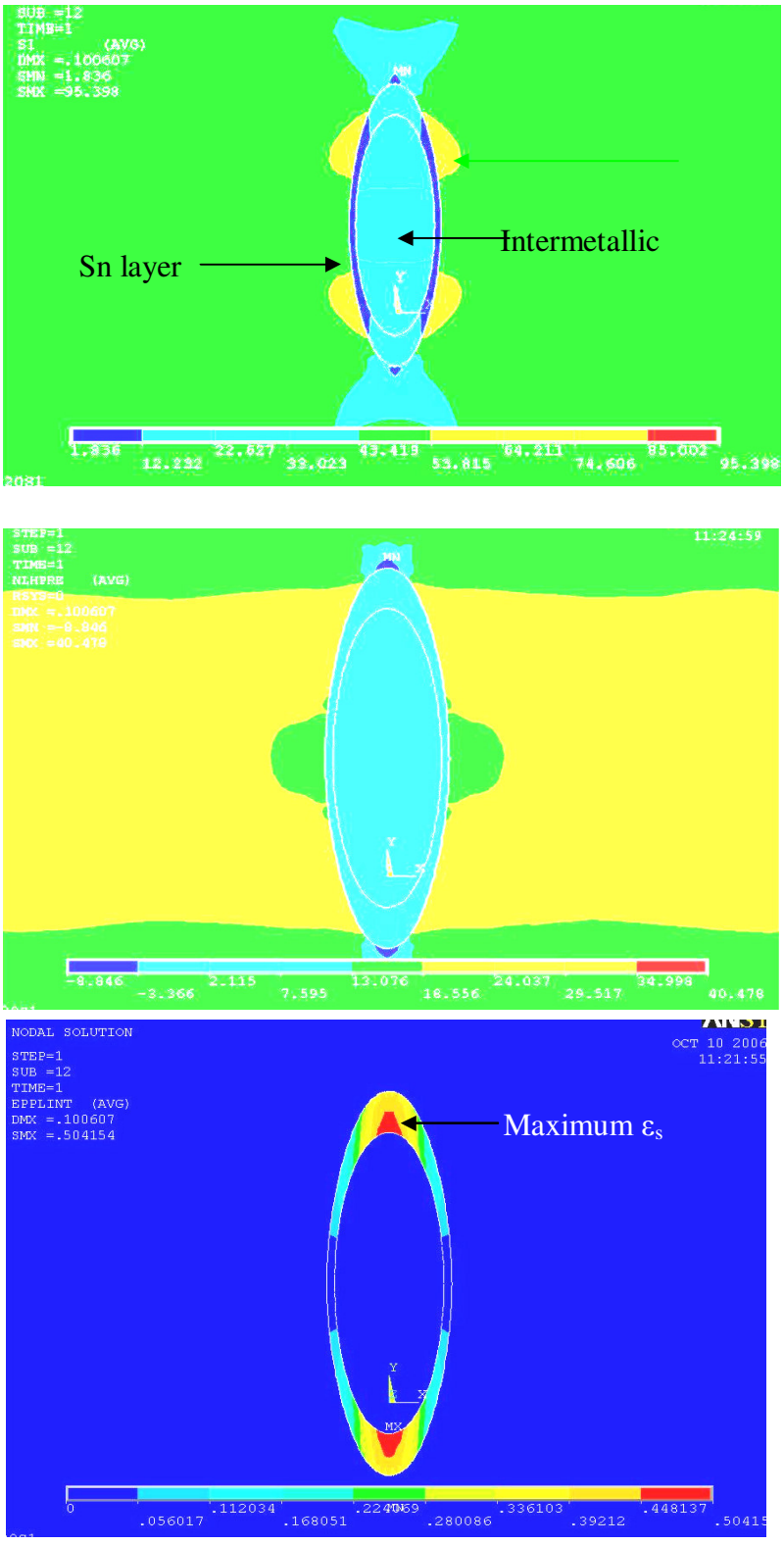

Figure 6.12: Disribution of (a) tensile stress (b) hydrostatic stress and (c) plastic shear strain in a tri-material FE model representing hard intermetallic encapsulated within soft *Sn* layer and embedded in *Al* core.

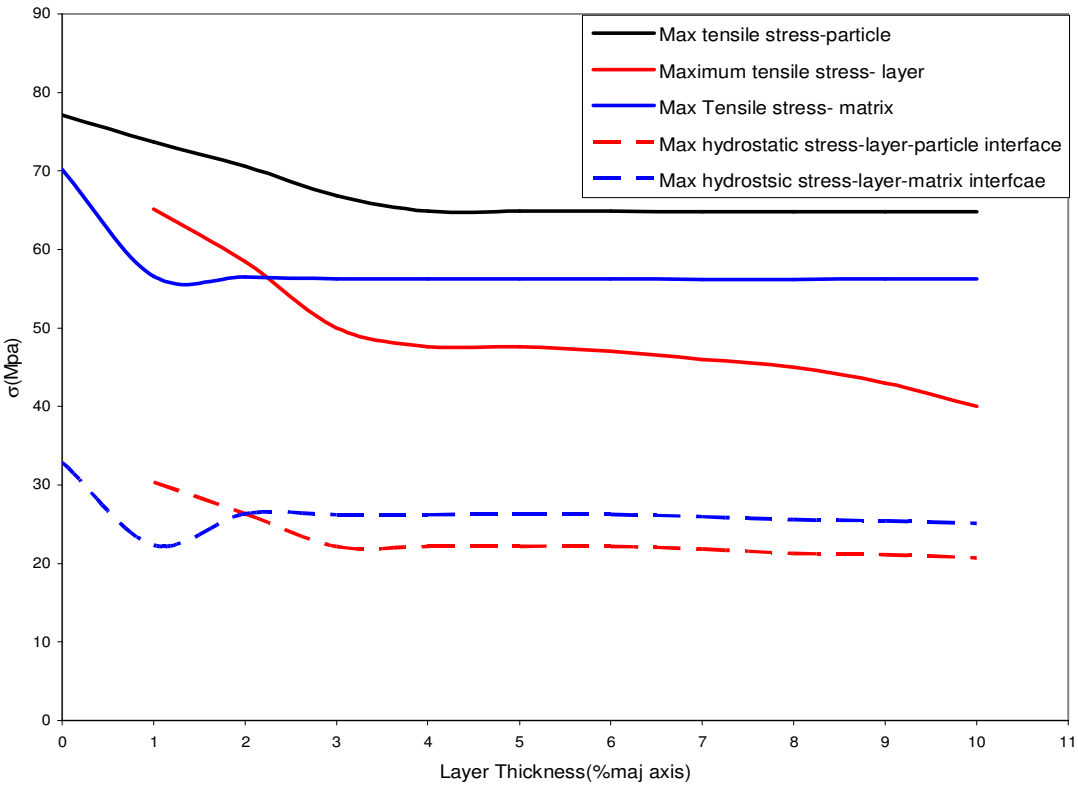

(a)

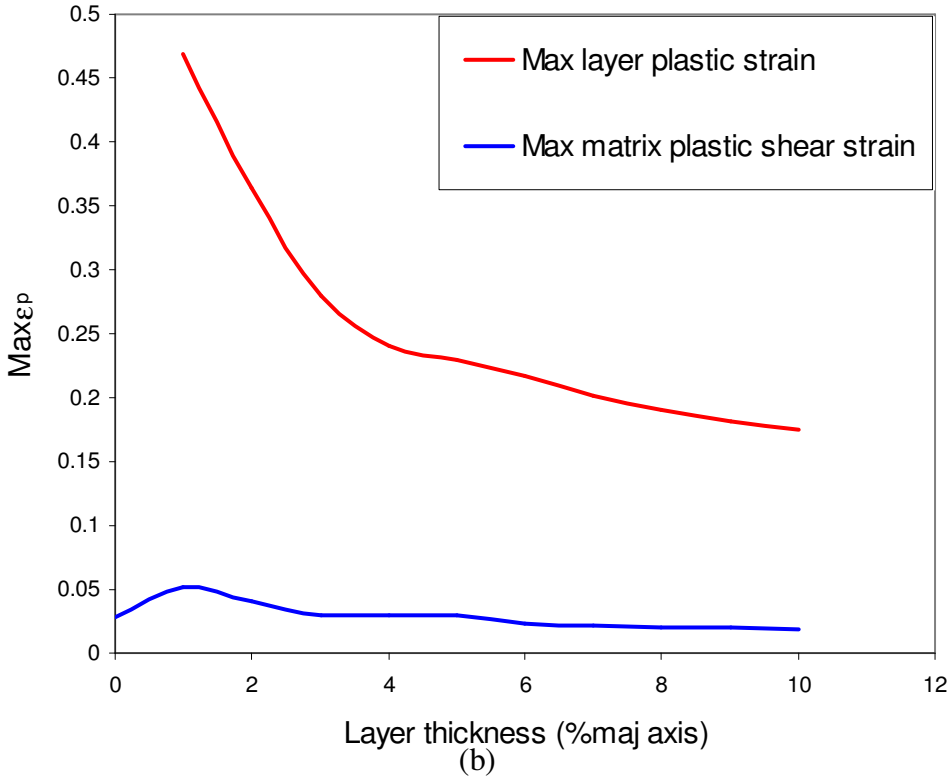

(b)

Figure 6.13: Variation of critical (a) stresses and (b) plastic shear strains with the change in *Sn* layer thickness around intermetallic particle.

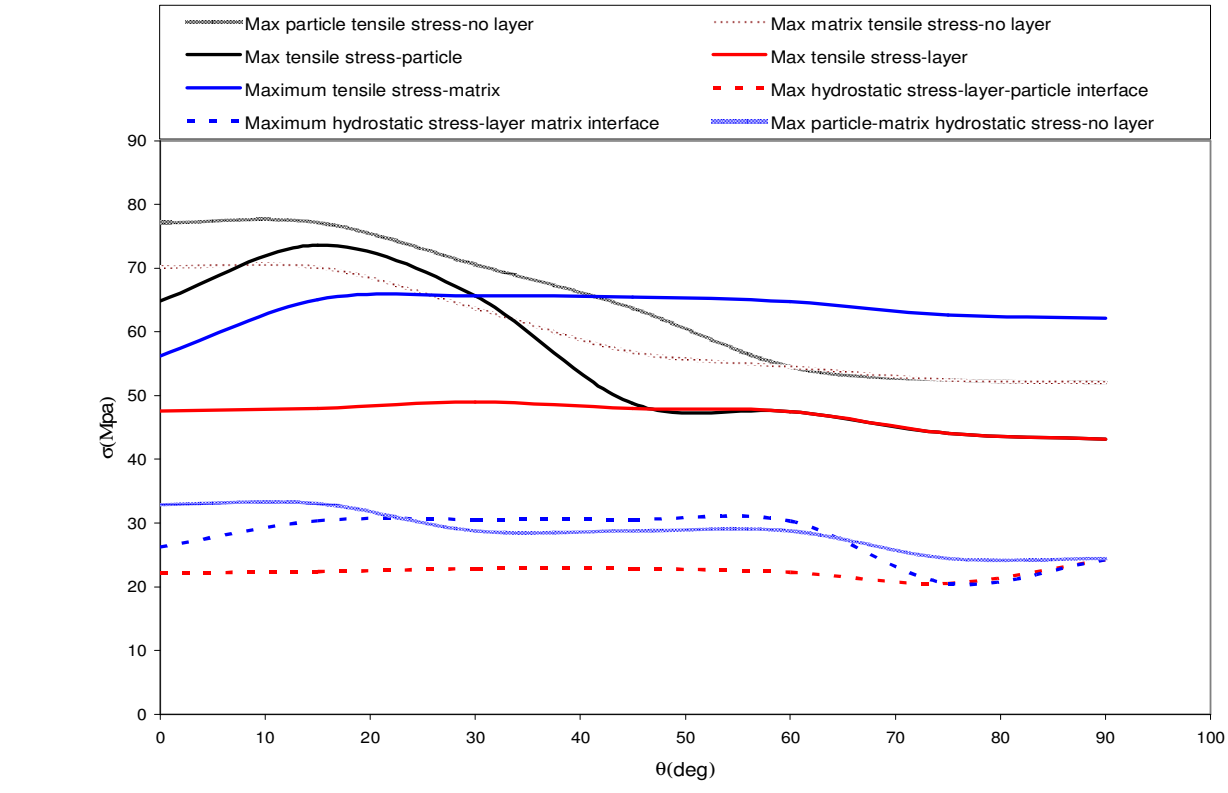

(a)

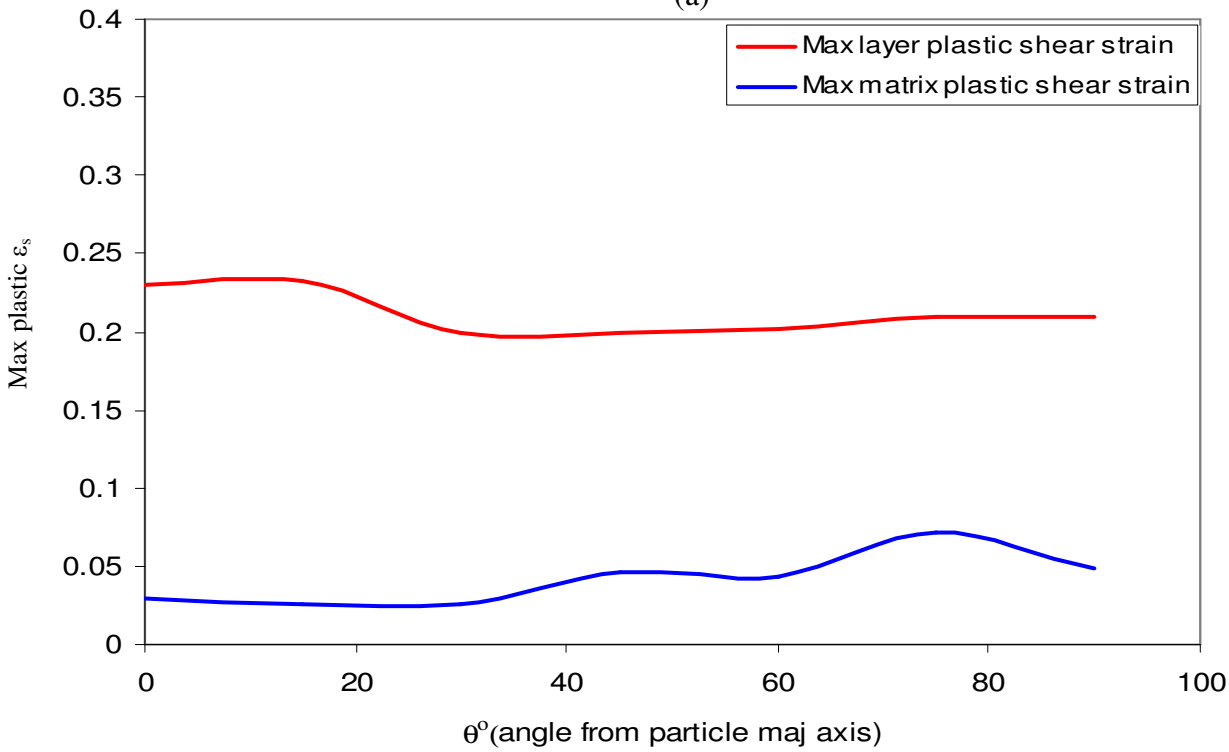

(b)

Figure 6.14: Variation of critical (a) stresses and (b) plastic shear strains with the change in orientation of intermetallic particle.

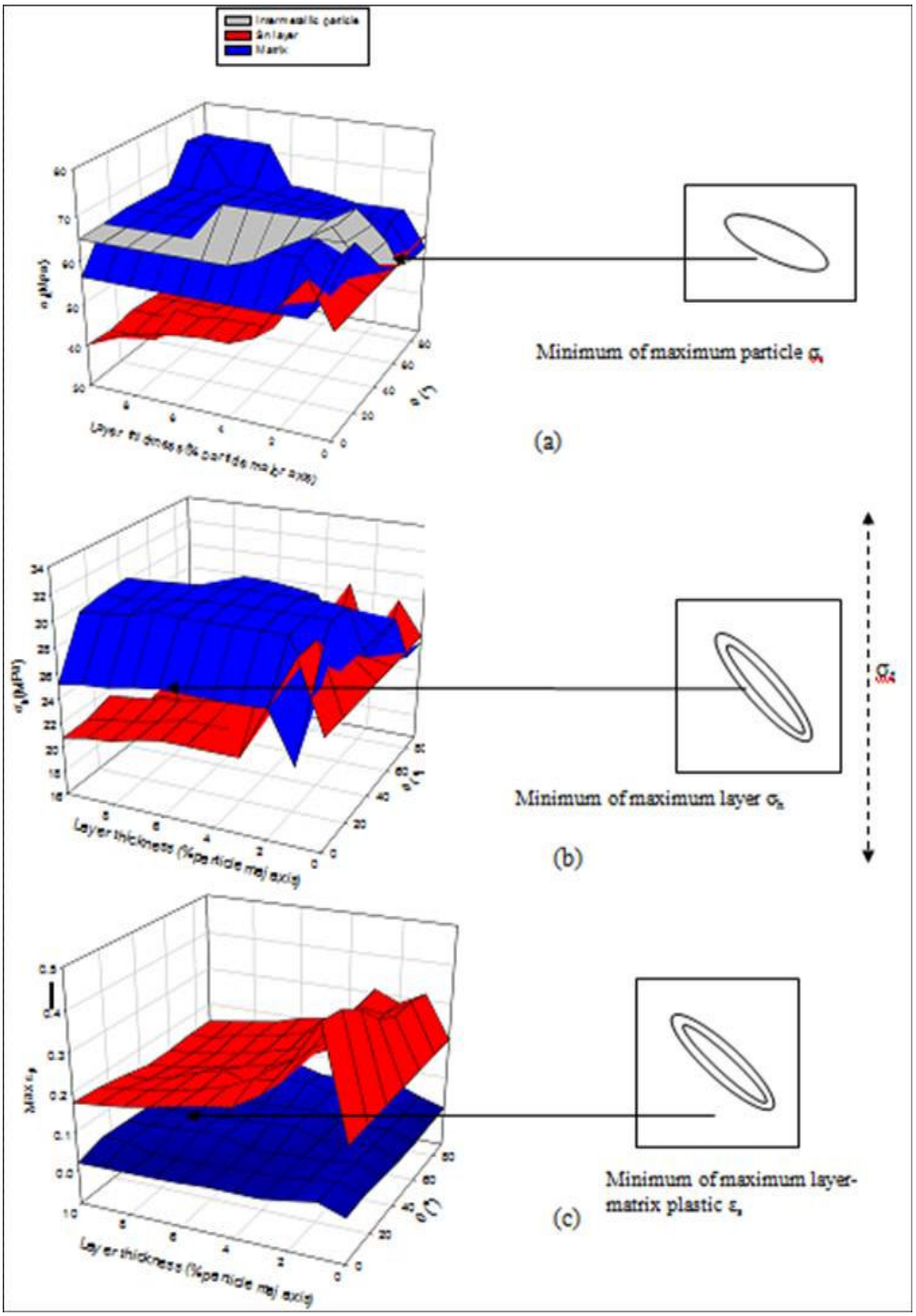

Figure 6.15: Variation of (a) tensile stresses (b) hydrostatic stress (c) plastic shear strain as a function of particle (intermetallic) orientation (θ) and *Sn* layer thickness at r_a=3.

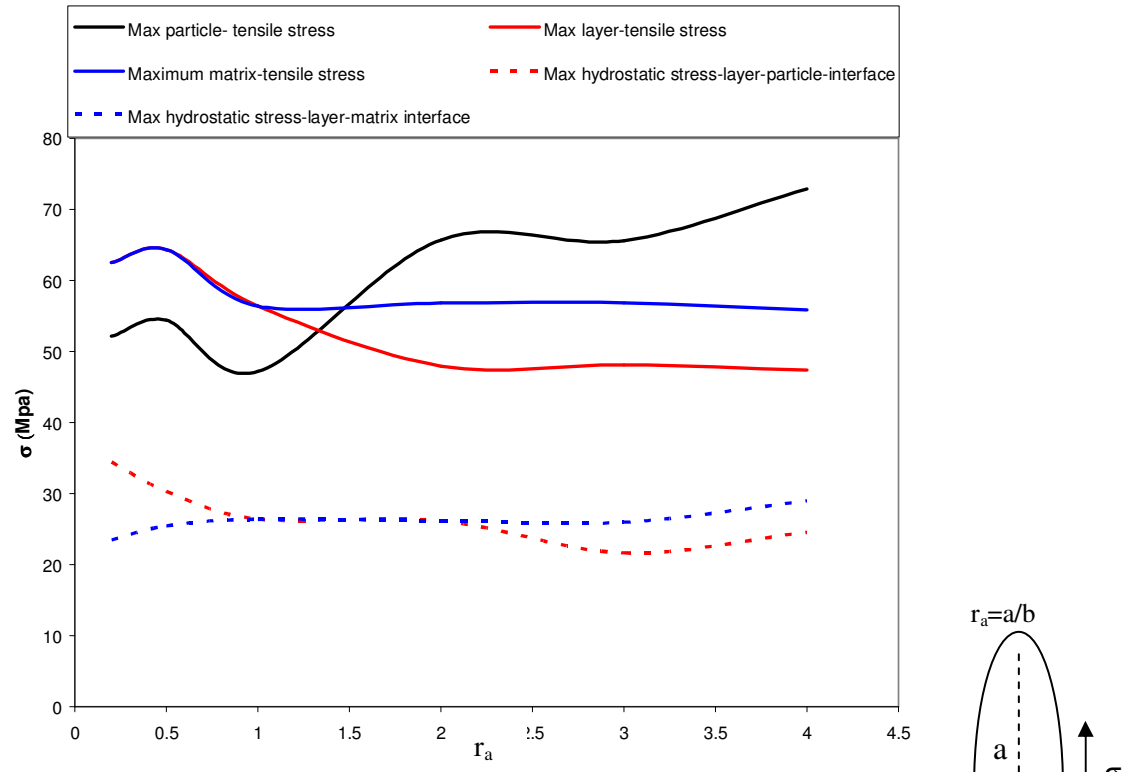

(a)

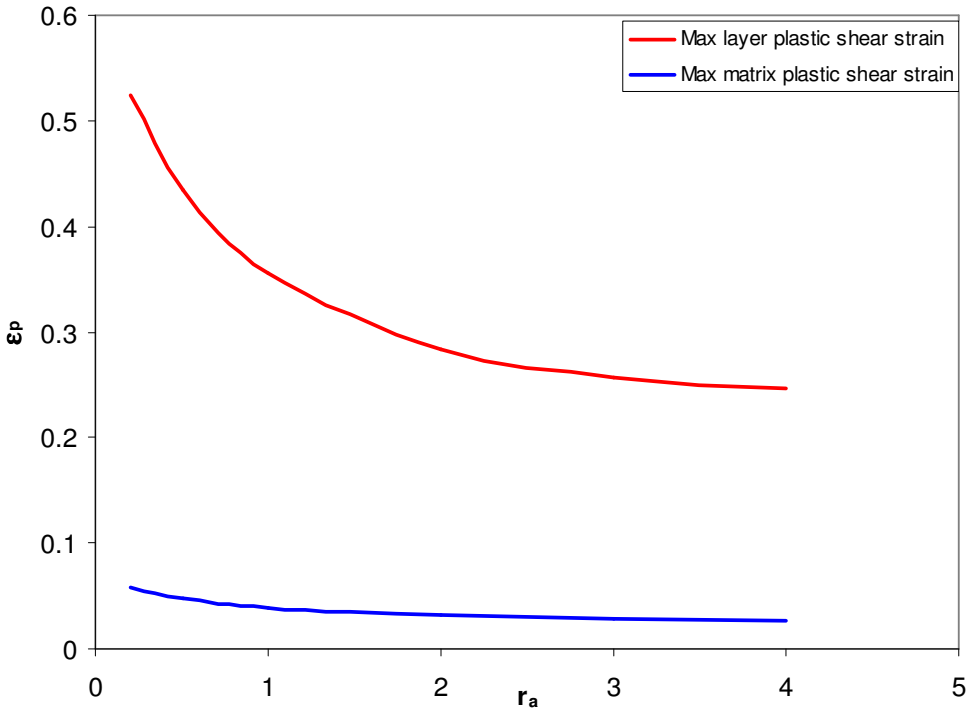

(b)

Figure 6.16: Variation of (a) stresses and (b) plastic shear strains with the r_a of the particle. The *Sn* layer thickness is kept constant at *l*=0.4a where 'a' is the major axis of the particle.

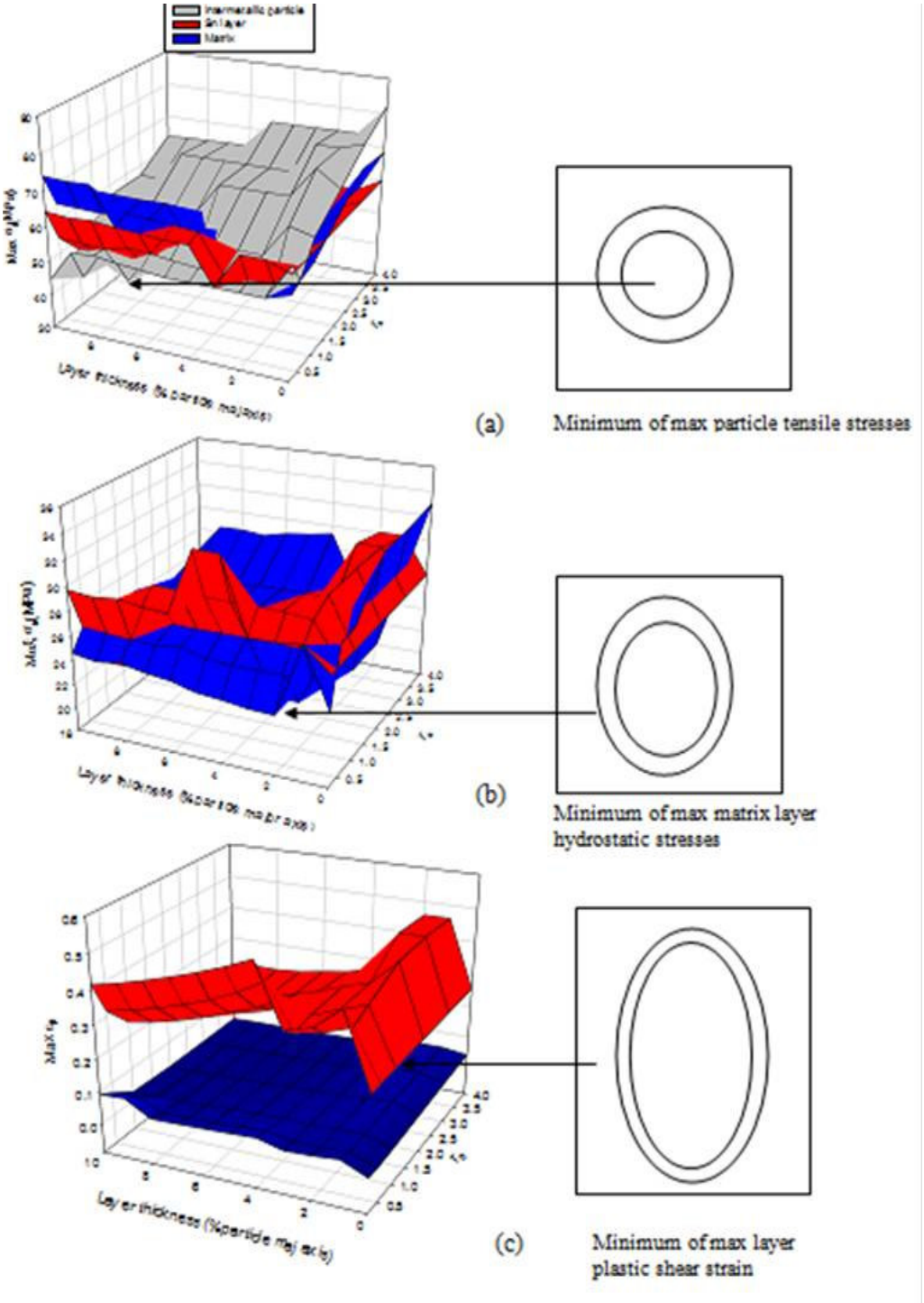

Figure 6.17: Variation of (a) tensile stresses (b) hydrostatic stress (c) plastic shear strain as a function of particle (intermetallic) r_a and *Sn* layer thickness.

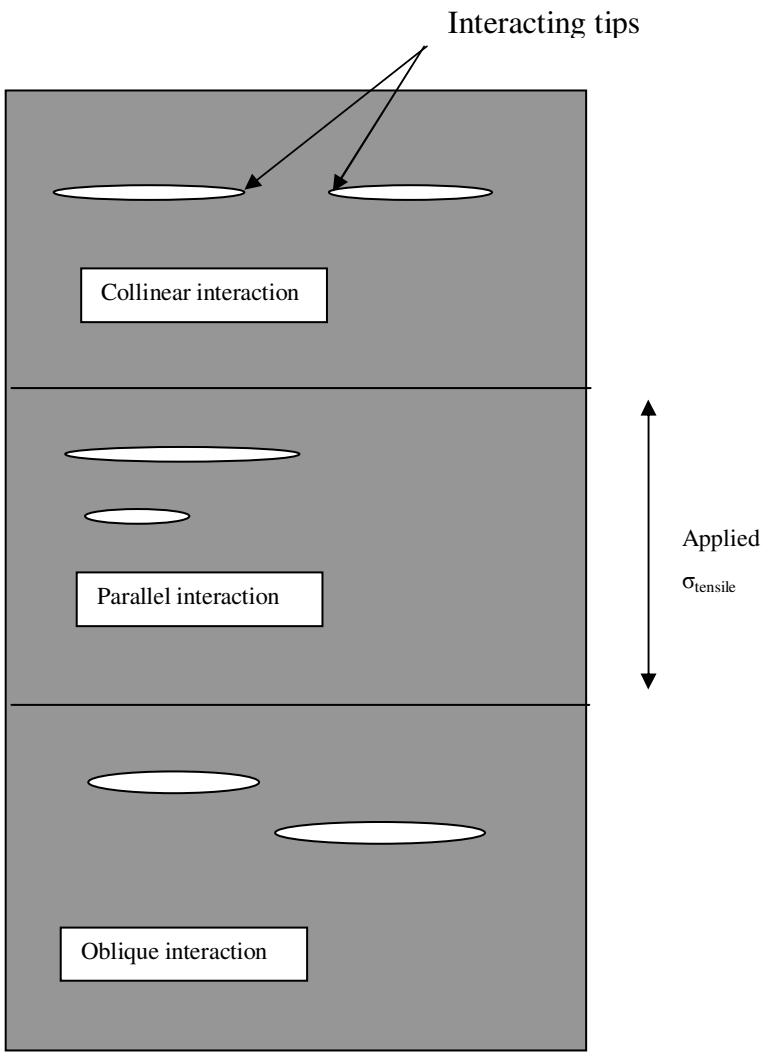

Figure 6.18: Schematic of the crack interaction definitions approach used by Joyce[10].

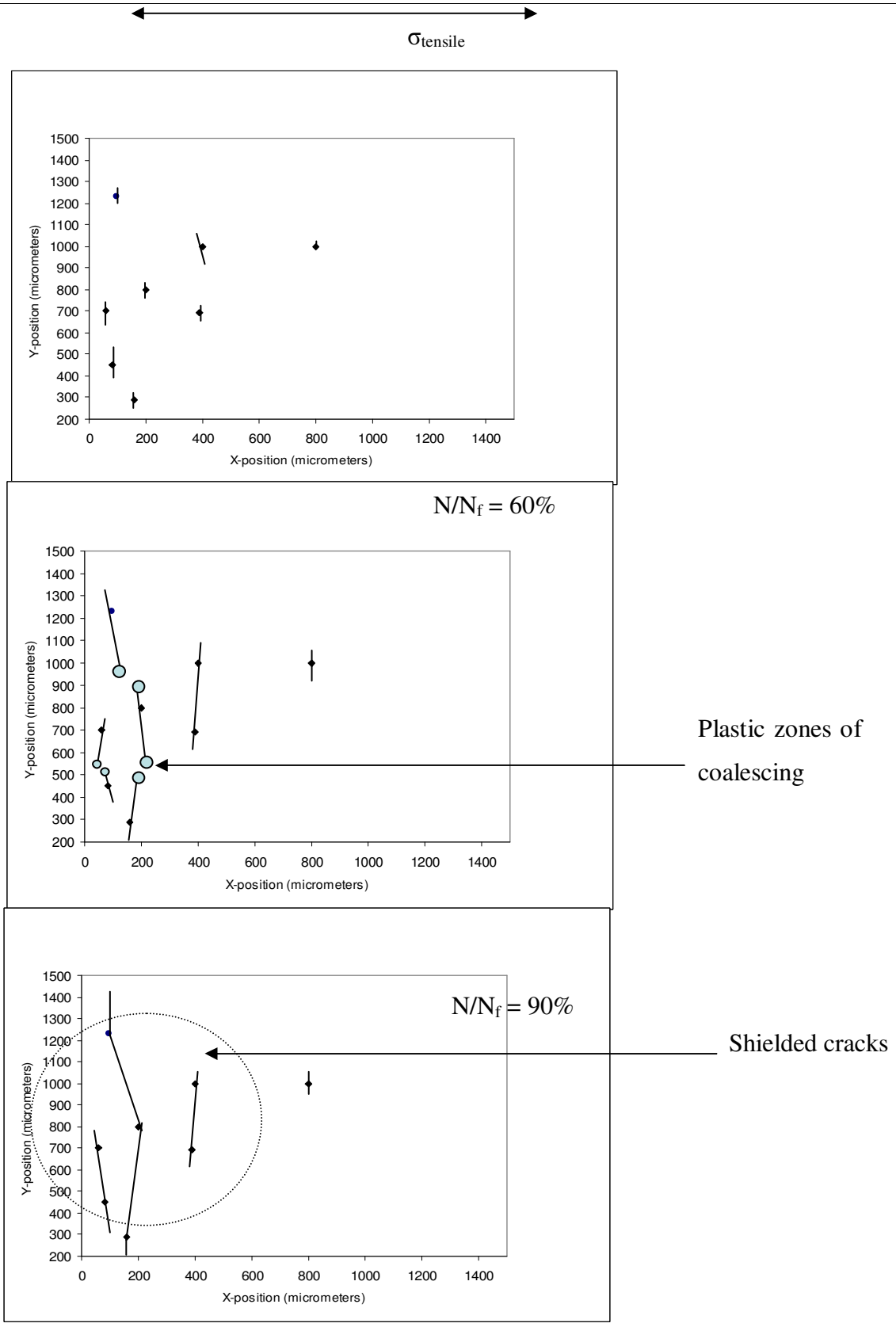

Figure 6.19 Short fatigue crack interactions at different life time fractions for AS20S lining.

$\sigma_{tensile}$

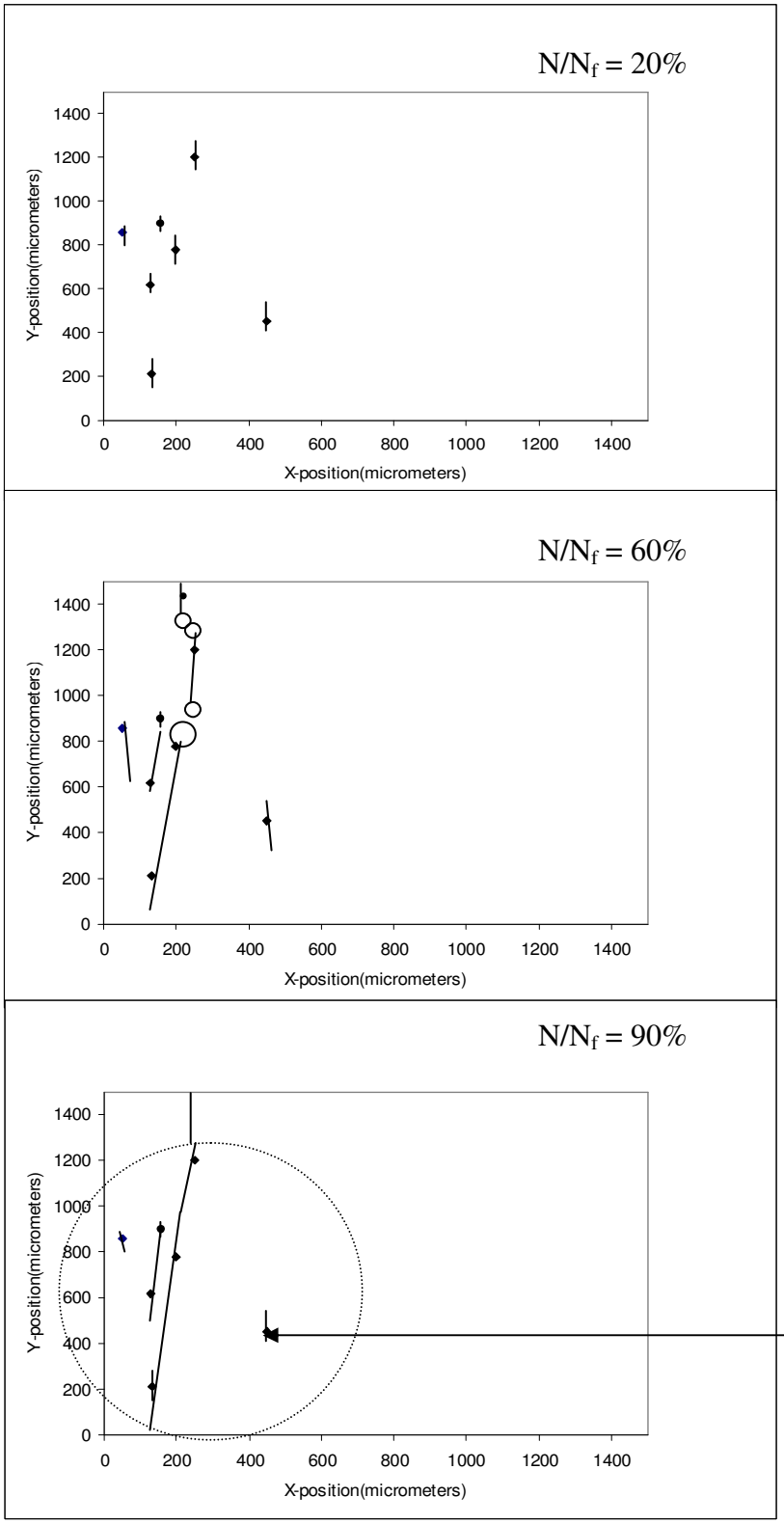

Figure 6.20: Short fatigue crack interactions at different life time fractions for AS20 lining.

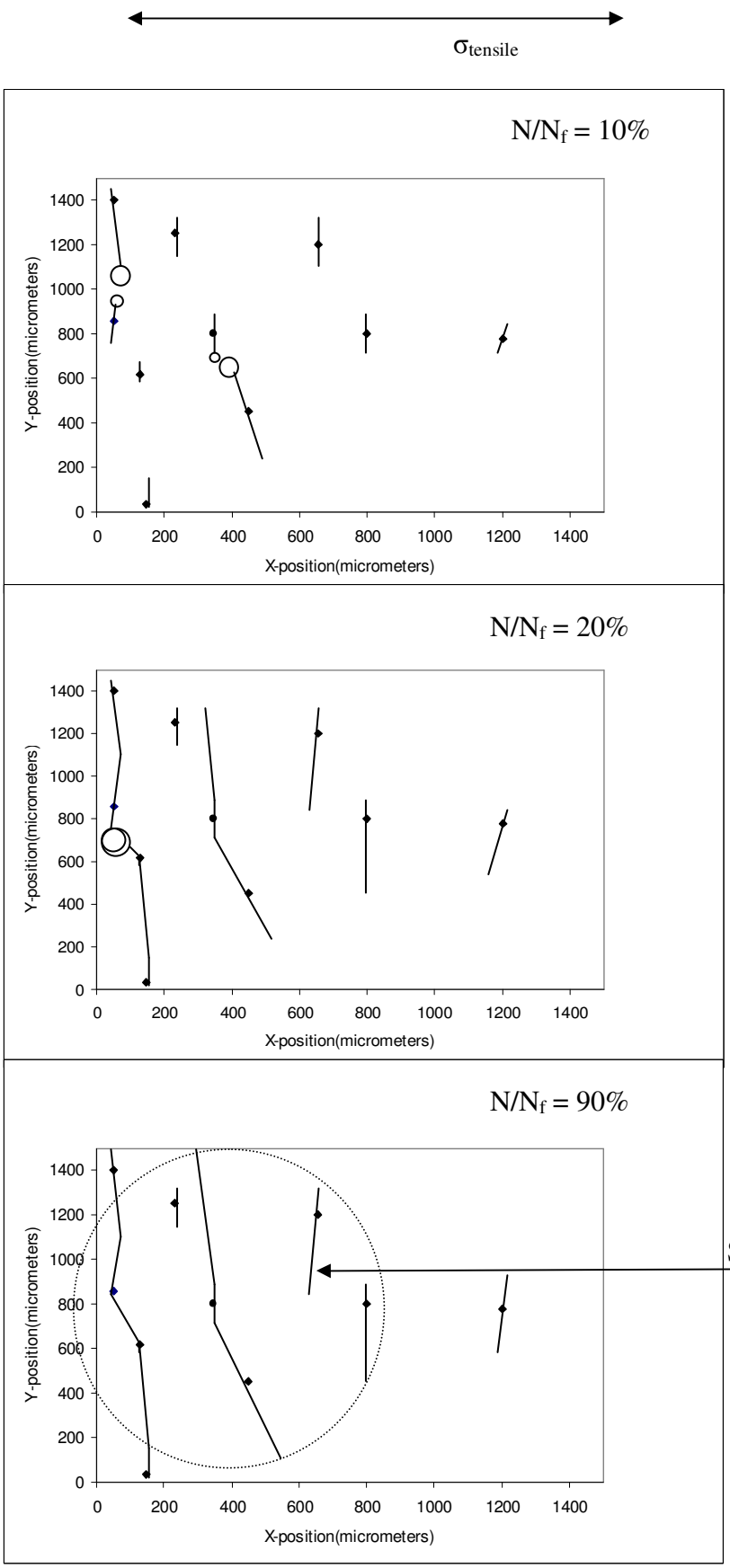
σtensile
N/Nf = 10%
Y-position(micrometers)
X-position(micrometers)
N/Nf = 20%
Y-position(micrometers)
X-position(micrometers)
N/Nf = 90%
Y-position(micrometers)
X-position(micrometers)
Shielded cracks

Figure 6.21: Short fatigue crack interactions at different life time fractions for HVOF lining.

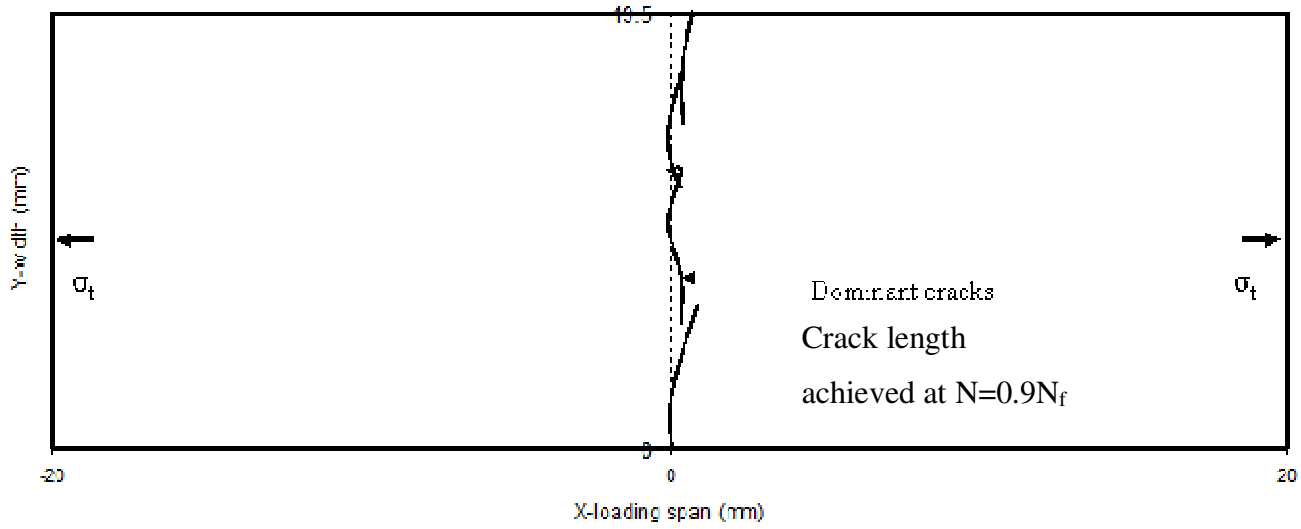

(a)

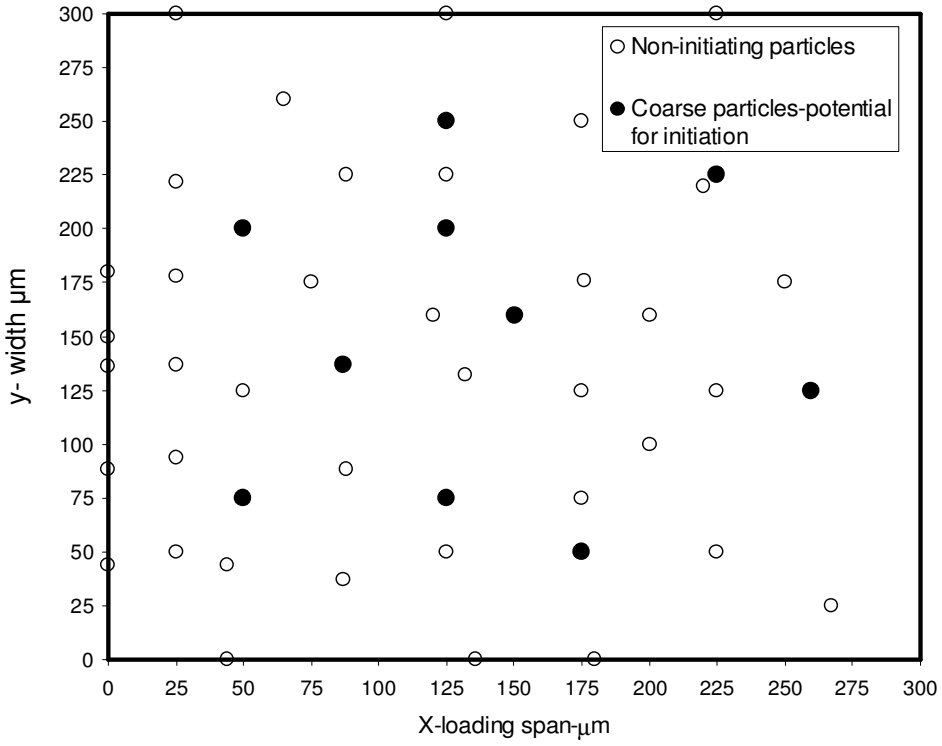

(b)

Figure 6.22: (a) A scaled schematic view of the AS20S flat bar lining loading span.(b) a magnified view of the central narrow width where microstructurally observed particle distribution is shown on the basis of FBT measured d_m.

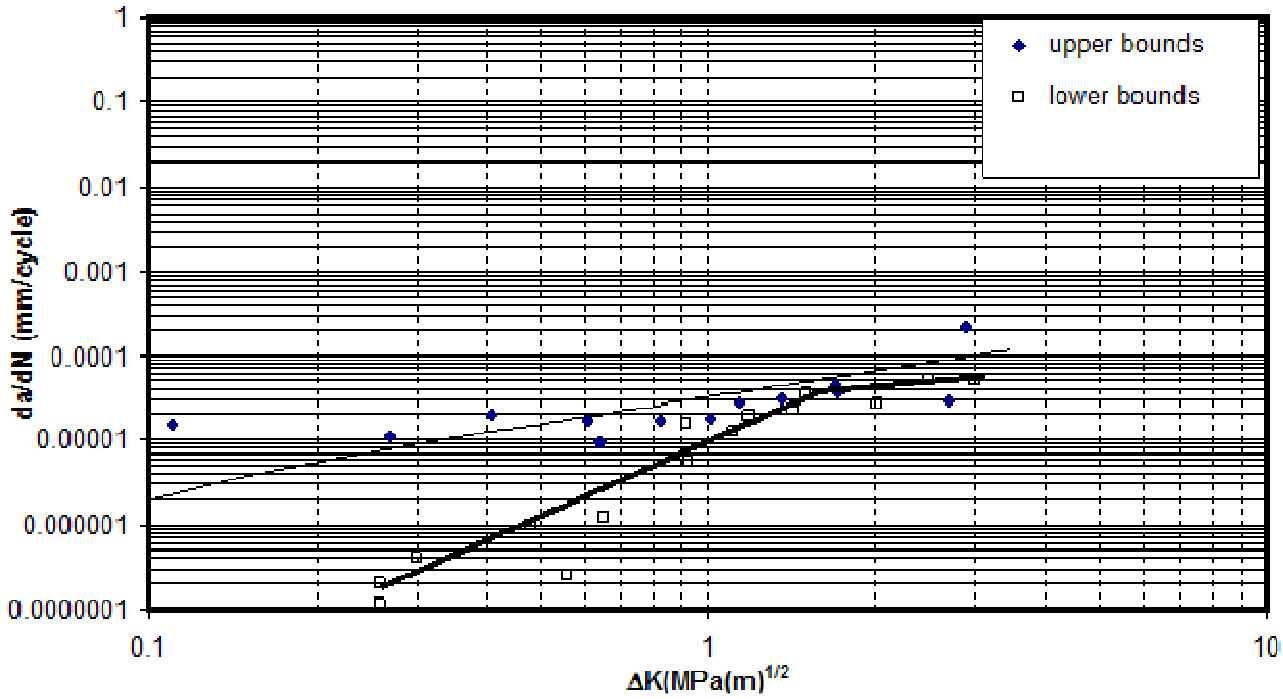

Figure 6.23: Experimentally measured and fitted upper and lower bounds of the crack growth curves.

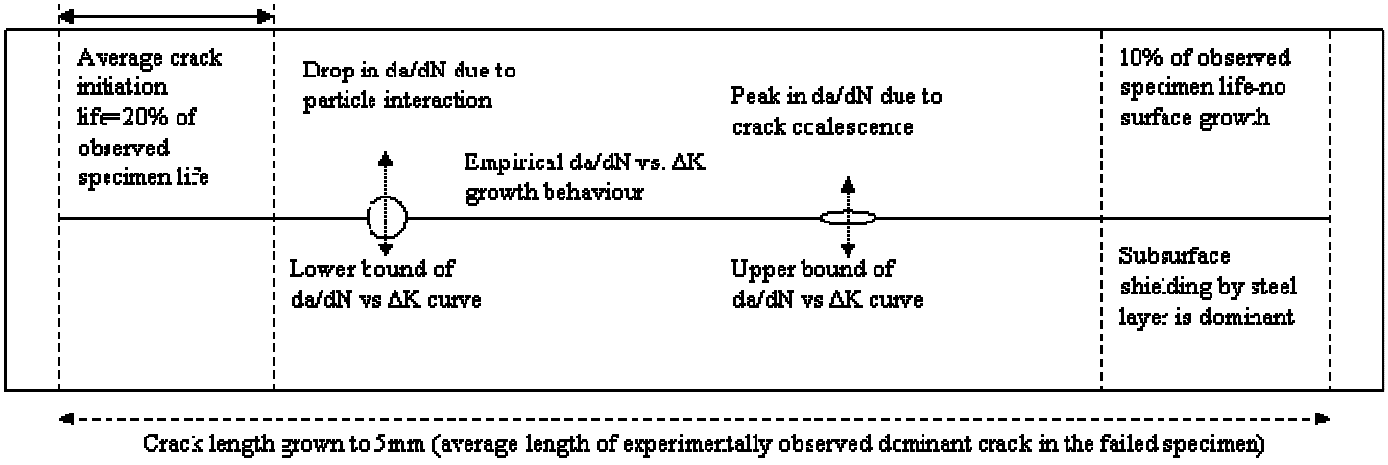

Figure 6.24: A schematic of assumed crack growth behaviour to a surface length of 5mm indicating the implementation of upper and lower growth bounds.

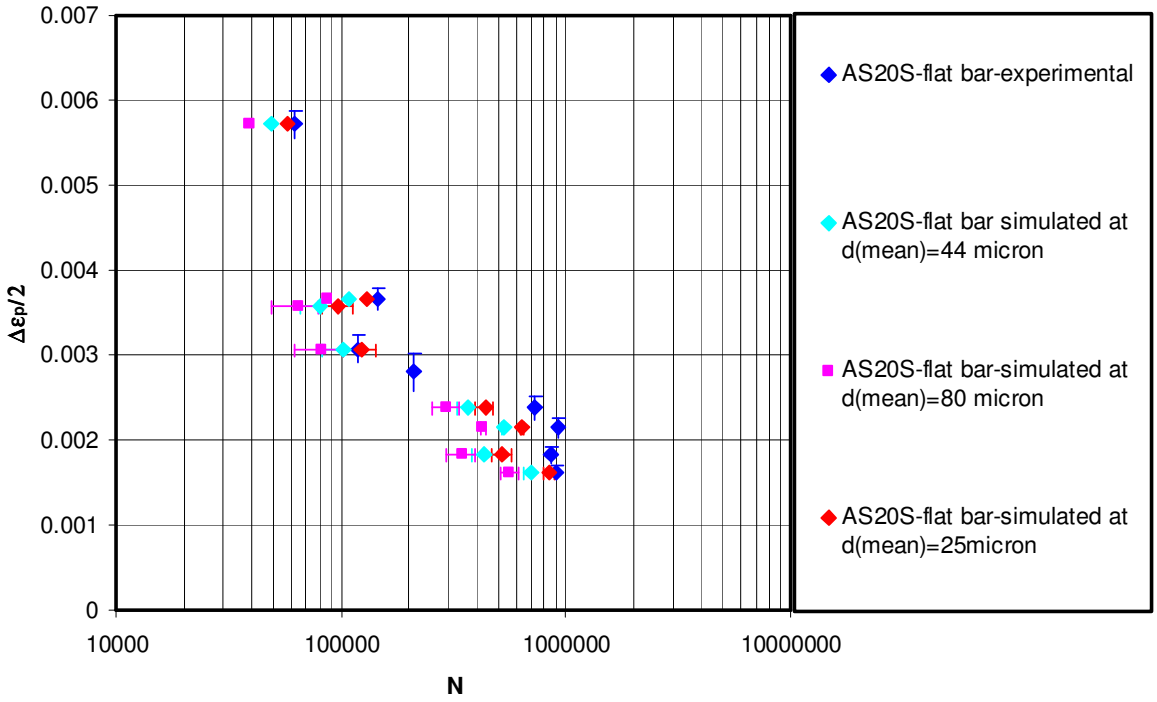

Figure 6.25: Fatigue life of AS20S flat bar specimens measured experimentally compared to the estimated life time data.

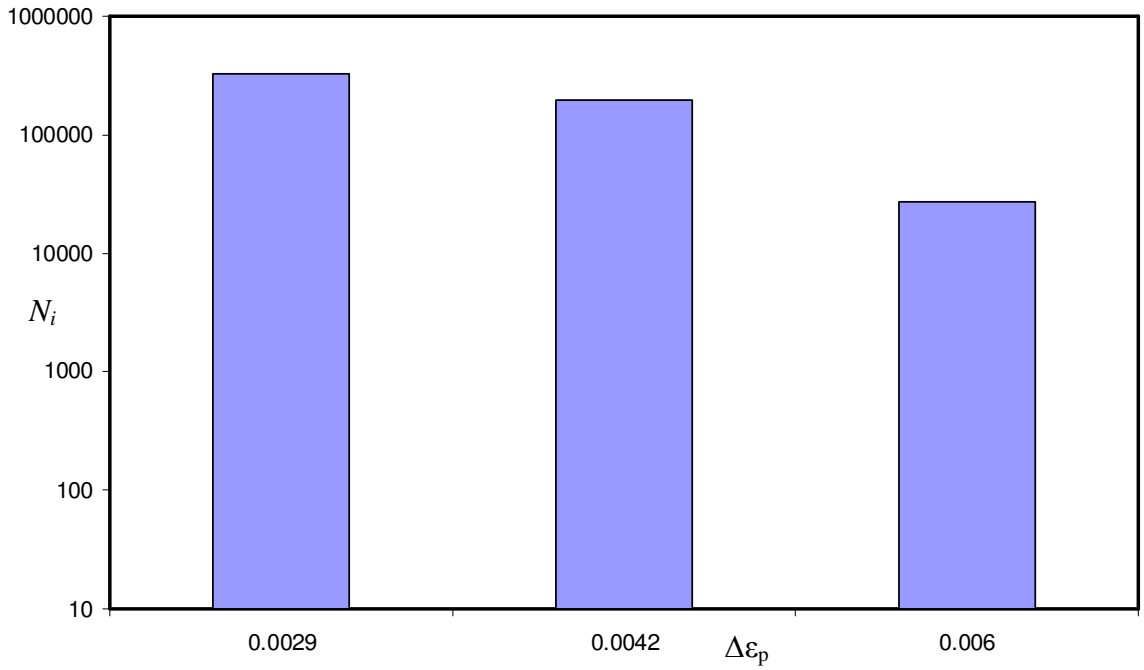
1000000
100000
10000
N_i
1000
100
10
0.0029
0.0042
$\Delta\varepsilon_p$
0.006

(a)

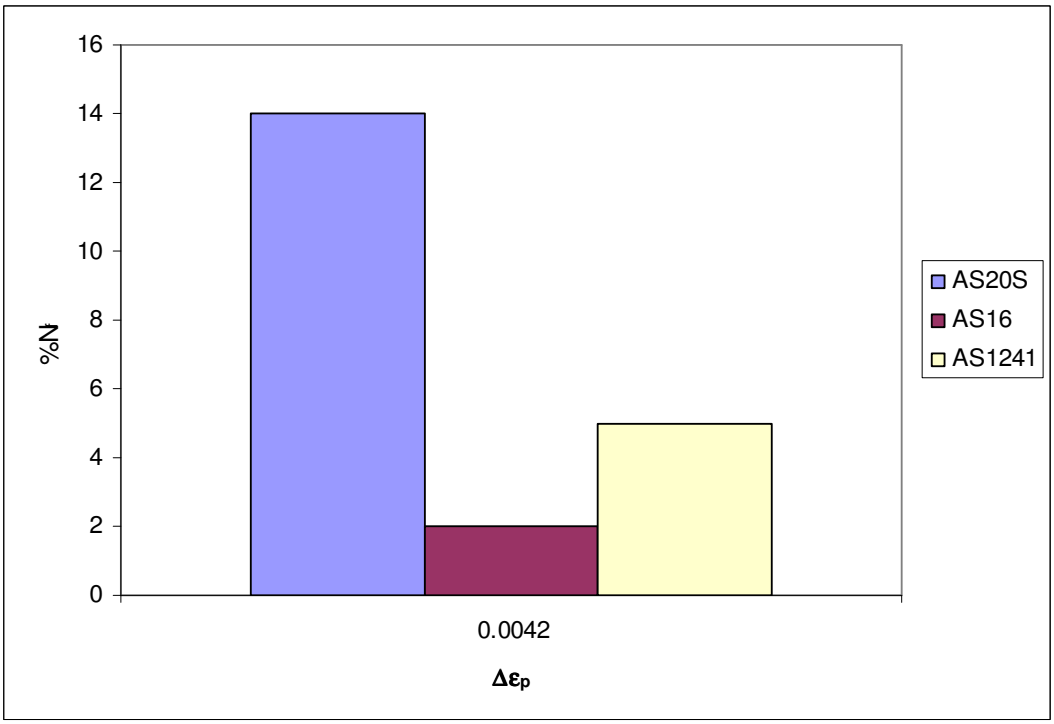
16
14
12
10
8
6
4
2
0
%N
0.0042
Δεp
AS20S
AS16
AS1241

(b)

Figure 6.26: (a) A comparison of fatigue initiation life of the AS20S flat bars at different plastic strain amplitudes. (b) A comparison of the fatigue initiation life of the AS20S flat bar with the previous RB systems at the same plastic strain levels.

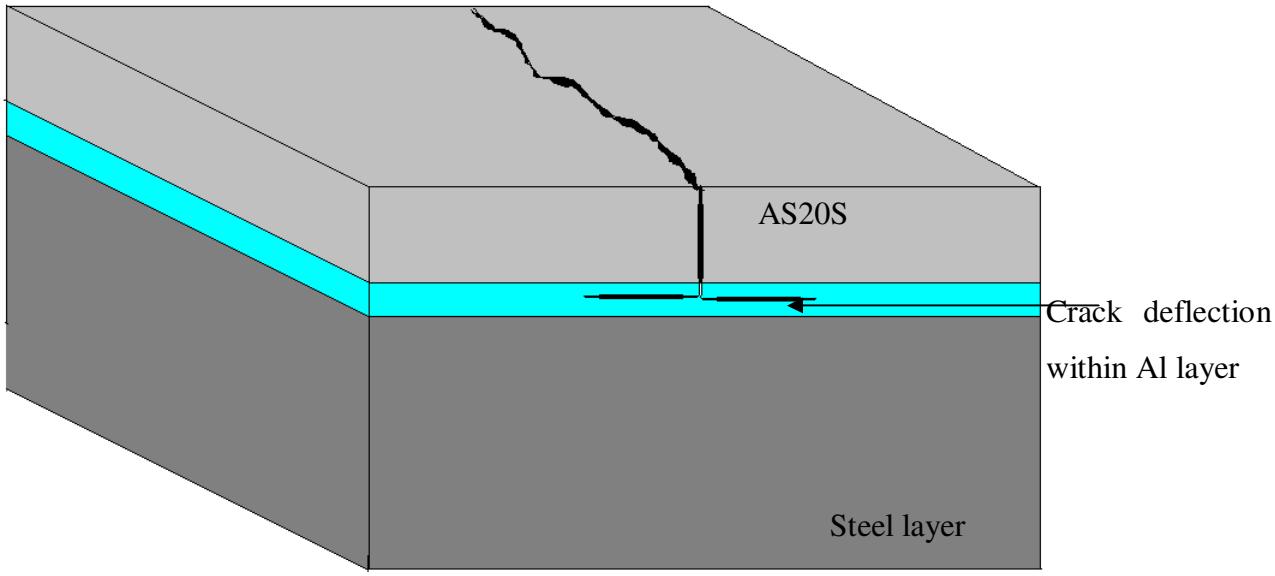

(a)

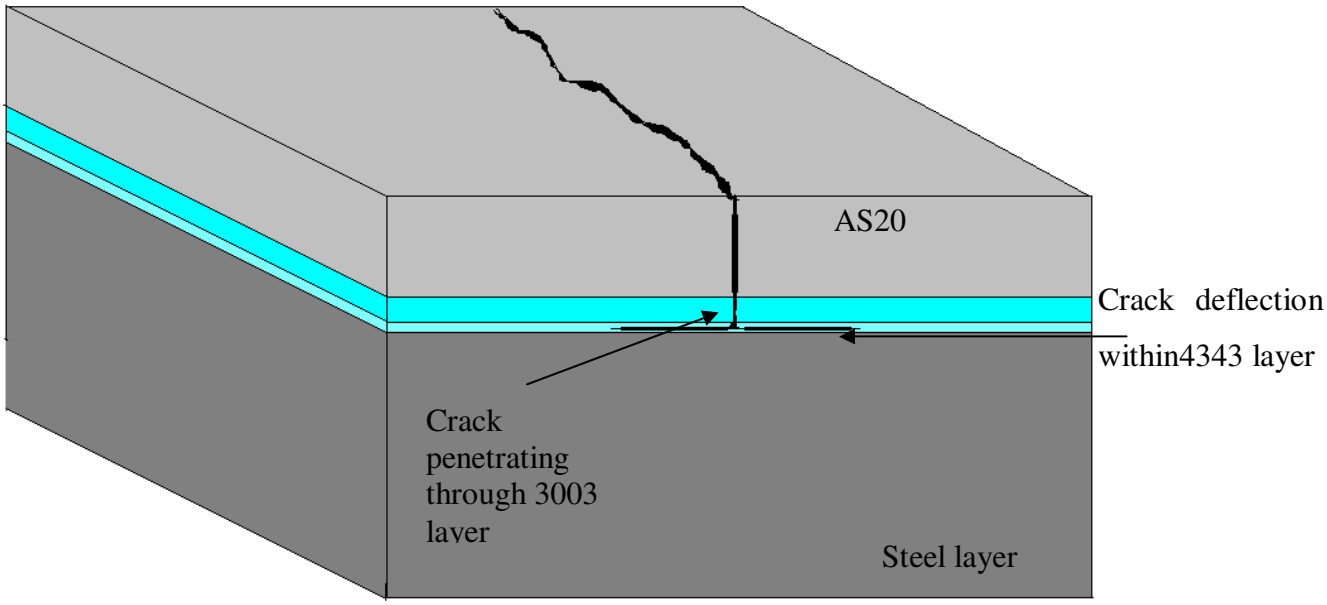

(b)

Figure 6.27: A schematic of layers showing effect of different layers on subsurface crack tip shielding.

7 SUMMARY, CONCLUSIONS AND FUTURE WORK

7.1. Summary of key results and conclusions

7.1.1. Microstructural and mechanical characteristics

Microstructural study of the cross section of roll bonded AS20S and AS20 systems (both in the form of finished bearings as well as flat bars) showed clearly distinguishable lining layer, interlayer and backing layers. The lining layer in the unetched condition appeared as a complex multiphase alloy. This layer was the same for both AS20S and AS20 systems, the only difference being the use of a rather complex interlayer (brazed sheet) for the AS20 system. Compared to the previous AS1241 (*Al-12Sn-4Si-1Cu*) and AS16 (*Al-20Sn-1Cu-0.25Mn*) lining alloys, the AS20S/AS20 lining (*Al-6.5Sn-2.5Si-1Cu-1Ni-0.25Mn*) showed widely scattered intermetallics ($AlNi_3$ type) encapsulated by *Sn* with the presence of very few individually identifiable *Sn* and *Si* particles. The intermetallics were found to be harder than *Sn* and comparable to *Si* particles. The AS20S lining alloy showed increased yield strength and hardness over the AS16 and AS1241 linings. Pure *Al* foil used as the interlayer of the AS20S appeared as homogeneous phase and was softer than the multi phase brazed sheet used in the AS20 system.

The composition of the HVOF lining was similar to the previous AS16 lining; however instead of using an interlayer, the lining material in molten powered form was directly sprayed on the grit blasted steel layer resulting in a rough interface. The use of very high cooling rate in the HVOF process has resulted in the distribution of very fine *Sn* particles 20-200nm), although some coarse *Sn* regions appeared to be smeared out in the microstructure as a result of molten *Sn* squeezed between unmelt powder particles appearing as circular regions in the microstructure. The steel layer of the HVOF lining was annealed (no work hardening effects) and hence was much softer than the steel used in the RB systems

RB168 bearings showed a more complex layer architecture. The bronze lining of the RB168 bearing was much harder than all the *Al* based linings, however the top *Sn* overlay was much softer which was followed by a harder *Ni* layer (both had thickness ~7microns).

Annealing the bearing specimens at varying temperatures between 180-190C^{o} resulted in the growth of Ni_3Sn_4 type intermetallic layer at the *Ni-Sn* interface. This layer was found to be harder than the top *Sn* layer.

7.1.2. Microscale fatigue damage initiation and growth

The fatigue resistance of the *Al* based systems was studied on the basis of short crack initiation, surface and subsurface propagation behaviour. The phenomenon of initiation and early growth was very much dependent upon the lining microstructure. The probability of fatigue initiation in the *Sn* rich alloys (AS16) via coarser *Sn* particles and *Sn-Si* containing alloys (AS1241) via decohesion of coarser *Si* has been reduced by a modified microstructure (AS20S) with much less of these two microstructural constituents. Instead, the presence of a large number of hard intermetallics ($AlNi_3$ type) has reduced early crack initiation considerably. This effect was more prominent at low plastic strains at the lining surface. However these intermetallics tend to break with some evidence of decohesion of occasional individual *Sn* particles (and *Sn* layers encapsulating the hard intermetallics). Analytical and numerical modelling has concluded that the breaking of harder and coarser intermetallics was due to load transfer of the far field stress. Numerical modelling used to investigate stress fields around complex particle shapes (*Sn* around the intermetallics) has concluded that the decohesion of the *Sn* particle was due to the emerging high hydrostatic stresses at the intermetallic-*Sn* and *Sn*-matrix interface. The optimum shape of these particles to minimize hydrostatic stress was a more globular and fine shape (r_a ~1). The cracks once initiated grew consistently throughout a significant proportion of the fatigue life.

The existence of ultra fine *Sn* particles in the HVOF lining was deemed to offer more fatigue resistance; however crack initiation life was very short with fast early growth. The latter growth was sluggish resulting in the comparable overall lifetime behaviour (although with much scatter) as the RB systems.

The bronze lining (in the RB168 system) was much stronger and harder than the *Al* linings, however it had a complex series of very thin overlay layers. The very thin *Sn* overlay (5-7 microns) showed a straight trajectory of cracks due to the absence of any secondary phase features that could affect the crack trajectory.

7.1.3. Layer architecture

Apart from the microstructural factors affecting fatigue initiation at the lining surface, subsurface growth behaviour of the cracks has been found to affect the general fatigue behaviour. The effect of the subsurface layer architecture has been identified as equally important. The presence of a harder backing layer resulted in the deflection of the AS20S crack at the *Al* interlayer. When this interlayer was replaced by a harder brazed sheet of the same thickness (AS20), the crack tip instead of being shielded accelerated into the softer 4343 (*Al-6Si*) layer of the brazed sheet where it deflected very close to the steel layer.

Under similar loading conditions, the HVOF lining- backing interface could not remain intact as the crack penetrated through the lining towards the interface. Crack deflection along the apparently weak interface resulted in debonding of the lining layer that could cause spalling off of the lining during service.

In the more complex RB168 bearing systems, crack deflection could not be verified within top very thin *Sn* and *Ni* overlay layers. However, there was a slight evidence of crack deflection at the lining backing-interface when propagating from comparatively softer lining to the harder backing layer.

7.1.4. Fatigue life

7.1.4.1.Al based systems

The observed fatigue life measured on the basis of laboratory failure criteria was analyzed in the light of short fatigue crack initiation and growth behaviour. Fatigue lifetime curves on the basis of maximum lining surface plastic strain amplitude (since applied stresses were higher than the yield stress of the lining) for various systems successfully reflected intrinsic material fatigue behaviour.

The failure criteria were set on the basis of similar visual lining surface damage for the two specimen geometries. Hence, the fatigue resistance of each alloy analyzed on the basis of the lining microstructure (using a flat bar geometry) reflected the fatigue behaviour of the corresponding bearing specimen of that particular system. The fatigue resistance of the AS20S system appeared to be higher than all previous *Al* based systems. The harder brazed sheet used as an interlayer in the basic AS20 system did not retard subsurface penetration of cracks and

hence the observed life of the AS20S system was not significantly different from that of the AS20 system.

The HVOF lining appeared comparable to the RB systems in overall fatigue life predictions; however there are critical issues of considerable lining detachment from the backing layer and hence the simple laboratory lifetime estimations in terms of ε_p range and observations of surface crack growth behaviour is not a guarantee of the comparable performance of the HVOF bearing during actual engine operation. The integrity of the bonds between the lining layers, interlayer and backing layers of the RB systems keeps them essentially intact even after the subsurface penetration of the cracks. Significant detachment of portions of the HVOF lining in service may result in seizure of the bearings.

Surface crack growth behaviour of the AS20S flat bar lining when combined with an empirical crack growth model helped in assessing the fatigue life of a specimen tested at different stress levels; however more precise modeling requires growth data at low plastic strain amplitudes. Such models could be extended to simulate the lifetime behaviour of various other alloy systems.

7.1.4.2.Bronze bearings

Both overlay *Sn* (*Ni*-underneath) and lining layers of the RB168 bearing systems were single phase materials, contrary to previous AS20S lining which was a multiphase *Al* alloy. Surface and subsurface fatigue crack growth in the RB168 was less deflected than in the AS20S system. However overall fatigue resistance based upon plastic strain life comparison of the non-heat treated RB168 bearing system was comparable to the AS20S system. The RB168 system when annealed at 190^{o}C formed an interfacial *Sn-Ni* intermetallic layer harder than the *Sn* layer. The fatigue resistance of such systems on the basis of maximum lining plastic strain was then higher than the AS20S and non-heat treated RB168 bearing specimens. This has been attributed to the presence of an interfacial intermetallic layer, harder than *Sn* layer, that might have resisted/deflected subsurface crack penetration at a very fine scale.

7.1.5. Bearing tests for in-service performance

The industrial bearing tests carried out at the sponsoring company on accelerated sapphire rigs for various time intervals resulted in bearing lining failure under hydrodynamic loading conditions in a bearing housing. Laboratory based 3-point bend fatigue test data, when

converted to the rig test data format (average projected pressure of the bearing vs. number of cycles to failure) coincided surprisingly well with the rig test lifetime curves. This gave more confidence in linking the laboratory based performance assessment with industrial requirements to assess service conditions.

The results presented in this research provide guidelines for bearing architecture (thickness and nature of various layers) as well as microstructural understanding of fatigue initiation which could be transferred to component level macro mechanical crack growth models, although considerable work is required at the component modelling level to fully exploit the micromechanical level modelling of fatigue initiation and growth behaviour.

7.2. Future work

The present work has covered extensive experimental analysis of the fatigue behaviour of various multilayered bearing systems with some modelling work to explain fatigue crack initiation and growth mechanisms. However, some aspects clearly require further research. Suggested experimental and modelling work is as follows:

7.2.1. Experimental work

7.2.1.1.Materials characterization

Al based bearing systems have been extensively characterized on the basis of microstructural and mechanical properties, however, more consistent data for the mechanical properties of secondary phase particles (intermetallics) are still required using instrumented hardness measurement. Similar tests are required for the RB168 systems to characterize interfacial intermetallic layer between *Sn* and *Ni* layers. A significantly large number of indents made will give more consistent data that can be further used in the FE modelling of the micro-scale stress-strain fields. A further study of the growth kinetics of Ni_3Sn_4 interfacial layer in the RB168 system through a number of heat treatment variables could be combined with compositional (EDX) and structural analysis (X-Ray diffraction) to understand its nature.

7.2.1.2.Fatigue crack initiation and growth

Analysis of fatigue crack initiation and growth during this work used conventional surface replication techniques during interrupted fatigue tests; however direct monitoring of fatigue crack initiation and growth through a suitable microscopy set up may facilitate analysis

at a number of stress levels for various specimens. Acoustic Emission approaches could perhaps be tailored to set appropriate frequencies and sensor positioning in order to monitor crack initiation and growth events.

7.2.1.3.Subsurface crack deflection

Monitoring crack deflection in the very thin (5-7 micron) overlay layers of the RB168 system is still challenging. It could be investigated by conducting bearing tests at very low plastic strain amplitudes and then sectioning the specimen to see the crack morphology (using microscopy) in these overlay layers.

7.2.2. Overall life models

Calculation of plastic zone sizes need to be modified to include the effect of secondary phase particles upon the approaching crack tips. More precise estimation of the plastic zone size with a better understanding of particle distribution could define crack coalescence and shielding events in a better way. This may lead to improvement in the crack growth modelling work. Using the available materials property data, FE modelling can be carried out to study subsurface crack growth behaviour through various layers of different mechanical properties. Hence subsurface crack growth data could be linked with surface crack growth results and derive more appropriate models for the total fatigue life.

APPENDIX A: INDUSTRIAL STEEL BUYING SPECIFICATIONS

SPEC No. MS1006	GLACIER VANDERVELL LIMITED	GLACIER VANDERVELL
TITLE	CS1 & HS1 STEEL MATERIALS SUPPLY SPECIFICATION	

1. INTRODUCTION

Metal purchasing specification for extra deep drawing, aluminium killed, basic oxygen route steel supplied in coil lengths to:

BS 1449 : SECTION 1.1 1991, GRADE CS1 & HS1

GLACIER VANDERVELL REFERENCE - CS1/1, CS1/2 AND CS1/3

Note :

Although the main reference for this steel is CS1 or HS1 it should be suffixed /1, /2 and /3 to denote our requirements for hardness values for product manufacture. The suffixes will be mutually recognised by both the steel suppliers and GVL during manufacturing processes at each other's sites.

2. APPLICATION.

During processing at GVL the steel can be subject to heavy reduction.

Subsequent operations include blanking, bending and forming.

Our product is not machined generally on the steel side and must have a surface finish of 0.4 - 0.8 microns Ra.

3. CONDITION.

3.1 PRIME CONDITION.

The steel we purchase must be fit for the purpose for which we intend to use it as set out in paragraph 2 above.

3.2 GENERAL CONDITION.

The steel will be cold rolled. Up to 7.2 mm thick will always be produced from a coil route, although supply above 5.89 mm thick may be supplied cut to length from a coil route.

The steel will be bright annealed up to and including 5.89 mm thick. Above 5.89 mm and including 7.2 mm thick the steel may be normalised. Bright annealing or normalising to be done in a non carburising protective atmosphere.

In an event normalising or annealing must form part of the prime condition of acceptance.

All trimming and shearing operations must be carried out prior to final rolling.

Cementite in the steel should be granular and not platelet in form.

3.3 FREEDOM FROM DEFECTS.

The surface must be free from pits, roaks, laps, shelling (surface laminations), score marks and inclusions of foreign particles. The strip must be free from rust and surface staining such as caused by incorrect annealing atmosphere or burnt on oil. The edges must be free from burrs, tears, laps, distortion and coiling kinking. The steel must not kink under subsequent zero tension uncoiling by the user. The steel must be free from laminations throughout.

4. SIZE RANGE.

4.1. THICKNESS.
As arranged between factory and supplier in the range 0.46 mm to 7.2 mm.

4.2. WIDTH.
As arranged between factory and supplier in the range 64 mm to 380 mm.

4.3. LENGTH.
Maximum achievable as single length per coil up to 1044 mm maximum O/D.

4.4. WEIGHT.
500 kg per coil.
500 kg per bundle, coil cut to length.

4.5. LENGTH SUPPLY FROM COIL ROUTE.
On material over 5.89 mm thick, the cut length will be 1.600 metres.

5. TOLERANCES.

5.1. THICKNESS.

Thickness Range Over	Up to and including	Under 250 mm Wide	Over 250 mm Wide
0.40	0.60	± 0.030 mm	± 0.035 mm
0.60	0.80	± 0.035 mm	± 0.040 mm
0.80	1.00	± 0.035 mm	± 0.045 mm
1.00	1.20	± 0.040 mm	± 0.050 mm
1.20	2.00	± 0.045 mm	± 0.055 mm
2.00	3.00	± 0.050 mm	± 0.060 mm
3.00	6.00	± 0.075 mm	± 0.090 mm

On material produced from coil but delivered in flat lengths, the tolerance must not be worse than ± 0.075 mm.

5.2. WIDTH.
Over range, ± 0.38 mm.

5.3. TAPER.
Maximum permissible across strip :
Up to 130 mm wide = 0.013 mm
Over 130 mm wide = 0.025 mm

5.4. STRAIGHTNESS.
12.7 mm in any 3.0 metres with cumulative maximum of 76.2 mm in any 18 metres.

On cut length material, 3.2 mm in 1.6 metres.

Straightness to be checked on a flat surface against a straight edge.

6. PROPERTY REQUIREMENTS.

6.1. CS1/1

6.1.1. CHEMICAL ANALYSIS.

Carbon	**(C)**	0.08% max.
Manganese	**(Mn)**	0.45% max.
Sulphur	**(S)**	0.03% max.
Phosphorous	**(P)**	0.025% max.
Aluminium	**(Al)**	0.020 - 0.065%

6.1.2. MECHANICAL / PHYSICAL PRPERTIES.

UTS	280 - 355 MN/m^2
Elongation	25% minimum
Hardness	105 HV maximum
For Concast Supply:	
Hardness	115 HV maximum
Grain Size	5 - 7 ASTM

6.2. CS1/2.

6.2.1. CHEMICAL ANALYSIS.

As CS1/1

6.2.2. MECHANICAL / PHYSICAL PRPERTIES.

Hardness	170 - 210 HV
For Concast Supply:	
Hardness	180 - 220 HV

It is not necessary to specify mechanical / physical properties other than hardness as this material is to CS1/1 in the cold rolled condition.

6.3. CS1/3.

6.3.1. CHEMICAL ANALYSIS.

As CS1/1

6.3.2. MECHANICAL / PHYSICAL PRPERTIES.

Hardness	85 HV maximum

It is not necessary to specify mechanical / physical properties other than hardness for this material.

APPENDIX B: AS20S BEARING 3-POINT BEND TEST MODEL INPUT FILE

Software: Ansys 10

```
/FILNAM,20Sbng
/TITLE,20Sbng
/UNITS,SI
/PREP7
*cfopen,AS20sbngresults,txt
ET,1,82,,,2
MP,EX,1,70.083e3                ! material's elastic properties
MP,NUXY,1,.33
mp,ex,2,67.108e3
mp,nuxy,2,0.3
MP,EX,3,200903.535
MP,NUXY,3,.3
*ulib,20slining,txt
*use,20slining,1
*ulib,Alfoil,txt
*use,Alfoil,2                   ! defining elasto-plastic materials properties
*ulib,20ssteel,txt
*use,20ssteel,3
load=3000
csys,0
K,,0,0
CIRCLE,1,28.143,,,90,4
CIRCLE,1,26.343,,,90,4          !defining geometry
circle,1,26.299,,,90,4
CIRCLE,1,26.113,,,90,4
l,17,12
l,12,7
l,7,2
l,6,11
l,11,16
l,16,21
al,1,2,3,4,20,8,7,6,5,19
al,18,5,6,7,8,21,12,11,10,9
al,17,9,10,11,12,22,16,15,14,13
lsel,s,line,,20,22
lesize,all,0.06
lsel,all
lsel,u,line,,17,22,1
lsel,u,line,,4,16,4
lesize,all,,,20
lsel,s,line,,4,16,4
lesize,all,,,20,0.0l
allsell
lsel,s,line,,1,4,1
lccat,all
lsel,s,line,,5,8,1
lccat,all
lsel,s,line,,9,12,1
lccat,all
lsel,s,line,,13,16,1
```

```
lccat,all
eshape,2
mat,3
amesh,1                                  !meshing different areas
mat,2
amesh,2
mat,1
amesh,3
finish
/solu
!lsel,s,line,,17,19,1
!nsll,s,1
!d,all,uy
dk,2,all
dl,20,1,symm
dl,21,2,symm
dl,22,3,symm
fload=(load*(-1))/(2*29.49)              !defining applied loads
fk,6,fy,fload
allsel
antype,stat
nlgeom,1
time,1
deltim,(50/load)
autots,off
outres,all,all
solve
/post1
set,last
*get,maxstep,active,,set,sbst
*do,stepno,1,maxstep,1
set,,stepno
*get,timeinc,active,,set,time
loadinc=timeinc*load
ksel,s,kp,,21
nslk,s,1
*get,nodn,node,,num,max
allsel
*get,nstrx,node,nodn,s,x
*get,neptox,node,nodn,epto,x                  !getting results
*get,nepplx,node,nodn,eppl,x
*get,nepelx,node,nodn,epel,x
*vwrite,loadinc,nstrx,neptox,nepplx,nepelx
(F9.3," ",E15.9," ",E15.9," ",E15.9," ",E15.9)
*enddo
*cfclos
finish
```

APENDIX C: AS20S FLAT BAR 3-POINT BEND TEST MODEL INPUT FILE

Software: Ansys 10

```
/filnam,f20s1
/title,f20S1
/prep7
*cfopen,f20S1results,txt
et,1,82,,,2
mp,ex,1,70.083e3                !material's elastic properties
mp,nuxy,1,0.33
mp,ex,2,200903.5
mp,nuxy,2,0.3
mp,ex,3,67.108e3
mp,nuxy,3,.3
*ulib,20slining,txt
*use,20Slining,1
*ulib,Alfoil,txt                !materila's elasto-plastic properties
*use,Alfoil,3
*ulib,20ssteel,txt
*use,20ssteel,2
load=1000
!allsel
!csys,0
!aclear,all
!adele,all
!ldele,all
!kdele,all
!AS20s
lthick=0.38
ithick=0.042
bthick=1.82
span=20                         !defining geometry of specimen
Width=19.5
k
k,,lthick
k,,lthick+Ithick
k,,lthick+Ithick+bthick
k,,,span
k,,lthick,span
k,,lthick+Ithick,span
k,,lthick+Ithick+bthick,span
!h's
l,1,2
l,2,3
l,3,4
l,5,6
l,6,7
l,7,8
!V's
l,1,5
l,2,6
l,3,7
l,4,8
```

```
al,1,8,4,7
al,2,9,5,8
al,3,10,6,9

lsel,s,length,,span
lesize,all,,,100,50
lsel,s,line,,1,2,1
lesize,all,0.042
lsel,s,line,,4,5,1
lesize,all,0.042
lsel,s,line,,3,6,3
lesize,all,0.3
eshape,2
mat,1
amesh,1                                  !meshing different areas
!!!alter this one for interlayer!!!!
mat,3
amesh,2
mat,2
amesh,3
/solu
dl,1,1,symm
dl,2,2,symm
dl,3,3,symm
dk,4,all
fk,5,fx,load/(2*width)                   !defining load
allsel
antype,stat
nlgeom,1
time=1
deltim,(10/load)
autots,off
outres,all,all
solve
finish
/post1
set,last
*get,maxstep,active,,set,sbst
*do,stepno,1,maxstep,1
set,,stepno
*get,timeinc,active,,set,time
loadinc=timeinc*load
ksel,s,kp,,1
nslk,s,1
*get,nodn,node,,num,max
*get,nstressy,node,nodn,s,y
*get,neptoy,node,nodn,epto,y             !writing result file
*get,nepply,node,nodn,eppl,y
*vwrite,lthick,loadinc,nstressy,neptoy,nepply
(F9.3," ",F9.3," ",F9.3," ",E15.9," "E15.9)
*enddo
*cfclos
Finish
```

APPENDIX D: BASIC INPUT FILE FOR PARTICLE-STRESS-STRAIN MODELLING

Software: Ansys 10

```
/filnam,20S1
/title,20S1
/prep7
*cfopen,PP_rst_20S1,txt

!This file contains the Ansys code to generat a 2-D model of AS20S lining with embedded elliptical
!intermetallic partical encapsulated by Sn layer
!Constants used
pi=3.14
theta1=pi/2 ! angle through which partilce orientation is changed i.e. vary between 0-pi/2

!defining geometry of the ellipses, there are two ellipses i.e. outer and inner.
!R for outer and RM for inner major and minor axis
!note subscripts indicate the relevent ellipse
AR=3!   aspect ratio of inner ellipse
RM1=0.407
R1=RM1*AR
pcnt1=1!% of major axis to be increased to make outer layer
pcnt2=AR*pcnt1 !%of minor axis to be increased to make an outer layer of uniform thickness. vary bewteen 1-10

RM2=RM1+0.01*pcnt2*RM1
R2=R1+0.01*pcnt1*R1

!Draw elipses
*do,theta,pi/25,2*pi,pi/25
!k,,min1*cos(theta),maj1*sin(theta)
xcore=RM1*cos(theta)!coordinates required to change the orientation
ycore=R1*sin(theta)
xcorex=RM2*cos(theta)
ycorex=R2*sin(theta)
k,,xcore*cos(theta1)+ycore*sin(theta1),xcore*sin(theta1)-ycore*cos(theta1)
k,,xcorex*cos(theta1)+ycorex*sin(theta1),xcorex*sin(theta1)-ycorex*cos(theta1)
*enddo
*do,tstep,2,98,2
l,tstep,tstep+2
*enddo
l,2,100
*do,tstep,1,97,2
l,tstep,tstep+2
*enddo
l,99,1
lsel,s,line,,51,100,1
al,all

!generating layered ellipse area3
l,73,74
l,25,26
lsel,s,line,,87,100,1
lsel,a,line,,51,62,1
lsel,a,line,,101,102
```

```
lsel,a,line,,1,12
lsel,a,line,,37,50
al,all
lsel,s,line,,63,86,1
lsel,a,line,,13,36,1
lsel,a,line,,101,102,1
al,all
aadd,2,3
!gerating outer circle area5
!Parameters of outer circle
A1=pi*RM1*R1 !representing the average area of intermetallic particles
A3=A1/0.0052 !denominator is the ratio of the intermetallic area to the cell area
R=sqrt(A3/PI)! radius of the outer circle
!defining points of outer circle
k,,0,0
circle,101,R
l,103,6
l,105,46
lsel,s,line,,102,103,1
lsel,a,line,,23,50,1
lsel,a,line,,1,2,1
lsel,a,line,,105,106,1
al,all
lsel,s,line,,104,106,1
lsel,a,line,,101
lsel,a,line,,3,22,1
al,all
aadd,2,3
!generating outer matrix area6
k,,20,20
k,,20,-20
k,,-20,-20
k,,-20,20
l,106,107
l,107,108
l,108,109
l,109,106
l,106,102
l,108,104
lsel,s,line,,107,110,1
lsel,a,line,,101,102,1
al,all
lsel,s,line,,103,106,1
lsel,a,line,,109,110,1
al,all
aadd,2,3

!Materials property data
mp,ex,1,120000   !intermetallic
mp,nuxy,1,0.17
mp,ex,2,44180.56              !Sn
mp,nuxy,2,0.33
mp,ex,3,67.108e3!Al
mp,nuxy,3,0.3
mp,ex,4,70.083e3
mp,nuxy,4,0.33    !AS20 lining
```

```
!!!!input lining data
*ulib,20slining,txt
*use,20slining,4
*ulib,Alfoil,txt
*use,Alfoil,3
*ulib,tindata3,txt
*use,tin,2
et,1,82,,,0
ESIZE,0.04,0,
MSHAPE,0,2D
MSHKEY,0
mat,1
ESIZE,0.02,0,
CM,_Y,AREA
ASEL, , , ,       1
CM,_Y1,AREA
CHKMSH,'AREA'
CMSEL,S,_Y
AMESH,_Y1
CMDELE,_Y
CMDELE,_Y1
CMDELE,_Y2
mat,2
ESIZE,0.018,0,
CM,_Y,AREA
ASEL, , , ,       4
CM,_Y1,AREA
CHKMSH,'AREA'
CMSEL,S,_Y
AMESH,_Y1
CMDELE,_Y
CMDELE,_Y1
CMDELE,_Y2
mat,3
ESIZE,1.2,0,
CM,_Y,AREA
ASEL, , , ,       5
CM,_Y1,AREA
CHKMSH,'AREA'
CMSEL,S,_Y
AMESH,_Y1
CMDELE,_Y
CMDELE,_Y1
CMDELE,_Y2
mat,4
ESIZE,1.8,0,
CM,_Y,AREA
ASEL, , , ,       6
CM,_Y1,AREA
CHKMSH,'AREA'
CMSEL,S,_Y
AMESH,_Y1
CMDELE,_Y
CMDELE,_Y1
CMDELE,_Y2
```

```
/solu
lsel,s,line,,106
nsll,s,1
d,all,all
lsel,s,line,,108
nsll,s,1
d,all,uy,0.08
allsel
antype,stat
/eof
antype,stat
solcon,1
nlgeom,1
time=1
deltim,0.1,0.01,.1
autots,1
solve
finish
/eof
```